Theses and Dissertations   Student Graduate Works

3-21-2013

Collisional Broadening and Shift of D1 and D2 Spectral Lines in Atomic Alkali Vapor - Noble Gas Systems

Robert D. Loper

Follow this and additional works at: https://scholar.afit.edu/etd

Part of the Physics Commons

COLLISIONAL BROADENING AND SHIFT OF D1 AND D2 SPECTRAL LINES IN ATOMIC ALKALI VAPOR - NOBLE GAS SYSTEMS

DISSERTATION

Robert D. Loper, Jr., Captain, USAF

AFIT- ENP-DS-13-M-03

DEPARTMENT OF THE AIR FORCE
AIR UNIVERSITY

AIR FORCE INSTITUTE OF TECHNOLOGY

Wright-Patterson Air Force Base, Ohio

AFIT- ENP-DS-13-M-03

COLLISIONAL BROADENING AND SHIFT OF D1 AND D2 SPECTRAL LINES IN ATOMIC ALKALI VAPOR – NOBLE GAS SYSTEMS

DISSERTATION

Presented to the Faculty

Department of Engineering Physics

Graduate School of Engineering and Management

Air Force Institute of Technology

Air University

Air Education and Training Command

In Partial Fulfillment of the Requirements for the

Degree of Doctor of Philosophy in Applied Physics

Robert D. Loper, Jr., BS Physics, MS Physics

Captain, USAF

March 2013

COLLISIONAL BROADENING AND SHIFT OF D1 AND D2 SPECTRAL LINES IN ATOMIC ALKALI VAPOR - NOBLE GAS SYSTEMS

Robert D. Loper, Jr., BS, MS

Captain, USAF

Approved:

_____   28 Feb 2013

David E. Weeks (Chairman)   Date
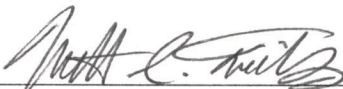
_____   28 FEB 2013

Glen P. Perram (Member)   Date
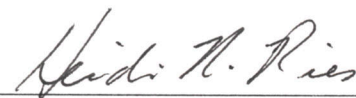
_____   28 Feb 2013

Matthew C. Fickus (Member)   Date

Accepted:

_____   4 Mar 2013

Heidi R. Ries   Date
Interim Dean, Graduate School of Engineering
    and Management

AFIT- ENP-DS-13-M-03

Abstract

The Baranger model is used to compute collisional broadening and shift of the D1 and D2 spectral lines of M + Ng, where M = K, Rb, Cs and Ng = He, Ne, Ar, using scattering phase shift differences which are calculated from scattering matrix elements. Scattering matrix elements are calculated using the Channel Packet Method where the collisions are treated non-adiabatically and include spin-orbit and Coriolis couplings. Non-adiabatic wavepacket dynamics are determined using the split-operator method together with a unitary transformation between adiabatic and diabatic representations. Scattering phase shift differences are thermally weighted and integrated over energies ranging from $E = 0$ Hartree up to $E = 0.0075$ Hartree and averaged over values of total angular momentum that range from $J = 0.5$ up to $J = 400.5$. Phase shifts are extrapolated linearly to provide an approximate extension of the energy regime up to $E = 0.012$ Hartree. Broadening and shift coefficients are obtained for temperatures ranging from $T = 100$ K up to $T = 800$ K and compared with experiment. Predictions from this research find application in laser physics and specifically with improvement of total power output of Optically Pumped Alkali Laser systems.

Acknowledgments

I would like to thank Professors David Weeks, Glen Perram and Matthew Fickus for their invaluable guidance at each step in this research, from initial concept to completed calculations and realized document. I would like to thank David Lewis for providing computer simulation code from his own dissertation research for calculating scattering matrix elements. I would like to thank L. Blank for providing interaction potentials from his own dissertation research and for providing data from his full integration of the Anderson-Talman model with which to compare results.

Robert D. Loper, Jr.

Table of Contents

List of Figures

List of Tables

Acronyms and Definitions

AFIT	Air Force Institute of Technology
AFRL	Air Force Research Laboratory
au	atomic units
CFT	Continuous Fourier Transform
COTS	Commercial Off-The-Shelf
CsAr	Cesium+Argon
CsHe	Cesium+Helium
CsNe	Cesium+Neon
DE	Directed Energy
DFT	Discrete Fourier Transform
DoD	Department of Defense
DSRC	DoD Supercomputing Resource Center
FFT	Fast Fourier Transform
FWHM	Full Width at Half Maximum
HPC	High-Performance Computing
HWHM	Half Width at Half Maximum
KAr	Potassium+Argon
KHe	Potassium+Helium
KNe	Potassium+Neon
M + Ng	Metal + Noble gas
Nd:YAG	Neodymium-doped Yttrium Aluminum Garnet
OPAL	Optically Pumped Alkali Laser
RbAr	Rubidium+Argon
RbHe	Rubidium+Helium
RbNe	Rubidium+Neon
USAF	United States Air Force

COLLISIONAL BROADENING AND SHIFT OF D1 AND D2 SPECTRAL LINES
IN ATOMIC ALKALI VAPOR - NOBLE GAS SYSTEMS

I. Introduction

This chapter introduces the dissertation research and its documentation. Section 1.1 provides the motivation for the research including its potential connection with ongoing experimental work and USAF research interests. Section 1.2 provides a basic summary of the objectives for this research. Section 1.3 concludes this chapter with an overview of the dissertation.

1.1.   Motivation

Early descriptions of the broadening and shifting of atomic spectral lines resulted in the ubiquitous *s, p, d, ...* notation, where *s* and *d* described sharp and diffuse spectral line shapes. This qualitative description was used in atomic spectroscopy before the principles of quantum mechanics had been developed. The first quantum-based efforts to describe the broadening and shifting of spectral lines began with Weisskopf, who attempted the first quantum description of line broadening using a WKB approximation in a semiclassical approach (Weisskopf, 1932a, 1932b), and Jabloński, who also used a WKB approximation but treated collisions quantum mechanically (Jabloński, 1945). These efforts culminated in the three principal models of Anderson-Talman (Anderson, 1949, 1952; Anderson and Talman, 1956; Tsao and Curnette, 1962), Baranger (Baranger 1958a, 1958b, 1958c, 1962), and Szudy-Baylis (Szudy and Baylis, 1977, 1996).

The Anderson-Talman model is a semiclassical model that uses the difference potential corresponding to the spectral line to be examined. This model assumes a classical straight-line trajectory of the perturber atom in the reference frame of the emitter/absorber atom and integrates collisions over the set of all possible impact parameters. Only the spectral line itself is treated quantum-mechanically. Usually the

difference potential to be used is either modeled as a Lennard-Jones potential or fit to the functional form of a Lennard-Jones potential (Jones, 1924a, 1924b). Experimental techniques include working Anderson-Talman in reverse, starting with the line shape, to estimate Lennard-Jones potential coefficients (Pitz, Wertepny, and Perram, 2009; Pitz, Fox, and Perram, 2010). Recent theoretical efforts have integrated the Anderson-Talman model rigorously using full *ab initio* interaction potentials (Blank, Weeks, and Kedziora, 2012). While the Anderson-Talman model does predict the full spectral line shape, including core and satellite features (Smith, Cooper, and Roszman, 1973), it is not a fully quantum-mechanical model. Because Anderson-Talman generates broadening and shift coefficients for each potential energy surface, it does not intrinsically handle coupling between surfaces during a collision, though an average can be estimated to handle coupled surfaces that contribute to a given spectral line. Lennard-Jones potentials can be constructed which under the Anderson-Talman model give results that compare well with experiment (Allard, Sahal-Brechot, and Biraud, 1974; Kielkopf and Knollenberg, 1975; Kielkopf, 1976; Kielkopf and Allard, 1979; Allard, Biraud, and Chevillot, 1988; Ciurylo and Szudy, 1997; Allard, Royer, Kielkopf, and Feautrier, 1999; Alioua and Bouledroua, 2006; Alioua, Bouledroua, Allouche, and Aubert-Frécon, 2008; Allouche, Alioua, Bouledroua, and Aubert-Frécon, 2009), but the constructed Lennard-Jones potentials do not correspond to physical potential energy surfaces.

The Baranger model builds directly from the work of Jabloński and is a fully quantum-mechanical model. Like Anderson-Talman, Baranger assumes the reference frame of the emitter/absorber atom. Baranger uses the impact approximation, which assumes that the duration of a collision is much shorter than the time between collisions. The impact limit forces one to focus more on the core features of the collision-broadened spectral line than on the wings or satellite features. Allard introduces an approximation of the Baranger model to include coupling (Allard and Kielkopf, 1982). Ciurylo and Szudy attempt to extend the Baranger model away from the impact limit to account for finite collision duration (Ciurylo and Szudy, 2001). The only predictions found in the literature have calculated broadening and shift under adiabatic potentials for lighter alkali (Li, Na, K) perturbed by He (Leo, Peach, and Whittingham, 2000; Mullamphy, Peach,

Venturi, Whittingham, and Gibson, 2007), primarily for astrophysical application. These calculations are limited by the semi-classical treatment of collisions (Peach, 2010) and the neglect of fine structure transitions (Mullamphy, Peach, Venturi, Whittingham, and Gibson, 2007).

The Szudy-Baylis model is a quantum-mechanical model that seeks to predict satellite features of spectral line shapes; that is, features that occur relatively far from the core of the spectral line. For these satellite features, the impact approximation breaks down (Szudy & Baylis, 1996). The Szudy-Baylis model uses Franck-Condon factors, radial overlap integrals of the final and initial one-perturber wavefunctions, to calculate features in the wings (or satellite features) of spectral lines. Calculations using the Szudy-Baylis model have given results for satellite features which compare well with experiment (Mies, Julienne, Band, and Singer, 1986; Alioua and Bouledroua, 2006; Alioua, Bouledroua, Allouche, and Aubert-Frécon, 2008).

Recent interest in the behavior of the non-adiabatic fine structure transitions of atomic alkali as they collide with noble gases has been generated by applications in astrophysics and the development of Optically Pumped Alkali Lasers (OPALs) (Rotondaro and Perram, 1997; Krupke, Beach, Kanz, and Payne, 2003; Beach, Krupke, Kanz, Payne, Dubinskii, and Merkle, 2004; Zhdanov, Ehrenreich, and Knize, 2006; Pitz, Wertepny, and Perram, 2009; Pitz, Fox, and Perram, 2010). Theoretical motivations include the study of line shapes to discover information about the potential energy surfaces that governs collisions between alkali and noble gases. Astrophysical applications include diagnostics for alkali environment, specifically in the measurement of spectral lines of alkali mixed with helium. Brown dwarf stars, in particular, have atmospheres that consist largely of helium with relatively small concentrations of light alkali such as lithium. Understanding the effects of collisional (or pressure) broadening can lead to a better understanding of the particular compositions of observed stellar atmospheres (Zhu, 2005, 2006; Mullamphy, 2007). OPAL applications include the broadening of spectral lines to increase absorption of energy from the optical pump. The analysis and modeling of pressure broadening and shifting of spectral lines has been

central to the study of spectroscopy. An Optically Pumped Alkali Laser (OPAL) utilizes an array of diode lasers as a pump source and an alkali vapor – noble gas mixture as a gain medium. Krupke specifies the goals for an OPAL system, "Application end-users continue to call for multi-kilowatt lasers with near-diffraction-limited output beam quality, wavelengths of < 1060 nm, higher efficiency and compactness, and decreased cost-of-ownership, compared to traditional lamp-pumped Nd:YAG solid state lasers and electrically-pumped CO_2 gas lasers" (Krupke, 2003). However, an OPAL is limited by two major factors: (1) the emission spectrum of the optical pump, and (2) the absorption spectrum of the alkali vapor – noble gas gain medium. The spectrum of the diode pump laser generally is much broader than the absorption lines of the gain medium, so much of the pump laser energy is lost in the system. There is ongoing research in the field of laser physics toward correcting both limiting factors, narrowing the emission spectra of optical pumps and broadening the absorption spectra of alkali vapor gain media. This dissertation focuses on the latter—investigation of collisional line broadening in the alkali vapor – noble gas system as an attempt to mitigate power loss by broadening the absorption lines of the gain medium to better match the pump laser emission characteristics.

1.2.   Objectives

This research uses the Baranger model to simulate collisional line broadening of relevant alkali vapor – noble gas mixtures under varied conditions (e.g., varying temperature and pressure). The particular mixtures of interest are those in typical use in OPAL systems. In principle, this examination should be applicable to any mixture of alkali vapor (Li, Na, K, Rb, Cs, or Fr) and noble gas (He, Ne, Ar, Kr, Xe, or Rn). However, the D_2 transitions for K, Rb, and Cs lie between 760 and 850 nm, an optical band in which the atmosphere is transparent. Powerful and efficient commercial off-the-shelf (COTS) laser diodes are available in this optical band (Krupke, 2003). The resulting OPAL system must radiate in wavelengths that transmit in Earth's atmosphere; if the laser attenuates significantly in the atmosphere, it is not useful because energy

cannot be delivered reliably and substantially to the target. As an additional limitation on mixtures, the spin-orbit splitting is small enough in Li and Na series that it is difficult to pump the D_2 line without also pumping the D_1 line. This significantly hinders the energy level population that is necessary for lasing to occur. Other concerns limit which noble gases may be viable for OPAL systems. First, Kr and Rn are both radioactive (as is the alkali Fr); since neither has a stable isotope, neither can be used reliably in such a system. Second is a matter of scientific interest: since Ne appears enough like either He or Ar (depending on the model used), some research groups simply omit the use of Ne altogether, but we will continue to consider it. Thus, we shrink from thirty-six potential combinations (Li, Na, K, Rb, Cs, or Fr with He, Ne, Ar, Kr, Xe, or Rn) to nine candidates (K, Rb, or Cs with He, Ne, or Ar).

The objective for this dissertation is to develop a model for line broadening in which the time evolution of the alkali vapor – noble gas system is handled through wavepacket propagation. The quantum-mechanical time-evolution operator for the system is governed by the Hamiltonian, and we will use the Fourier transform (specifically, the Fast Fourier Transform, or FFT) and its inverse to transform the wavefunction of the system between the momentum and position representations, as appropriate, in order to operate with the momentum-dependent and position-dependent portions, respectively, of the time-evolution operator. This method will be explained in detail in section 2.4. The normal method of examining atomic collisions is to approximate the colliding system of two atoms as a diatomic molecular system. This allows one to describe the system using appropriate Hund's states (Allard & Kielkopf, 1982; Bransden & Joachain, 2003; Drake, 2006; Zare, 1988). It is through this approximation to molecular dynamics that we will utilize difference potentials in the context of this dissertation research.

This research exhibits several new features which set it apart from the current state of the field. First, the full *ab initio* potential energy surfaces are used; these potential energy surfaces have been calculated through many-body calculations by Blank (Blank, Weeks, and Kedziora, 2012). Second, collisions are treated quantum-

mechanically and nonadiabatically and include spin-orbit and Coriolis coupling. Third, calculations are made with no approximations beyond those of the impact limit.

1.3.   Overview

This dissertation will begin with an overview of collisional line broadening from the perspective of the Anderson-Talman model and then the Baranger model. Following the overview of these two models we will outline the research methodology used to calculate spectral line broadening and shift coefficients. This portion of the dissertation will outline the overall research process and a detailed description of the simulation process. The primary programming language used in writing computer simulations for this research is Fortran 90, with some Fortran 77 legacy code used where appropriate, compiled and executed on AFIT's Linux Cluster and on supercomputers run by the DoD High Performance Computing Modernization Program. Preparation of initial wavepackets and analysis of the output data are achieved using Matlab code. Here, the dissertation will include discussion of the potential limitations in simulation methods and theory-experiment interface. Finally, the dissertation will lay out research results and a discussion of the potential impact of those results.

II. Theoretical Background

This chapter presents the technical background for major concepts that will be utilized and developed in this dissertation research. This chapter is not intended necessarily as a 'first principles' development but rather to provide sufficient detail for the research to be carried out in a manner that can be repeated and verified. This chapter provides a basic overview of the physics involved, from the quantum physics of spectral lines and collisional line broadening, to the wavepacket propagation algorithm used to generate scattering matrix elements, to the Anderson-Talman model and the Baranger model which are the standards for this field. Section 2.6 gives an overview of how coupling processes could be handled, especially in the context of the Baranger model.

2.1.   Quantum Physics of Spectral Lines

An isolated atom, going through a transition between quantum states, radiates or absorbs at a single frequency corresponding to the difference in the energies of the two quantum states, given by $\omega = \Delta E / \hbar$. If we plot intensity as a function of frequency, we get a *spectral line* that looks like a Dirac delta function at ω, the frequency corresponding to the transition.

$$f(\omega) = \delta(\omega - \omega_0)$$
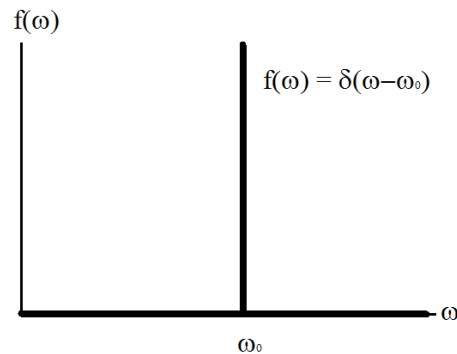
Fig. 2.1a: Dirac delta function

However, we find that isolated atoms do not exist in nature, and that transitions do not occur at a specific single frequency, so we should already expect that a given atomic transition might correspond to a distribution of frequencies. This distribution of frequencies causes the shape of the spectral line to be broadened from the Dirac delta function.

Three primary physical processes contribute to spectral line broadening. First, the natural lifetime of excited atomic states creates what is called *natural broadening*. Second, the statistical distribution of velocities of atoms at a given temperature gives rise to *Doppler broadening*. Third, collisions between atoms at a given pressure give rise to *collisional broadening* (or pressure broadening). Since only collisional broadening depends on the particular mixture of atoms—that is, only this form changes the spectrum of one atom according to the particular type of other atom in a chamber with it—the background for this dissertation will concentrate on collisional broadening. Specifically, this dissertation is concerned with the application of two particular models of collisional line broadening: the semiclassical Anderson-Talman model (Anderson, 1949, 1952; Anderson & Talman, 1956; Allard & Kielkopf, 1982) and the quantum model of Baranger (Baranger, 1958a, 1958b, 1958c, 1962).

2.2.   Anderson-Talman Model

The Anderson-Talman model is a semiclassical model of collisional line broadening. This model views atomic collisions as classical collisions in the reference frame of a single atom. In other words, Anderson-Talman views the spectral features of a single atom as multiple atoms collide with it in a classical manner. Since spectral lines arise through quantum mechanics, and the collisions are treated classically, this is a semiclassical model of line broadening. Anderson and Talman claim that this semiclassical approach yields a fully functional model:

The theory to be developed here is exact when its basic assumptions about intermolecular forces are correct, except insofar as the actual numerical calculations may involve approximations. These intermolecular force assumptions, while not entirely realistic, are nonetheless the same as those of most previous statistical or generalized theories. Thus, while the present theory is of only limited importance as a calculation of actual experimental line shapes, it gives correctly, and we claim considerably clarifies, the relationship between statistical and impact theories. (Anderson & Talman, 1956)

The basic setup for this model is shown in Fig. 2.2a, below:
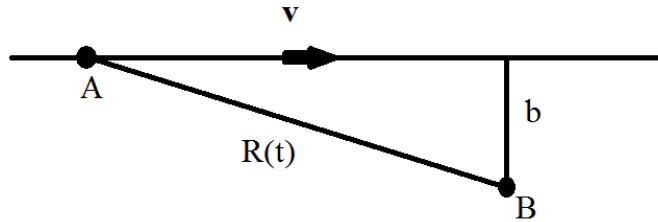
Fig. 2.2a: A classical collision

In this classical collision, atom A is assumed to scatter off of atom B with impact parameter (distance of closest approach) b. In the classical sense, atom A is considered to continue in straight-line motion at velocity **v** regardless of any interaction with atom B. The position of atom A at time t is:

$$x(t) = x_0 + vt, \tag{2.1}$$

where $(x - x_0)$ is the displacement of atom A. The electric field radiated by atom B, in the dipole approximation, is

$$E_z(t) = Cp_z(t) = Cqz(t). \tag{2.2}$$

Where C is a constant and $p_z(t) = qz(t)$ is the dipole moment of the radiator. We can include a phase factor, $e^{i\varphi(t)}$, to obtain:

$$E_z(t) = Cqz_0 e^{i\varphi(t)} = E_0 exp\{i\varphi(t)\}. \tag{2.3}$$

The phase is the instantaneous phase

$$\varphi(t) = \int_0^t dt'\omega(t') = \int_0^t dt'[\omega_0 + V_{ij}(t')], \tag{2.4}$$

where ω_0 is the unperturbed frequency, and $V_{ij}(t')$ is the difference potential between atoms A and B. (Note that the difference potential here has units of ω and is not the same as the potential.) So the radiated electric field is given by

$$E_z(t) = E_0 exp\left\{i\int_0^t dt'[\omega_0 + V_{ij}(t')]\right\}$$
$$= E_0 exp\left\{i\omega_0 t + i\int_0^t dt' V_{ij}(t')\right\}. \tag{2.5}$$

In general, we can split the last term of (2.5) into two pieces, representing elastic and inelastic collisions, respectively:

$$E_z(t) = E_0 exp\left\{i\omega_0 t + i\eta(t) - \frac{\gamma t}{2}\right\}. \tag{2.6}$$

We define $\eta(t)$ as the phase shift that results from elastic collisions, and we define the last term to represent damping from inelastic collisions. The first term represents the unperturbed oscillator. This brings us to another assumption of Anderson-Talman, the adiabatic assumption—the "perturbation changes in time slowly enough that other states do not mix appreciably with the excited and ground states" (Anderson & Talman, 1956). According to Anderson and Talman, the adiabatic assumption, "while never exactly valid, is, when carefully handled, seldom the source of serious errors" (Anderson & Talman, 1956).

Now we can calculate the line intensity as a function of frequency, which is given by:

$$I(\omega - \omega_0) = |\boldsymbol{E}(\omega - \omega_0)|^2$$

$$= E_z^*(\omega - \omega_0)E_z(\omega - \omega_0). \tag{2.7}$$

But our electric field is time-dependent, so we need to Fourier-transform the field from time-dependence to frequency-dependence in order to perform this intensity calculation. The Fourier transform gives us:

$$E_z(\omega - \omega_0) = \int_{-\infty}^{\infty} dt' \, E_z(t')e^{i(\omega-\omega_0)t'}. \tag{2.8}$$

With this Fourier-transformed field, we can calculate the line intensity:

$$I(\omega - \omega_0) = \int_{-\infty}^{\infty} dt \, E_z^*(t)e^{-i(\omega-\omega_0)t} \int_{-\infty}^{\infty} dt' \, E_z(t')e^{i(\omega-\omega_0)t'}$$

$$= \int_{-\infty}^{\infty} dt' \int_{-\infty}^{\infty} dt \, E_z^*(t)E_z(t')e^{i(\omega-\omega_0)(t'-t)}. \tag{2.9}$$

We can make the substitutions $\tau = t' - t$, or $t' = t + \tau$, so $dt' = d\tau'$ and (2.9) transforms into

$$I(\omega - \omega_0) = \int_{-\infty}^{\infty} d\tau \left[\int_{-\infty}^{\infty} dt \, E_z^*(t)E_z(t + \tau) \right] e^{i(\omega-\omega_0)\tau}. \tag{2.10}$$

We define the expression in square brackets in this equation to be the correlation function, $\Phi(\tau)$, and we define the squared field magnitude at t = 0 to be I_0, so the intensity becomes

$$I(\omega - \omega_0) = I_0 \int_{-\infty}^{\infty} d\tau \, \Phi(\tau)e^{i(\omega-\omega_0)(\tau)}. \tag{2.11}$$

As a related aside, let us consider the ergodic hypothesis, introduced by Boltzmann in 1871. According to the ergodic hypothesis, "the trajectory of a representative point passes, in the course of time, through each and every point of the relevant region of the phase space" (Pathria, 1996). This means that the ensemble average of a physical quantity is equal to the time average of that physical quantity (Pathria, 1996). Connecting back to our classical collision problem, since collisions are characterized by impact parameter (for a given type of collider), and the ergodic hypothesis represents an ensemble of collisions that fills the relevant space, the average over collisions can be replaced equivalently with an average over impact parameter and initial starting points x_0.

Now, the correlation function accounts for the total phase shift over the course of the radiation of the system:

$$\Phi(\tau) = exp\{-ng(\tau)\}. \tag{2.12}$$

This takes a time average of all the perturbations affecting the radiation, where n is the number density of the perturbers. Using the ergodic hypothesis, we can deduce that $g(\tau)$ is the average perturbation resulting from an impact:

$$g(\tau) = 2\pi \int_0^\infty b \, db \int_{-\infty}^\infty dx_0 \left[1 - exp\left\{ -\frac{i}{\hbar} \int_0^\tau dt \, V_{ij} \left[\{b^2 + (x_0 + \bar{v}t)^2\}^{1/2} \right] \right\} \right], \tag{2.13}$$

where, again, V_{ij} is the difference potential as a function of $\{b^2 + (x_0 + \bar{v}t)^2\}^{1/2}$, and we integrate over an annulus of impact parameters and over positions, as indicated in Fig. 2.2b, below.

$b+db$

b

B

A

$\bar{v}d\tau$

$dA = 2\pi b db$

$n = N/V = density$
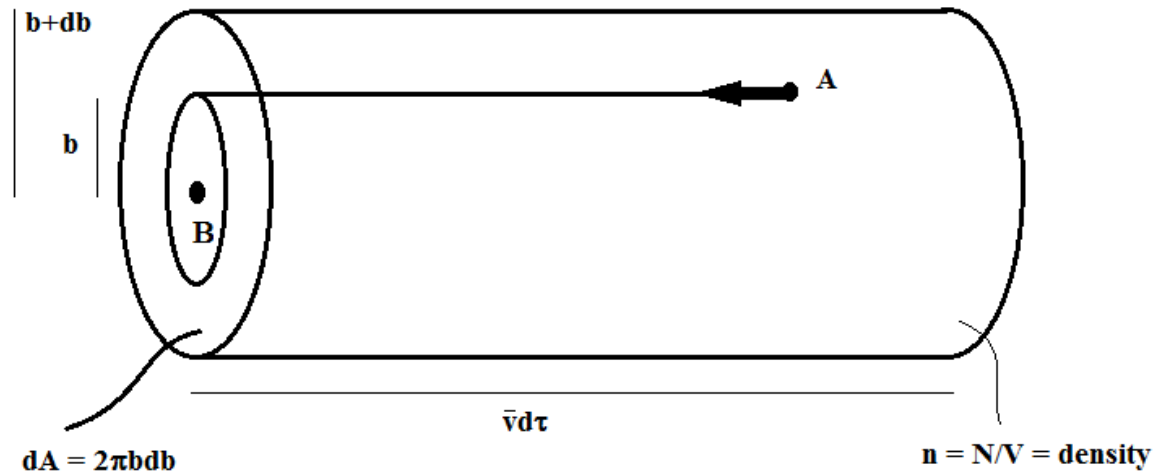
Fig. 2.2b: Integration over an annulus of impact parameters

In a sense, the exponential in $g(\tau)$ looks like a quantum-mechanical time-evolution operator.

Two limits are usually considered in the literature (Allard & Kielkopf, 1982). The first limit is the impact approximation, which takes the limit of $g(\tau)$ in the case of low perturber density n. This is equivalent to the limit of long times between collisions. The second limit is the static approximation, which takes the limit of $g(\tau)$ in the case of high perturber density.

The impact approximation also assumes a relatively short range for the potential, as indicated in Fig. 2.2c, below.

x_0

R

range of potential

$x_0 + \bar{v}\tau$

x

$V_{ij} = 0$

$V_{ij} \neq 0$

$V_{ij} = 0$
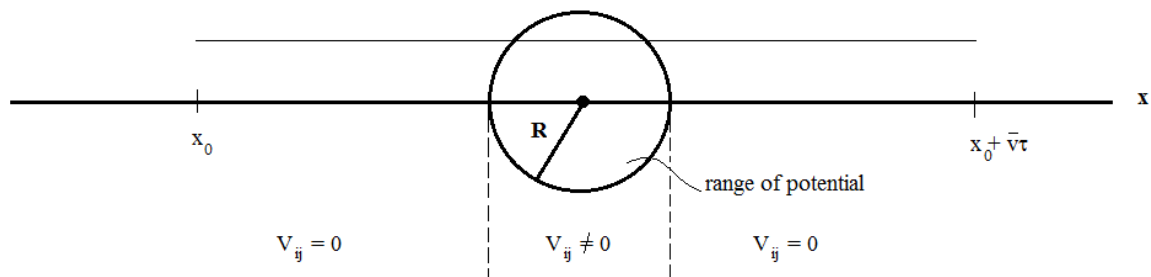
Fig. 2.2c: Impact approximation

13

We can recalculate (2.13) as

$$g(\tau) = 2\pi \int_0^\infty b \, db \int_{-\infty}^\infty dx_0 \left[1 - exp\left\{-\frac{i}{\hbar}\eta_s\right\}\right], \qquad (2.14)$$

where

$$\eta_s = \int_0^\tau dt \, V_{ij}\left[\{b^2 + (x_0 + \bar{v}t)^2\}^{1/2}\right], \qquad (2.15)$$

and we assume that V_{ij} does not contribute to η_s outside the sphere in Fig. 4 (that is, outside the range of the potential). This η_s integral essentially is an integral over trajectories of the perturber between x_0 and $x_0 + \bar{v}t$. We see some sample trajectories in Fig. 2.2d.
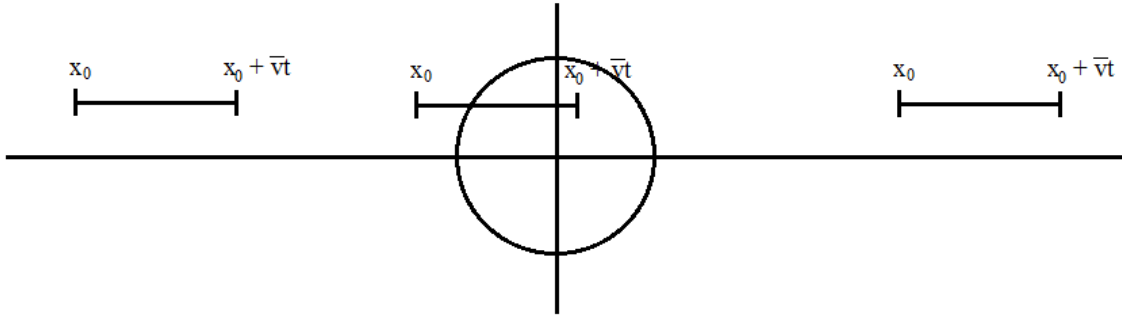
Fig. 2.2d: Sample impact trajectories

The η_s integral gains no contribution for trajectories which have no overlap with the region of influence of the potential (the circle in Fig. 2.2d). Now, η_s is constant for all trajectories that straddle the potential, as shown in Fig. 2.2e.

14
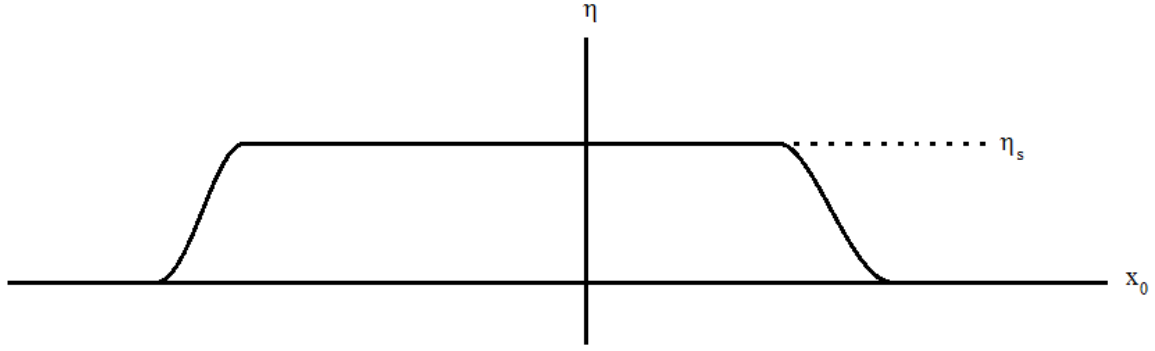
Fig. 2.2e: Trajectory overlap contributions

Since η_s is a constant where the trajectory straddles the potential, so is the quantity $\left[1 - exp\left\{-\frac{i}{\hbar}\eta_s\right\}\right]$, which is illustrated in Fig. 2.2f.
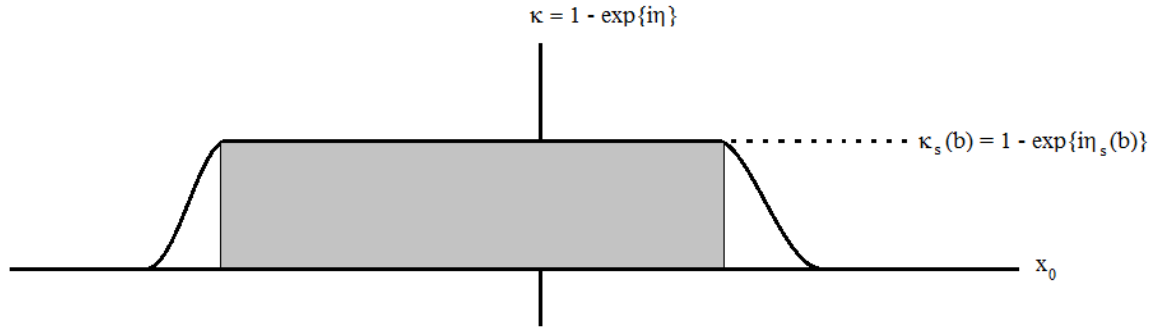
Fig. 2.2f: Trajectory straddles potential

Now, the quantity $\left[1 - exp\left\{-\frac{i}{\hbar}\eta_s\right\}\right]$ appears in (2.14), and evaluates to

$$\int_{-\infty}^{\infty} dx_0 \left[1 - exp\left\{-\frac{i}{\hbar}\eta_s\right\}\right] = \bar{v}\tau\left[1 - exp\left\{-\frac{i}{\hbar}\eta_s\right\}\right] + C, \qquad (2.16)$$

15

where $\bar{v}\tau$ is the length of the trajectory, $\left[1 - exp\left\{-\frac{i}{\hbar}\eta_s\right\}\right] = \kappa_s(b)$, their product is the shaded area in Fig. 2.2f, and C is the area of the wings. We plug this "evaluated" integral back into (2.14) to find

$$g(\tau) = 2\pi \int_0^\infty b\ db\left\{\bar{v}\tau\left[1 - exp\left\{-\frac{i}{\hbar}\eta_s\right\}\right] + C\right\}. \tag{2.17}$$

This integral was "evaluated" (using the quotation marks) only because the integration of the wings has not really been done. We will now assume that the area of the wings, integrated over all impact parameters, is negligible in comparison with the shaded area in Fig. 2.2f, so

$$g(\tau) \approx 2\pi\bar{v}\tau \int_0^\infty b\ db\left(1 - exp\left\{-\frac{i}{\hbar}\eta_s(b)\right\}\right). \tag{2.18}$$

Now that we have an expression for $g(\tau)$, we can find the correlation function and, eventually, the line intensity. We can rewrite (2.18) as

$$g(\tau) \approx \bar{v}\tau\sigma, \tag{2.19}$$

where we define

$$\sigma = 2\pi \int_0^\infty b\ db\left(1 - exp\left\{-\frac{i}{\hbar}\eta_s(b)\right\}\right) \tag{2.20}$$

and, since σ has both real and imaginary parts,

$$g(\tau) = [\bar{v}\ Re(\sigma) + i\ \bar{v}\ Im(\sigma)]\tau \tag{2.21}$$

$$= (\alpha_1 + i\beta_1)\tau + (\alpha_0 + i\beta_0). \tag{2.22}$$

If we plot $g(\tau)$ versus τ, the slope of the linear portion gives us α_1 and β_1. Now, the correlation function is given by

$$\Phi(\tau) = exp\{-ng(\tau)\} = exp\{(-n\alpha_1 - in\beta_1)\tau\}, \qquad (2.23)$$

where $n\alpha_1$ is the line width and $n\beta_1$ is the line shift, and the line intensity is given by

$$I(\omega - \omega_0) = I_0 \int_{-\infty}^{\infty} d\tau \, \Phi(\tau) e^{i(\omega - \omega_0)(\tau)} \qquad (2.24)$$

$$\propto \frac{I_0}{(\omega - \omega_0 - n\beta_1)^2 + (n\alpha_1)^2} \,. \qquad (2.25)$$

The second limit usually considered in the literature (Allard & Kielkopf, 1982) is the static approximation, which takes the limit of $g(\tau)$ in the case of small $\bar{v}t$; that is, the limit of high density. Going back to our initial equation (2.13), we have

$$g(\tau) = 2\pi \int_0^{\infty} b \, db \int_{-\infty}^{\infty} dx_0 \left[1 - exp\left\{ -\frac{i}{\hbar} \int_0^{\tau} dt \, V_{ij}\left[\{b^2 + (x_0 + \bar{v}t)^2\}^{1/2} \right] \right\} \right]. \qquad (2.13)$$

If we now take the static limit, we can drop the $\bar{v}t$ out of this equation. We then make the substitution

$$\{b^2 + (x_0 + \bar{v}t)^2\}^{1/2} = R \;\; ; \;\; V_{ij}\left(\{b^2 + (x_0 + \bar{v}t)^2\}^{1/2} \right) = V_{ij}(R)$$

Converting to polar coordinates, we transform our equation into the form

$$g(\tau) = 4\pi \int_0^{\infty} R^2 \, dR \left[1 - exp\left\{ -\frac{i}{\hbar} V_{ij}(R)\tau \right\} \right], \qquad (2.26)$$

where the integrand gives the volume of the region of influence of the potential, modified by a periodic term. As with the impact limit, the evaluated form of $g(\tau)$ depends on the functional form of the difference potential $V_{ij}(R)$. Once the $g(\tau)$ is evaluated for a given functional form of difference potential, the correlation function, line width, line shift, and line intensity can be calculated in the same manner as with the impact limit.

Now we can begin to do some calculations with the Anderson-Talman model. For the purposes of illustration, we shall perform sample calculations with Rb + He, but the results of similar calculations for all nine alkali-noble gas pairs can be found later in this section. For any pair, the expression for $g(\tau)$ in (2.13) is fairly straightforward to calculate for a 6-12 (Lennard-Jones) potential:

$$V(r) = \frac{C_{12}}{r^{12}} - \frac{C_6}{r^6} \tag{2.27a}$$

or

$$V(r) = d\left[\frac{\rho^{12}}{r^{12}} - \frac{2\rho^6}{r^6}\right] \tag{2.27b}$$

The parameters for (2.27a) and (2.27b) are listed in Table 2.2a for Rb + He, below, where d and ρ are calculated by $d = {-C_6^2}\big/{4C_{12}}$ and $\rho = \left({2C_{12}}\big/{C_6}\right)^{1/6}$, which can be inverted easily by $C_{12} = d\rho^{12}$ and $C_6 = 2d\rho^6$, with the conversion factors (for C_6) $1\,J \cdot m^6 = 104.46 \times 10^{77}\,au$ and (for C_{12}) $1\,J \cdot m^{12} = 4.5769 \times 10^{140}\,au$ (au signifies atomic units). The Lennard-Jones coefficients are calculated backward using theoretical potential surfaces:
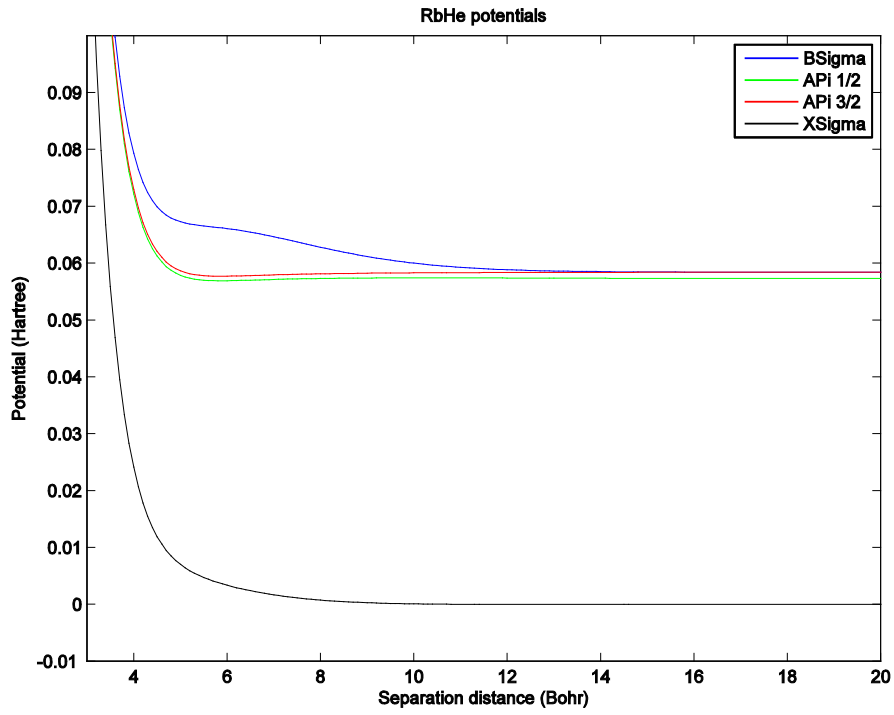
Fig. 2.2g. Rb + He potentials
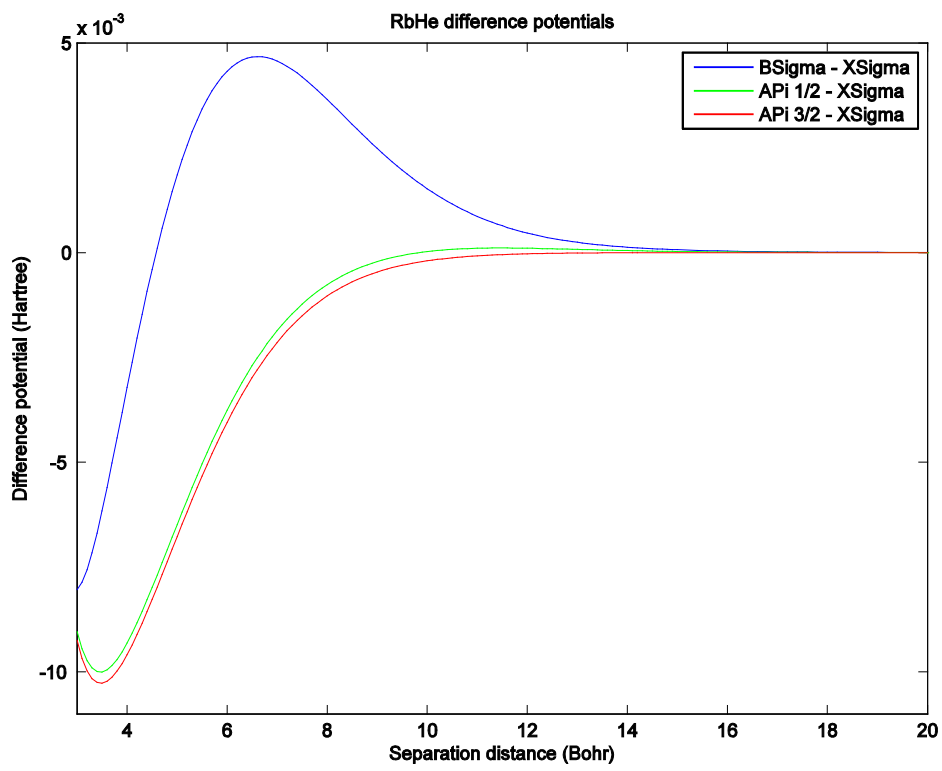
Fig. 2.2h. Rb + He difference potentials

19

We start with values of d and ρ from the surfaces and perform the inverse calculations as described above to find the starting data in Table 2.2a. We confirm the values of d and ρ by fitting a 6-12 potential curve (2.27b) to the local maximum in each of the difference potential curves. We use the local maxima (or bumps) corresponding to the relevant features in the potential energy surfaces; for example, we can see clearly the shoulder or bump in the $B^2\Sigma_{1/2}$ surface (Fig. 2.2g) and its corresponding local maximum in difference potential (Fig. 2.2h). Similarly, for the $A^2\Pi_{1/2}$ and $A^2\Pi_{3/2}$ surfaces we see dips in the potential surfaces (Fig. 2.2g) which correspond to local minima in their difference potentials (Fig. 2.2h). We expect minima in difference potential to correspond to redshifting of a spectral line and maxima in difference potential to blueshifting of a spectral line. We therefore generally expect the Anderson-Talman model to yield two redshifted lines (corresponding to the $A^2\Pi_{1/2}$ and $A^2\Pi_{3/2}$ surfaces) and one blueshifted line (corresponding to the $B^2\Sigma_{1/2}$ surface). As we will see with the uncoupled case in the Baranger model, each excited state corresponds to one broadening coefficient and one shift coefficient.

Even from the outset, we do not expect this to be a perfect model. First, we are approximating a difference potential surface by a 6-12 potential given by (2.27b), and a 'pure' 6-12 potential curve does not fit any of the CsAr difference potential surfaces perfectly. At best, we have assembled a 6-12 curve to mimic the position and height of the local maximum of the surface. As we can see in Figs. 2.2i and 2.2j, below, the curve fits are acceptable at separations greater than those corresponding to the local maxima, but they diverge significantly for closer interactions. These divergences are due to the influence of the local minima in the surfaces which do not appear in the 'pure' 6-12 curves.
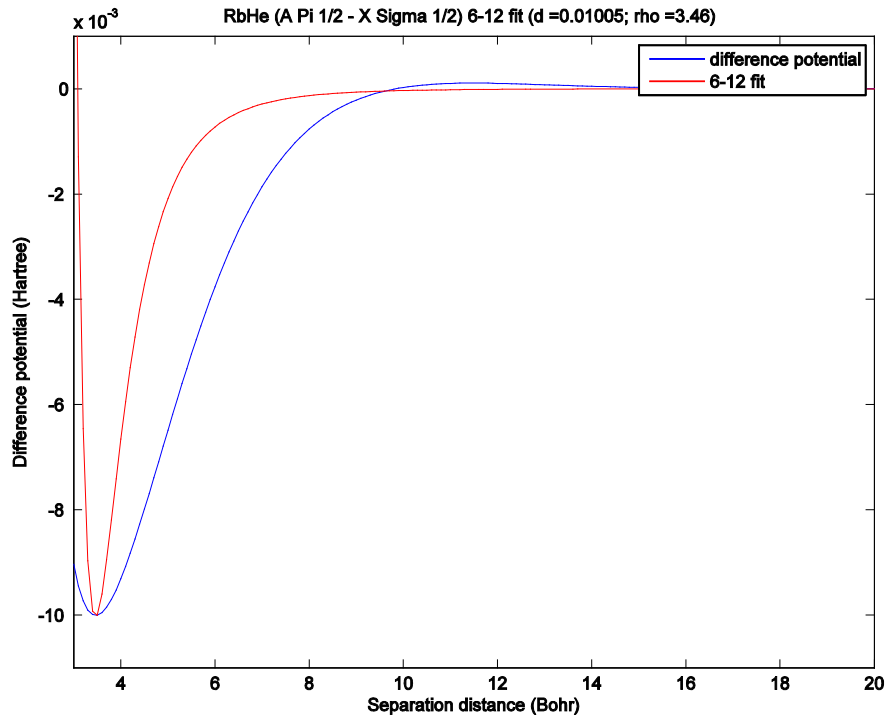
Fig. 2.2i. 6-12 curve fit to the $A^2\Pi_{1/2} - X^2\Sigma_{1/2}$ difference potential
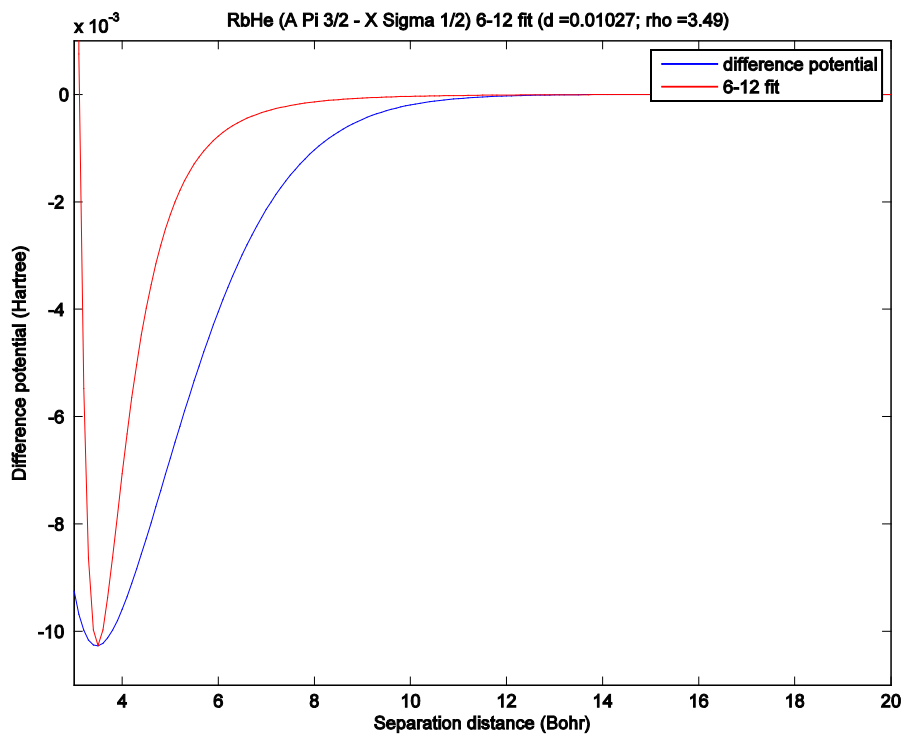
Fig. 2.2j. 6-12 curve fit to the $A^2\Pi_{3/2} - X^2\Sigma_{1/2}$ difference potential
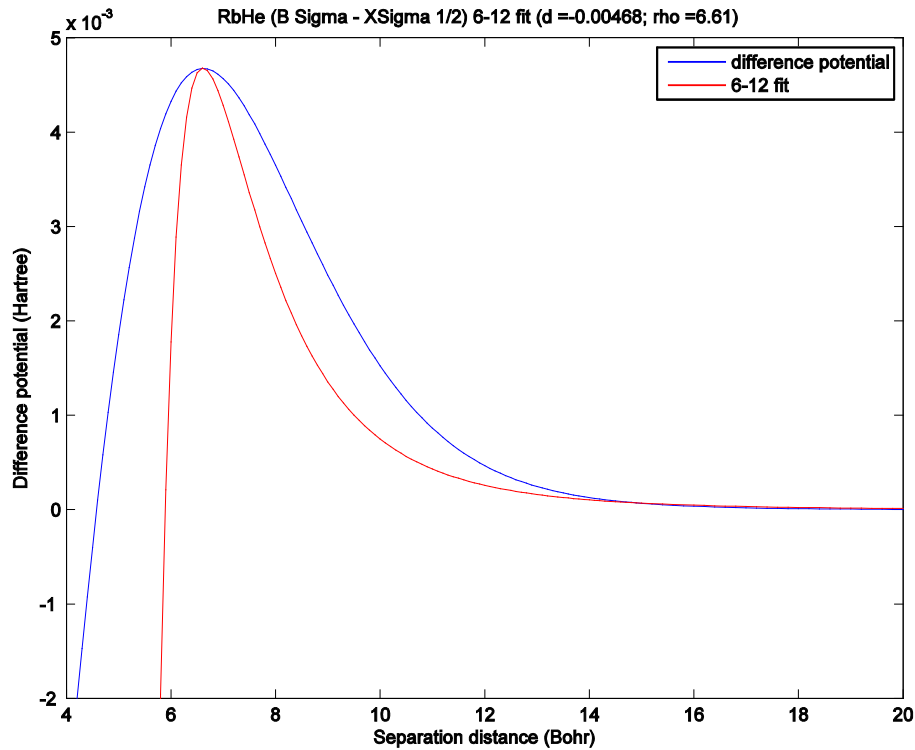
Fig. 2.2k. 6-12 curve fit to the $B^2\Sigma_{1/2} - X^2\Sigma_{1/2}$ difference potential

Table 2.2a: Lennard-Jones parameters for Rubidium + Helium lines.

Difference potential	C_6		C_{12}		d		ρ	
	$(10^{-77}$ J-$m^6)$	(au)	$(10^{-134}$ J-$m^{12})$	$(10^6$ au)	(au)	(cm^{-1})	(Bohr)	(Å)
$A^2\Pi_{1/2} - X^2\Sigma_{1/2}$ (D$_1$ line)	0.330	34.49	0.0066	0.030	0.01005	2206	3.46	1.83
$A^2\Pi_{3/2} - X^2\Sigma_{1/2}$ (D$_{2a}$)	0.355	37.12	0.0074	0.034	0.01027	2254	3.49	1.85
$B^2\Sigma_{1/2} - X^2\Sigma_{1/2}$ (D$_{2b}$)	-7.474	-780.7	-7.1227	-32.6	-0.00468	-1027	6.61	3.50

We calculate the average velocity in (2.13) from the temperature:

$$\bar{v} = \sqrt{\frac{8 k_B T}{\pi \mu}} \qquad (2.27\text{c})$$

where k_B is Boltzmann's constant, T the temperature, and μ the reduced mass of the colliding perturber-emitter system. From here, one can integrate (2.13) numerically to find $g(\tau)$, then plug those results into (2.12) to get the correlation function $\Phi(\tau)$, which depends on the number density of perturbers, n. Finally, we use the numerical result for the correlation function to calculate the line shape by (2.11).

Although this is the full-up Anderson-Talman calculation, we can make an impact approximation along the way. In doing so, we can take the results of linear fits of the real and imaginary parts of $g(\tau)$, along with (2.24), to find numerical values for the line width $n\alpha_1$ and the line shift $n\beta_1$. The results are listed in Table 2.2b, below, compared with experimental results at a temperature of 394 K, which can be adjusted for temperature by the formula

$$g(T_2) = g(T_1)\left(\frac{T_1}{T_2}\right)^m \qquad (2.27\text{d})$$

where $m = \frac{1}{2}$, assuming the cross-section is independent of speed (Pitz, Wertepny, and Perram, 2009; Pitz, Fox, and Perram, 2010).

The results we obtain for α and β are in atomic units, or (Bohr^3 × atomic unit of frequency). In order to compare these theoretical results with experiment, we must convert to SI units and divide by kT, since when we compare (2.23b) and (2.24) with the ideal gas law, we have $n = \frac{P}{kT}$ and we want to construct α and β in units of MHz/Torr (that is, with $g(\tau)$ in units of inverse-pressure). We find that the unit conversion simplifies to (for T = 394 K; changes in temperature change both the prediction of $g(\tau)$ and the $\frac{P}{kT}$ dependence in n):

$$\alpha\{MHz/torr\} = \alpha\{atomic\ units\} \times 30.089\,\frac{MHz/Torr}{atomic\ unit} \qquad (2.27\text{e})$$

The conversion for β is exactly the same. The resulting Anderson-Talman theoretical results are given in Table 2.2b.

Table 2.2b: Line broadening and shift parameters for Rb + He lines (T = 394 K)

Transition	α (FWHM, MHz/Torr)		β ($\Delta\omega$, MHz/Torr)	
	Theory	experiment	theory	experiment
$A^2\Pi_{1/2} - X^2\Sigma_{1/2}$ (D$_1$ line)	6.27	18.9 ± 0.2	4.44	4.71 ± 0.04
$A^2\Pi_{3/2} - X^2\Sigma_{1/2}$ (D$_{2a}$)	6.32	14.04 (avg)	20.0 ± 0.14	4.77	-5.57 (avg)	0.37 ± 0.06
$B^2\Sigma_{1/2} - X^2\Sigma_{1/2}$ (D$_{2b}$)	21.75			-15.91		

Because the 6-12 Lennard-Jones difference potentials are used and not the physical potential energy surfaces, these calculations are not intended to be predictive but instead are presented only as checks for later calculations using the Baranger model. Tables 2.2c and 2.2d show Lennard-Jones parameters and broadening and shift coefficients for all nine M + Ng pairs.

One major issue that arises with the Anderson-Talman model is that there is no accounting for coupling between the excited states. Because the model calculates one α and one β for each potential surface, it does so for each of the three excited states, rather than the two measured lines (D$_1$ and D$_2$). Another issue is that the theoretical calculations using the Anderson-Talman model yield results which diverge significantly from the corresponding measurements.

Table 2.2c: Lennard-Jones parameters for all nine M + Ng pairs.

	$A^2\Pi_{1/2} - X^2\Sigma_{1/2}$ (D$_1$)		$A^2\Pi_{3/2} - X^2\Sigma_{1/2}$ (D$_{2a}$)		$B^2\Sigma_{1/2} - X^2\Sigma_{1/2}$ (D$_{2b}$)	
	d (au)	ρ (Bohr)	d (au)	ρ (Bohr)	d (au)	ρ (Bohr)
K + He	0.01208	3.09	0.01218	3.08	-0.00618	5.89
K + Ne	0.0078	2.70	0.0080	2.70	-0.00386	6.24
K + Ar	0.00791	4.21	0.00805	4.19	-0.00423	7.09
Rb + He	0.01005	3.46	0.01027	3.49	-0.00468	6.61
Rb + Ne	0.00690	2.8	0.00730	2.8	-0.00303	6.89
Rb + Ar	0.00702	4.48	0.00739	4.43	-0.00333	7.74
Cs + He	0.00707	3.93	0.00756	3.99	-0.00259	7.87
Cs + Ne	0.00430	4.0	0.00494	3.96	-0.00178	7.92
Cs + Ar	0.00488	5.03	0.00556	5.01	-0.00192	8.85

Table 2.2d: Broadening and shift coefficients (in MHz/torr) for all nine M + Ng pairs, using Lennard-Jones (6-12) potentials in Anderson-Talman.

	$A^2\Pi_{1/2} - X^2\Sigma_{1/2}$ (D$_1$)		$A^2\Pi_{3/2} - X^2\Sigma_{1/2}$ (D$_{2a}$)		$B^2\Sigma_{1/2} - X^2\Sigma_{1/2}$ (D$_{2b}$)	
	α (FWHM)	β ($\Delta\omega$)	α (FWHM)	β ($\Delta\omega$)	α (FWHM)	β ($\Delta\omega$)
K + He	4.79	3.54	4.83	3.49	17.50	-12.56
K + Ne	2.01	1.47	2.02	1.47	11.20	-8.25
K + Ar	5.25	3.78	5.18	3.77	14.13	-10.12
Rb + He	6.27	4.44	6.32	4.77	21.75	-15.91
Rb + Ne	2.10	1.53	2.15	1.53	13.03	-9.48
Rb + Ar	5.51	4.11	5.56	4.03	15.47	-11.21
Cs + He	6.92	5.06	7.40	5.38	23.68	-17.13
Cs + Ne	3.76	2.71	3.87	2.81	13.56	-9.80
Cs + Ar	5.73	4.17	6.01	4.43	15.44	-11.01

Instead of using approximations, or even curve fits, to Lennard-Jones potentials as above, one could use the actual potential energy surfaces for each M + Ng pair and run the Anderson-Talman model rigorously under the resulting difference potentials. Blank has performed the many-body calculations to develop physical potential energy surfaces (Blank, Weeks, and Kedziora, 2012) and used those in the Anderson-Talman model. The results are shown for three different temperatures in Tables 2.2e-g (Blank, in preparation). We will compare these results with Baranger model calculations in Chapter III.

Table 2.2e: Broadening and shift coefficients (in MHz/torr) for all nine M + Ng pairs, using the *ab initio* potentials in Anderson-Talman, at T = 250K.

T = 250K	$A^2\Pi_{1/2} - X^2\Sigma_{1/2}$ (D$_1$)		$A^2\Pi_{3/2} - X^2\Sigma_{1/2}$ (D$_{2a}$)		$B^2\Sigma_{1/2} - X^2\Sigma_{1/2}$ (D$_{2b}$)	
	α (FWHM)	β ($\Delta\omega$)	α (FWHM)	β ($\Delta\omega$)	α (FWHM)	β ($\Delta\omega$)
K + He	20.36	6.23	17.08	-2.44	31.89	4.11
K + Ne	14.39	3.35	8.97	-1.12	16.98	1.73
K + Ar	13.14	0.43	8.56	-1.36	14.49	-2.01
Rb + He	30.47	6.79	17.49	-2.35	34.59	5.17
Rb + Ne	15.21	1.76	8.50	-0.88	16.97	1.77
Rb + Ar	11.86	-0.58	7.53	-0.91	13.51	-1.37
Cs + He	32.26	4.70	18.76	-2.16	36.77	5.16
Cs + Ne	14.82	1.70	8.94	-0.68	17.83	1.81
Cs + Ar	12.00	-1.06	7.58	-0.49	13.98	-1.86

Table 2.2f: Broadening and shift coefficients (in MHz/torr) for all nine M + Ng pairs, using the *ab initio* potentials in Anderson-Talman, at T = 350K.

T = 350K	$A^2\Pi_{1/2} - X^2\Sigma_{1/2}$ (D₁)		$A^2\Pi_{3/2} - X^2\Sigma_{1/2}$ (D₂ₐ)		$B^2\Sigma_{1/2} - X^2\Sigma_{1/2}$ (D₂ᵦ)	
	α (FWHM)	β ($\Delta\omega$)	α (FWHM)	β ($\Delta\omega$)	α (FWHM)	β ($\Delta\omega$)
K + He	15.53	4.72	14.00	-2.05	26.14	3.47
K + Ne	10.99	2.87	7.38	-0.94	13.97	1.51
K + Ar	10.24	0.73	7.06	-1.09	11.89	-1.28
Rb + He	23.70	6.09	14.36	-1.98	28.25	4.33
Rb + Ne	12.80	1.65	7.01	-0.76	13.95	1.55
Rb + Ar	10.01	-0.30	6.24	-0.74	11.11	-0.83
Cs + He	26.70	4.48	15.44	-1.85	30.12	4.32
Cs + Ne	12.24	1.38	7.39	-0.62	14.66	1.58
Cs + Ar	9.80	-0.61	6.30	-0.44	11.48	-1.20

Table 2.2g: Broadening and shift coefficients (in MHz/torr) for all nine M + Ng pairs, using the *ab initio* potentials in Anderson-Talman, at T = 450K.

T = 450K	$A^2\Pi_{1/2} - X^2\Sigma_{1/2}$ (D₁)		$A^2\Pi_{3/2} - X^2\Sigma_{1/2}$ (D₂ₐ)		$B^2\Sigma_{1/2} - X^2\Sigma_{1/2}$ (D₂ᵦ)	
	α (FWHM)	β ($\Delta\omega$)	α (FWHM)	β ($\Delta\omega$)	α (FWHM)	β ($\Delta\omega$)
K + He	12.76	3.78	12.06	-1.79	22.53	3.05
K + Ne	8.94	2.49	6.38	-0.83	12.07	1.36
K + Ar	8.44	0.81	6.19	-0.93	10.27	-0.89
Rb + He	19.41	5.47	12.38	-1.74	24.28	3.78
Rb + Ne	11.15	1.62	6.07	-0.68	12.04	1.39
Rb + Ar	8.87	-0.11	5.42	-0.64	9.61	-0.55
Cs + He	22.86	4.34	13.34	-1.65	25.93	3.78
Cs + Ne	10.71	1.20	6.40	-0.57	12.67	1.42
Cs + Ar	8.44	-0.40	5.48	-0.40	9.92	-0.84

2.3.   Baranger Model

While the Anderson-Talman model is a semiclassical model of collisional line broadening, the Baranger model treats the collisional dynamics quantum-mechanically. Both models treat radiation classically, and both models view atomic collisions in the reference frame of emitter/absorber atom. However, Baranger begins with the impact approximation—the limit of low density or the limit in which the time between collisions is much longer than the duration of a given collision—and this approximation pervades the entire work of Baranger (Baranger, 1958a, 1958b, 1958c).

In his model, Baranger considers a fixed radiating atom with initial state $|i>$, final state $|f>$, surrounded by moving perturbers (Baranger, 1958a; Allard & Kielkopf, 1982). The total power emitted by dipole transitions between these two states is given by

$$P(\omega) = \frac{4\omega^4}{3c^3} I(\omega) \tag{2.28}$$

This is consistent with the nonrelativistic limit of classical dipole radiation (Jackson, 1999). The intensity is given by (Allard & Kielkopf, 1982):

$$I(\omega) = \sum_{if} \delta\left(\omega - \omega_{if}\right) |\langle f|\boldsymbol{d}|i\rangle|^2 \rho_i \tag{2.29}$$

where ω_{if} is the frequency corresponding to the unperturbed atomic transition between initial and final states (here, the standard practice is to use units in which $\hbar = 1$), ρ_i is the weighted statistical intrinsic probability for the initial state $|i>$, $\boldsymbol{d}$ is the dipole moment of the radiator (not the entire system) assuming a pure dipole radiator (which is a reasonable assumption for a single transition), and the sum is over all possible initial and final states.

Because it is easier to compute directly the Fourier transform of the line shape (Baranger, 1958a), we define a correlation function

$$\Phi(\tau) = \int_{-\infty}^{\infty} I(\omega)e^{-i\omega\tau}d\omega \qquad (2.30)$$

and the Fourier transform of the correlation function,

$$I(\omega) = \frac{1}{2\pi} \int_{-\infty}^{\infty} \Phi(\tau)e^{i\omega\tau}d\tau \qquad (2.31)$$

Since the radiation intensity is real, we restrict computations of the correlation function to positive values of τ and use the condition

$$\Phi(-\tau) = \Phi^*(\tau) \qquad (2.32)$$

to compute correlation functions for negative values of s (Baranger, 1958a; Allard & Kielkopf, 1982). Using this condition (2.32), the intensity (2.31) becomes

$$I(\omega) = \frac{1}{2\pi} \int_{-\infty}^{0} \Phi(\tau)e^{i\omega\tau}d\tau + \frac{1}{2\pi} \int_{0}^{\infty} \Phi(\tau)e^{i\omega\tau}d\tau \qquad (2.33a)$$

or

$$I(\omega) = \frac{1}{2\pi} \int_{0}^{\infty} \Phi(-\tau)e^{-i\omega\tau}d\tau + \frac{1}{2\pi} \int_{0}^{\infty} \Phi(\tau)e^{i\omega\tau}d\tau$$

$$= \frac{1}{2\pi} \int_{0}^{\infty} \Phi^*(\tau)e^{-i\omega\tau}d\tau + \frac{1}{2\pi} \int_{0}^{\infty} \Phi(\tau)e^{i\omega\tau}d\tau \qquad (2.33b)$$

$$= \frac{1}{2\pi} \int_{0}^{\infty} \left[\{\Phi(\tau)e^{i\omega\tau}\} + \{\Phi(\tau)e^{i\omega\tau}\}^*\right]d\tau$$

or

$$I(\omega) = \frac{1}{\pi} Re\left\{\int_{0}^{\infty} \Phi(\tau)e^{i\omega\tau}d\tau\right\} \qquad (2.33c)$$

Combining (2.29) with (2.30), we get

$$\Phi(\tau) = \int\limits_{-\infty}^{\infty} \left[\sum_{if} \delta(\omega - \omega_{if}) |\langle f|\boldsymbol{d}|i\rangle|^2 \rho_i \right] e^{-i\omega\tau} d\omega \tag{2.34}$$

Now, one of the basic properties of the Dirac delta-function tells us that

$$\int\limits_{-\infty}^{\infty} \delta(\omega - \omega_{if}) f(\omega) d\omega = f(\omega_{if}) \tag{2.35}$$

So the integral in (2.34) evaluates simply as

$$\Phi(\tau) = \sum_{if} e^{-i\omega_{if}\tau} |\langle f|\boldsymbol{d}|i\rangle|^2 \rho_i \tag{2.36}$$

In the case of multiple perturbers, the net correlation function is the product of the single-perturber correlation functions (Baranger, 1958a; Allard & Kielkopf, 1982) because we have assumed separability. In the case of N identical perturbers,

$$\Phi(\tau) = [\varphi(\tau)]^N \tag{2.37}$$

where $\varphi(\tau)$ is the single-perturber correlation function (that is, in (2.36) the expression is actually $\varphi(\tau)$, and if there is only one perturber then (2.36) gives $\Phi(\tau)$) which Baranger estimates, from the impact approximation that most of the time the perturber does not influence the emitter/absorber atom (Baranger, 1958a) because the time between collisions is much longer than the duration of the collision. Baranger introduces a small correction to account for the time during which the perturber is close to the emitter/absorber atom:

$$\varphi(\tau) = 1 - \mathcal{V}^{-1} g(\tau) \tag{2.38}$$

where $\mathcal{V}$ is the volume of the container and $g(\tau)$ is some function that has not yet been defined (but begins to resemble the $g(\tau)$ of Anderson-Talman; see section 2.2). If we have N perturbers in our container, then the perturber number density is

$$n = N\mathcal{V}^{-1} \tag{2.39}$$

and the correlation function is given by (2.37) and (2.38):

$$\Phi(\tau) = [1 - \mathcal{V}^{-1} g(\tau)]^N \tag{2.40}$$

Now, assuming the correction is small in (2.38), then we can replace (2.38) with the Taylor-series expansion for the exponential,

$$e^\gamma = 1 + \gamma + \frac{\gamma^2}{2} + \frac{\gamma^3}{3} + \cdots \approx 1 + \gamma \tag{2.41}$$

So (2.38) becomes

$$\varphi(\tau) = exp[-\mathcal{V}^{-1}g(\tau)] \tag{2.42}$$

and the full correlation function (2.40) becomes

$$\Phi(\tau) = exp[-N\mathcal{V}^{-1}g(\tau)] = exp[-ng(\tau)] \tag{2.43}$$

which begins to look like (2.12) in Anderson-Talman. Once we have $\Phi(\tau)$ we can calculate the line shape $I(\omega)$, but we need to find $g(\tau)$ in order to find $\Phi(\tau)$.

We start from the single-perturber form of (2.36),

$$\varphi(\tau) = \sum_{if} e^{-i\omega_{if}\tau}|\langle f|\boldsymbol{d}|i\rangle|^2\rho_i \tag{2.36'}$$

In atomic units, $\omega_{if} = E_i - E_f$ and

$$\begin{aligned}
\varphi(\tau) &= \sum_{if} e^{-i(E_i-E_f)\tau}\{\langle f|\boldsymbol{d}|i\rangle\}^\dagger\{\langle f|\boldsymbol{d}|i\rangle\}\rho_i \\
&= \sum_{if} e^{-i(E_i-E_f)\tau}\langle i|\boldsymbol{d}|f\rangle\langle f|\boldsymbol{d}|i\rangle\rho_i \\
&= \sum_{if} \langle i|\boldsymbol{d}|f\rangle\langle f|e^{iE_f\tau}\boldsymbol{d}e^{-iE_i\tau}|i\rangle\rho_i
\end{aligned} \tag{2.44}$$

Here, Baranger uses the Hamiltonian of the perturber when the atom is in its initial and final state. Thus, (2.44) becomes

$$\varphi(\tau) = \sum_{if} \langle i|\boldsymbol{d}|f\rangle\langle f|e^{iH\tau}\boldsymbol{d}e^{-iH\tau}|i\rangle\rho_i \tag{2.45}$$

By completeness,

$$\sum_f |f\rangle\langle f| = 1 \tag{2.46}$$

so

$$\varphi(\tau) = \sum_i \langle i| \mathbf{d} e^{iH\tau} \mathbf{d} e^{-iH\tau} |i\rangle \rho_i \tag{2.47}$$

Here, we see the time evolution operator (Allard & Kielkopf, 1982):

$$T(\tau) = e^{-iH\tau} \tag{2.48}$$

where the Hamiltonian includes contributions from the atom, perturbers, and their interaction potential, respectively:

$$H = H_A + H_P + V \tag{2.49}$$

and (2.47) becomes

$$\varphi(\tau) = \sum_i \langle i| \mathbf{d} T^\dagger(\tau) \mathbf{d} T(\tau) |i\rangle \rho_i \tag{2.50}$$

This sum over initial states is simply the trace of the matrix product:

$$\varphi(\tau) = Tr[\mathbf{d} T^\dagger(\tau) \mathbf{d} T(\tau) \rho] \tag{2.51}$$

where ρ is the Boltzmann-Gibbs density matrix for the system (Allard & Kielkopf, 1982).

We can assume that the system is separable into an atom (emitter) system and a perturber system. This separability allows us to write the density matrix of the system as a product of the density matrices of the atom and perturbers:

$$\rho = \rho_A \rho_P \tag{2.52}$$

The time-evolution operator can be expressed similarly:

$$T(\tau) = T_A(\tau) T_P(\tau) \tag{2.53}$$

where $T_A(\tau)$ incorporates the atom and interaction potential terms of the Hamiltonian and $T_P(\tau)$ incorporates the perturber term of the Hamiltonian. Further, the wavefunction can be expressed as a product of atom and perturber wavefunctions:

$$|\psi(t)\rangle = |\phi(t)\rangle |\chi(t)\rangle \tag{2.54}$$

The atom density matrix is given by:

$$\rho_A \simeq \frac{1}{Z(T)} g_i e^{-(H_A + \bar{V})/kT} \qquad (2.55)$$

where g_i is the degeneracy in the initial state, $\bar{V}$ is the statistical average of the perturbation potential (Allard & Kielkopf, 1982) and $Z(T)$ is the partition function of the atomic system (Pathria, 1996; Cooper, 1967):

$$Z(T) = \sum_i g_i e^{-(H_A + \bar{V})/kT} = Tr[g e^{-(H_A + \bar{V})/kT}] \qquad (2.56)$$

so

$$\rho_A \simeq \frac{g_i e^{-(H_A + \bar{V})/kT}}{\sum_i g_i e^{-(H_A + \bar{V})/kT}} = \frac{g_i e^{-(H_A + \bar{V})/kT}}{Tr[g e^{-(H_A + \bar{V})/kT}]} \qquad (2.57)$$

From (2.51),

$$\varphi(\tau) = Tr[\boldsymbol{d} T^\dagger(\tau) \boldsymbol{d} T(\tau) \rho] \qquad (2.51)$$

We can now break this out using (2.52) and (2.53) to get

$$\varphi(\tau) = Tr[\boldsymbol{d} T_P{}^\dagger(\tau) T_A{}^\dagger(\tau) \boldsymbol{d} T_A(\tau) T_P(\tau) \rho_A \rho_P]$$
$$= \sum_i \langle i | \boldsymbol{d} T_P{}^\dagger(\tau) T_A{}^\dagger(\tau) \boldsymbol{d} T_A(\tau) T_P(\tau) \rho_A \rho_P | i \rangle \qquad (2.58)$$

From (2.46),

$$\varphi(\tau) = \sum_{if} \langle i | \boldsymbol{d} | f \rangle \langle f | T_P{}^\dagger(\tau) T_A{}^\dagger(\tau) \boldsymbol{d} T_A(\tau) T_P(\tau) \rho_A \rho_P | i \rangle$$
$$= \sum_{if} \langle i | \boldsymbol{d} | f \rangle \langle f | e^{+i(H_A + H_P + \bar{V})\tau} \boldsymbol{d} e^{-i(H_A + H_P + \bar{V})\tau} | i \rangle \rho_A \rho_P$$
$$= \sum_{if} \langle i | \boldsymbol{d} | f \rangle \langle f | e^{+i H_P \tau} \boldsymbol{d}(\tau) e^{-i H_P \tau} | i \rangle \rho_A \rho_P \qquad (2.59)$$

where in the interaction picture $\boldsymbol{d}(\tau) = e^{+i(H_A + \bar{V})\tau} \boldsymbol{d} e^{-i(H_A + \bar{V})\tau}$.

33

For now, we will simply define the time-dependent dipole matrix element as $d(\tau)$; we will revisit it shortly. Using (2.36'), (2.44), (2.47) and (2.59), we have

$$\varphi(\tau) = \sum_{if} e^{-i\omega_{if}\tau} \langle i|d(\tau)|f\rangle\langle i|d|f\rangle \rho_A \rho_P \tag{2.60}$$

which, with (2.55), becomes

$$\varphi(\tau) = \sum_{if} \left[\frac{1}{Z(T)} g_i e^{-(H_A + \bar{V})/kT} \langle i|d(\tau)|f\rangle\langle i|d|f\rangle\right]_{Av} \tag{2.61}$$

where the Av subscript refers to the average over the ensemble of perturber states (Allard & Kielkopf, 1982).

Now, we revisit the time-dependent dipole matrix element $d(\tau)$ (Allard & Kielkopf, 1982):

$$d(\tau) = T^\dagger(t + \tau, t)dT(t + \tau, t) \tag{2.62}$$

where we essentially break up the time-evolution operator in (2.62), $T(t + \tau, t)$, into the contribution from the unperturbed atom, $T_A(\tau)$, and a time-evolution operator resulting from the interaction potential in the interaction picture:

$$T(t + \tau, t) = T_A(\tau)U(t + \tau, t) \tag{2.63}$$

According to the interaction picture, $U(t + \tau, t)$ becomes (Cohen-Tannoudji, et al, 2005), again using atomic units:

$$U(t + \tau, t) = 1 + \frac{1}{i}\int_t^{t+\tau} dt_1 \tilde{V}_T(t_1) + \frac{1}{i^2}\int_t^{t+\tau} dt_1 \tilde{V}_T(t_1)\int_t^{t_1} dt_2 \tilde{V}_T(t_2) + \cdots \tag{2.64}$$

where $\tilde{V}_T(t_1)$ is the unitary-transformed V_T, ignoring the perturbation (Allard & Kielkopf, 1982; Cohen-Tannoudji, et al, 2005; Cooper, 1967):

$$\begin{aligned}
\tilde{V}_T(t_1) &= T_A{}^\dagger(t_1)V_T(t_1)T_A(t_1) \\
&= e^{iH_A t_1}V_T(t_1)e^{-iH_A t_1}
\end{aligned} \tag{2.65}$$

Now, because of the order of integration in (2.64), we require that

$$\tau > t_1 > t_2 > \cdots > t_n \tag{2.66}$$

That is, the duration of the interaction is short relative to the time between interactions; thus we have the impact approximation. The order of integration is embodied by the use of a time-ordering (or sequencing) operator, $\mathcal{T}$, which takes into account the ordering of the t_i in the integrals in (2.64) since the $\tilde{V}_T(t_i)$ do not commute in general (Baranger, 1958b; Allard & Kielkopf, 1982). This being the case, we can reverse the power-series expansion of $U(t + \tau, t)$ in (2.64) to get

$$U(t + \tau, t) = \mathcal{T}\exp\left[\frac{1}{i}\int_t^{t+\tau}\tilde{V}_T(t)dt\right] \tag{2.67}$$

Then, the average over perturber states in (2.61) moves inward and really only affects the time-dependent dipole matrix element $\boldsymbol{d}(\tau)$:

$$\varphi(\tau) = \sum_{if}\frac{1}{Z(T)}g_ie^{-(H_A+\overline{V})/kT}\langle i|\boldsymbol{d}|f\rangle\langle i|[\boldsymbol{d}(\tau)]_{Av}|f\rangle \tag{2.68}$$

where

$$
\begin{aligned}
{[\boldsymbol{d}(\tau)]}_{Av} &= [T^\dagger(t + \tau, t)\boldsymbol{d}T(t + \tau, t)]_{Av} \\
&= [U^{-1}(t + \tau, t)T_A{}^\dagger(\tau)\boldsymbol{d}T_A(\tau)U(t + \tau, t)]_{Av} \\
&= [U^{-1}(t + \tau, t)e^{iH_A\tau}\boldsymbol{d}e^{-iH_A\tau}U(t + \tau, t)]_{Av}
\end{aligned} \tag{2.69}
$$

Now, the time-evolution operator $U(t + \tau, t)$ is a matrix operator, so we can express the product (2.69) in terms of the components of the matrix product (Allard & Kielkopf, 1982):

$$\langle f|[\boldsymbol{d}(\tau)]_{Av}|i\rangle = \sum_{pq}\left[U_{fp}^{-1}(t + \tau, t)e^{i\omega_p\tau}\langle p|\boldsymbol{d}|q\rangle e^{-i\omega_q\tau}U_{qi}(t + \tau, t)\right]_{Av} \tag{2.70}$$

Or

$$\langle f|[\boldsymbol{d}(\tau)]_{Av}|i\rangle = \sum_{pq}\left[U_{fp}^{-1}(t + \tau, t)\langle p|\boldsymbol{d}|q\rangle e^{-i\omega_{qp}\tau}U_{qi}(t + \tau, t)\right]_{Av} \tag{2.71}$$

Finally, if the initial and final states are angular momentum states of an atom, $|jm\rangle$, and $U_{fp}^{-1}(t + \tau, t) = \langle f|U^{-1}|p\rangle$ then we must express the time-dependent dipole matrix element $\boldsymbol{d}(\tau)$ as:

35

$$\langle j_f m_f | [\boldsymbol{d}(\tau)]_{Av} | j_i m_i \rangle$$

$$= \sum_{m_1 m_2} \left[e^{-i\omega_{if}\tau} \langle j_f m_f | U^{-1} | j_f m_1 \rangle \langle j_f m_1 | \boldsymbol{d} | j_i m_2 \rangle \langle j_i m_2 | U | j_i m_i \rangle \right]_{Av} \qquad (2.72)$$

To evaluate the matrix element $\langle j_f m_1 | \boldsymbol{d} | j_i m_2 \rangle$, we use the Wigner-Eckart theorem (Sakurai, 1994): the matrix elements of tensor operators (of rank k) with respect to angular-momentum eigenstates satisfy

$$\left\langle \alpha', j'm' \middle| T_q^{(k)} \middle| \alpha, jm \right\rangle = \langle jk; mq | jk; j'm' \rangle \frac{\langle \alpha'j' \| T^{(k)} \| \alpha j \rangle}{\sqrt{2j+1}} \qquad (2.73)$$

$\langle \alpha'j' \| T^{(k)} \| \alpha j \rangle$ is the reduced matrix element (or double-bar matrix element) and is independent of m, m', and q. Now, the Clebsch-Gordan coefficients $\langle jk; mq | jk; j'm' \rangle$ in (2.73) can be expressed in terms of the Wigner 3-j symbol (Sakurai, 1994):

$$\langle j_1 j_2; m_1 m_2 | j_1 j_2; jm \rangle = (-1)^{j_1 - j_2 + m} \sqrt{2j+1} \begin{pmatrix} j_1 & j_2 & j \\ m_1 & m_2 & -m \end{pmatrix} \qquad (2.74)$$

It is worth noting here that the ket on the left side of (2.74), $|j_1 j_2; jm\rangle$, is a simultaneous eigenket of $\boldsymbol{J}_1^2, \boldsymbol{J}_2^2, \boldsymbol{J}^2, J_z$ (Sakural, 1994); in atomic units:

$$\boldsymbol{J}_1^2 |j_1 j_2; jm\rangle = j_1(j_1 + 1)|j_1 j_2; jm\rangle \qquad (2.75a)$$

$$\boldsymbol{J}_2^2 |j_1 j_2; jm\rangle = j_2(j_2 + 1)|j_1 j_2; jm\rangle \qquad (2.75b)$$

$$\boldsymbol{J}^2 |j_1 j_2; jm\rangle = j(j + 1)|j_1 j_2; jm\rangle \qquad (2.75c)$$

$$J_z |j_1 j_2; jm\rangle = m|j_1 j_2; jm\rangle \qquad (2.75d)$$

The Clebsch-Gordan coefficients exhibit orthogonality relations (Sakurai, 1994):

$$\sum_{jm} \langle j_1 j_2; m_1 m_2 | j_1 j_2; jm \rangle \langle j_1 j_2; m'_1 m'_2 | j_1 j_2; jm \rangle = \delta_{m_1 m'_1} \delta_{m_2 m'_2} \qquad (2.76a)$$

$$\sum_{m_1 m_2} \langle j_1 j_2; m_1 m_2 | j_1 j_2; jm \rangle \langle j_1 j_2; m_1 m_2 | j_1 j_2; j'm' \rangle = \delta_{jj'} \delta_{mm'} \qquad (2.76b)$$

Incidentally, these orthogonality relations, combined with the definition of the Wigner 3-j symbol in (2.74), give us the 3-j symbol orthogonality relations:

$$\sum_{jm}(2j+1)\begin{pmatrix} j_1 & j_2 & j \\ m_1 & m_2 & -m \end{pmatrix}\begin{pmatrix} j_1 & j_2 & j \\ m'_1 & m'_2 & -m \end{pmatrix} = \delta_{m_1 m'_1}\delta_{m_2 m'_2} \qquad (2.76c)$$

$$(2j+1)\sum_{m_1 m_2}\begin{pmatrix} j_1 & j_2 & j \\ m_1 & m_2 & -m \end{pmatrix}\begin{pmatrix} j_1 & j_2 & j' \\ m_1 & m_2 & -m' \end{pmatrix} = \delta_{jj'}\delta_{mm'} \qquad (2.76d)$$

Going back to the matrix element $\langle j_f m_1|\boldsymbol{d}|j_i m_2\rangle$, $\boldsymbol{d}$ is a vector (that is, a tensor of rank 1) so the Wigner-Eckart theorem (2.73) gives us

$$\langle j_f m_f|\boldsymbol{d}|j_i m_i\rangle = \langle j_i 1; m_i 0|j_i 1; j_f m_f\rangle\frac{\langle j_f\|d\|j_i\rangle}{\sqrt{2j_i+1}} \qquad (2.77)$$

Now, the Clebsch-Gordan coefficients have the symmetry property (Bransden & Joachain, 2003; Cohen-Tannoudji, et al, 2005):

$$\langle j_1 j_2; m_1 m_2|j_1 j_2; jm\rangle = (-1)^{j_1+j_2-j}\langle j_2 j_1; m_2 m_1|j_2 j_1; jm\rangle \qquad (2.78a)$$

$$= (-1)^{j_1+j_2-j}\langle j_1 j_2; -m_1 -m_2|j_1 j_2; j-m\rangle \qquad (2.78b)$$

$$= (-1)^{j_1-m_1}\left(\frac{2j+1}{2j_2+1}\right)^{1/2}\langle j_1 j; m_1-m|j_1 j; j_2-m_2\rangle \qquad (2.78c)$$

Using (2.78c), then (2.78a), then (2.78c) again, we find a fourth symmetry property that is of special interest in this analysis:

$$\langle j_1 j_2; m_1 m_2|j_1 j_2; jm\rangle = (-1)^{2j_1-j_2+2j-m_1+m}\langle jj_2; -mm_2|jj_2; j_1-m_1\rangle \qquad (2.78d)$$

Using (2.74) to express (2.78d) in terms of a 3-j symbol, we find that

$$\langle j_1 j_2; m_1 m_2|j_1 j_2; jm\rangle = (-1)^{2j_1-2j_2+3j-2m_1+m}\sqrt{2j_1+1}\begin{pmatrix} j & j_2 & j_1 \\ -m & m_2 & m_1 \end{pmatrix} \qquad (2.79)$$

Now, the Clebsch-Gordan coefficients vanish unless $m = m_1 + m_2$ (Sakurai, 1994) and $|j_1-j_2| \le j \le j_1+j_2$ (Cohen-Tannoudji, et al, 2005; Sakurai, 1994). For the Clebsch-Gordan coefficient under consideration, $\langle j_i 1; m_i 0|j_i 1; j_f m_f\rangle$, we have the variable substitutions $j_1 = j_i; j_2 = 1; j = j_f; m_1 = m_i; m_2 = 0; m = m_f$. In this case, we know that $j_1 - j_2 + j$ is an integer and that $m_1 = m$, so (2.79) reduces to

$$\langle j_i 1; m_i 0|j_i 1; j_f m_f\rangle = (-1)^{j_f-m_f}\sqrt{2j_i+1}\begin{pmatrix} j_f & 1 & j_i \\ -m_f & 0 & m_i \end{pmatrix} \qquad (2.80)$$

In terms of the 3-j symbols, the Wigner-Eckart theorem (2.73) can be expressed as (Allard & Kielkopf, 1982; Cooper, 1967):

$$\langle j_f m_f | T_q^{(k)} | j_i m_i \rangle = (-1)^{j_f - m_f} \begin{pmatrix} j_f & k & j_i \\ -m_f & q & m_i \end{pmatrix} \langle j_f \| T^{(k)} \| j_i \rangle \qquad (2.81)$$

The matrix element (2.77) thus becomes

$$\langle j_f m_f | \boldsymbol{d} | j_i m_i \rangle = (-1)^{j_f - m_f} \begin{pmatrix} j_f & 1 & j_i \\ -m_f & 0 & m_i \end{pmatrix} \langle j_f \| d \| j_i \rangle \qquad (2.82)$$

which agrees with the normal result (Allard & Kielkopf, 1982).

Now, we examine the reduced matrix element of (2.69) to find

$$\langle j_f \| [\boldsymbol{d}(\tau)]_{Av} \| j_i \rangle = \langle j_f \| \left[U^{-1} e^{i H_A \tau} \boldsymbol{d} e^{-i H_A \tau} U \right]_{Av} \| j_i \rangle$$

$$= \left[\langle j_f \| U^{-1} e^{i H_A \tau} \boldsymbol{d} e^{-i H_A \tau} U \| j_i \rangle \right]_{Av}$$

$$= \left[\langle j_f \| U^{-1} \| j_f \rangle \langle j_f \| e^{i H_A \tau} \| j_f \rangle \langle j_f \| \boldsymbol{d} \| j_i \rangle \langle j_i \| e^{-i H_A \tau} \| j_i \rangle \langle j_i \| U \| j_i \rangle \right]_{Av}$$

$$= \left[\langle j_f \| U^{-1} \| j_f \rangle e^{-i \omega_{if} \tau} \langle j_f \| \boldsymbol{d} \| j_i \rangle \langle j_i \| U \| j_i \rangle \right]_{Av} \qquad (2.83)$$

We can calculate the angular average in (2.83) by using the symmetry properties of the Wigner 3-j symbols (and their corresponding Clebsch-Gordan coefficients) (Allard & Kielkopf, 1982; Bransden & Joachain, 2003; Cohen-Tannoudji, et al, 2005; Cooper, 1967; Sakurai, 1994). Essentially, this involves an inverse application of the Wigner-Eckart theorem to the reduced matrix elements $\langle j_f \| U^{-1} \| j_f \rangle$ and $\langle j_i \| U \| j_i \rangle$ in (2.83), which introduces additional sums into the final result (Allard & Kielkopf, 1982):

$$\langle j_f \| [\boldsymbol{d}(\tau)]_{Av} \| j_i \rangle = \langle j_f \| d \| j_i \rangle e^{-i \omega_{if} \tau} \left[U_{ff}^{-1}(t + \tau, t) U_{ii}(t + \tau, t) \right]_{Av} \qquad (2.84a)$$

where

$$\left[U_{ff}^{-1}(t + \tau, t) U_{ii}(t + \tau, t) \right]_{Av}$$

$$= \sum_{m_i m_f m_1 m_2 M} (-1)^{2 j_f + m_i + m_1} \begin{pmatrix} j_f & 1 & j_i \\ m_f & M & -m_2 \end{pmatrix} \begin{pmatrix} j_f & 1 & j_i \\ m_f & M & -m_i \end{pmatrix}$$

$$\times \langle j_f m_f | U_C^{-1} | j_f m_1 \rangle \langle j_i m_2 | U_C | j_i m_i \rangle \qquad (2.84b)$$

U_C refers to the the operator U_{ii} along the axis of the collision, and (2.84b) represents a transformation between space-fixed coordinates (or the lab frame), which requires an angular average, and body-fixed coordinates (Rose, 1957; Zare, 1988; Sakurai, 1994; Lewis, 2011).

Now, we have to look again at $U(t + \tau, t)$. We go back to (2.67), where $\tilde{V}_T$ is the total interaction which accounts for all the individual interactions, $\tilde{v}_i$, due to all the perturbers that collide with the radiator during the time τ (Allard & Kielkopf, 1982). Within the impact approximation, we include the assumption that the collisions occur separately; that is, we assume that the collisions occur one at a time, with enough time between collisions that they do not overlap. In this case, $\tilde{V}_T$ can be written as the sum of the individual $\tilde{v}_i$, and (2.67) becomes

$$U(t + \tau, t) = \mathcal{T}\exp\left[\frac{1}{i}\int_t^{t+\tau}\left[\sum_{i=1}^{N}\tilde{v}_i(t')\right]dt'\right] \tag{2.85}$$

Since the collisions are separated in time, only one of the individual $\tilde{v}_i$ is nonzero at any given time, so the $\tilde{v}_i$ commute with one another (Allard & Kielkopf, 1982). Thus, we can rewrite (2.85) as

$$U(t + \tau, t) = \mathcal{T}\prod_{i=1}^{N}\exp\left[\frac{1}{i}\int_t^{t+\tau}\tilde{v}_i(t')dt'\right] \tag{2.86}$$

and, if we define the interaction potential time-evolution operator from an individual perturber as

$$u_i(t + \tau, t) = \mathcal{T}\exp\left[\frac{1}{i}\int_t^{t+\tau}\tilde{v}_i(t')dt'\right] \tag{2.87}$$

then the overall operator becomes

$$U(t + \tau, t) = \prod_{i=1}^{N}u_i(t + \tau, t) \tag{2.88}$$

From this, and the commutation of the $\tilde{v}_i$, we return to the calculation of

$$\left[U_{ff}^{-1}(t+\tau,t)U_{ii}(t+\tau,t)\right]_{Av} = \left[\left(\prod_{i=1}^{N}u_i\right)_{ff}^{-1}\left(\prod_{i=1}^{N}u_i\right)_{ii}\right]_{Av}$$

$$= \left[\prod_{i=1}^{N}u_{i\,ff}^{-1}u_{i\,ii}\right]_{Av}$$

$$= \left[u_{ff}^{-1}u_{ii}\right]_{Av}^{N} \tag{2.89}$$

In this last line of (2.89), since the perturbations are assumed to be independent of each other, the average of the products is equal to the product of the averages (Allard & Kielkopf, 1982).

We can use the same Taylor-series approximation that led us from (2.38) to (2.42), $(1-\alpha)^N \simeq \exp(-N\alpha)$, for small α and large N (Allard & Kielkopf, 1982), to give

$$(U^{-1}U)_{Av} = \exp\left[-N\left(1 - u_{ff}u_{ii}\right)_{Av}\right] \tag{2.90}$$

Now, we need to calculate the average over perturber velocities and positions. As in earlier considerations, we integrate over the volume $\mathcal{V}$ of the container, with $f(v)$ being the Maxwell distribution of velocities, b the impact parameter, and t the collision time:

$$\left(1 - u_{ff}^{-1}u_{ii}\right)_{Av} = \frac{1}{\mathcal{V}}\int_0^\infty f(v)dv \int_{-\infty}^\infty \int_0^\infty 2\pi b\,db\,v\,dt\left[\left(1 - u_{ff}^{-1}u_{ii}\right)_{Ang\,Av}\right] \tag{2.91}$$

so, from (2.90) and (2.91),

$$(U^{-1}U)_{Av} = \exp\left\{-n\int_0^\infty f(v)dv \int_{-\infty}^\infty \int_0^\infty 2\pi b\,db\,v\,dt\left[\left(1 - u_{ff}^{-1}u_{ii}\right)_{Ang\,Av}\right]\right\}$$

$$= \exp[-ng(\tau)] \tag{2.92}$$

where n is the number density of perturbers and we define $g(\tau)$ as the triple integral in (2.92).

We can now recast (2.68) in these terms. Since our line profile can be renormalized by a constant common factor, we can ignore everything that is constant through the line profile (Allard & Kielkopf, 1982). What remains is:

$$\varphi(\tau) = \sum_{if} e^{-i\omega_{if}\tau} \exp[-ng(\tau)] \tag{2.93a}$$

where

$$g(\tau) = \int_0^\infty f(v)dv \int_0^\infty 2\pi b\,db \int_{-\infty}^\infty v\,dt \left[1 - \left(u_{ff}^{-1}u_{ii}\right)_{Ang\ Av}\right] \tag{2.93b}$$

The result (2.93b) is a more general result by Allard and Kielkopf, based on the Baranger model (Allard & Kielkopf, 1982). As in the Anderson-Talman model, the impact approximation (which is followed by Baranger throughout) simplifies our result further (Allard & Kielkopf, 1982):

$$g(\tau) = \alpha_0 + i\beta_0 + (\alpha_1 + i\beta_1)\tau \tag{2.94}$$

where the Anderson-Talman result (2.23b) assumes only the τ-dependent term contributes. Here, the third integral in (2.93b) integrates to give $\int_{-\infty}^\infty dt = \tau$, with the rest being independent of t. Thus, the τ-dependent term can be derived from the scattering matrix elements:

$$\alpha_1 + i\beta_1 = \int_0^\infty f(v)v\,dv \int_0^\infty 2\pi b\,db \left[1 - \left(S_{ff}^{-1}S_{ii}\right)_{Ang\ Av}\right] \tag{2.95}$$

The scattering matrix elements and the potential are related by a unitary transformation (Baranger, 1962):

$$U(\infty, -\infty) = e^{iH_A t_0} S e^{-iH_A t_0} \tag{2.96}$$

The scattering matrix elements can be written in the form (Allard & Kielkopf, 1982; Baranger, 1962):

$$S_{ff}^{-1}S_{ii} = \exp[-\zeta + i\eta] \tag{2.97}$$

where the diagonal elements of the scattering matrix (or S-matrix) are given by (Baranger, 1962):

$$S_{ii} = \langle i|S|i\rangle = \exp[-\delta_i - i\varepsilon_i] \tag{2.98a}$$
$$S_{ff}^{-1} = S_{ff}^\dagger = \exp[-\delta_f + i\varepsilon_f] \tag{2.98b}$$

so

$$S_{ff}^{-1}S_{ii} = \exp[-\zeta + i\eta] \tag{2.99}$$

where $\zeta = \delta_i + \delta_f$ and $\eta = \varepsilon_i - \varepsilon_f$. Integrating over frequencies:

$$\int (1 - S_{ff}^{-1}S_{ii})dv = \int (1 - \exp[-\zeta + i\eta])dv$$

$$= \int (1 - e^{-\zeta}\cos\eta)dv + i\int e^{-\zeta}\sin\eta \, dv$$

$$= \int \mathrm{Re}\{1 - S_{ff}^{-1}S_{ii}\}dv + i\int \mathrm{Im}\{1 - S_{ff}^{-1}S_{ii}\}dv \tag{2.100}$$

so we find the width $(n\alpha_1)$ and shift $(n\beta_1)$ of the collision-broadened line are given by

$$n\alpha_1 = n\int_0^\infty f(v)v\,dv\int_0^\infty 2\pi b\,db\left[1 - e^{-\zeta}\cos\eta\right] \tag{2.101a}$$

$$n\beta_1 = n\int_0^\infty f(v)v\,dv\int_0^\infty 2\pi b\,db\, e^{-\zeta}\sin\eta \tag{2.101b}$$

Allard and Kielkopf point out the special case of Lorentz scattering, in which ζ is infinite. In this case, $e^{-\zeta} = 0$, and the line is unshifted $(n\beta_1 = 0)$. The width of the line in this case is the collision frequency. Additionally, if $\zeta = 0$, then the collision is completely elastic (Allard & Kielkopf, 1982). We can then define the phase shift of the collision, $\theta = \eta + i\zeta$, so that (2.99) becomes

$$S_{ff}^{-1}S_{ii} = \exp[i\theta] \tag{2.102}$$

and the width and shift become

$$n\alpha_1 = n\int_0^\infty f(v)v\,dv\int_0^\infty 2\pi b\,db[1 - \cos\theta] \tag{2.103a}$$

$$n\beta_1 = n\int_0^\infty f(v)v\,dv\int_0^\infty 2\pi b\,db\, \sin\theta \tag{2.103b}$$

in a manner similar to the semiclassical theory from Anderson (Kielkopf, 1976).

The integral over impact parameters can be recast as a sum over orbital angular momenta using what Drake calls the Langer modification (Drake, 2006)

$$b = \frac{L}{\hbar k} = \frac{\sqrt{l(l+1)}}{k} \qquad (2.104a)$$

where k is the wave number, L is the magnitude of the orbital angular momentum, and l is its quantum number (and l is constrained to integer values, which makes $dl = 1$). Classically, the orbital angular momentum is $L = b\mu v$, where μv is the linear momentum (Zare, 1988). We can rewrite (2.104a) by squaring both sides and taking a derivative to find that

$$bdb = \frac{(2l+1)dl}{2k^2} \qquad (2.104b)$$

The integrals over impact parameter in equations (2.101a)-(2.103b) therefore convert to

$$\int_0^\infty 2\pi b db \, F(\eta \text{ or } \theta) = \sum_{l=0}^\infty 2\pi \frac{(2l+1)}{2k^2} F(l) \qquad (2.104c)$$

since our phase shift (and S-matrix elements) depend on l.

Baranger's approach to the integral over impact parameters is to express the forward scattering amplitude as a sum over partial waves (Baranger, 1958a; Baranger, 1962). The scattering amplitude for a given angle θ is given by:

$$f(k,\theta) = \sum_{l=0}^\infty f_l(k) P_l(\cos\theta) = \sum_{l=0}^\infty \frac{2l+1}{2ik} \left(e^{2i\delta_l(k)} - 1 \right) P_l(\cos\theta) \qquad (2.105)$$

Now, to find the forward scattering amplitude, we set $P_l(\cos\theta) = 1$, so the forward scattering amplitude is given by:

$$f(k) = \sum_{l=0}^\infty \frac{2l+1}{2ik} \left(e^{2i\delta_l(k)} - 1 \right) \qquad (2.106)$$

Baranger expresses the width and shift of an isolated line in terms of this forward scattering amplitude (Baranger, 1962):

$$n\alpha_1 = \frac{2\pi\hbar n}{m}\,\mathrm{Im}[f(k)]_{Av} = \left[\frac{\pi\hbar n}{mk}\sum_{l=0}^{\infty}(2l+1)(1-\cos 2\delta_l)\right]_{Av} \tag{2.107a}$$

$$n\beta_1 = -\frac{2\pi\hbar n}{m}\,\mathrm{Re}[f(k)]_{Av} = -\left[\frac{\pi\hbar n}{mk}\sum_{l=0}^{\infty}(2l+1)(\sin 2\delta_l)\right]_{Av} \tag{2.107b}$$

where the averages are taken over k. Since the collision momentum can be expressed as $\hbar k = mv$, from the DeBroglie relation, the width and shift become

$$n\alpha_1 = n\left[\frac{\pi v}{k^2}\sum_{l=0}^{\infty}(2l+1)(1-\cos 2\delta_l)\right]_{Av} \tag{2.108a}$$

$$n\beta_1 = -n\left[\frac{\pi v}{k^2}\sum_{l=0}^{\infty}(2l+1)(\sin 2\delta_l)\right]_{Av} \tag{2.108b}$$

This looks just like the width and shift given by (2.103a) and (2.103b), after changing the integral over impact parameters to a sum over angular momenta, except that this method replaces the integral over v with a sum over k, and then the sum with an average by the expression (Szudy & Baylis, 1974)

$$\langle G(k)\rangle_k = \sum_k P(k)G(k) \tag{2.109}$$

where $P(k)$ is the probability that an initial state has wave number k. This also differs in that Baranger's scattering phase shift δ_l is half of the phase shift of the collision, θ, discussed above. If the potentials are spherically symmetric, $\delta_l = \delta_l^{(U)} - \delta_l^{(L)}$, where $\delta_l^{(U)}$ and $\delta_l^{(L)}$ are the phase shifts for the upper and lower states of the atom, respectively. Further, Szudy and Baylis assert that the width $n\alpha_1$ is the HWHM (Half Width at Half-Maximum), rather than the FWHM (Szudy & Baylis, 1996).

If we assume the probability distribution to be a Boltzmann distribution, and if we assume an ideal gas ($PV = Nk_BT$, or $P = nk_BT$, where k_B is the Boltzmann constant)—that is, if we have a thermally-distributed ideal gas—we can combine equations (2.103a)-(2.104c) to find

$$\frac{n\alpha_1}{P} = \sqrt{\frac{2\pi}{\mu^3}}\, \hbar^2 (k_B T)^{-5/2} \sum_{E=0}^{\infty} \exp(-\frac{E}{k_B T})\Delta E \sum_{J=0.5}^{\infty} (2J+1)[1 - \cos\theta_J(E)] \qquad (2.110a)$$

$$\frac{n\beta_1}{P} = -\sqrt{\frac{2\pi}{\mu^3}}\, \hbar^2 (k_B T)^{-5/2} \sum_{E=0}^{\infty} \exp(-\frac{E}{k_B T})\Delta E \sum_{J=0.5}^{\infty} (2J+1)\sin\theta_J(E) \qquad (2.110b)$$

The left-hand side of each equation gives the width and shift, divided by the pressure. We can calculate these values in the standard experimental units of MHz/torr.

Kielkopf indicates one means of estimating the phase shift, given the difference potential. Assuming adiabaticity and the classical path approximation, he writes his estimate of the phase shift as (Kielkopf, 1976):

$$\theta(x, b, u) = 2\pi \frac{c}{v} \int_0^u \Delta W[(x^2 + y^2) + b^2]^{1/2} dy \qquad (2.111)$$

where $\Delta W[(x^2 + y^2) + b^2]^{1/2} = \Delta W(R)$ is the difference potential in wavenumbers, b is the impact parameter of the collision, the integration of y is in units of cm, c is the speed of light, $v = \sqrt{3kT/\mu}$ is the mean velocity of the perturber, and μ is the reduced mass (Kielkopf, 1976). In the static approximation, u is very small, ΔW does not vary significantly over the range of u (and so can be pulled out of the integral), and the phase shift becomes

$$\theta(x, b, u)_{static} = 2\pi \frac{c}{v} \Delta W(R) u \qquad (2.112a)$$

In the impact approximation, which the Baranger model assumes (Baranger, 1958a), u is very large, and the calculation becomes largely independent of x. The phase shift looks like

$$\theta(b)_{impact} = 2\pi \frac{c}{v} \int_{-\infty}^{\infty} \Delta W[y^2 + b^2]^{1/2} dy \qquad (2.112b)$$

and

$$\alpha_1 = \int_0^\infty 2\pi b\, db\, [1 - \cos\theta] \qquad\qquad (2.113a)$$

$$\beta_1 = \int_0^\infty 2\pi b\, db\ \sin\theta \qquad\qquad (2.113b)$$

just as in the Anderson-Talman model, where (Kielkopf, 1976)

$$\alpha = \alpha_1 u + \alpha_0 \qquad\qquad (2.114a)$$
$$\beta = \beta_1 u + \beta_0 \qquad\qquad (2.114b)$$

For a given alkali-noble gas mixture, we could use the difference potentials that appear in Fig. 9 in place of ΔW in (2.111b). In order to perform a rigorous calculation of the integral in (2.112b), we first need a curve fit for the difference potentials plotted in Fig. 2.2h.

In order to perform a fully quantum-mechanical calculation, however, we use the *ab initio* potentials developed by L. Blank (Blank, Weeks, and Kedziora, 2012) to calculate scattering matrix (S-matrix) elements by the Channel Packet Method. We can use those S-matrix elements to calculate the phase shift of a given state during a collision. We use the phase shifts (and, more importantly, the phase difference between a given excited state and the ground state) rather than a more direct calculation using $S_{ff}^{-1} S_{ii}$ because calculations of the phase differences provides an intermediate check of the viability of the calculation (that is, whether the phase difference vanishes at high values of E and J). We then use the calculated phase difference $\theta_J(E)$ to numerically integrate equations (2.110a) and (2.110b) to find the broadening (width) and shift of the given spectral line.

2.4. Calculation of S-Matrix Elements

The Baranger model requires that we know the S-matrix (or scattering matrix) elements in order either to integrate directly using (2.95) or to perform the calculation of phase differences which are then integrated using (2.110a) and (2.110b). In either case, however, we require some method of calculating the S-matrix elements.

The scattering operator $\hat{S}$ identifies how reactants $|\Psi_{in}\rangle$ in the infinite past map to products $|\Psi_{out}\rangle$ in the infinite future,

$$|\Psi_{out}\rangle = \hat{S}\,|\Psi_{in}\rangle \tag{2.115}$$

where $\hat{S}$ is unitary (that is, $\hat{S}^{-1} = \hat{S}^{\dagger}$) and time-independent and contains all of the information about the interaction potential (Tannor and Weeks, 1992; Weeks and Tannor, 1993). The scattering operator can be defined in terms of the Channel Moller operators in the limit of infinite time before or after the collision:

$$\hat{S} = \Omega_{-}^{\dagger}\Omega_{+} \tag{2.116}$$

where the Channel Moller operators are given by:

$$\Omega_{\pm} = \lim_{t \to \mp\infty} \left[\exp(+\frac{iHt}{\hbar})\exp(-\frac{iH_0 t}{\hbar}) \right] \tag{2.117}$$

Now, we can use completeness to write the incoming reactant (or outgoing product) state in the form

$$|\Psi_{in\,(out)}\rangle = \int_{-\infty}^{\infty} dk\, |k_\gamma\gamma\rangle\langle k_\gamma\gamma|\Psi_{in\,(out)}\rangle = \int_{-\infty}^{\infty} dk\, \eta_{+(-)}|k_\gamma\gamma\rangle \tag{2.118}$$

where the $|k_\gamma\gamma\rangle$ are a separable set of reactant and product states and γ represents the full set of internal quantum states of the reactants and products (Lewis, 2011). The Channel Moller operators are then used to compute reactant and product Moller states:

$$|\Psi_{\pm}\rangle = \Omega_{\pm}|\Psi_{in\,(out)}\rangle \tag{2.119}$$

Having calculated the Moller reactant state, we propagate the wavepacket through the collision process to determine the Moller product state. The correlation function is a measure of the time-dependent overlap between the Moller product state and the Moller reactant state; that is, the projection of the Moller product (time-evolved) state onto the Moller reactant (initial, or $t = 0$) state or, in our collision process, the projection of the outbound state (the state after the collision) onto the inbound state (the state before the collision). In atomic units the time-dependent correlation function, $C(t)$, has the form

$$C(t) = \langle \Psi_{-}|\exp(-iHt)|\Psi_{+}\rangle \tag{2.121}$$

We can now calculate the scattering matrix element, S, by calculating the Fourier transform of the correlation function and dividing by the channel packet expansion coefficents (Tannor and Weeks, 1992; Weeks and Tannor, 1993). In atomic units,

$$S = \frac{(2\pi)^{-1}[|k'||k|]^{1/2}}{\eta_-^*(k')\eta_+(k)} \int_{-\infty}^{\infty} dt \, \exp(iHt)C(t) \qquad (2.122)$$

This yields a scattering matrix element as a function of energy. Since the total Hamiltonian of the system depends on J, so does the scattering matrix element.

We begin our propagation at an interatomic separation of 100 Bohr, and we consider anything farther out than 20 Bohr to be "asymptotic" with regard to the interaction potential. However, the centrifugal effective potential reaches farther out for relevant values of the total angular momentum J, so even if we place the initial wavepacket at around 100 Bohr we still see a significant difference with J. We therefore need to generate the relevant Moller reactant states, one for each value of J, which we can use in the Channel Packet Method (Lewis, 2011). Given infinite amounts of time and computational resources, the obvious method of generating a Moller reactant state would be to generate a Gaussian wavepacket starting an infinite amount of time before the collision ($t = -\infty$) and then propagate that wavepacket until $t = 0$ to form the initial state. Since time and computational resources are finite, however, we must choose a suitably large time for "$t = -\infty$" such that the Moller reactant states can be calculated in a reasonable amount of time but that the wavepacket at the time we call "$t = -\infty$" does not overlap so much with the centrifugal effective potentials for relevant values of J that it misbehaves significantly at low kinetic energies. Figure 2.4a shows the intermediate Moller state, in the position representation, for Rb + He compared with the centifugal effective potentials at J = 50.5, 100.5, 150.5.

Wavepacket propagation is a method by which the wavepacket representing an atom is propagated through time-evolution operators in a stepwise fashion to model the atom's behavior under the influence of a potential.
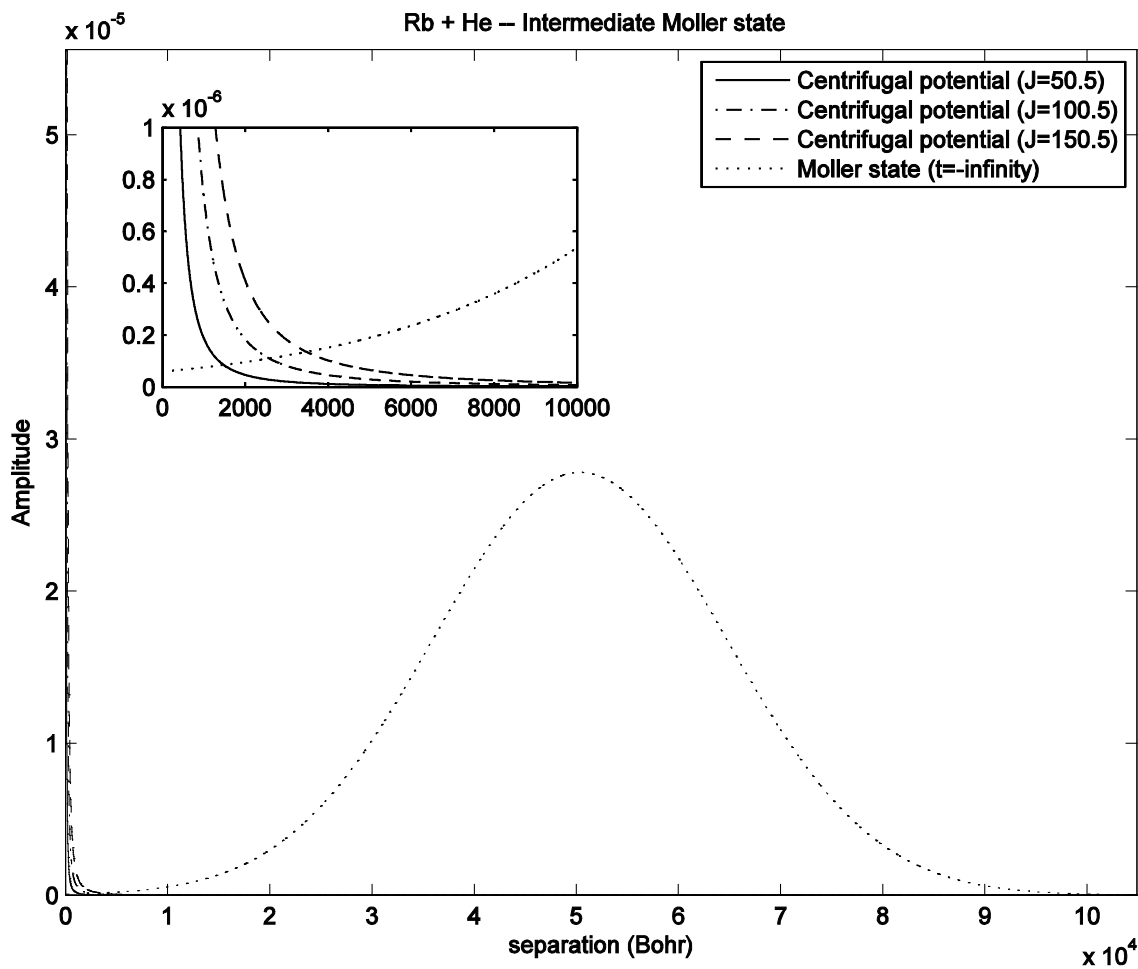

Fig. 2.4a: Intermediate Moller states overlapped with centrifugal effective potentials. The inset graph is a zoom into the lower-left corner of the main graph in order to show the overlap of the centrifugal potentials and the intermediate Moller state. As J increases the centrifugal effective potential increases and has greater impact on the Moller states.

We begin with the Schrödinger equation:

$$i\hbar \frac{d}{dt}|\psi(t)\rangle = H|\psi(t)\rangle \tag{2.123}$$

where the time-dependent wavefunction can be expressed in terms of a time-evolution of an initial wavefunction:

$$|\psi(t)\rangle = e^{-iHt/\hbar}|\psi(0)\rangle \tag{2.124}$$

Now, the Hamiltonian can be expressed in terms of the kinetic and potential energies of the system: $H = T + V$, so

$$|\psi(t)\rangle = e^{-i(T+V)t/\hbar}|\psi(0)\rangle \tag{2.125}$$

where V is the potential and $T = p^2/2\mu$ is the kinetic energy, also expressed through the de Broglie relation as

$$T = \frac{(2\pi\hbar k)^2}{2\mu} = \frac{2\pi^2\hbar^2}{\mu}k^2 \tag{2.126}$$

Here, we use the split operator formalism, which splits the action of the potential on either side of the propagation. For short time intervals (small Δt),

$$e^{-iHt/\hbar} \approx e^{-i\left(\frac{V}{2}\right)t/\hbar}e^{-i\frac{2\pi^2\hbar^2}{\mu}k^2 t/\hbar}e^{-i\left(\frac{V}{2}\right)t/\hbar} \tag{2.127}$$

We then operate, in turn, with each of the exponentials in (2.127) on the wavefunction (and we use the Taylor-series expansion of the exponential where necessary to be able to operate with the operators embedded within the exponentials).

Since the time-evolution operator (2.127) contains operators in both position-space and momentum-space, we must be able to transform our wavefunction between

position and momentum representations. To achieve this, we use the Fourier transformation and its inverse:

$$|\psi(k,t)\rangle = \frac{1}{\sqrt{2\pi}} \int_{-\infty}^{\infty} dx\, e^{-ikx}\, |\psi(x,t)\rangle \tag{2.128a}$$

$$|\psi(x,t)\rangle = \frac{1}{\sqrt{2\pi}} \int_{-\infty}^{\infty} dx\, e^{+ikx}\, |\psi(k,t)\rangle \tag{2.128b}$$

In order to achieve this in a computer model, it is necessary to use a Discrete Fourier Transform (DFT). The usual approach to performing a DFT on a computer is to use a Fast Fourier Transform (FFT), which reduces the number of calculations for a wavefunction with N elements from N^2 to $N \log N$ (Cooley & Tukey, 1965).

Computationally, one cycle—that is, the propagation of the wavepacket through one time increment—looks like the following, where *FT* denotes a Fourier Transform:

$$\psi(x, t_{q+1}) = e^{-i\left(\frac{V}{2}\right)t/\hbar} \cdot FT^{-1}\left\{ e^{-i\frac{2\pi^2\hbar^2}{\mu}k^2 t/\hbar} \cdot \left[FT\left(e^{-i\left(\frac{V}{2}\right)t/\hbar}\psi(x, t_q) \right) \right] \right\} \tag{2.129}$$

In step-by-step form, the wavepacket propagation looks like:

1. Operate on the wavefunction with $e^{-i\left(\frac{V}{2}\right)t/\hbar}$: $\psi(x, t_0) \rightarrow \psi(x, t'_0)$.
2. Fourier-transform to momentum space: $\psi(x, t'_0) \rightarrow \psi(k, t'_0)$.
3. Operate with the kinetic energy operator, $e^{-i\frac{2\pi^2\hbar^2}{\mu}k^2 t/\hbar}$: $\psi(k, t'_0) \rightarrow \psi(k, t''_0)$.
4. Invert the Fourier transform: $\psi(k, t''_0) \rightarrow \psi(x, t''_0)$.
5. Operate on the wavefunction with $e^{-i\left(\frac{V}{2}\right)t/\hbar}$: $\psi(x, t''_0) \rightarrow \psi(x, t_1)$.
6. Repeat as necessary to cover the total time $t_0 \dots t$.

The method we use is to begin with a Gaussian wavepacket at $t = 0$. We propagate the wavepacket backward as if it were a free particle for a long enough time that it does not overlap significantly with the centrifugal effective potential. We then propagate this "intermediate Moller state" forward in time under the full Hamiltonian

until $t = 0$. This effectively generates an intermediate state (at infinity) that would have evolved into a pure Gaussian wavepacket under no potential but that instead evolves into the relevant Moller reactant state under the full Hamiltonian of the system. Figure 2.4b shows, in the position representation, both the initial Gaussian wavepacket (which would be identical to the Moller reactant state if we could have $J = 0$) and the Moller reactant states for Rb + He at J = 50.5, 100.5, 150.5. Since we calculate the Moller reactant states in the asymptotic limit of the potential energy surfaces, they do not depend on the molecular state of the system but only on J and the reduced mass, μ, of the system.
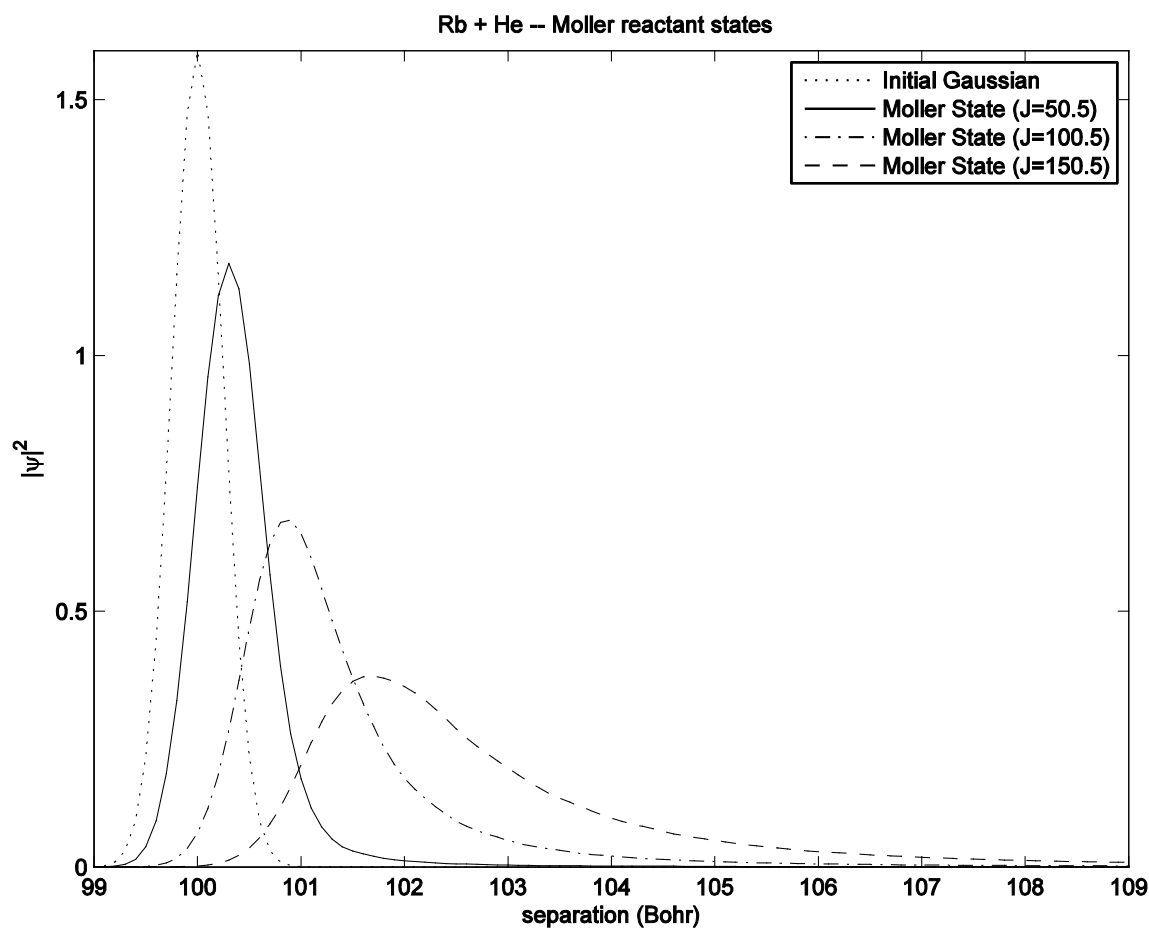
Fig. 2.4b: Moller reactant states and initial Gaussian for Rb + He, for $J = 50.5$, 100.5, 150.5. As J increases the centrifugal effective potential increases and causes the initial reactant Moller state to be broadened and shifted from the starting point of 100 Bohr.

In order to calculate the scattering matrix, or S-matrix, elements, we first calculate the correlation function. We propagate the Moller reactant states through the collision process to determine the Moller product states and then calculate the time-dependent correlation functions using equation (2.121). The wavepacket is propagated using the split operator method, in which the time evolution of wavepackets is given by (Weeks, Niday, and Yang, 2006):

$$
\begin{pmatrix} \Phi_1(R,\Delta t) \\ \Phi_2(R,\Delta t) \\ \vdots \end{pmatrix} = \exp\left[-i\begin{pmatrix} H_{11} & H_{12} & \cdots \\ H_{21} & H_{22} & \cdots \\ \vdots & \vdots & \ddots \end{pmatrix}\frac{\Delta t}{\hbar}\right]\begin{pmatrix} \Phi_1(R,0) \\ \Phi_2(R,0) \\ \vdots \end{pmatrix}
$$

$$
\approx \exp\left[-i\begin{pmatrix} V_{11} & V_{12} & \cdots \\ V_{21} & V_{22} & \cdots \\ \vdots & \vdots & \ddots \end{pmatrix}\frac{\Delta t}{2\hbar}\right]\exp\left[-i\begin{pmatrix} T_{11} & T_{12} & \cdots \\ T_{21} & T_{22} & \cdots \\ \vdots & \vdots & \ddots \end{pmatrix}\frac{\Delta t}{\hbar}\right] \qquad (2.130)
$$

$$
\times \exp\left[-i\begin{pmatrix} V_{11} & V_{12} & \cdots \\ V_{21} & V_{22} & \cdots \\ \vdots & \vdots & \ddots \end{pmatrix}\frac{\Delta t}{2\hbar}\right]\begin{pmatrix} \Phi_1(R,0) \\ \Phi_2(R,0) \\ \vdots \end{pmatrix}
$$

and we use a unitary transformation between adiabatic and diabatic representations to ensure that the potential and kinetic energy terms operate correctly. In body-fixed coordinates, the close-coupled Hamiltonian is (Lewis, 2011):

$$
\hat{\mathbf{H}} = -\frac{1}{2\mu}\left(\mathbf{I}\frac{d}{dR}+\mathbf{F}\right)^2 + \frac{\hat{\mathbf{J}}^2+\hat{\mathbf{j}}^2-\hat{\mathbf{j}}_z^2}{2\mu R^2} + \frac{-\left(\mathbf{j}_-\mathbf{J}^+ + \mathbf{j}_+\mathbf{J}^-\right)}{2\mu R^2} + \hat{\mathbf{H}}^0_{M\,Ng} + \hat{\mathbf{V}}^M_{ls} \qquad (2.131)
$$

For the $A^2\Pi_{1/2}$, $A^2\Pi_{3/2}$, and $B^2\Sigma_{1/2}$ states, the Hamiltonian has matrix elements of the form (Blank, Weeks, and Kedziora, 2012; Allard and Kielkopf, 1982):

$$H = -\frac{1}{2\mu}\begin{pmatrix} \frac{d}{dR} & 0 & 0 & 0 & 0 & 0 \\ 0 & \frac{d}{dR} & 0 & 0 & 0 & 0 \\ 0 & 0 & \frac{d}{dR} & 0 & 0 & 0 \\ 0 & 0 & 0 & \frac{d}{dR} & 0 & 0 \\ 0 & 0 & 0 & 0 & \frac{d}{dR} & 0 \\ 0 & 0 & 0 & 0 & 0 & \frac{d}{dR} \end{pmatrix}^2$$

$$+ \begin{pmatrix} \Pi + \frac{a(R)}{2} & 0 & 0 & 0 & 0 & 0 \\ 0 & \frac{(2\Sigma+\Pi)}{3} + \frac{a(R)}{2} & -\frac{\sqrt{2}}{3}(\Sigma-\Pi) & 0 & 0 & 0 \\ 0 & -\frac{\sqrt{2}}{3}(\Sigma-\Pi) & \frac{(\Sigma+2\Pi)}{3} - a(R) & 0 & 0 & 0 \\ 0 & 0 & 0 & \Pi + \frac{a(R)}{2} & 0 & 0 \\ 0 & 0 & 0 & 0 & \frac{(2\Sigma+\Pi)}{3} + \frac{a(R)}{2} & \frac{\sqrt{2}}{3}(\Sigma-\Pi) \\ 0 & 0 & 0 & 0 & \frac{\sqrt{2}}{3}(\Sigma-\Pi) & \frac{(\Sigma+2\Pi)}{3} - a(R) \end{pmatrix} \quad (2.132a)$$

$$+ \begin{pmatrix} \frac{J(J+1)-\frac{3}{4}}{2\mu R^2} & -\frac{\left[3\left(J-\frac{1}{2}\right)\left(J+\frac{3}{2}\right)\right]^{1/2}}{2\mu R^2} & 0 & 0 & 0 & 0 \\ -\frac{\left[3\left(J-\frac{1}{2}\right)\left(J+\frac{3}{2}\right)\right]^{1/2}}{2\mu R^2} & \frac{J(J+1)+\frac{13}{4}}{2\mu R^2} & 0 & 0 & -\frac{2(J+1)}{2\mu R^2} & 0 \\ 0 & 0 & \frac{J(J+1)+\frac{3}{4}}{2\mu R^2} & 0 & 0 & -\frac{J+1}{2\mu R^2} \\ 0 & 0 & 0 & \frac{J(J+1)-\frac{3}{4}}{2\mu R^2} & -\frac{\left[3\left(J-\frac{1}{2}\right)\left(J+\frac{3}{2}\right)\right]^{1/2}}{2\mu R^2} & 0 \\ 0 & -\frac{2(J+1)}{2\mu R^2} & 0 & -\frac{\left[3\left(J-\frac{1}{2}\right)\left(J+\frac{3}{2}\right)\right]^{1/2}}{2\mu R^2} & \frac{J(J+1)+\frac{13}{4}}{2\mu R^2} & 0 \\ 0 & 0 & -\frac{J+1}{2\mu R^2} & 0 & 0 & \frac{J(J+1)+\frac{3}{4}}{2\mu R^2} \end{pmatrix}$$

Note that the omission of the $\frac{J+1}{2\mu R^2}$ terms in the (2,5), (3,6), (5,2), and (6,3) elements of the third matrix in (2.132a) has a small effect on the calculations and permits the 6x6 matrix to be approximated by a 3x3 matrix.

When we refer to coupling in this work, we must be careful to distinguish between two coupling scenarios. The first scenario involves the potential matrix as shown in (2.132a) and approximated by a 3x3 matrix. We will consider the second scenario, in which we calculate broadening and shift coefficients for the D2 line using its constituent potential energy surfaces, in section 2.6. In the first scenario, we consider two configurations of the system, coupled or uncoupled. Whether the system is coupled in this scenario is determined by which version of the potential matrix we use. We begin from (2.132a), which we call the fully-coupled 6x6 potential energy matrix in the diabatic representation. The first approximation we make is the omission of the $\frac{J+\frac{1}{2}}{2\mu R^2}$ terms as discussed above, which transforms (2.132a) into block-diagonal form with two identical 3x3 blocks; we use the top-left 3x3 block with the understanding that each state is two-fold degenerate in spin. We then have for our 3x3 coupled potential energy matrix

$$V_{eff} = \begin{pmatrix} \Pi + \frac{a(R)}{2} + \frac{J(J+1)-\frac{3}{4}}{2\mu R^2} & -\frac{\left[3\left(J-\frac{1}{2}\right)\left(J+\frac{3}{2}\right)\right]^{1/2}}{2\mu R^2} & 0 \\ -\frac{\left[3\left(J-\frac{1}{2}\right)\left(J+\frac{3}{2}\right)\right]^{1/2}}{2\mu R^2} & \frac{(2\Sigma+\Pi)}{3} + \frac{a(R)}{2} + \frac{J(J+1)+\frac{13}{4}}{2\mu R^2} & -\frac{\sqrt{2}}{3}(\Sigma-\Pi) \\ 0 & -\frac{\sqrt{2}}{3}(\Sigma-\Pi) & \frac{(\Sigma+2\Pi)}{3} - a(R) + \frac{J(J+1)+\frac{3}{4}}{2\mu R^2} \end{pmatrix} \quad (2.132b)$$

where Π and Σ are the diabatic potentials. Equation (2.132b) is the effective potential matrix we use to generate coupled S-matrix elements. We generate uncoupled S-matrix elements by making the further approximation that the off-diagonal Coriolis terms (the (1,2) and (2,1) elements in the 3x3 matrix) are zero, which then allows us to diagonalize the potential matrix in terms of the adiabatic potentials of the three excited states:

$$V_{eff} = \begin{pmatrix} V(\Pi_{3/2}) + \frac{J(J+1)-\frac{3}{4}}{2\mu R^2} & 0 & 0 \\ 0 & V(\Sigma_{1/2}) + \frac{J(J+1)+\frac{13}{4}}{2\mu R^2} & 0 \\ 0 & 0 & V(\Pi_{1/2}) + \frac{J(J+1)+\frac{3}{4}}{2\mu R^2} \end{pmatrix} \quad (2.132c)$$

Equation (2.132c) is the effective potential matrix we use in the uncoupled case.

Because the coupling between the positive-spin states and the negative-spin states is not significant, this research will use the 3x3 matrix version of this coupling, represented by the upper-left 3x3 block in each term of (2.132a). Since we are now propagating the wavepacket under the full Hamiltonian in a region where all portions of the Hamiltonian contribute to the dynamics of the system, our correlation functions depend not only on J but also on the initial molecular state of the system. Figure 2.4c shows the correlation functions as a function of time for the $A^2\Pi_{1/2}$ state of Rb + He, for $J = 50.5, 100.5, 150.5$. Here we include both the spin-orbit and Coriolis couplings, which we call the "fully-coupled" case.
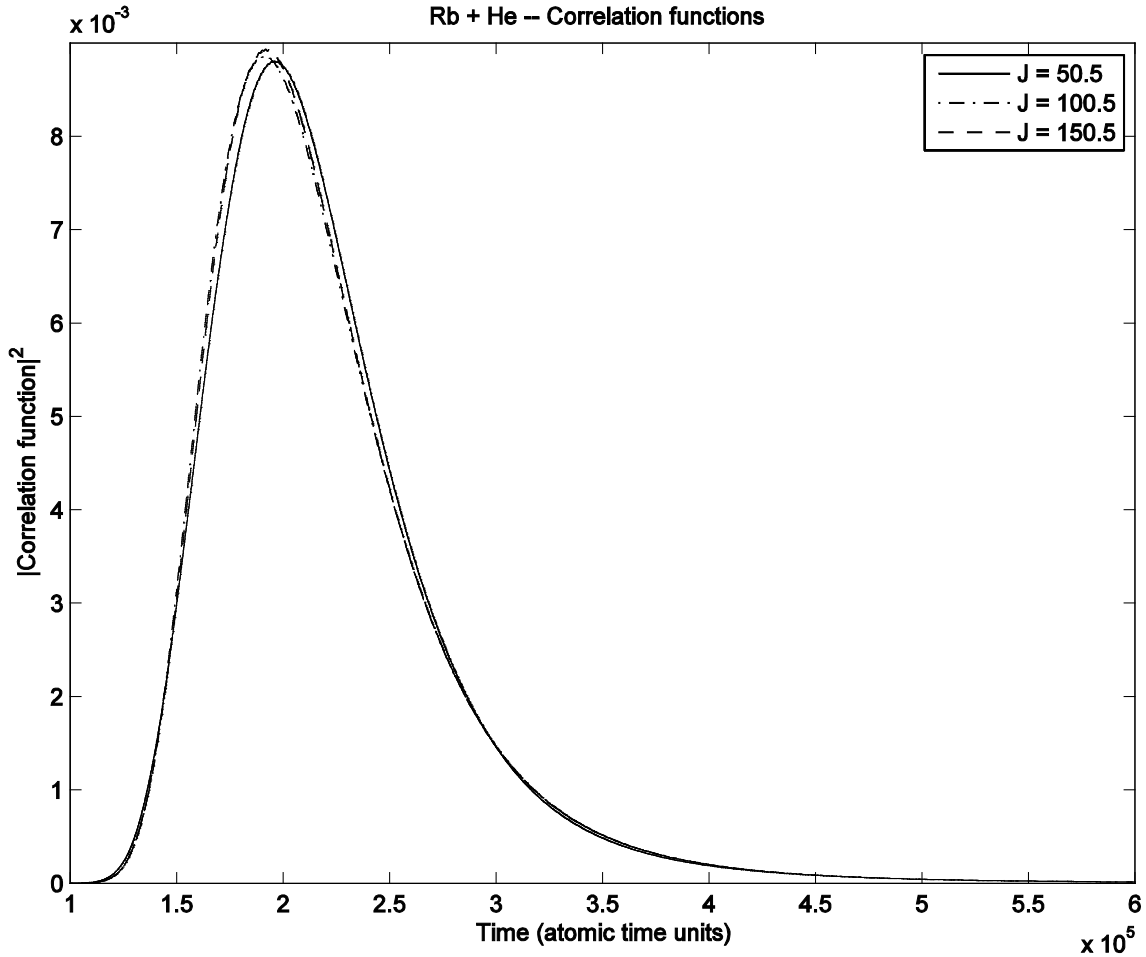
Fig. 2.4c: Squares of correlation functions for the $A^2\Pi_{1/2}$ state of Rb + He.

We can then calculate the S-matrix elements using equation (2.122). This yields a scattering matrix element as a function of energy and J. Figure 2.4d shows the square of the S-matrix element as a function of energy for the $A^2\Pi_{1/2} \rightarrow A^2\Pi_{1/2}$ transition in Rb + He, for $J = 50.5, 100.5, 150.5$.
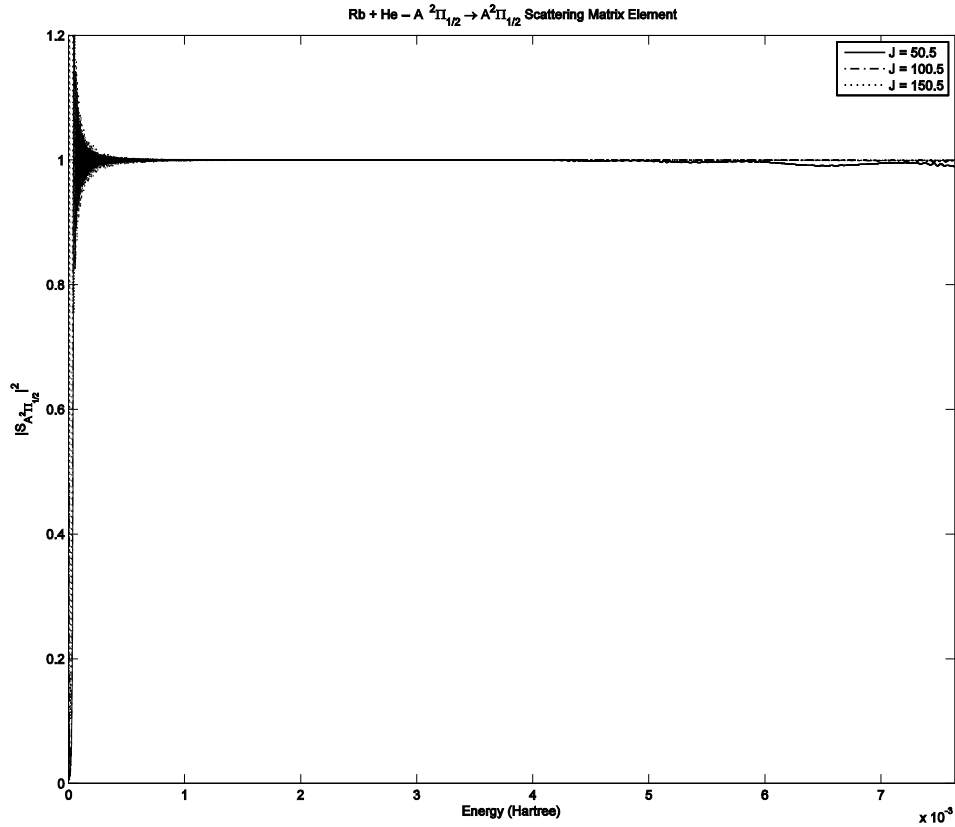
Fig. 2.4d: Squares of the S-Matrix elements for the $A^2\Pi_{1/2} \rightarrow A^2\Pi_{1/2}$ transition in Rb + He.

2.5.   Calculation of Line Broadening and Shift Coefficients

In order to find the broadening and shift coefficients, we must perform the sums in (2.110a) and (2.110b) over kinetic energy (E) and total angular momentum (J). Total angular momentum is constrained to be of half-integer quantity (in atomic units), while energy is quantized only by the energy resolution in the computer code we use to calculate scattering matrix elements (in this case, our energy resolution is $\Delta E = (0.01\ \text{Hartree})/8192 = 1.22 \times 10^{-6}\text{Hartree}$). We calculate the scattering phase shifts from the corresponding (complex) S-matrix elements:

$$\varphi = \tan^{-1}\left(\frac{\text{Im}(S)}{\text{Re}(S)}\right) \tag{2.133}$$

Since the arctangent function is periodic, we have to check for the start of a new cycle in phase, and then add 2π to allow the total phase to accumulate. Fig. 2.5a shows the scattering phase shift, as a function of J and E, for the $A^2\Pi_{1/2}$ state of Rb + He, in the uncoupled case. Fig. 2.5b shows the scattering phase shift for the $X^2\Sigma_{1/2}$ (ground) state of Rb + He, in the uncoupled case.

We then calculate the scattering phase shift difference between a given excited state and the ground state:

$$\theta_J(E) = \varphi_{\text{excited state}} - \varphi_{\text{ground state}} \tag{2.134}$$

Once we have the scattering phase shift difference for the entire range (in J and E) over which the collision can be said to occur, we can subtract an overall constant phase from the entire data set without loss of generality; here we determine an arbitrary zero of phase, in exactly the same way that the zero of potential energy is an arbitrary choice.
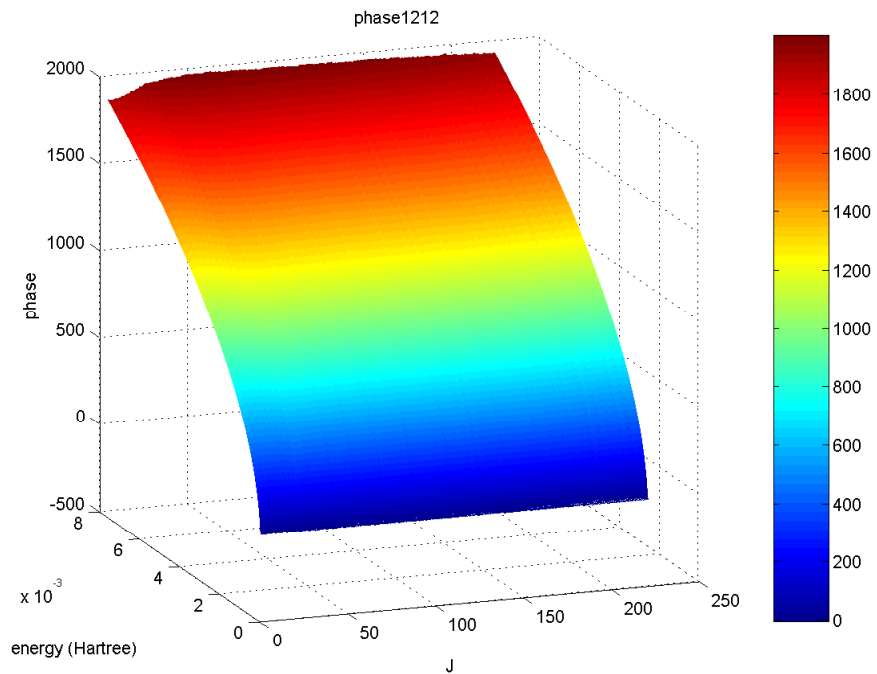
Fig. 2.5a: Phase shift for the $A^2\Pi_{1/2}$ state of Rb + He, uncoupled. See (2.132c).
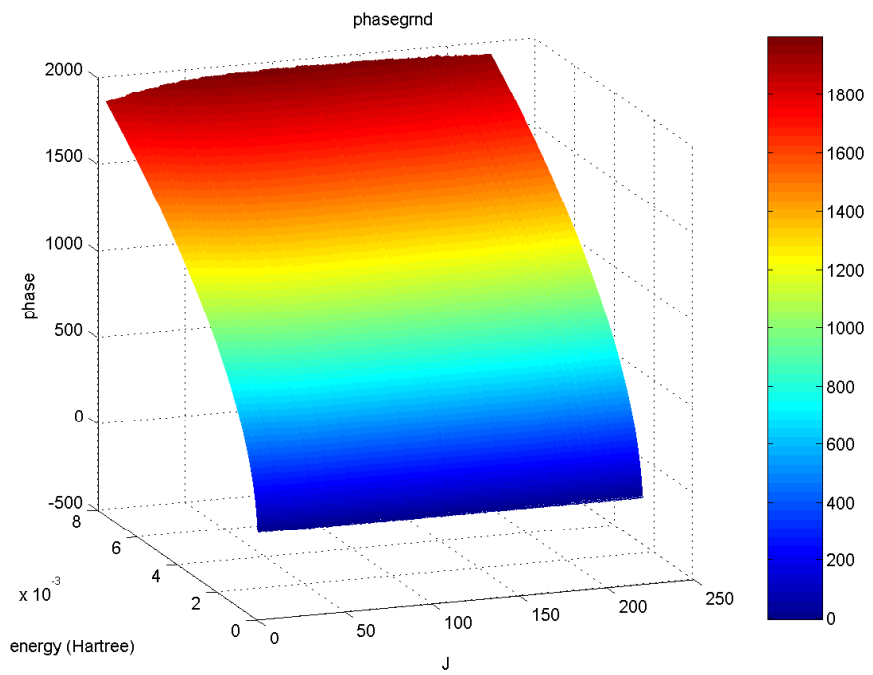
Fig. 2.5b: Phase shift for the ground state of Rb + He, uncoupled. See (2.132c).
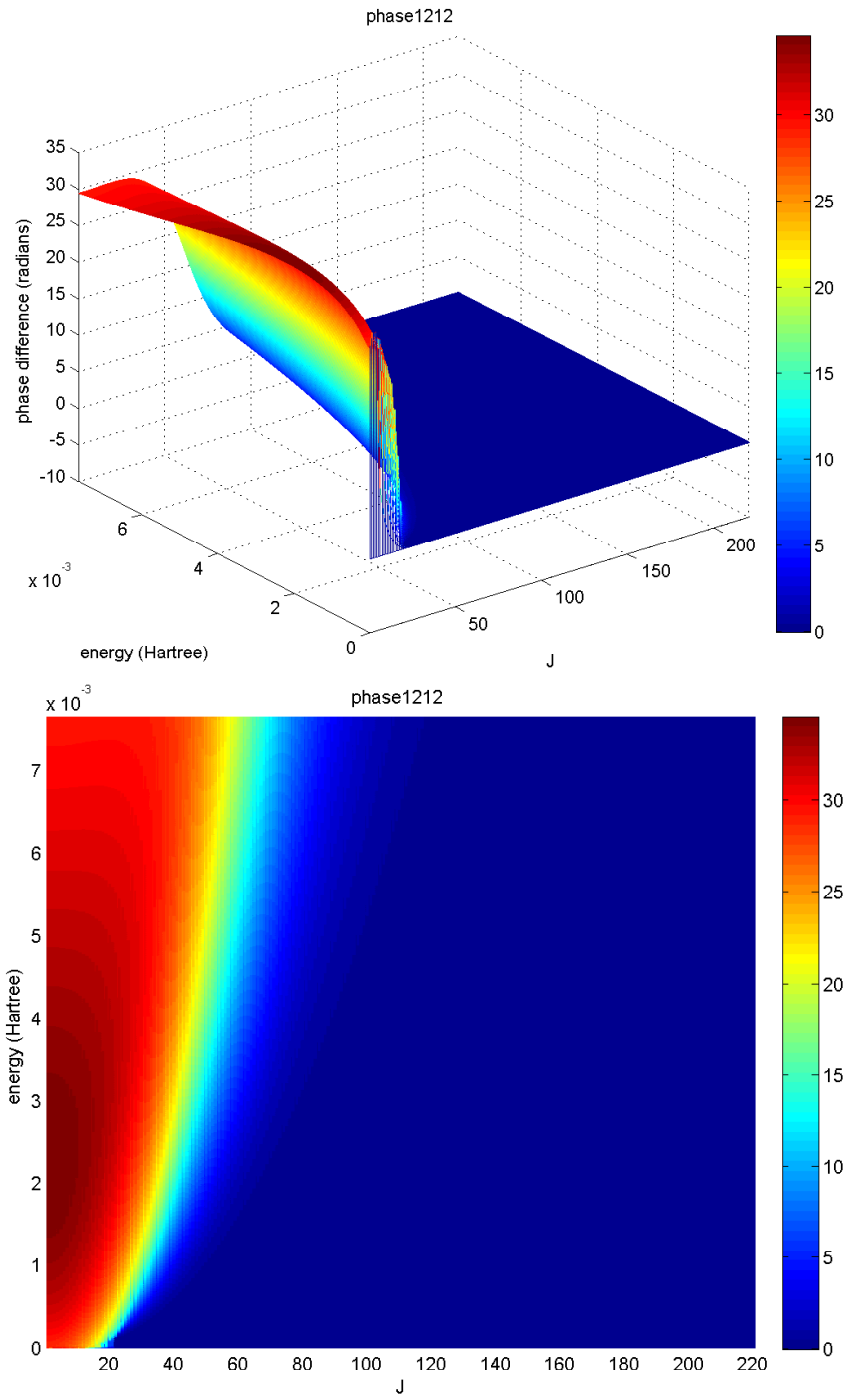
Fig. 2.5c: Phase shift difference for the $A^2\Pi_{1/2}$ state of Rb + He, uncoupled, side view (top) and top-down view (bottom) . See (2.132c).

Fig. 2.5c shows the scattering phase shift difference between Figs. 2.5a and 2.5b, as calculated by (2.134), for energies ranging from $E = 0$ Hartree to $E = 0.0075$ Hartree and total angular momenta ranging from $J = 0.5$ to $J = 220.5$. Since the phase shifts in Figs. 2.5a and 2.5b are approximately linear for larger energies (beyond $E = 0.006$ Hartree), we can extend the phase shifts by assuming a linear progression in energy beyond E = 0.0075 Hartree (for which we have rigorous calculations). In general we will extend the phase shifts out to E = 0.012 Hartree, which is our limit with the values of J we have calculated; we also have no concrete information about what new phenomena might occur at higher energies, so we would be naïve to extend the phase shifts linearly too much farther. In Fig. 2.5d, we do the same as in Fig. 2.5c, but here the calculations include both the spin-orbit and Coriolis couplings, which we call the "fully-coupled" case. Note by comparing Fig. 2.5c (above) with Fig. 2.5d (below), and by comparing Figs. 2.5e-f with Figs. 2.5g-h (below), it is possible to see how non-adiabatic dynamics influences terms in the broadening and shift calculations.

We then calculate the sine and cosine of the scattering phase shift differences and sum these results over total angular momentum and kinetic energy, as prescribed in (2.110a) and (2.110b), to find the broadening and shift coefficients (and then convert units to MHz/torr). Figs. 2.5e-f show the sine and cosine of the scattering phase shift difference, scaled by the Boltzmann distribution at temperatures T = 100 K, 394 K, and 800 K, for the $A^2\Pi_{1/2}$ state of the uncoupled case of Rb + He. Figs. 2.5g-h show the same quantities in the fully-coupled case. Figs. 2.5a-h look similar for all nine M + Ng pairs, so it is difficult to gain physical insight at a glance, even though there are subtle differences that give rise to different broadening and shift coefficients when integrated. Therefore we will limit the output to the more-instructive broadening and shift coefficient calculations in Chapter III.
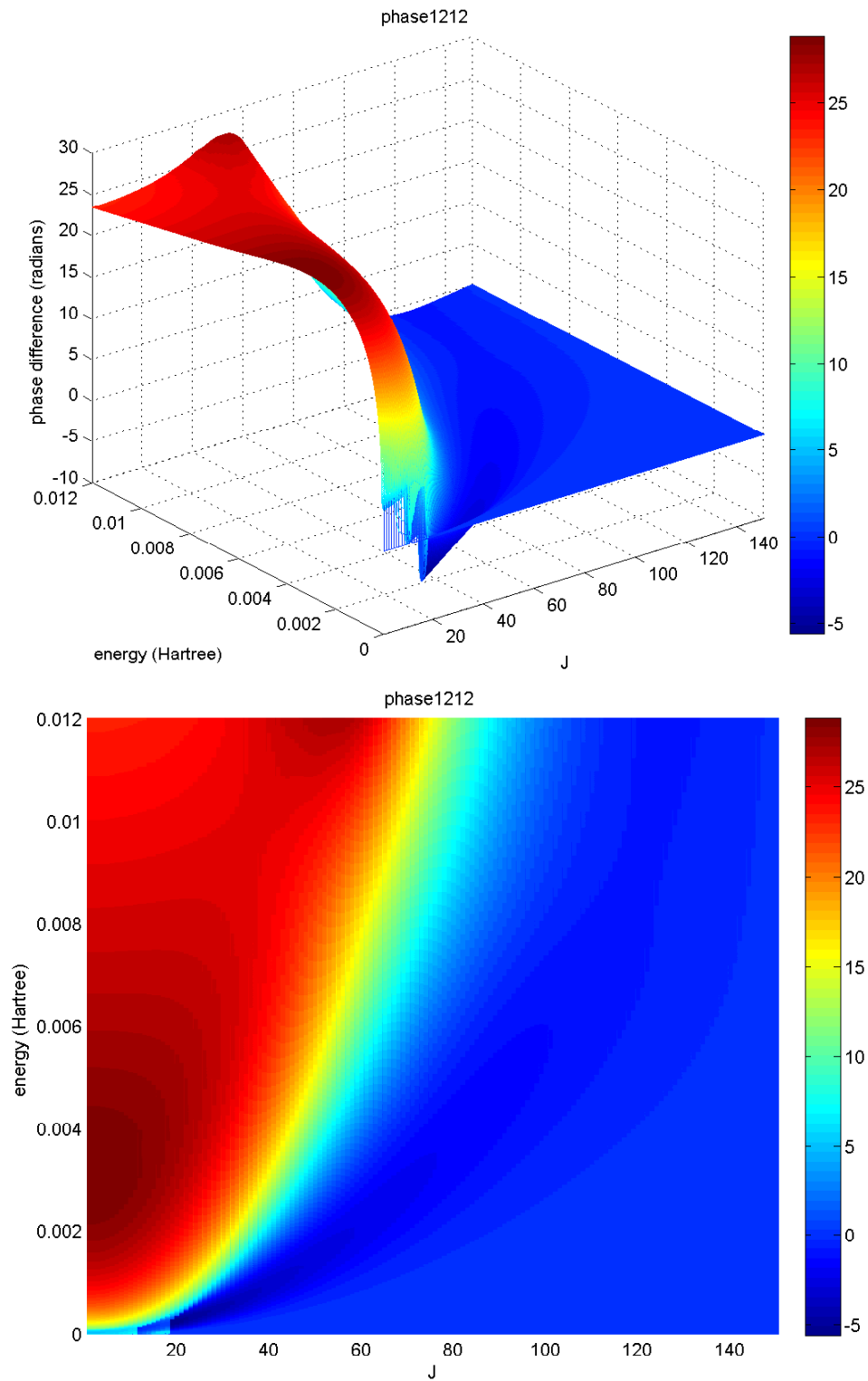
Fig. 2.5d: Phase shift difference for the $A^2\Pi_{1/2}$ state of Rb + He, fully coupled, side view (top) and top-down view (bottom) . See (2.132b).
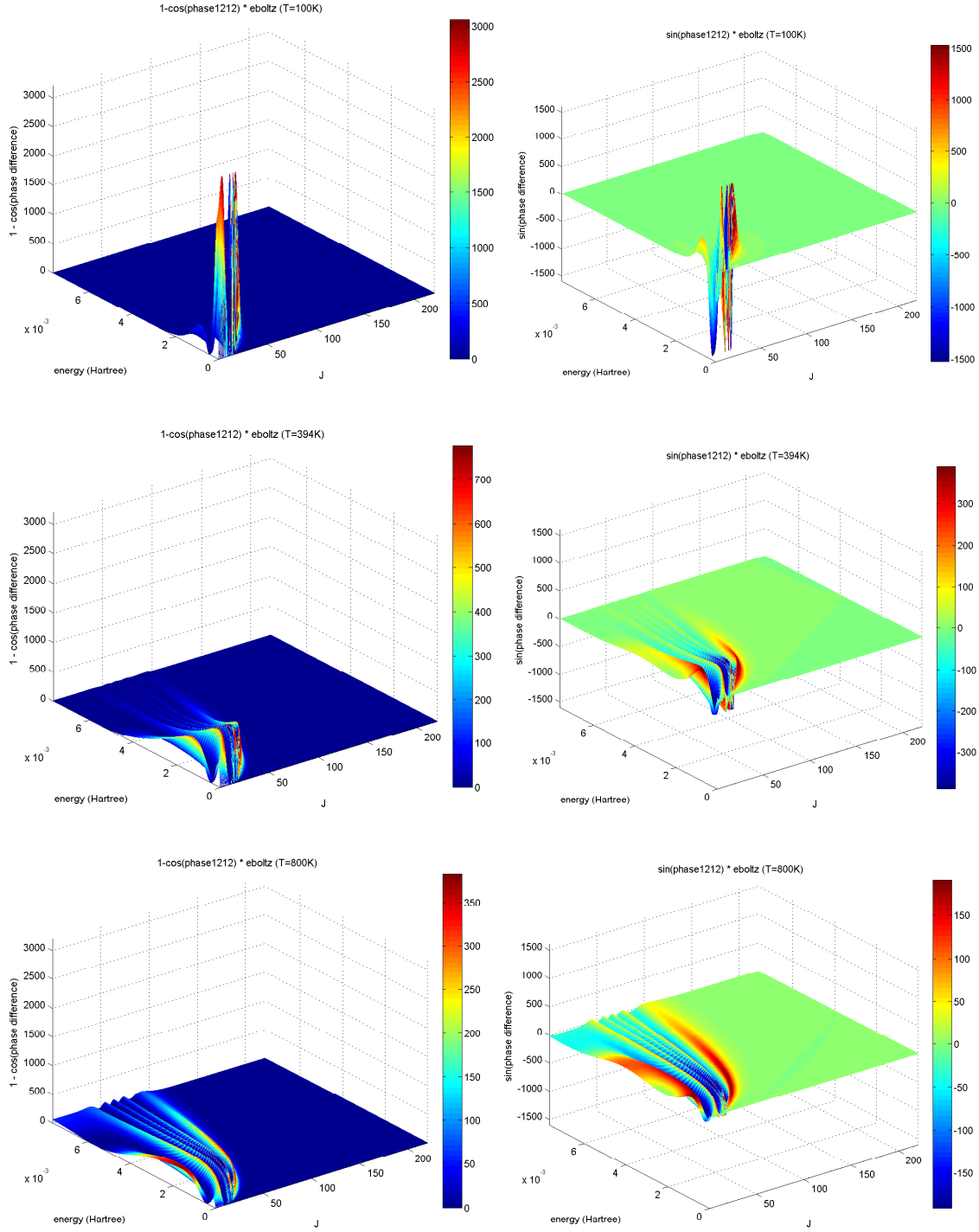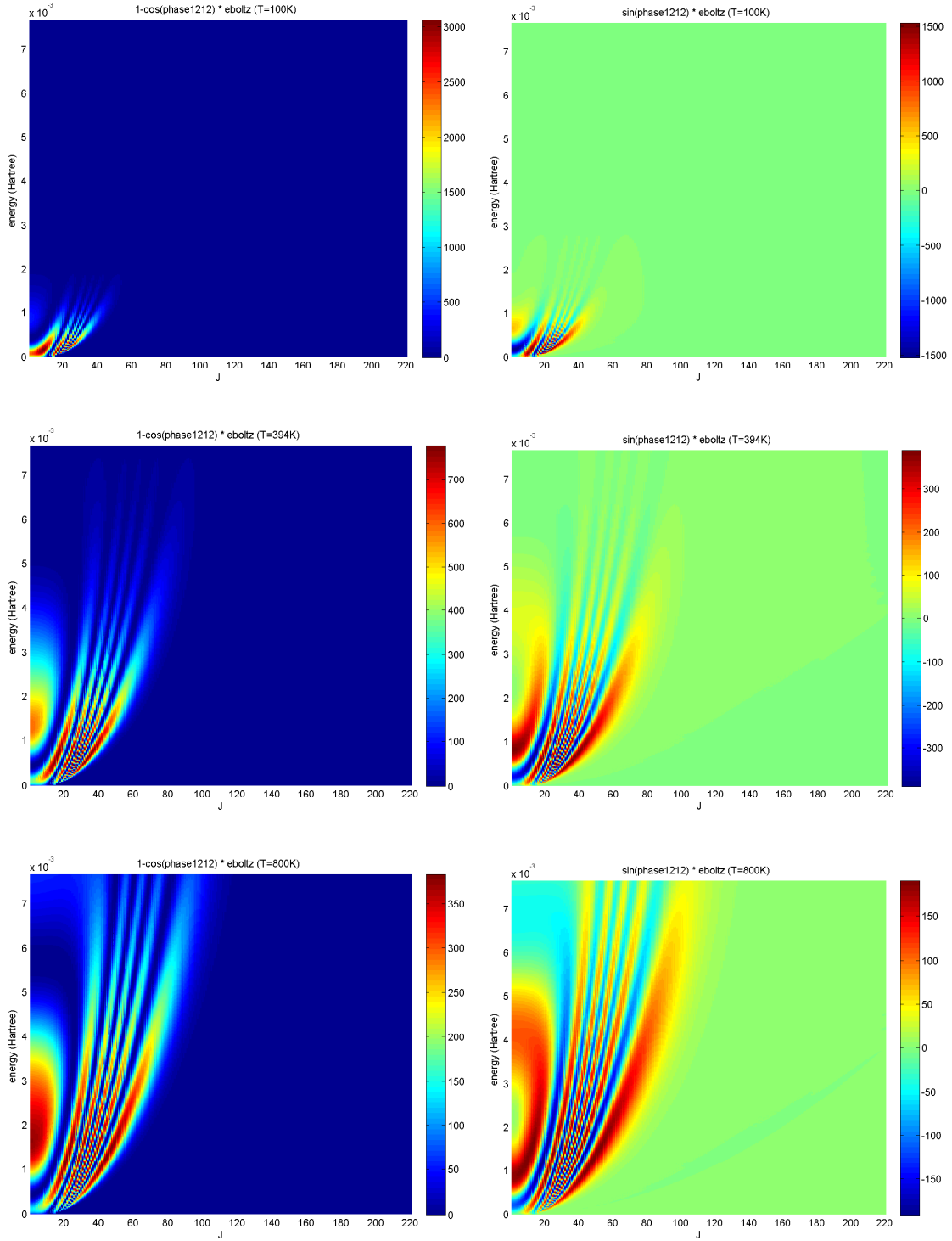
Fig. 2.5e: $\left[1 - \cos\theta_J(E)\right] \times$ Boltzmann distribution (left) and $\sin\theta_J(E) \times$ Boltzmann distribution (right) for the $A^2\Pi_{1/2}$ state of the uncoupled case of Rb + He, at T = 100 K (top), T = 394 K (middle), and T = 800 K (bottom), side view. See (2.132c).
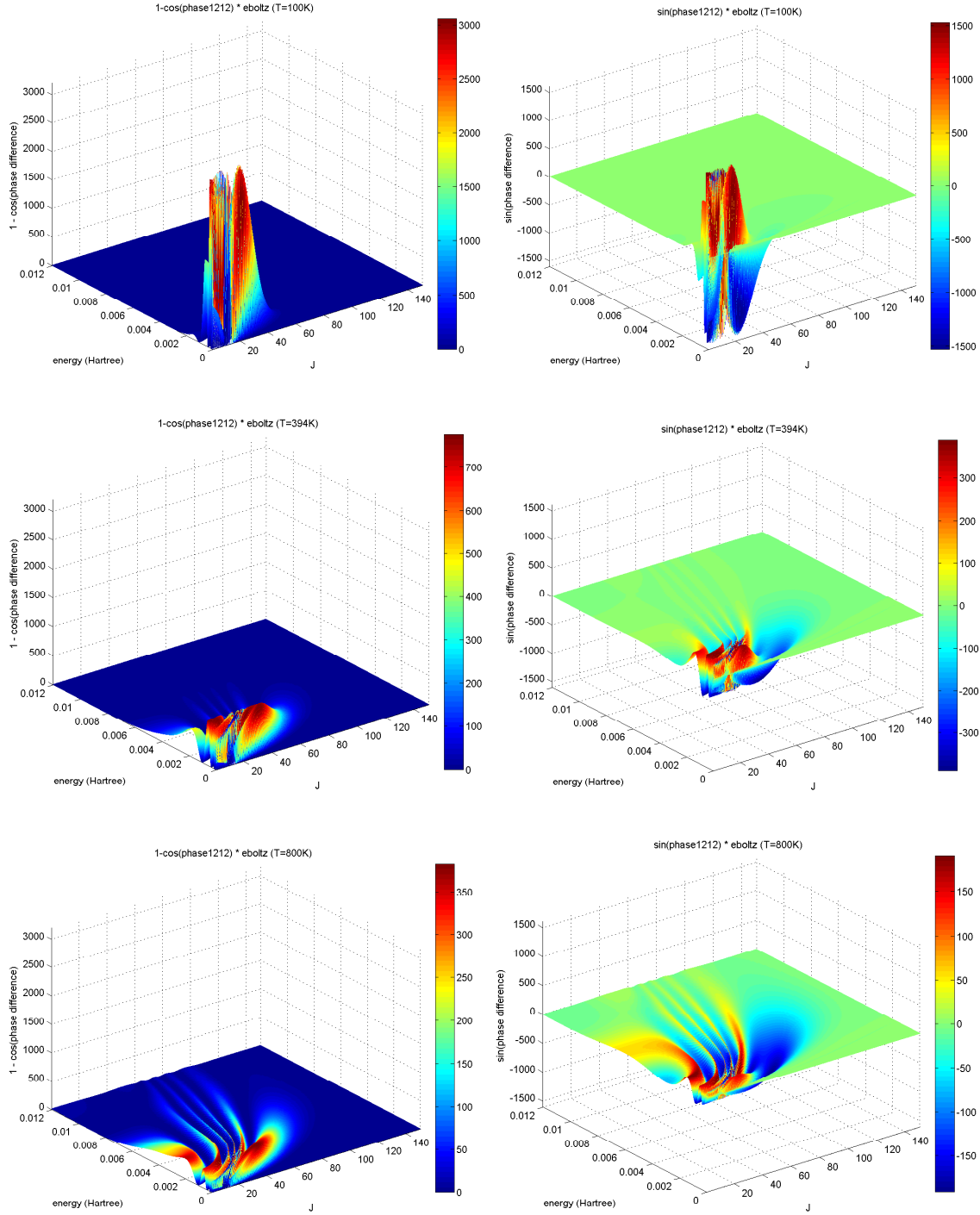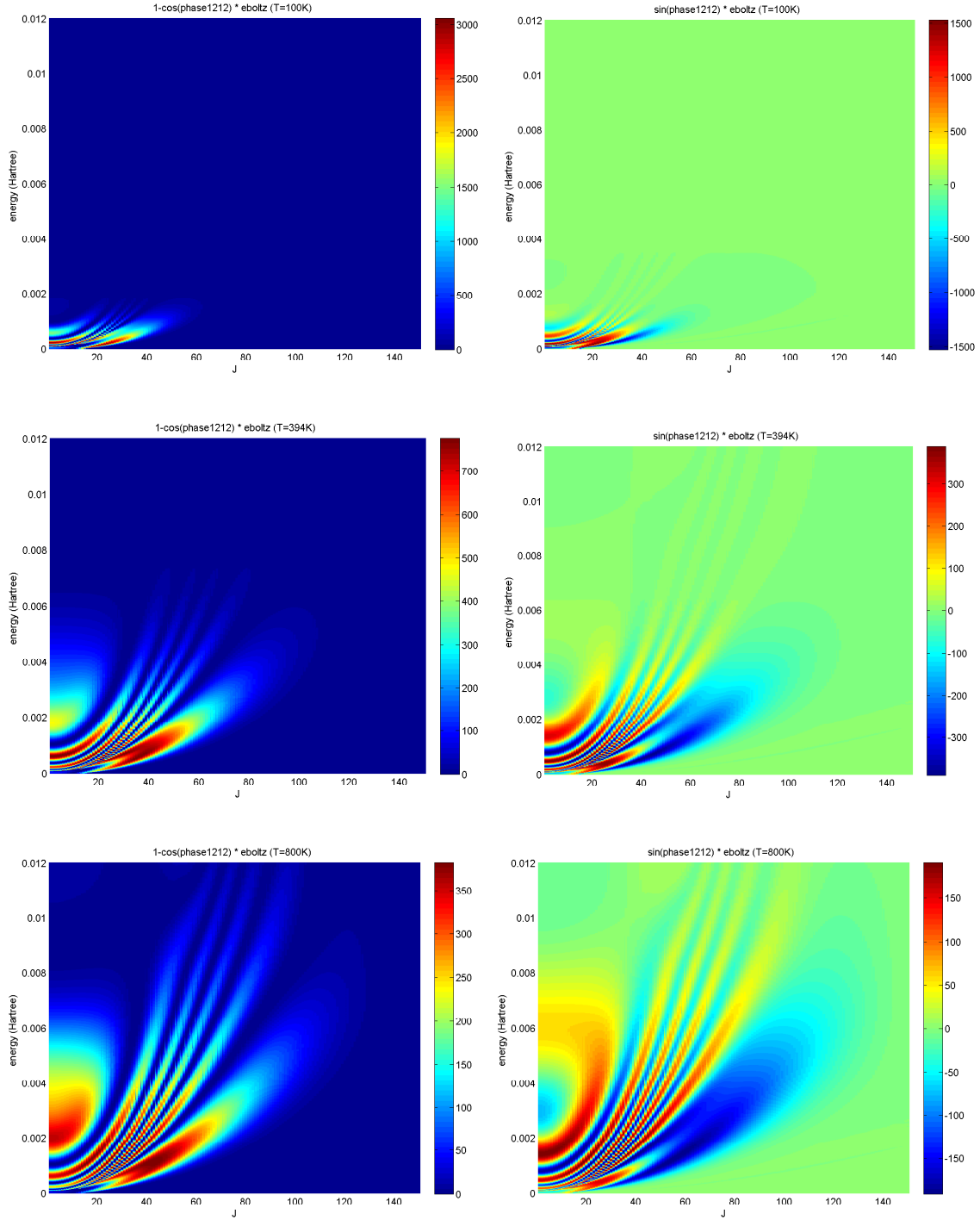
Fig. 2.5f: $\left[1 - \cos\theta_J(E)\right] \times$ Boltzmann distribution (left) and $\sin\theta_J(E) \times$ Boltzmann distribution (right) for the $A^2\Pi_{1/2}$ state of the uncoupled case of Rb + He, at T = 100 K (top), T = 394 K (middle), and T = 800 K (bottom), top-down view. See (2.132c).

64

Fig. 2.5g: $\left[1 - \cos\theta_J(E)\right] \times$ Boltzmann distribution (left) and $\sin\theta_J(E) \times$ Boltzmann distribution (right) for the $A^2\Pi_{1/2}$ state of the fully coupled case of Rb + He, at T = 100 K (top), T = 394 K (middle), and T = 800 K (bottom), side view. See (2.132b). These plots are shown primarily to compare with Fig. 2.5e. Their actual form is modified somewhat when used to calculate the broadening coefficient, as discussed in section 2.6.

Fig. 2.5h: $[1 - \cos\theta_J(E)] \times$ Boltzmann distribution (left) and $\sin\theta_J(E) \times$ Boltzmann distribution (right) for the $A^2\Pi_{1/2}$ state of the fully coupled case of Rb + He, at T = 100 K (top), T = 394 K (middle), and T = 800 K (bottom), top-down view. See (2.132b). These plots are shown primarily to compare with Fig. 2.5f. Their actual form is modified somewhat when used to calculate the shift coefficient, as discussed in section 2.6.

66

Figs. 2.5e and 2.5g are then integrated to determine broadening and shift coefficients at a given temperature. The calculations of (2.110a) and (2.110b) are then repeated for multiple temperatures. Figs. 2.5i and 2.5j show the uncoupled broadening and shift coefficients, as functions of temperature, compared with results from the Anderson-Talman model (Blank, Weeks, and Kedziora, 2012; Anderson, 1949 and 1952; Anderson and Talman, 1956).
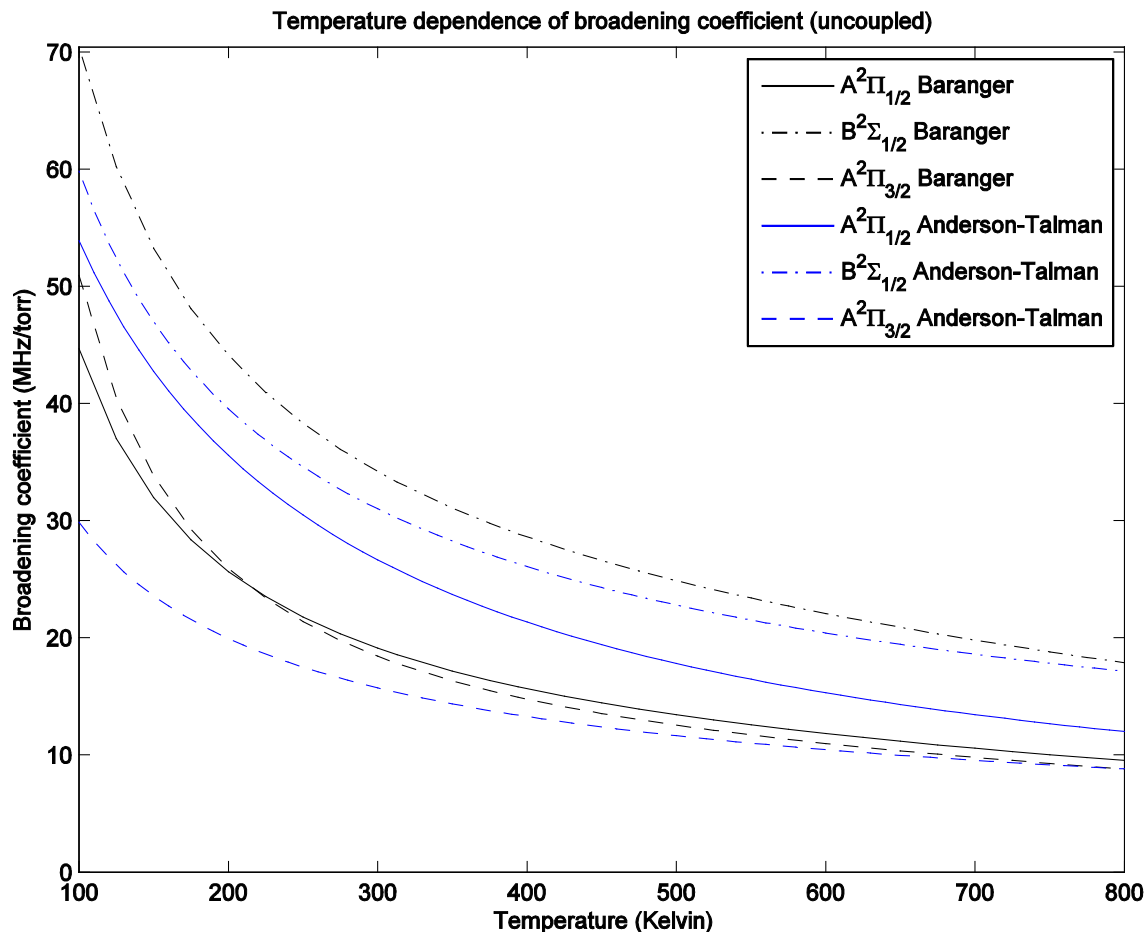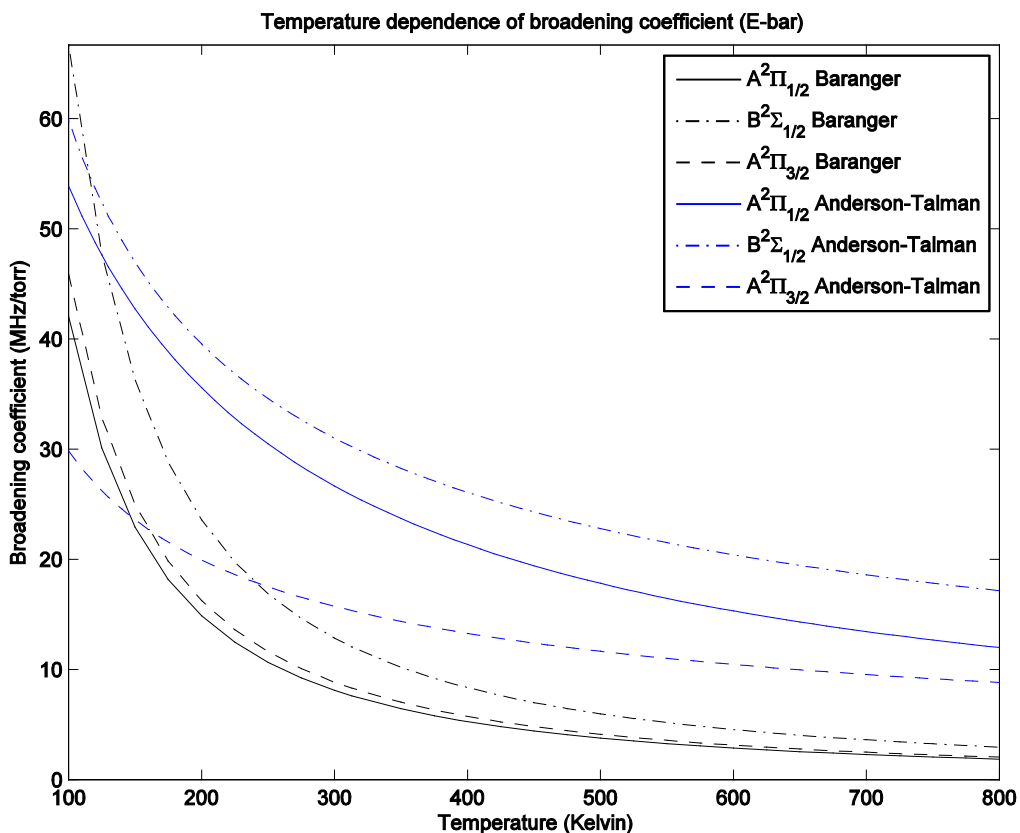

Fig. 2.5i: Broadening coefficients vs. temperature for Rb + He, uncoupled
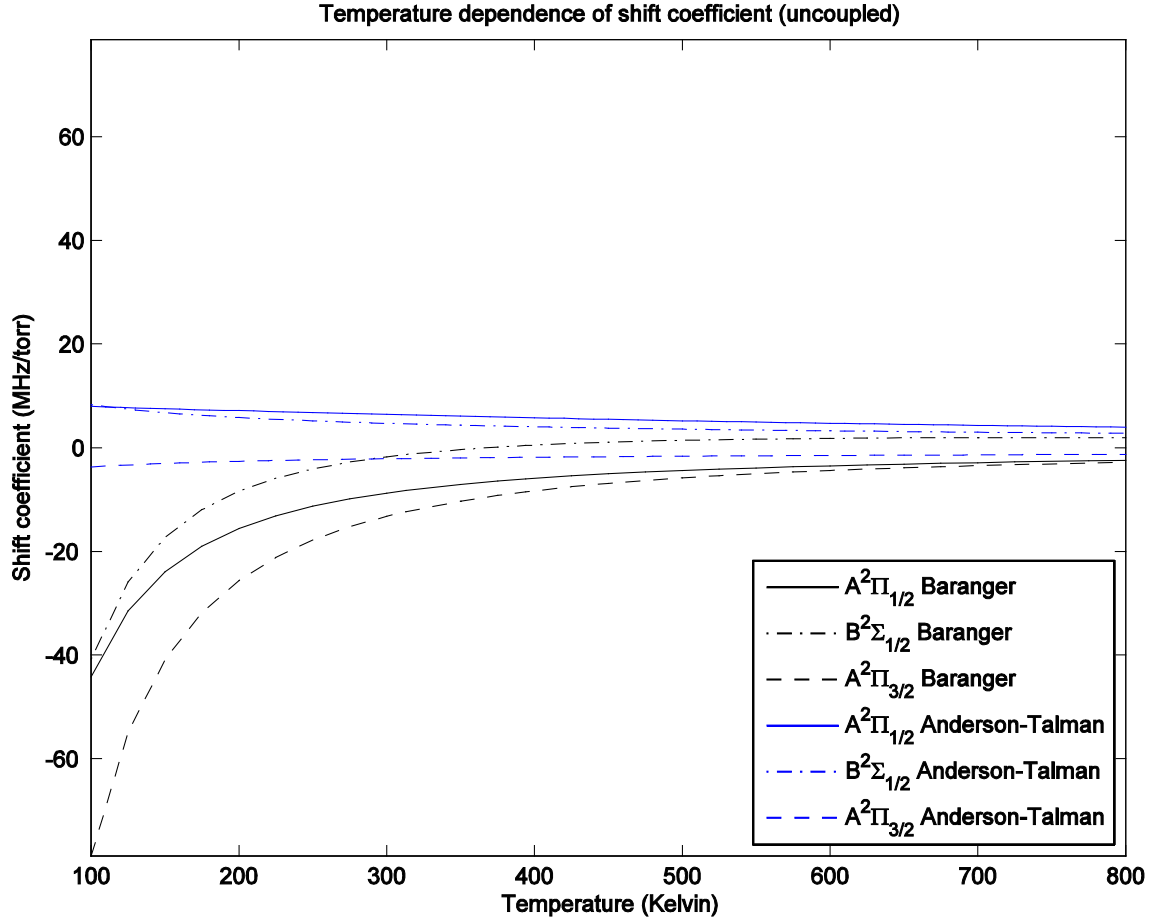
Fig. 2.5j: Shift coefficients vs. temperature for Rb + He, uncoupled

The calculations of (2.110a) and (2.110b) can be repeated in a special case that makes it more aptly compared with the Anderson-Talman model. In particular, the Anderson-Talman model does not assume a thermal distribution of kinetic energies in the collision phase space; rather, all collisions are assumed to occur at the thermal average velocity determined by (2.27c). If we assume the same average velocity in the Baranger model, we replace the Boltzmann distribution with an average kinetic energy,

$$\bar{E} = \frac{1}{2}\mu\bar{v}^2 = \frac{4k_B T}{\pi} \tag{2.135}$$

The broadening and shift coefficients of (2.110a) and (2.110b) thus become

$$\frac{n\alpha_1}{P} = \pi\hbar^2 \sqrt{\frac{2}{\mu^3}} \bar{E}^{-1/2} \sum_{J=0.5}^{\infty} (2J+1)[1 - \cos\theta_J(E)] \tag{2.136a}$$

$$\frac{n\beta_1}{P} = -\pi\hbar^2 \sqrt{\frac{2}{\mu^3}} \bar{E}^{-1/2} \sum_{J=0.5}^{\infty} (2J+1) \sin\theta_J(E) \tag{2.136b}$$

Figs. 2.5k and 2.5l show the uncoupled broadening and shift coefficients in this average kinetic energy case, as functions of temperature, compared with results from the Anderson-Talman model.

Fig. 2.5k: Broadening coefficients vs. temperature for Rb + He, uncoupled, average kinetic energy
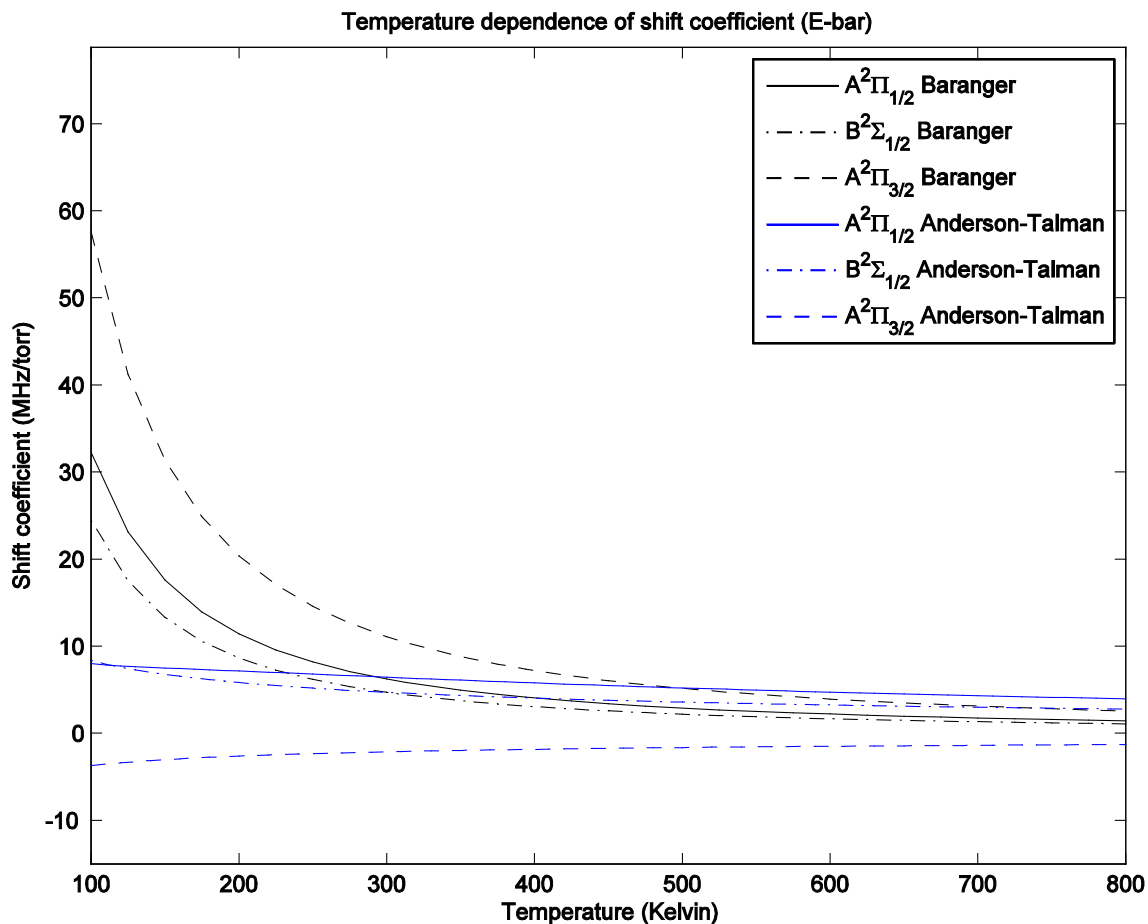
Fig. 2.5l: Shift coefficients vs. temperature for Rb + He, uncoupled, average kinetic energy

Once we have the broadening and shift coefficients, we can calculate the broadening and shift cross sections. The first step is to recast the broadening and shift coefficients in terms of rates per concentration rather than rates per pressure. We do this by multiplying by $k_B T = \dfrac{P}{n}$ so that we deal with α_1 and β_1 rather than $\dfrac{n\alpha_1}{P}$ and $\dfrac{n\beta_1}{P}$ as in (2.136a-b). Results for these are shown in Figs. 2.5m-n.
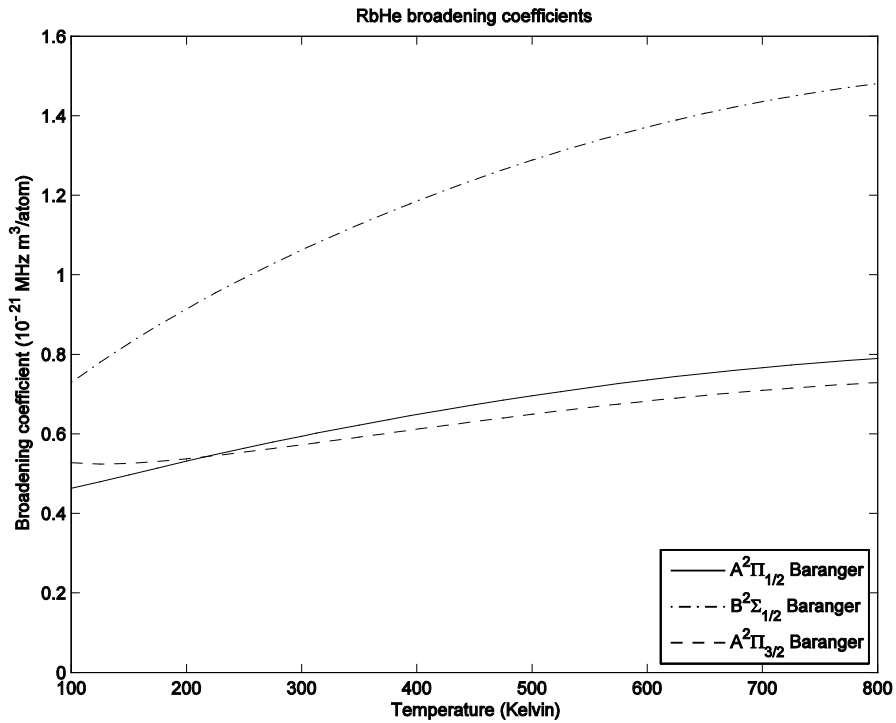
Fig. 2.5m: Broadening rates vs. temperature for Rb + He.
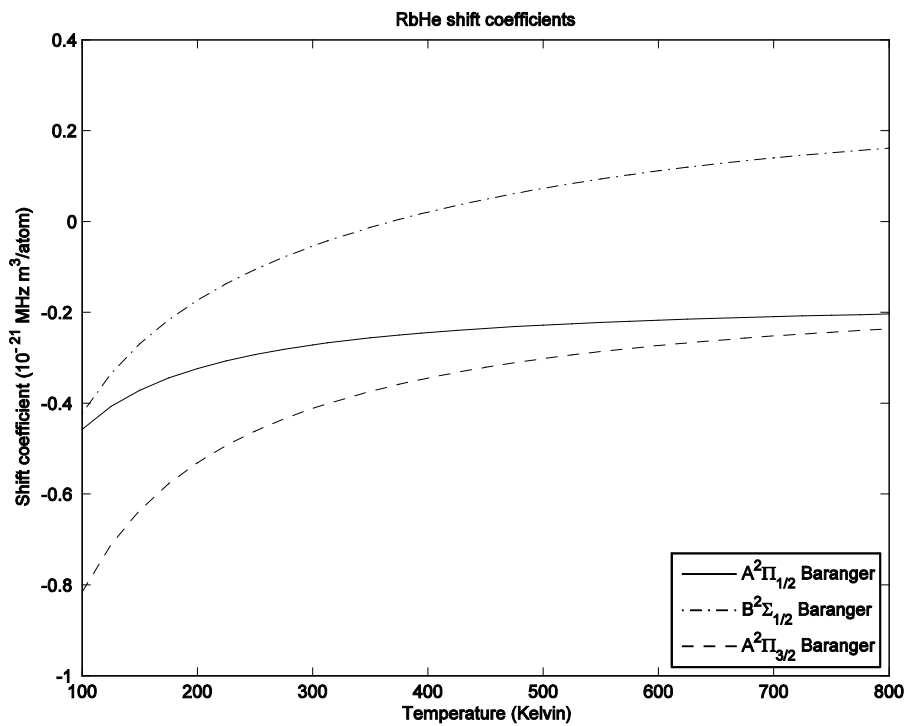
Fig. 2.5n: Shift rates vs. temperature for Rb + He.

71

Once we have α_1 and β_1 we can calculate the broadening and shift cross sections. Assuming the cross section, σ, is independent of the relative speed during the collision process, we can divide the broadening or shift coefficient by the average speed at a given temperature (Pitz, Fox, and Perram, 2010):

$$\sigma_\alpha(T) = \alpha_1 \left(\frac{8k_B T}{\pi\mu}\right)^{-1/2} \tag{2.137a}$$

$$\sigma_\beta(T) = \beta_1 \left(\frac{8k_B T}{\pi\mu}\right)^{-1/2} \tag{2.137b}$$

Here, we must be careful that the thermal average speed does vary with temperature, so we are not simply dividing the results in Figs. 2.5m-n by a constant. The result is a cross section that decays with increasing temperature; we expect that a greater kinetic energy results in a lesser fractional change (and less time spent) within the potential energy curve during the collision process. The results for the cross sections of Rb + He are shown in Figs. 2.5o-p below.
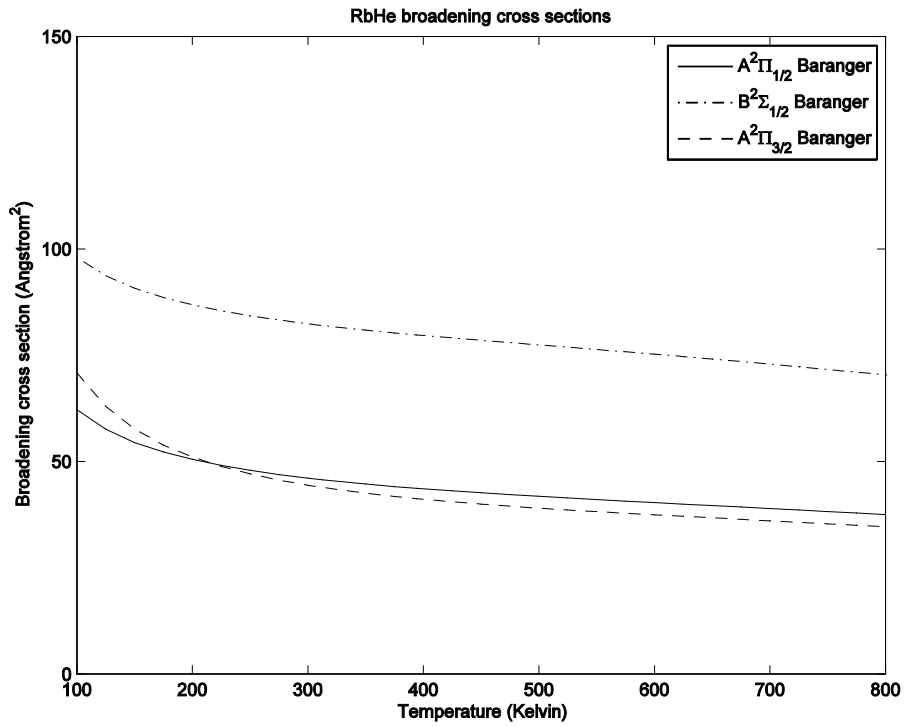
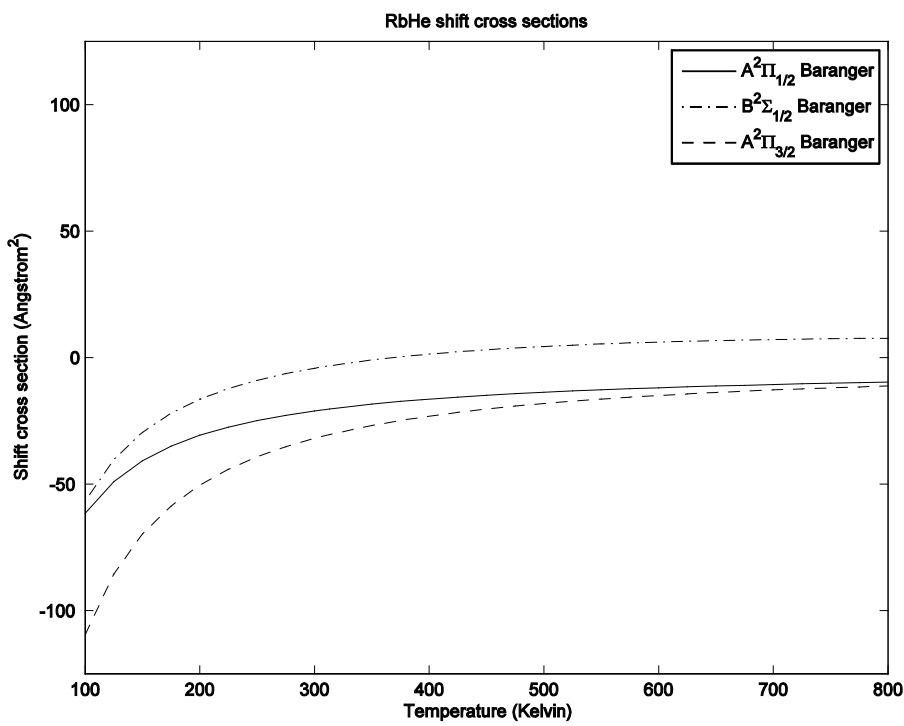Fig. 2.5o: Broadening cross sections vs. temperature for Rb + He.

Fig. 2.5p: Shift cross sections vs. temperature for Rb + He.

73

2.6 Coupling scenario for D2 line calculation in the Baranger Model

Going back to the Baranger model, as extended by Allard and Kielkopf (Allard & Kielkopf, 1982) we have a starting point for our study of spectral line broadening in equations (2.93a) and (2.93b):

$$\varphi(\tau) = \sum_{if} e^{-i\omega_{if}\tau} \exp[-ng(\tau)] \tag{2.93a}$$

$$g(\tau) = \int_0^\infty f(v)dv \int_0^\infty 2\pi b db \int_{-\infty}^\infty v dt \left[1 - \left(u_{ff}^{-1}u_{ii}\right)_{Ang\,Av}\right] \tag{2.93b}$$

As Allard and Kielkopf point out, such a calculation is "nontrivial in all but two-level atoms [atoms with only one potential difference curve, or adiabatic processes] because of fine-structure transitions between excited states that occur during the collision" (Allard & Kielkopf, 1982). That is, fine-structure mixing produces a set of coupled equations which must be solved numerically; further, such calculations were prohibitively computationally-intensive at that time. However, this is a critical problem in any consideration of an Optically Pumped Alkali Laser system, because a two-level system generally will not perform as a laser. Such effects are part of the physical processes involved in spectral line broadening. A perturber can, for instance, propagate inward (toward the emitter atom) along one potential surface, go through a transition, and then propagate outward (away from the emitter atom) along a different potential surface. The conventional workaround to modeling nonadiabatic coupling in atomic collisions is to approximate the colliding system as a diatomic molecular system and each stage of the collision as an appropriate Hund's state (Allard & Kielkopf, 1982; Bransden & Joachain, 2003; Drake, 2006; Zare, 1988). Allard begins with (2.93b), where comparing (2.90) and (2.93b) gives

$$\left[1 - \left(u_{ff}^{-1}u_{ii}\right)_{Ang\,Av}\right]$$

$$= 1 - \sum_{m_i m_f m_{i'} m_{f'} M} (-1)^{-2J_f + m_i + m_{i'}} \begin{pmatrix} J_f & 1 & J_i \\ m_f' & M & -m_i' \end{pmatrix} \begin{pmatrix} J_f & 1 & J_i \\ m_f & M & -m_i \end{pmatrix}$$

$$\times \langle J_f m_f | U_C^{-1} | J_f m_f' \rangle \langle J_i m_i' | U_C | J_i m_i \rangle \tag{2.138}$$

Allard uses spherical symmetry (Allard and Kielkopf, 1982) to claim that if $m_f = m_f{'}$ (that is, the final state is the ground state), (2.76d) becomes

$$(2J_i + 1) \sum_{m_f{'}m_f M} \begin{pmatrix} J_f & 1 & J_i \\ m_f{'} & M & -m_i{'} \end{pmatrix} \begin{pmatrix} J_f & 1 & J_i \\ m_f & M & -m_i \end{pmatrix} = \delta_{m_i m_i{'}} \qquad (2.139)$$

And (2.138) becomes

$$\left[1 - \left(u_{ff}^{-1} u_{ii} \right)_{Ang\ Av} \right]$$

$$= 1 - \frac{1}{(2J_i + 1)} \langle J_f | U_C^{-1} | J_f \rangle \sum_{m_i=-J_i}^{+J_i} (-1)^{-2(J_f + m_i)} \langle J_i m_i | U_C | J_i m_i \rangle \qquad (2.140)$$

Now, J_f and m_i are constrained to be half-integers, so $J_f + m_i$ is an integer. Thus, $(-1)^{-2(J_f + m_i)} = 1$, and using (2.98a) and (2.98b),

$$\left[1 - \left(u_{ff}^{-1} u_{ii} \right)_{Ang\ Av} \right] = 1 - \frac{1}{(2J_i + 1)} e^{i\delta_{m_f}} \sum_{m_i=-J_i}^{+J_i} e^{-i\delta_{m_i}} \qquad (2.141)$$

For the $^2P_{1/2}$ manifold, $J_i = 1/2$ and (2.141) becomes

$$\left[1 - \left(u_{ff}^{-1} u_{ii} \right)_{Ang\ Av} \right] = 1 - \frac{1}{2} e^{i\delta_f} \sum_{m_i=-\frac{1}{2}}^{+\frac{1}{2}} e^{-i\delta_{m_i}} = 1 - e^{i(\delta_f - \delta_i)} \qquad (2.142a)$$

For the $^2P_{3/2}$ manifold, $J_i = 3/2$ and (2.141) becomes

$$\left[1 - \left(u_{ff}^{-1} u_{ii}\right)_{Ang\ Av}\right] = 1 - \frac{1}{4} e^{i\delta_f} \sum_{m_i=-\frac{3}{2}}^{+\frac{3}{2}} e^{-i\delta_{m_i}} = 1 - \frac{1}{2} e^{i\delta_f} \sum_{m_i=+\frac{1}{2}}^{+\frac{3}{2}} e^{-i\delta_{m_i}}$$

$$= 1 - \frac{1}{2} e^{i(\delta_f - \delta_{i=\frac{1}{2}})} - \frac{1}{2} e^{i(\delta_f - \delta_{i=\frac{3}{2}})}$$

(2.142b)

The Allard-coupled broadening and shift coefficients thus differ from the uncoupled case only for the D$_2$ line, which corresponds to transitions from the $^2P_{3/2}$ manifold. That result becomes:

$$\frac{n\alpha_1}{P} = \sqrt{\frac{2\pi}{\mu^3}} \hbar^2 (k_B T)^{-5/2} \sum_{E=0}^{\infty} \exp\left(-\frac{E}{k_B T}\right) \Delta E$$

$$\times \sum_{J=0.5}^{\infty} (2J+1)\left[1 - \frac{1}{2}\cos\theta_{f1}^J(E) - \frac{1}{2}\cos\theta_{f2}^J(E)\right]$$

(2.143a)

$$\frac{n\beta_1}{P} = -\sqrt{\frac{2\pi}{\mu^3}} \hbar^2 (k_B T)^{-5/2} \sum_{E=0}^{\infty} \exp\left(-\frac{E}{k_B T}\right) \Delta E$$

$$\times \sum_{J=0.5}^{\infty} (2J+1)\left[\frac{1}{2}\sin\theta_{f1}^J(E) + \frac{1}{2}\sin\theta_{f2}^J(E)\right]$$

(2.143b)

where θ_{f1}^J and θ_{f2}^J are the uncoupled scattering phase shift differences corresponding to the two states on the $^2P_{3/2}$ manifold (that is, the $A^2\Pi_{3/2}$ and $B^2\Sigma_{1/2}$ states). Figs. 2.6a and 2.6b show the broadening and shift coefficients as functions of temperature for Rb + He in the Allard-coupled case.
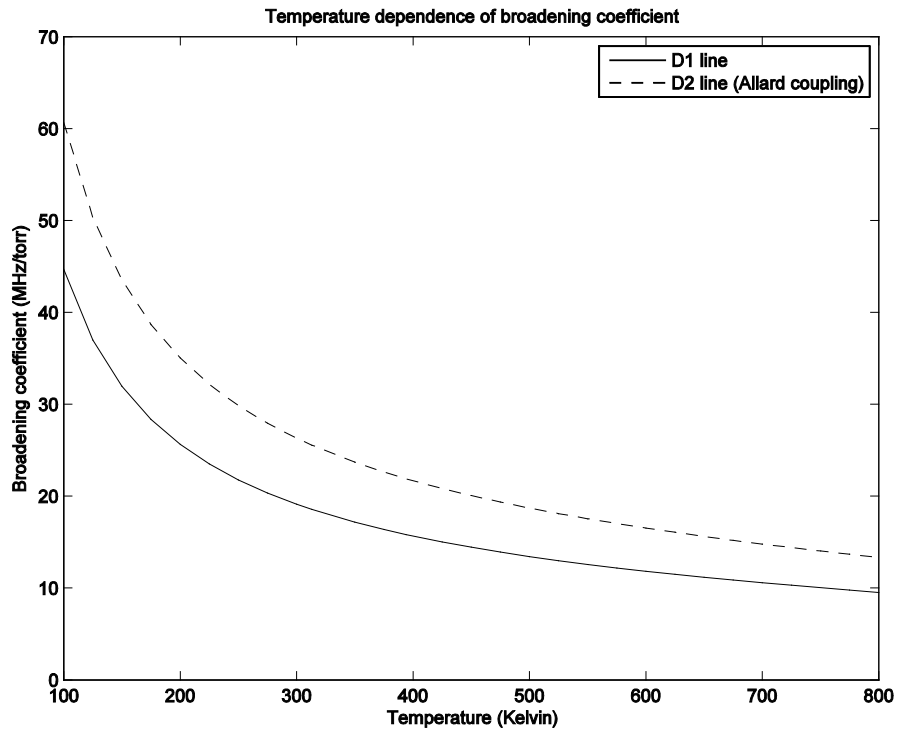
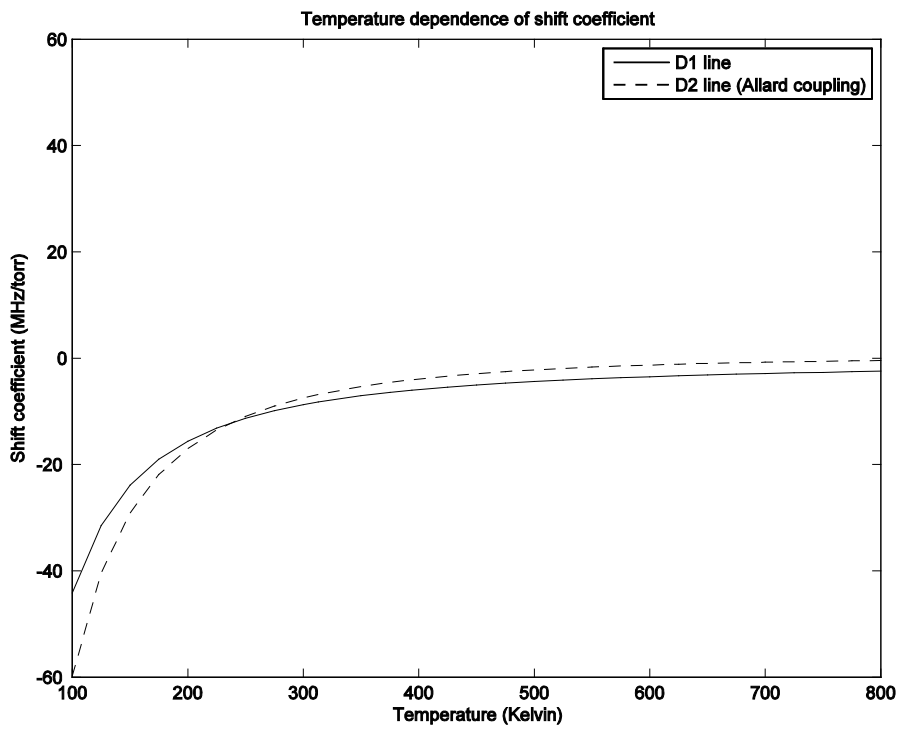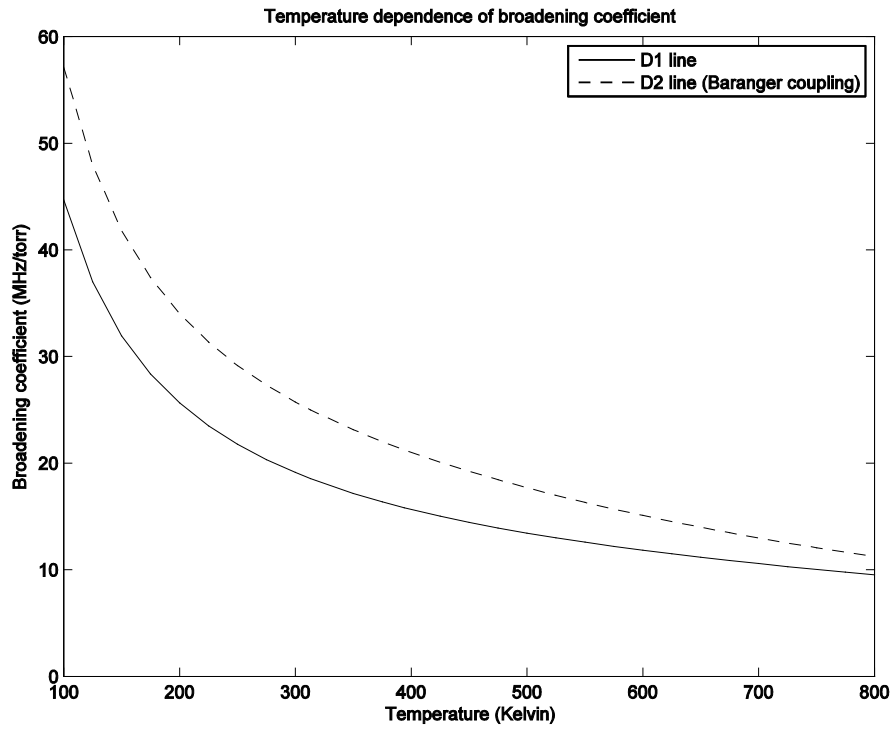Fig. 2.6a: Broadening coefficients vs. temperature for Rb + He, Allard-coupled

Fig. 2.6b: Shift coefficients vs. temperature for Rb + He, Allard-coupled

In the Allard-coupled case, the states in the $^2P_{3/2}$ manifold are coupled in a 50/50 split, as shown by the factors of ½ in (2.143a) and (2.143b). We can modify the coupling somewhat, to account for a variable coupling; to do this, we replace the factor of ½ with the probability for being in each corresponding state after the collision, which corresponds to the square of each state's corresponding scattering matrix element. This approach stems from the work of Baranger, reflected in equations (2.97) - (2.101b), where ζ is nonzero. The broadening and shift coefficients then become:

$$\frac{n\alpha_1}{P} = \sqrt{\frac{2\pi}{\mu^3}}\hbar^2(k_BT)^{-5/2}\sum_{E=0}^{\infty}\exp\left(-\frac{E}{k_BT}\right)\Delta E$$

$$\times \sum_{J=0.5}^{\infty}(2J+1)[1 - Q_{f1}^J\cos\theta_{f1}^J(E) - Q_{f2}^J\cos\theta_{f2}^J(E)]$$

(2.144a)

$$\frac{n\beta_1}{P} = -\sqrt{\frac{2\pi}{\mu^3}}\hbar^2(k_BT)^{-5/2}\sum_{E=0}^{\infty}\exp\left(-\frac{E}{k_BT}\right)\Delta E$$

$$\times \sum_{J=0.5}^{\infty}(2J+1)[Q_{f1}^J\sin\theta_{f1}^J(E) + Q_{f2}^J\sin\theta_{f2}^J(E)]$$

(2.144b)

where $Q_{f1}^J = \left|S_{f1}^J(E)\right|^2 = e^{-\zeta_{f1}^J}$ and $Q_{f2}^J = \left|S_{f2}^J(E)\right|^2 = e^{-\zeta_{f2}^J}$ are the normalized squares of the scattering matrix elements and $e^{-\zeta_{f1}^J}$ and $e^{-\zeta_{f2}^J}$ are decay coefficients as they appear in the form $e^{-\zeta}$ in equations (2.101a-b) and $Q_{f1}^J + Q_{f2}^J = e^{-\zeta_{f1}^J} + e^{-\zeta_{f2}^J} \approx 1$. We can thus approximate (2.144a-b) in the form:

$$\frac{n\alpha_1}{P} \approx \sqrt{\frac{2\pi}{\mu^3}}\,\hbar^2 (k_B T)^{-5/2} \sum_{E=0}^{\infty} \exp\left(-\frac{E}{k_B T}\right) \Delta E \tag{2.144c}$$

$$\times \sum_{J=0.5}^{\infty} (2J+1)[Q_{f1}^J(1 - \cos\theta_{f1}^J(E)) + Q_{f2}^J(1 - \cos\theta_{f2}^J(E))]$$

$$\frac{n\beta_1}{P} \approx -\sqrt{\frac{2\pi}{\mu^3}}\,\hbar^2 (k_B T)^{-5/2} \sum_{E=0}^{\infty} \exp\left(-\frac{E}{k_B T}\right) \Delta E \tag{2.144d}$$

$$\times \sum_{J=0.5}^{\infty} (2J+1)[Q_{f1}^J \sin\theta_{f1}^J(E) + Q_{f2}^J \sin\theta_{f2}^J(E)]$$

Like the Allard-coupled case, the Baranger coupling case does not change the D_1 line results (which depend only on the single state on the $^2P_{1/2}$ manifold) but changes only the D_2 line results (which depend on the two states on the $^2P_{3/2}$ manifold). Figs. 2.6c and 2.6d show broadening and shift coefficients as functions of temperature for Rb + He in the Baranger coupling case. Because this form of coupling requires data about the behavior of the scattering matrix elements and not just phases, these results cannot be extended in the energy regime in the same way as the other cases. Thus, the broadening and shift coefficients must be limited to lower temperatures in order to prevent error due to truncation of the Boltzmann distribution at the maximum energy.

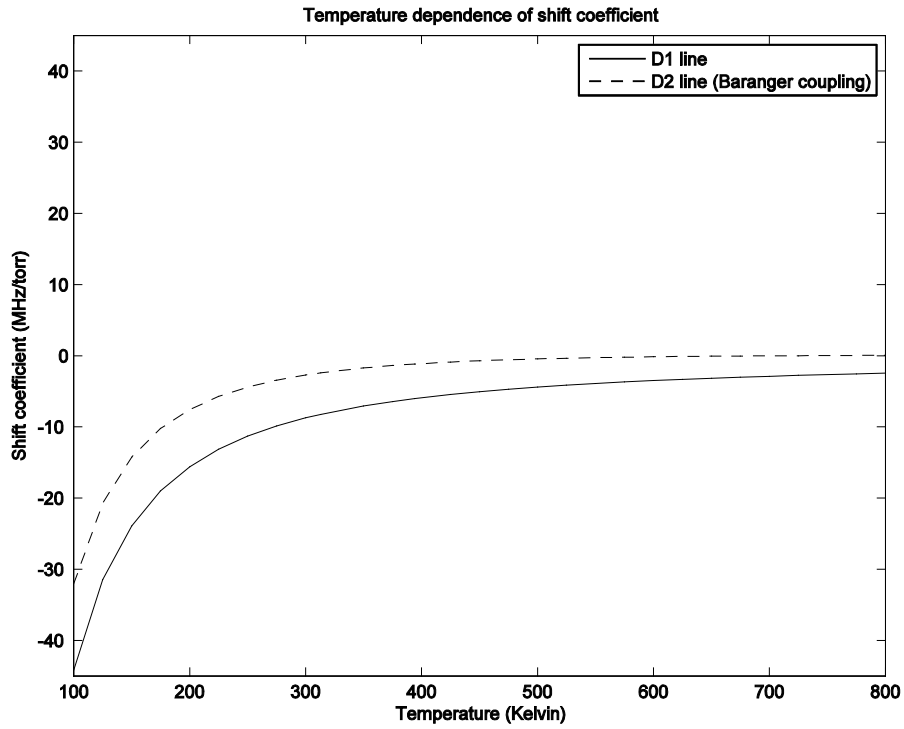Fig. 2.6c: Broadening coefficient vs. temperature for Rb + He, Baranger coupling

Fig. 2.6d: Shift coefficient vs. temperature for Rb + He, Baranger coupling

III. Research Results

This chapter analyzes the overall research results. The primary programming language used in writing computer simulations for this research is Fortran 90, with some Fortran 77 legacy code used where appropriate, compiled and executed on AFIT's Linux Cluster for the sake of computational efficiency. Preparation of initial wavepackets and analysis of the output data are achieved using Matlab code, executed primarily on a Hewlett-Packard P6620F (AMD Phenom II X4 830 quad-core 2.80-GHz processor; 6 GB RAM, running 64-bit Windows 7 OS). Here, we will lay out the results of the research and will discuss those results as well as potential limitations in simulation methods and theory-experiment interface. In this section we repeat the calculations of Chapter II for the Baranger model for all nine M + Ng pairs in four cases: (1) uncoupled (integrating over Boltzmann-distributed energies), (2) uncoupled using average energy instead of integrating over the Boltzmann distribution (solely for comparison with Anderson-Talman results), (3) Allard coupling (integrating over Boltzmann-distributed energies), and (4) Baranger coupling (integrating over Boltzmann-distributed energies).

For each M + Ng pair, the broadening and shift of the D_1 line is plotted for the Boltzmann energy distribution (which covers all coupling cases because the D_1 line includes only the $A^2\Pi_{1/2}$ state) and the thermal average energy given by (2.135). Then the broadening and shift of the D_2 line is plotted for each of the $A^2\Pi_{3/2}$ and $B^2\Sigma_{1/2}$ states for the Boltzmann energy distribution and the thermal average energy, along with the coupled D_2 line calculations in the Allard and Baranger coupling cases. In each case, Anderson-Talman results (Blank, in preparation) are plotted from Tables 2.2e-g, and experimental results (Pitz, Wertepny, and Perram, 2009; Pitz, Fox, and Perram, 2010) are compared. Then the broadening and shift cross sections are plotted, as calculated in (2.137a-b); in the case of Rb + He, these plots are the same as Figs. 2.5m-n but are presented in this chapter for completeness.

Additionally, plots are provided which compare the D_2 line broadening and shift coefficients using the Allard (and Baranger) coupling under different conditions. The Allard-coupled equations (2.143a-b) are assumed in most cases to use the phase shifts $\theta_{fi}^J(E)$ computed from the uncoupled scattering matrix elements, whereas the Baranger-coupled equations (2.144a-b) use phase shifts and weights from the fully coupled scattering matrix elements. One can perform the calculations much more quickly using the uncoupled scattering matrix elements because the uncoupled scattering matrix elements can be calculated in a single run, whereas the coupled scattering matrix elements require three runs (one run per input state).

3.1. Potassium + Helium (K + He)
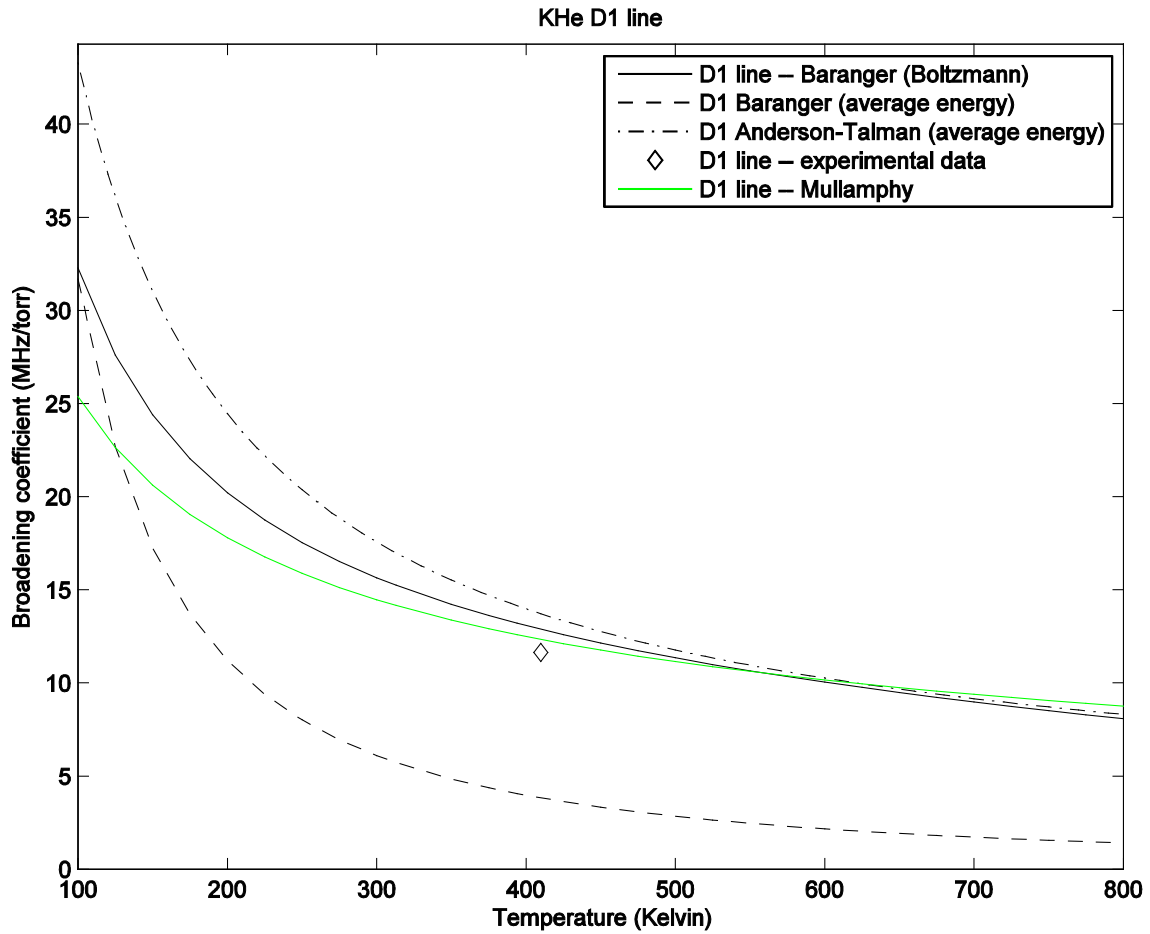
Fig. 3.1a: Broadening coefficients for the D1 line of K + He. The dashed line represents Baranger model calculations at the thermal average energy for each temperature. The solid line represents Baranger model calculations using the Boltzmann distribution and represents our best results. Both the Baranger model and the Anderson-Talman model provide excellent connection with experimental result (Lwin and McCartan, 1978).
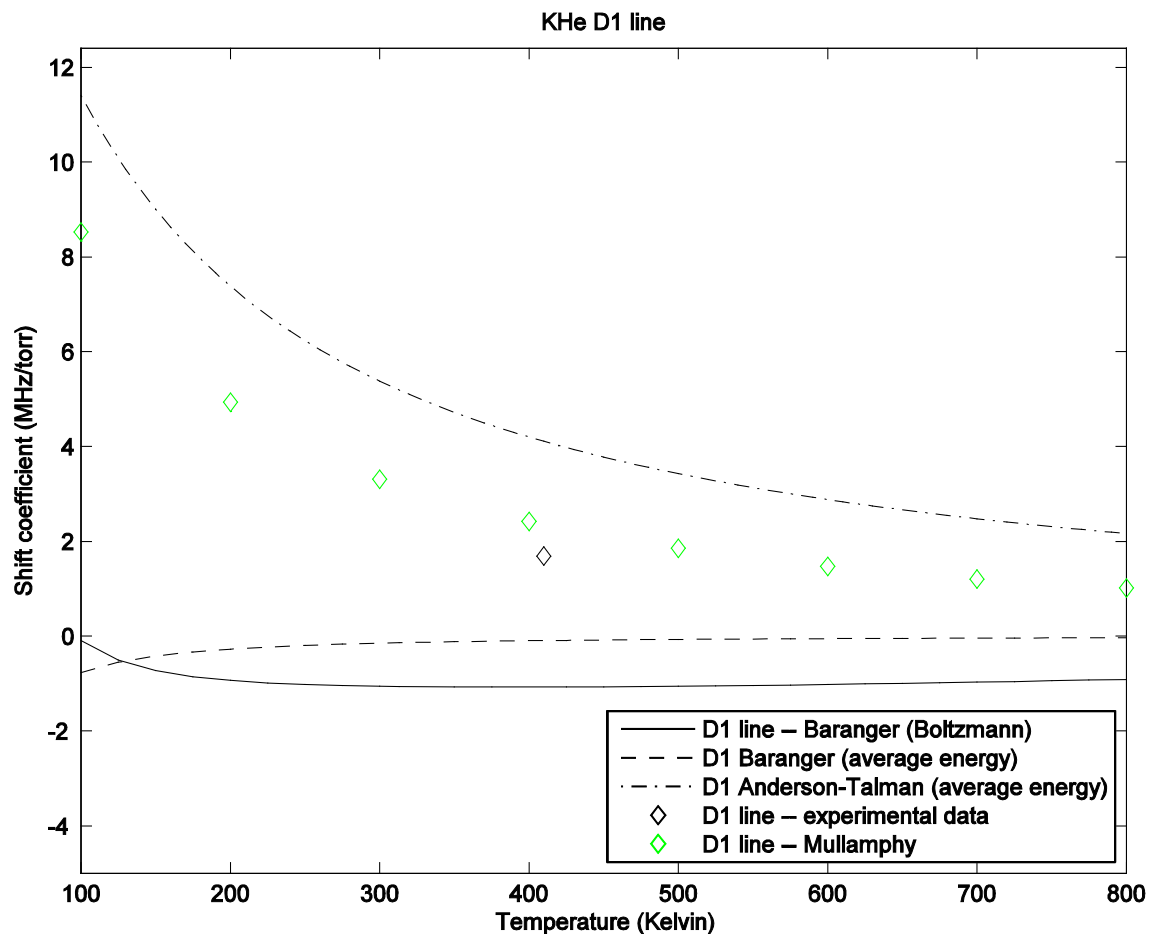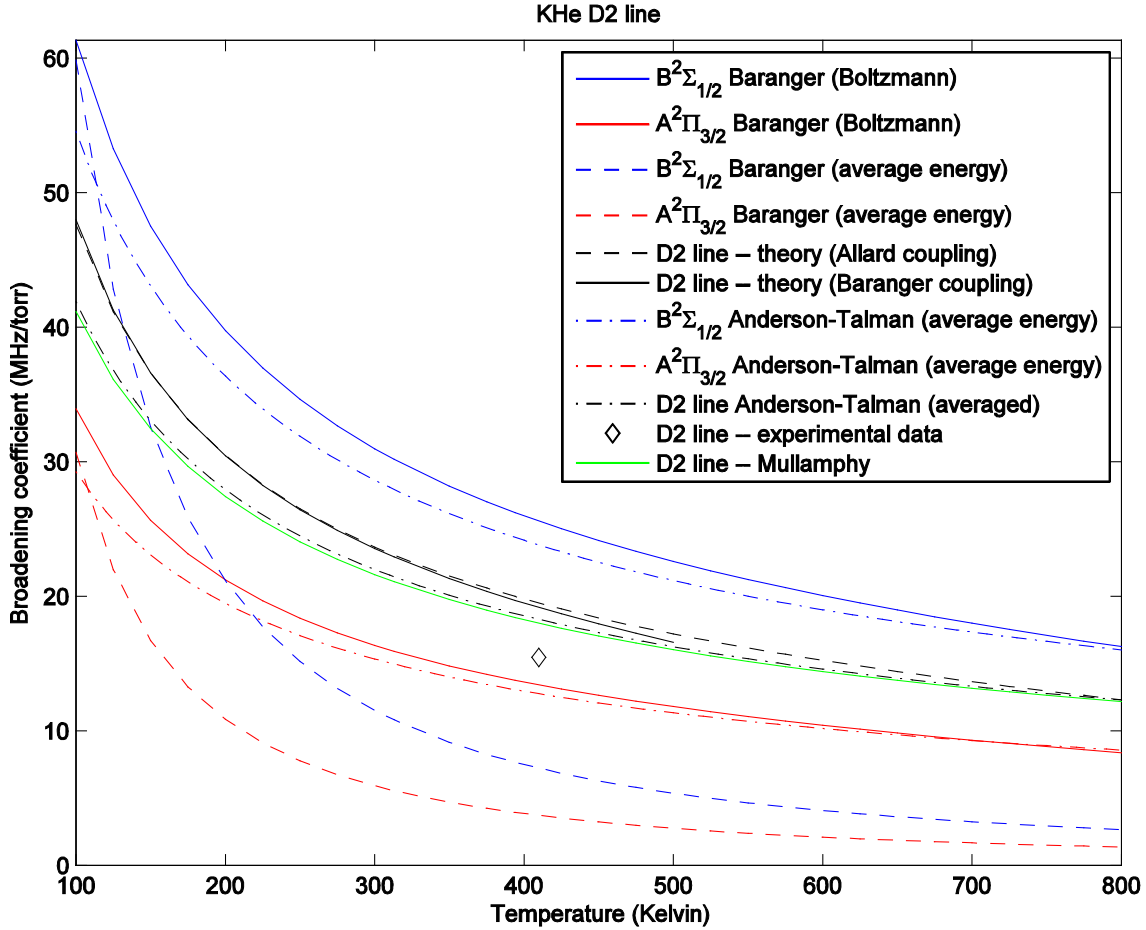
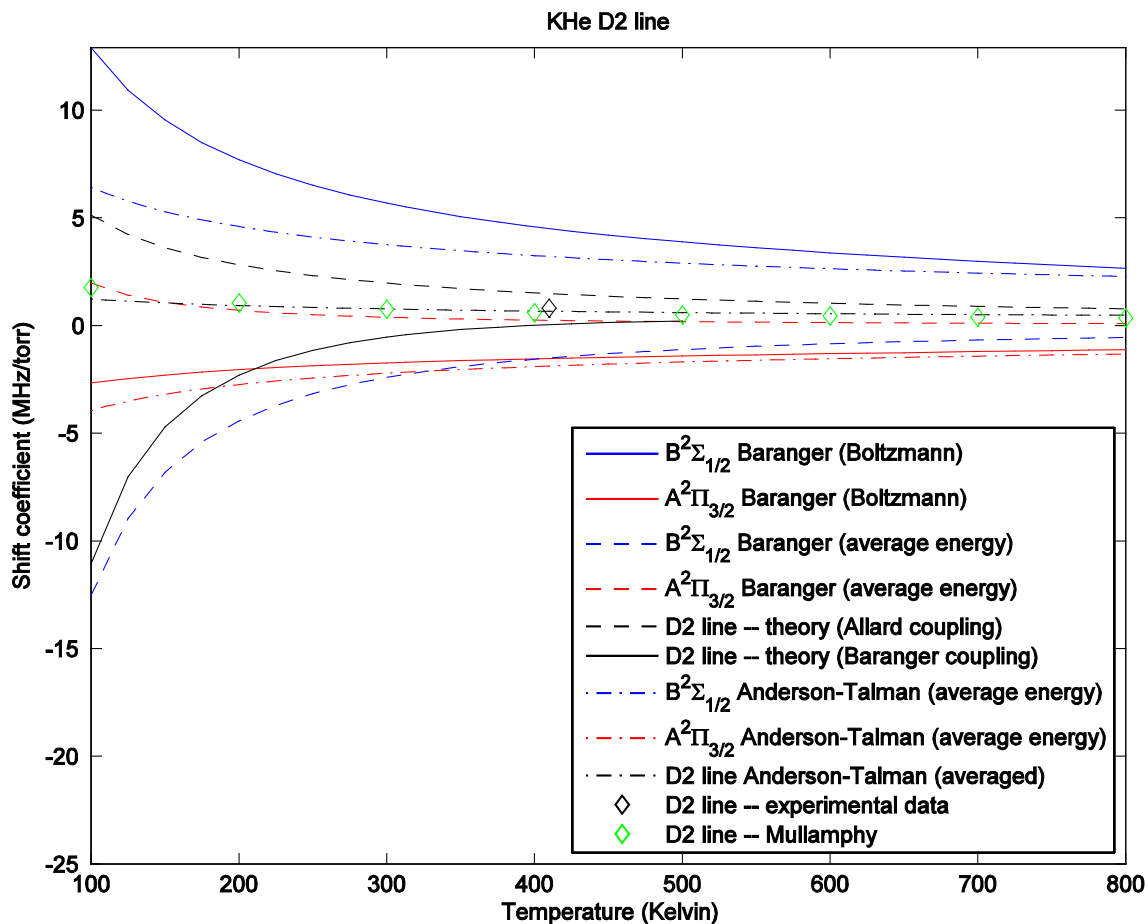Fig. 3.1b: Shift coefficients for the D1 line of K + He. The dashed line represents Baranger model calculations at the thermal average energy for each temperature. The solid line represents Baranger model calculations using the Boltzmann distribution and represents our best results. Neither the Baranger model nor the Anderson-Talman model provides good connection with experimental result (Lwin and McCartan, 1978).

Fig. 3.1c: Broadening coefficients for the D2 line of K + He. Red and blue indicate results for calculations on the individual surfaces, while black indicates results on the D2 line (Anderson-Talman by taking an average of the red and blue results, Baranger by calculating a coupled case). The black dashed line represents Baranger model calculations using the Allard coupling (50/50 weighting with uncoupled phase shifts). The black solid line represents Baranger model calculations using the Baranger coupling (weightings and phase shifts determined by the fully coupled scattering matrix elements) and represents our best results. The two coupling cases track each other for nearly the full range of temperatures for which we calculate the Baranger coupling. Both the Baranger model and the Anderson-Talman model provide good connection with experimental result (Lwin and McCartan, 1978).

Fig. 3.1d: Shift coefficients for the D2 line of K + He. Red and blue indicate results for calculations on the individual surfaces, while black indicates results on the D2 line (Anderson-Talman by taking an average of the red and blue results, Baranger by calculating a coupled case). The black dashed line represents Baranger model calculations using the Allard coupling (50/50 weighting with uncoupled phase shifts). The black solid line represents Baranger model calculations using the Baranger coupling (weightings and phase shifts determined by the fully coupled scattering matrix elements) and represents our best results. The two coupling cases provide good connection with the magnitude of the experimental result (Lwin and McCartan, 1978) at 400 K but diverge from each other significantly at low temperatures, even predicting opposite shifts.
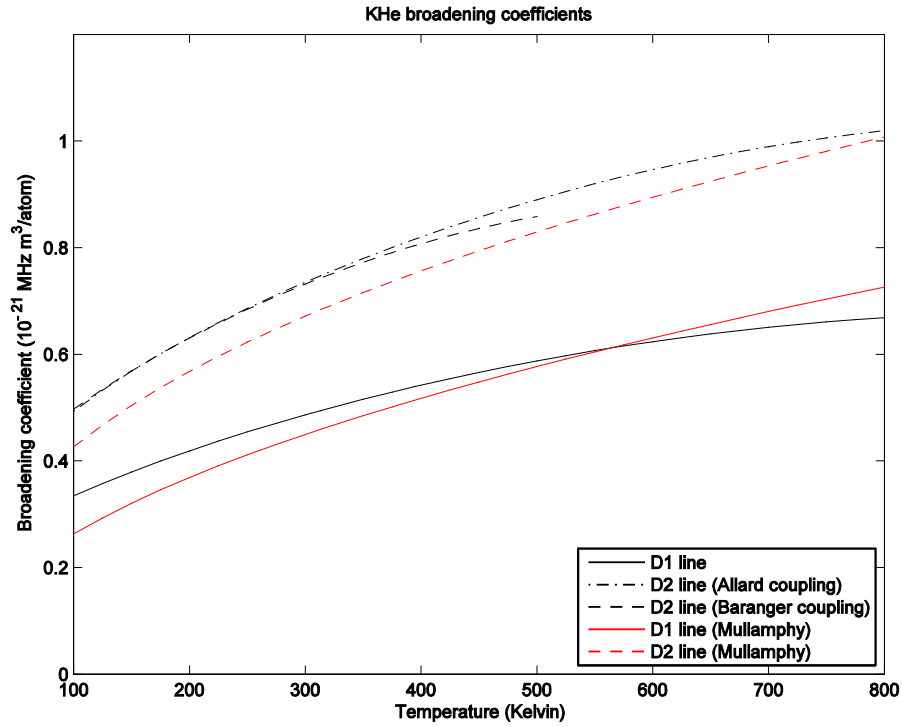
Fig. 3.1e: Broadening rates vs. temperature for K + He.
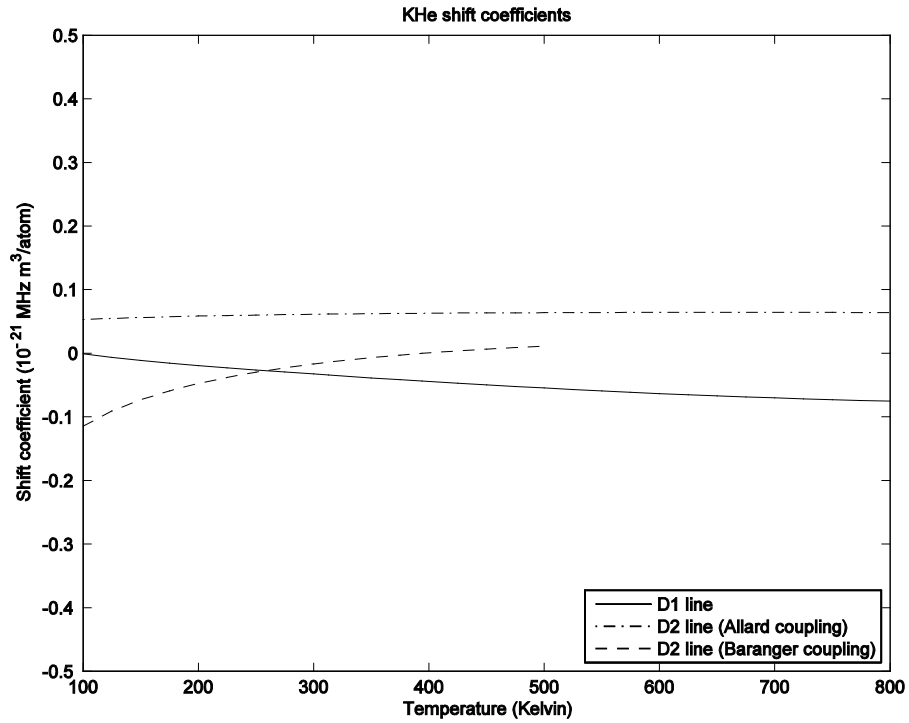
Fig. 3.1f: Shift rates vs. temperature for K + He.
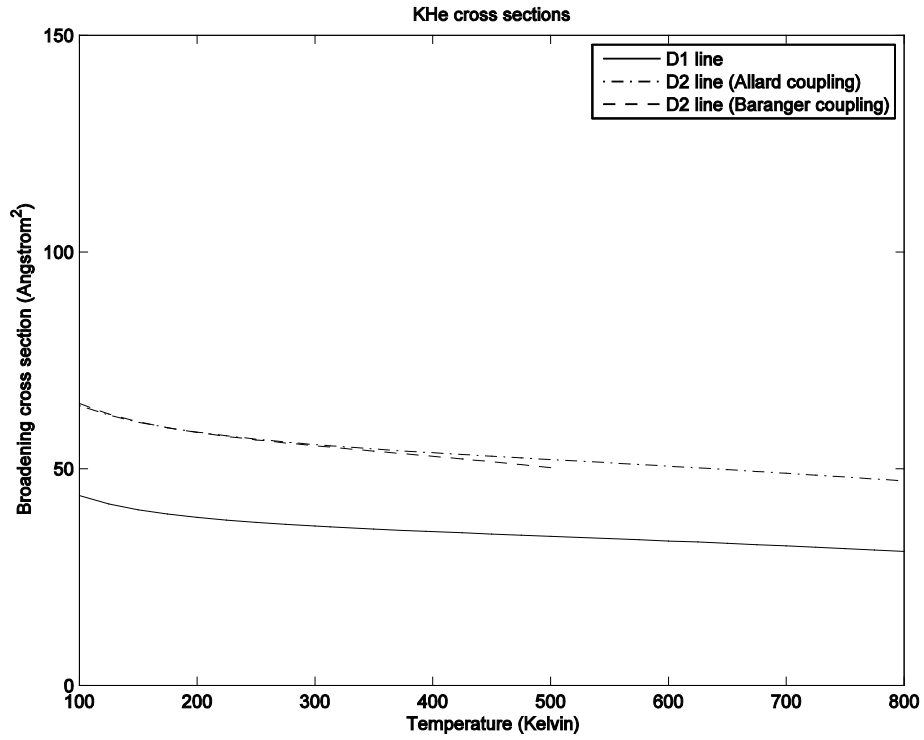
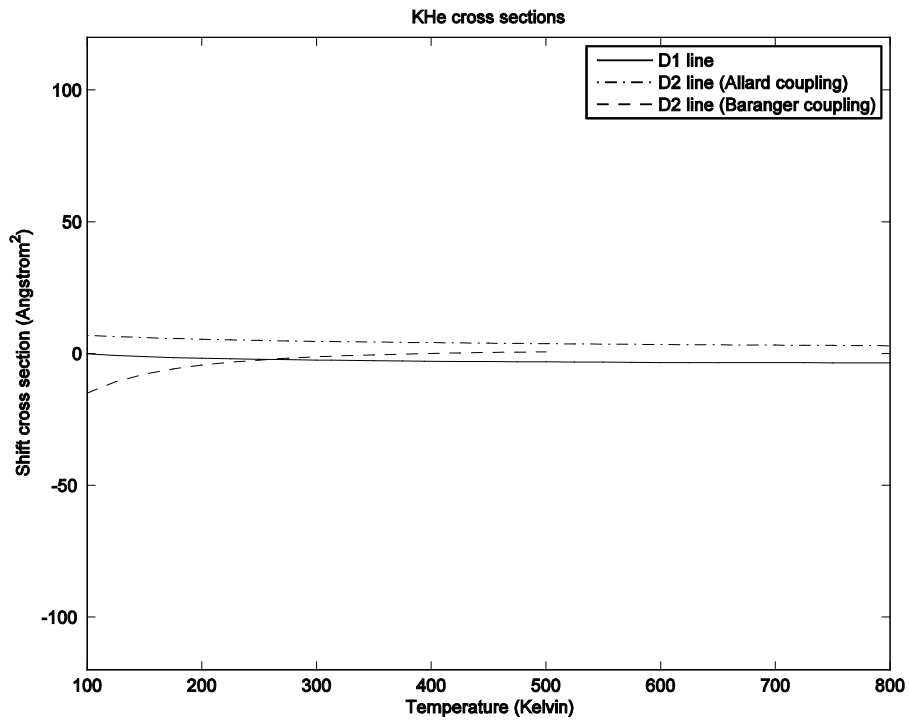Fig. 3.1g: Broadening cross sections vs. temperature for K + He.

Fig. 3.1h: Shift cross sections vs. temperature for K + He.

88

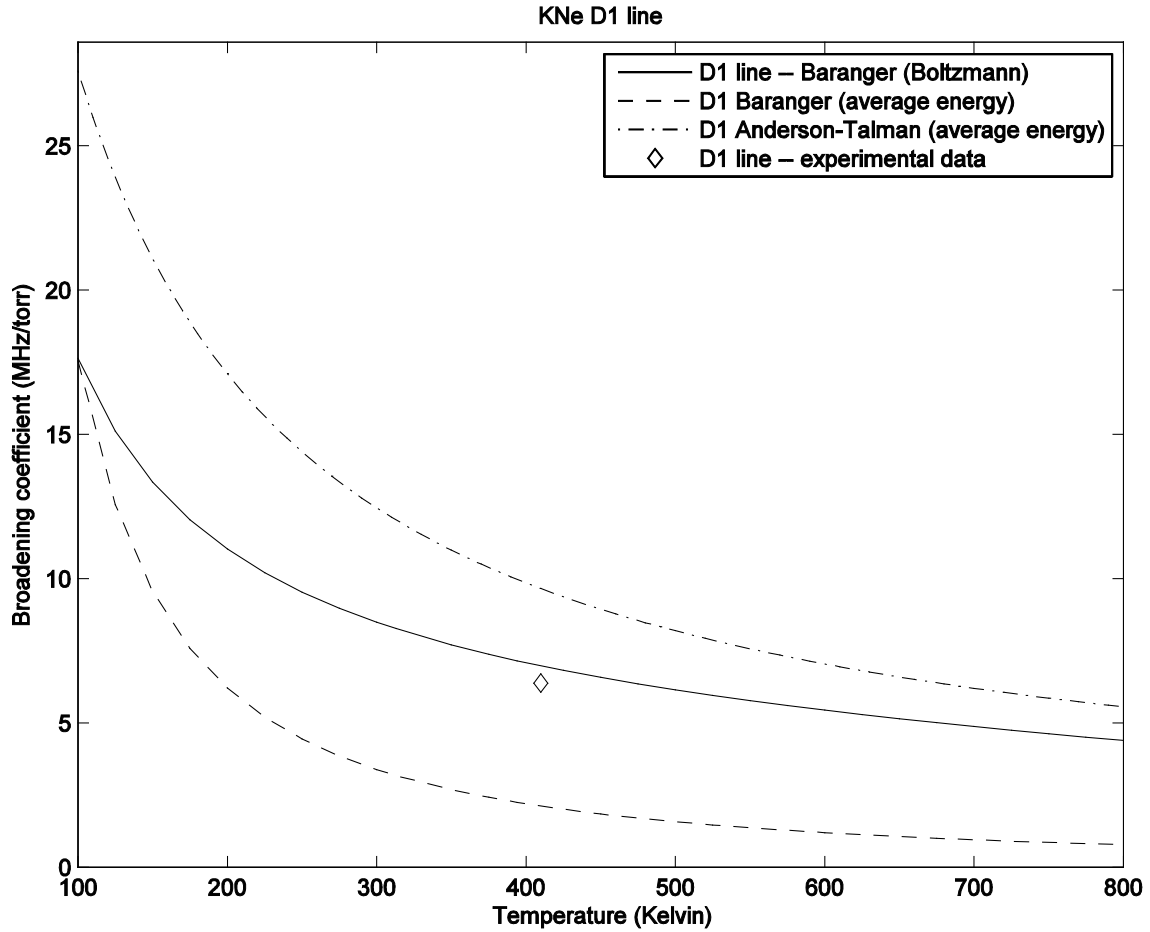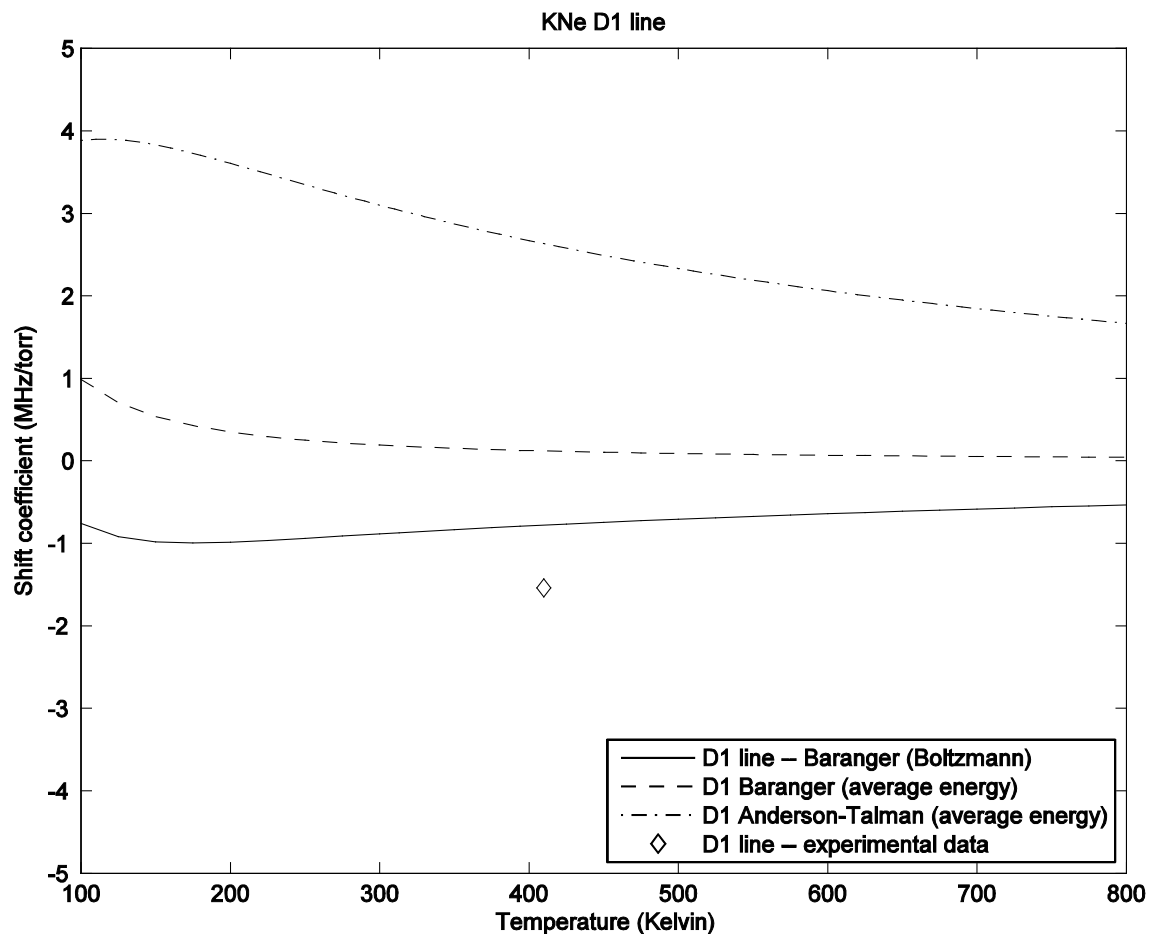## 3.2.   Potassium + Neon (K + Ne)

Fig. 3.2a: Broadening coefficients for the D1 line of K + Ne. The dashed line represents Baranger model calculations at the thermal average energy for each temperature. The solid line represents Baranger model calculations using the Boltzmann distribution and represents our best results. Here the Baranger model provides better connection with experimental result (Lwin and McCartan, 1978) than the Anderson-Talman model.

Fig. 3.2b: Shift coefficients for the D1 line of K + Ne. The dashed line represents Baranger model calculations at the thermal average energy for each temperature. The solid line represents Baranger model calculations using the Boltzmann distribution and represents our best results. Here the Baranger model provides better connection with experimental result (Lwin and McCartan, 1978) than the Anderson-Talman model.
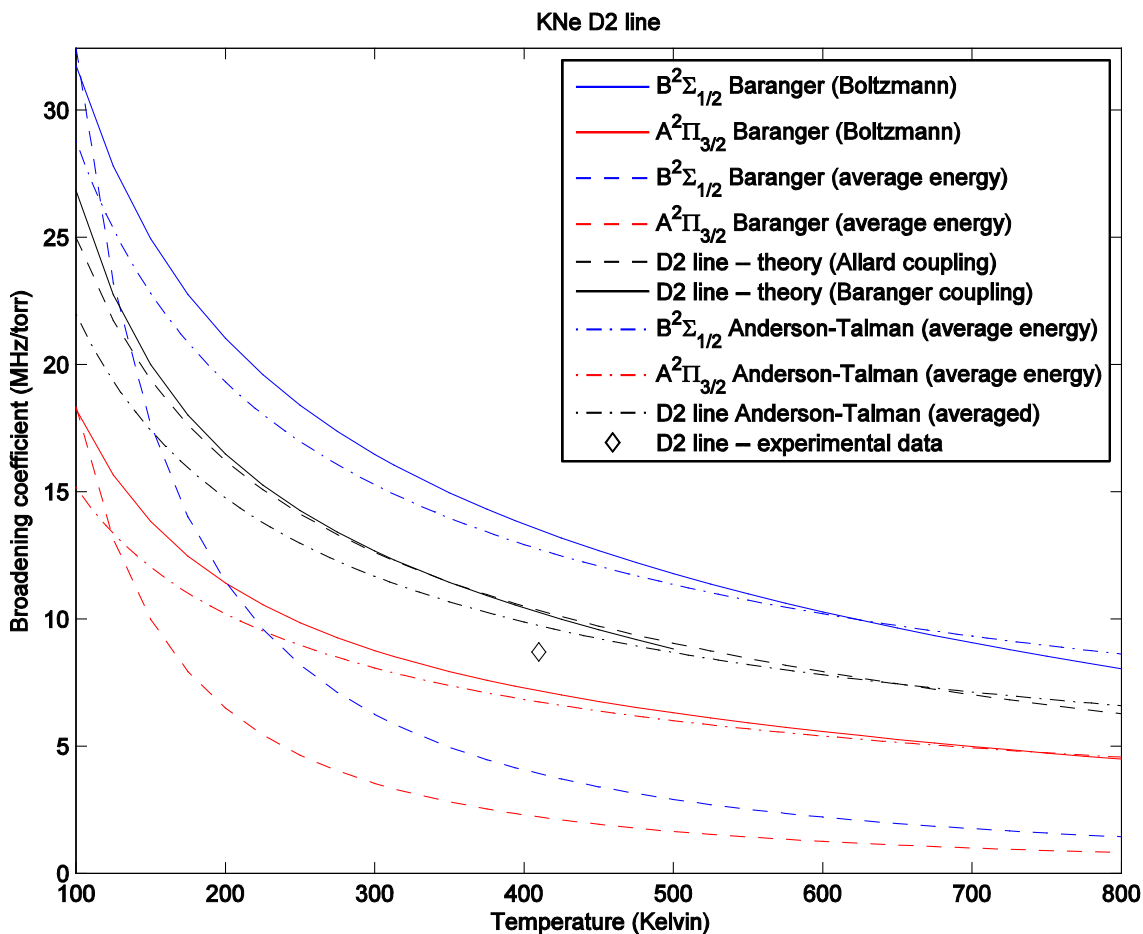
Fig. 3.2c: Broadening for the D2 line of K + Ne. Red and blue indicate results for calculations on the individual surfaces, while black indicates results on the D2 line (Anderson-Talman by taking an average of the red and blue results, Baranger by calculating a coupled case). The black dashed line represents Baranger model calculations using the Allard coupling (50/50 weighting with uncoupled phase shifts). The black solid line represents Baranger model calculations using the Baranger coupling (weightings and phase shifts determined by the fully coupled scattering matrix elements) and represents our best results. The two coupling cases track each other for nearly the full range of temperatures for which we calculate the Baranger coupling. Both the Baranger model and the Anderson-Talman model provide good connection with experimental result (Lwin and McCartan, 1978).
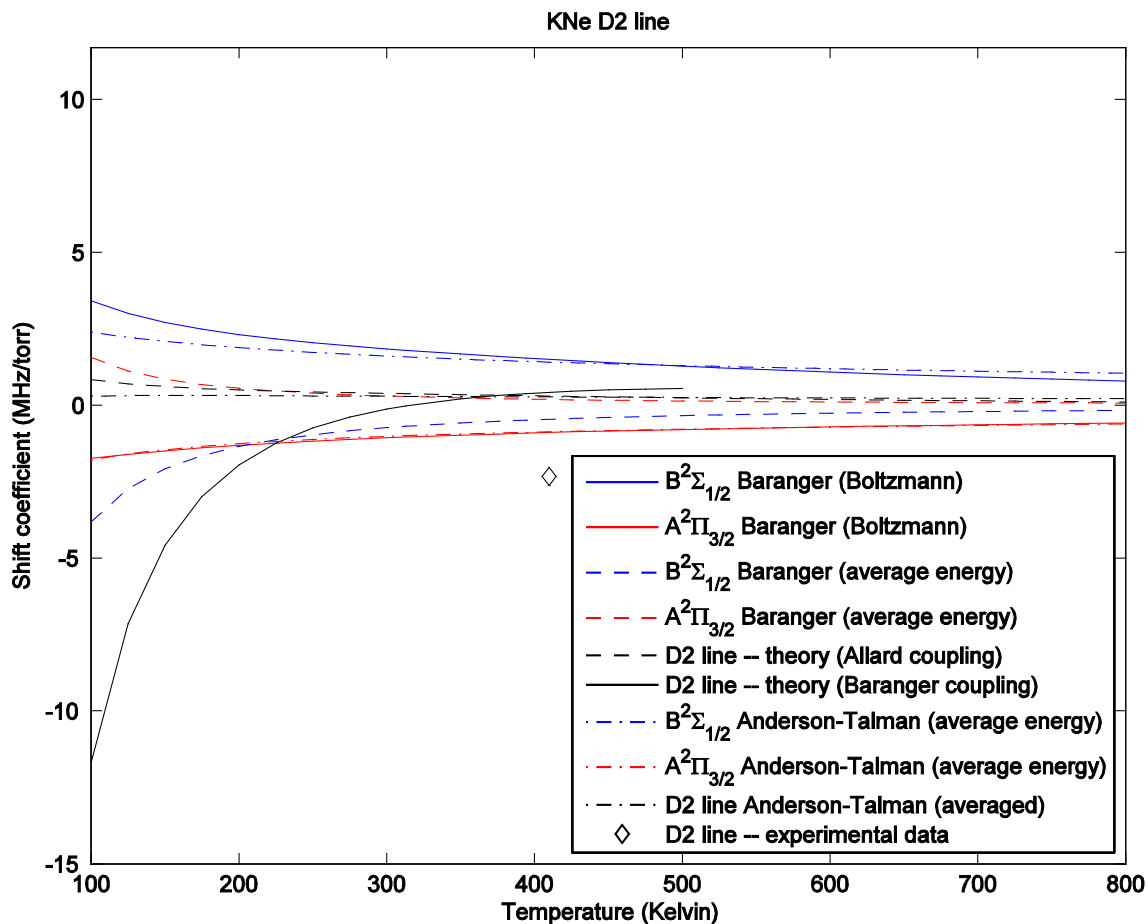
Fig. 3.2d: Shift coefficients for the D2 line of K + Ne. Red and blue indicate results for calculations on the individual surfaces, while black indicates results on the D2 line (Anderson-Talman by taking an average of the red and blue results, Baranger by calculating a coupled case). The black dashed line represents Baranger model calculations using the Allard coupling (50/50 weighting with uncoupled phase shifts). The black solid line represents Baranger model calculations using the Baranger coupling (weightings and phase shifts determined by the fully coupled scattering matrix elements) and represents our best results. Here the Allard coupling provides a closer match with the Anderson-Talman model, though neither model provides particularly good connection with experimental result (Lwin and McCartan, 1978). The two coupling cases diverge significantly at low temperatures because of the coupling between states during the collision process.
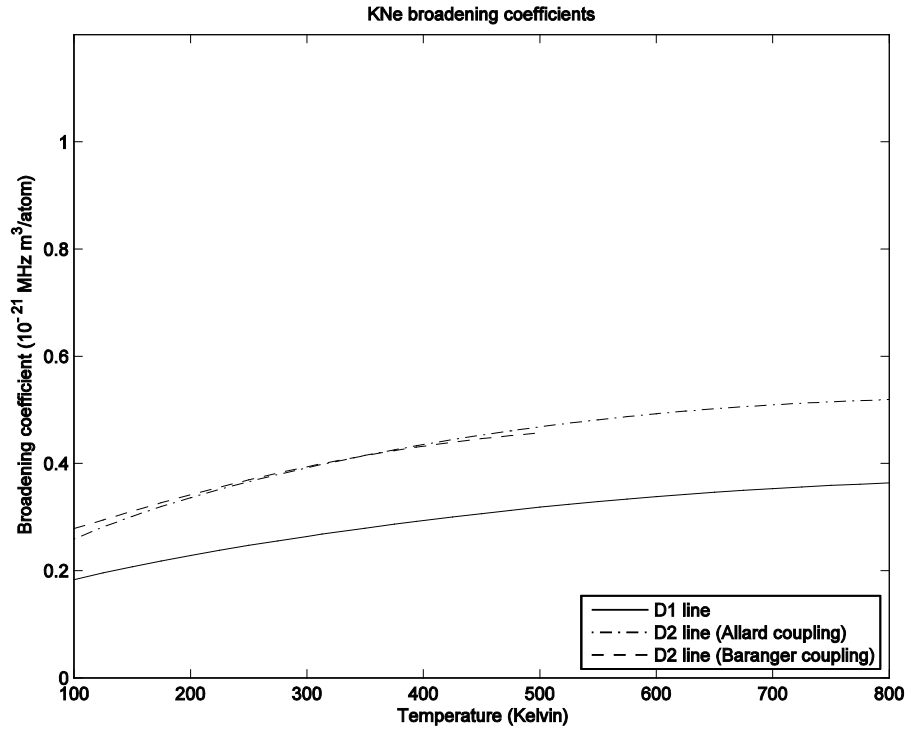
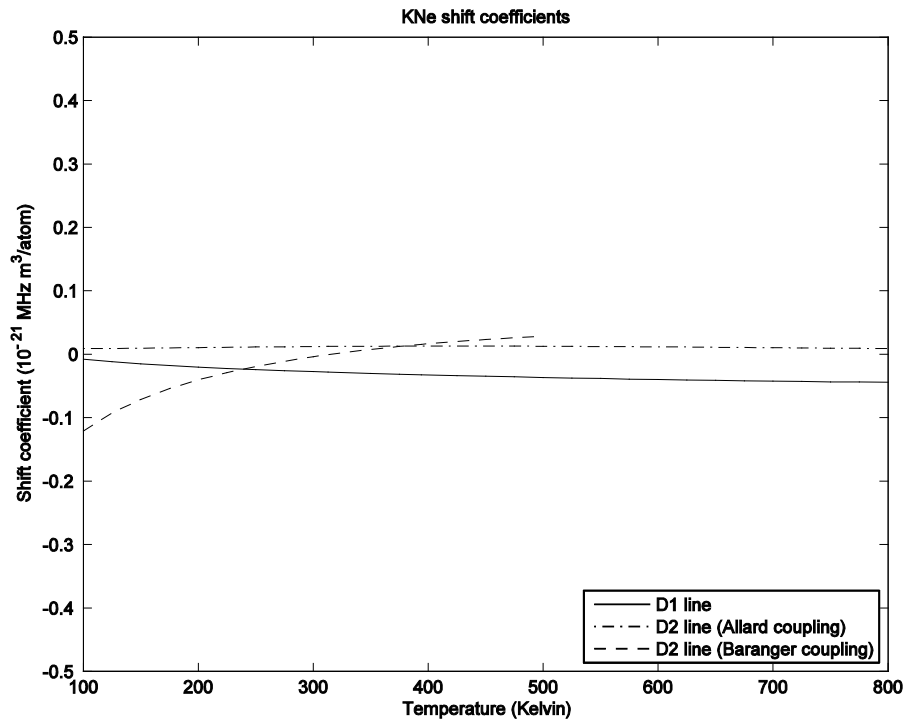Fig. 3.2e: Broadening rates vs. temperature for K + Ne.
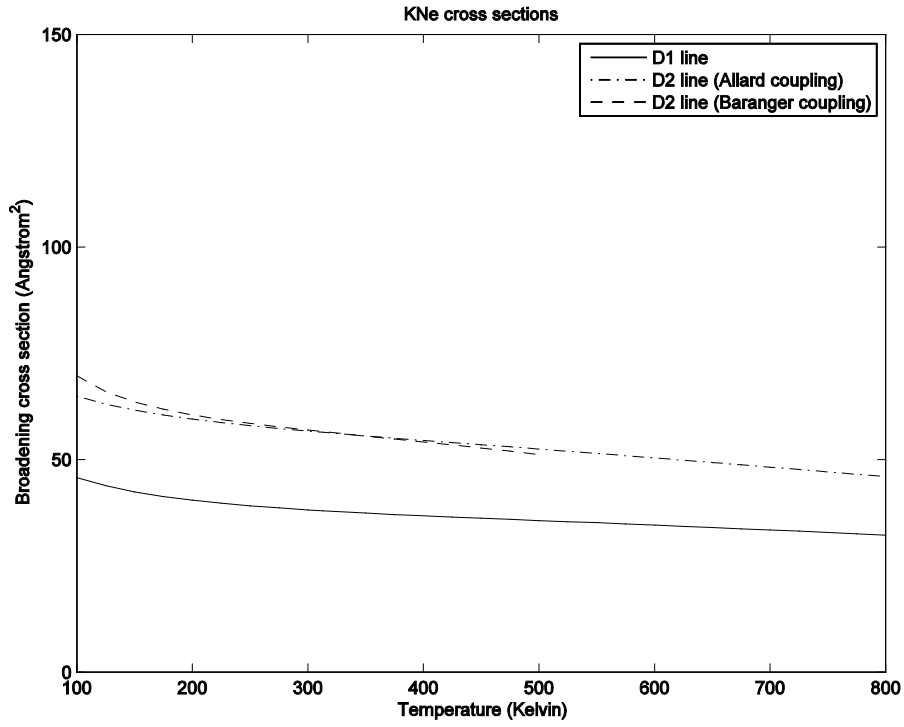

Fig. 3.2f: Shift rates vs. temperature for K + Ne.

93

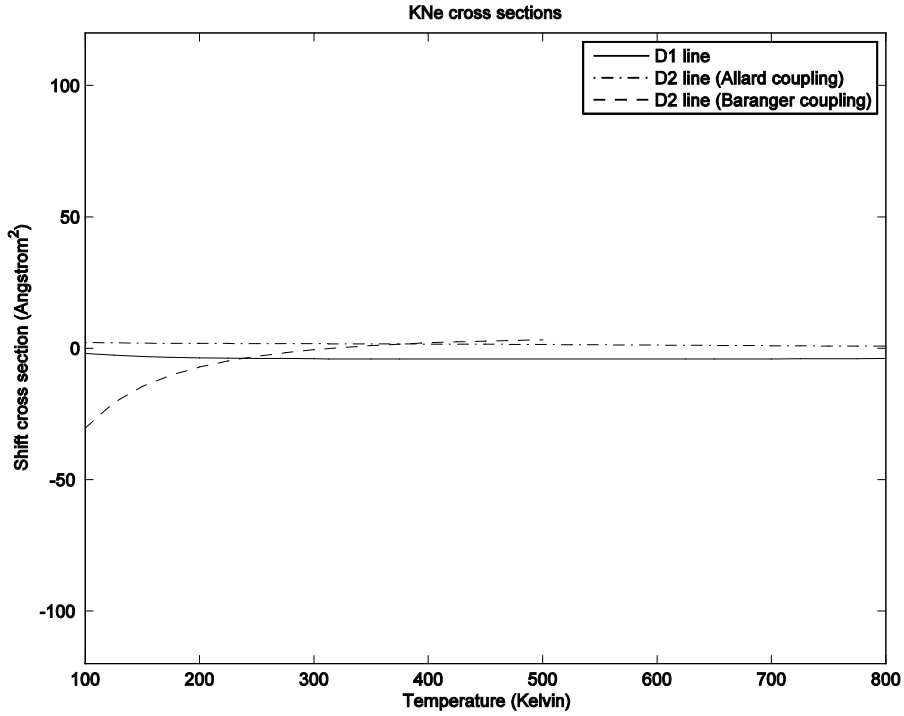Fig. 3.2g: Broadening cross sections vs. temperature for K + Ne.

Fig. 3.2h: Shift cross sections vs. temperature for K + Ne.

94

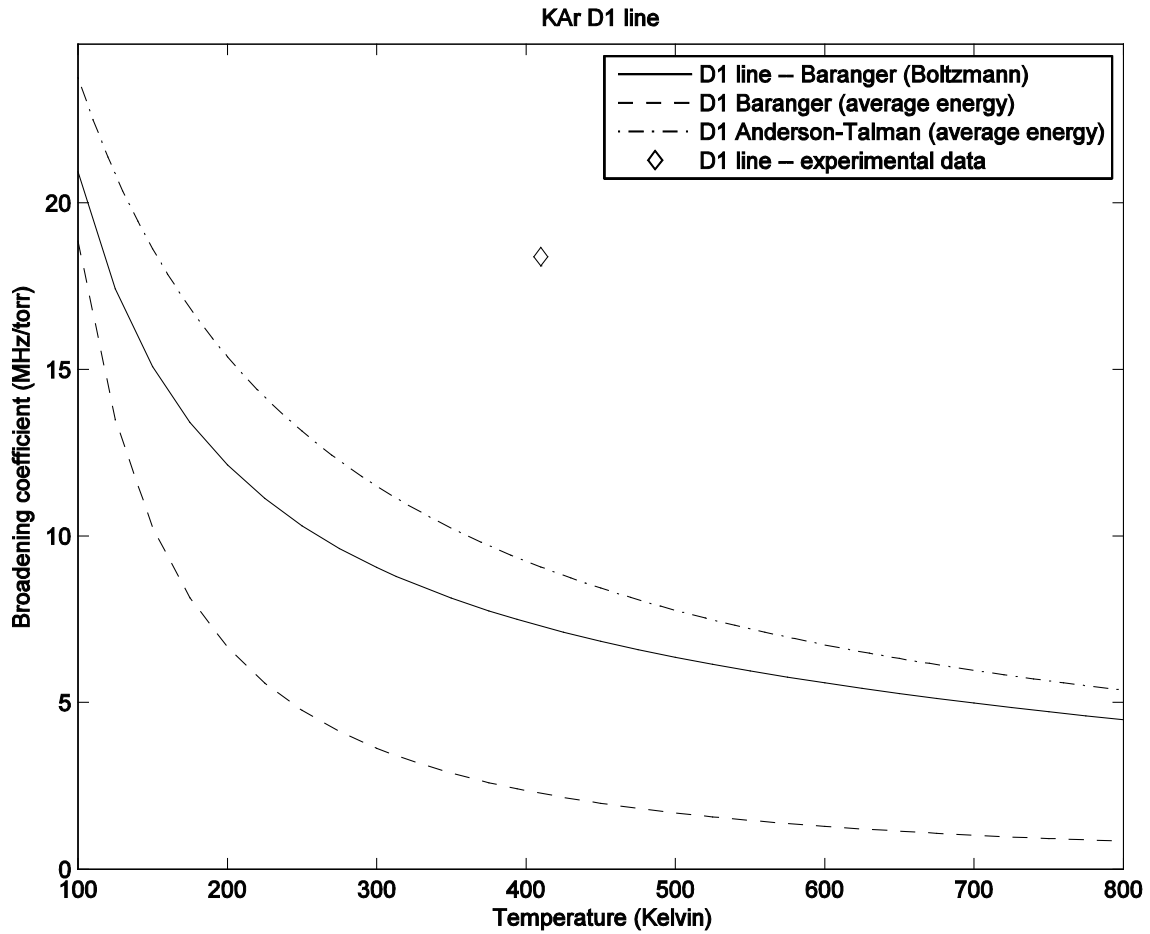## 3.3.   Potassium + Argon (K + Ar)

Fig. 3.3a: Broadening coefficients for the D1 line of K + Ar. The dashed line represents Baranger model calculations at the thermal average energy for each temperature. The solid line represents Baranger model calculations using the Boltzmann distribution and represents our best results. Here both the Baranger model and the Anderson-Talman model underestimate the measured broadening rate (Lwin and McCartan, 1978).
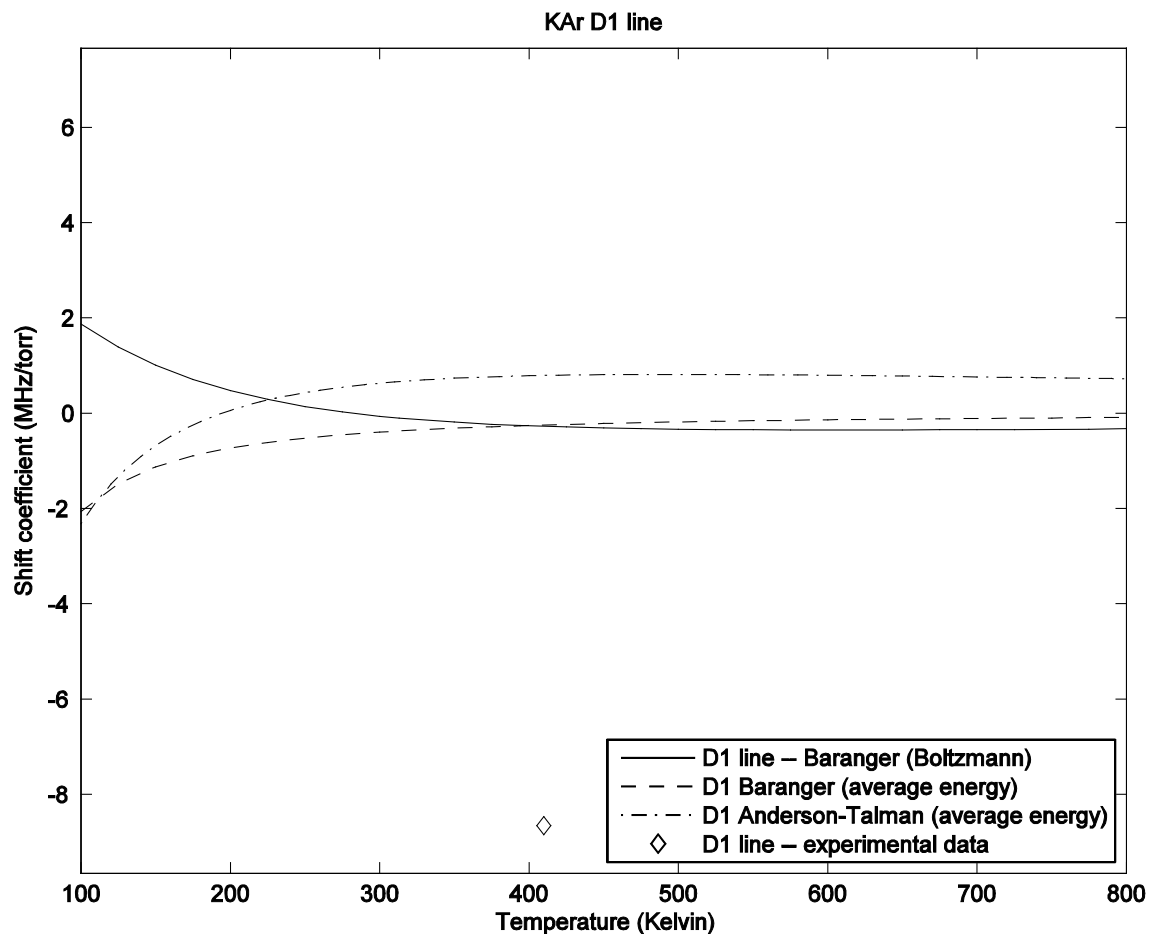
KAr D1 line

Fig. 3.3b: Shift coefficients for the D1 line of K + Ar. The dashed line represents Baranger model calculations at the thermal average energy for each temperature. The solid line represents Baranger model calculations using the Boltzmann distribution and represents our best results. Here both the Baranger model and the Anderson-Talman model underestimate the measured line shift rate (Lwin and McCartan, 1978).
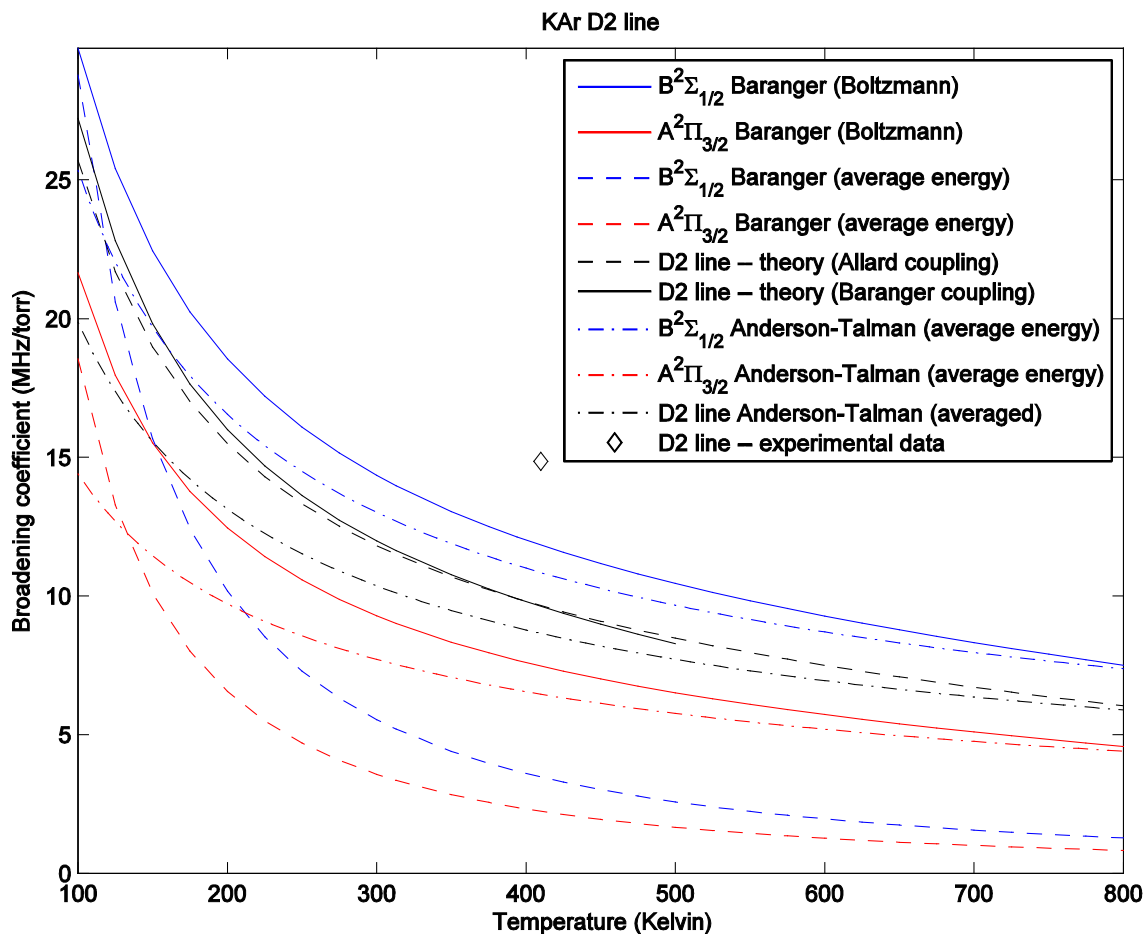
Fig. 3.3c: Broadening coefficients for the D2 line of K + Ar. Red and blue indicate results for calculations on the individual surfaces, while black indicates results on the D2 line (Anderson-Talman by taking an average of the red and blue results, Baranger by calculating a coupled case). The black dashed line represents Baranger model calculations using the Allard coupling (50/50 weighting with uncoupled phase shifts). The black solid line represents Baranger model calculations using the Baranger coupling (weightings and phase shifts determined by the fully coupled scattering matrix elements) and represents our best results. The two coupling cases appear to track each other for nearly the full range of temperatures for which we calculate the Baranger coupling. The Baranger model and Anderson-Talman models predict similar results, but both models underestimate the measured broadening rate (Lwin and McCartan, 1978).
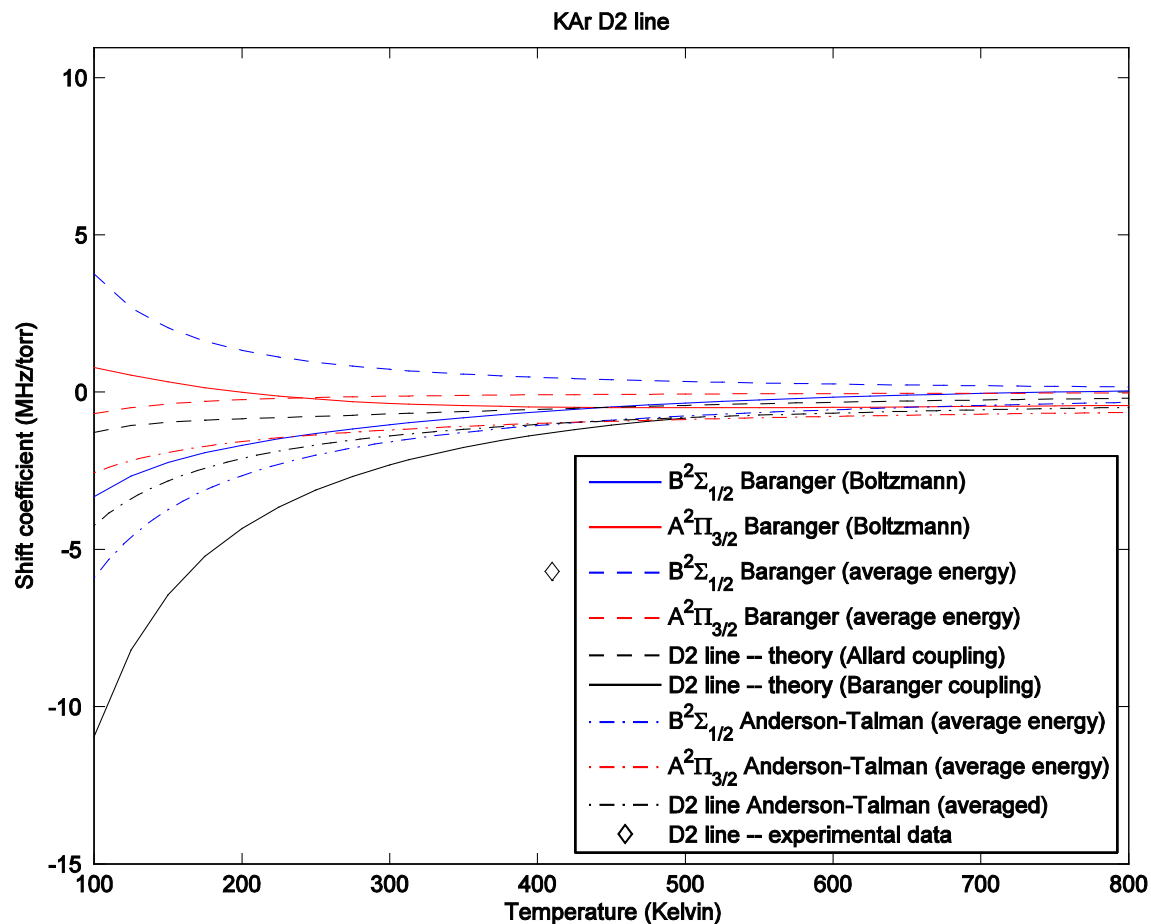
Fig. 3.3d: Shift coefficients for the D2 line of K + Ar. Red and blue indicate results for calculations on the individual surfaces, while black indicates results on the D2 line (Anderson-Talman by taking an average of the red and blue results, Baranger by calculating a coupled case). The black dashed line represents Baranger model calculations using the Allard coupling (50/50 weighting with uncoupled phase shifts). The black solid line represents Baranger model calculations using the Baranger coupling (weightings and phase shifts determined by the fully coupled scattering matrix elements) and represents our best results. Both the Baranger model and the Anderson-Talman model underestimate the measured line shift rate (Lwin and McCartan, 1978).
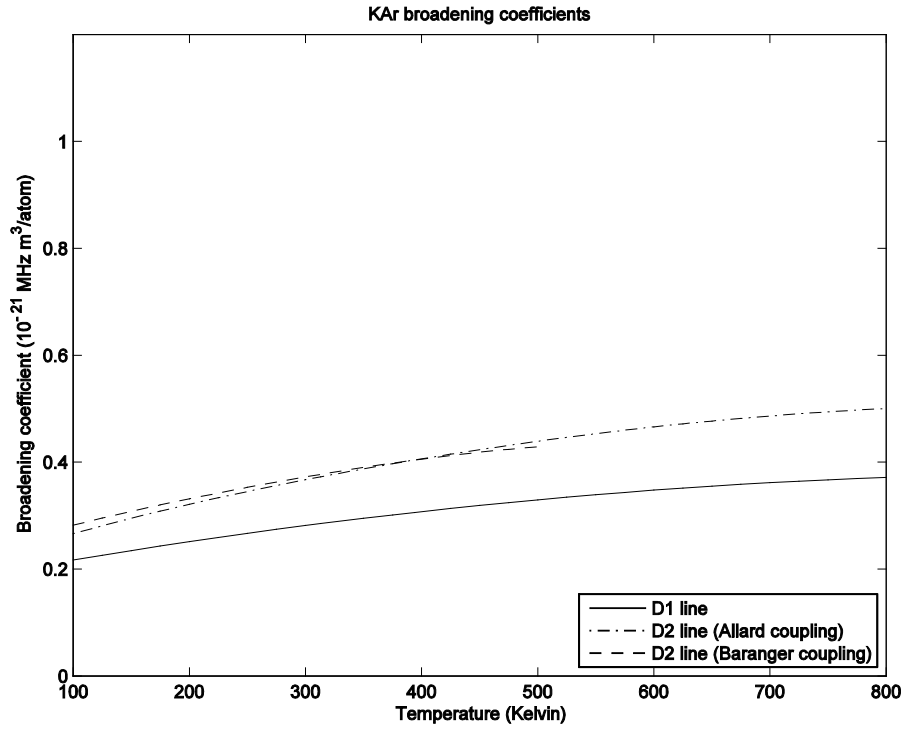
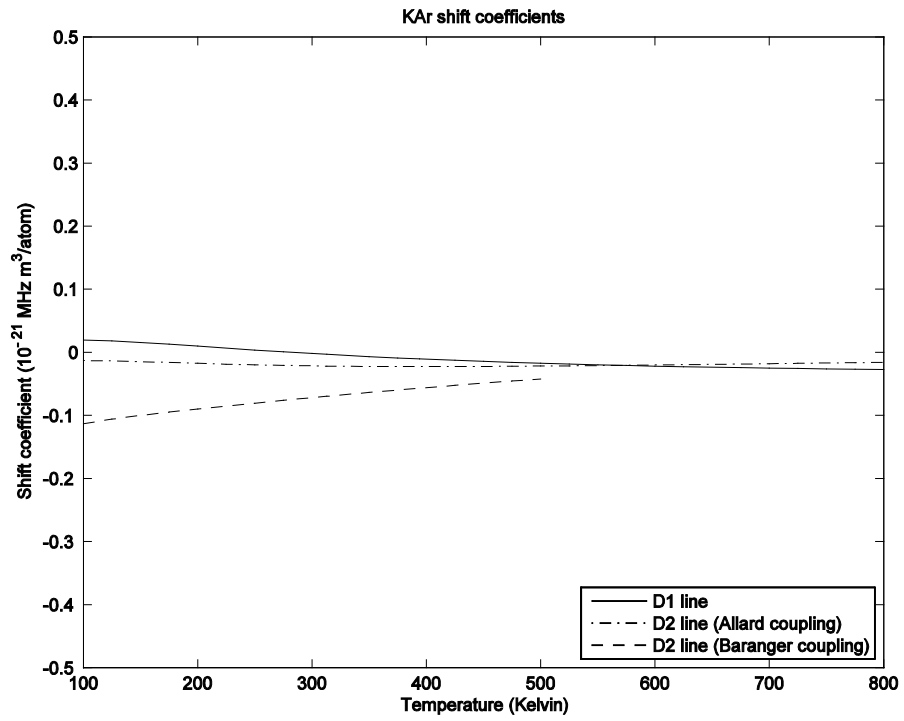Fig. 3.3e: Broadening rates vs. temperature for K + Ar.
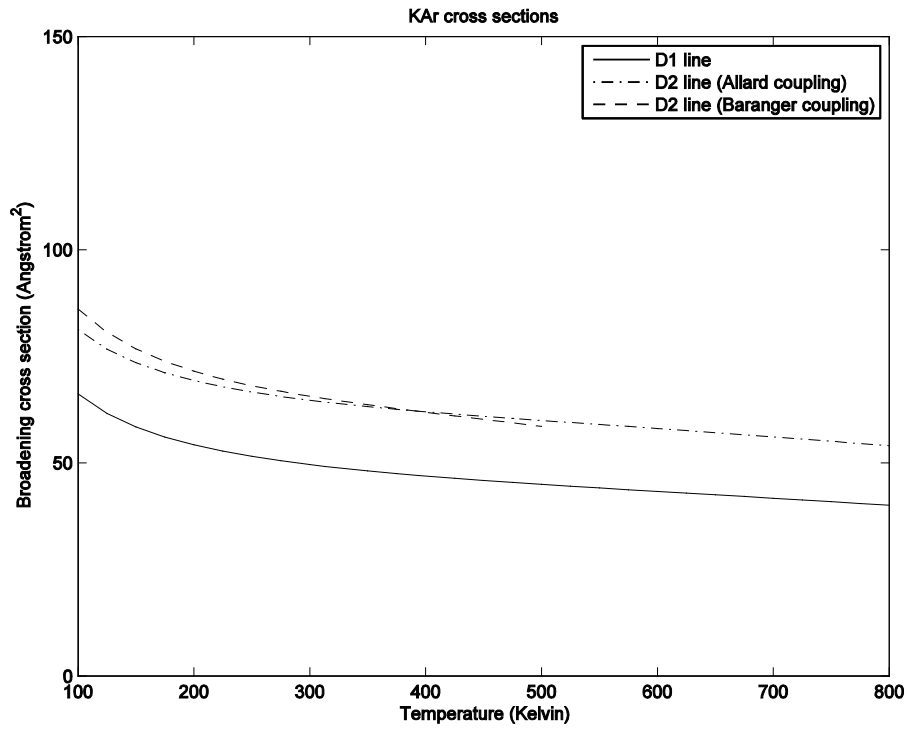

Fig. 3.3f: Shift rates vs. temperature for K + Ar.

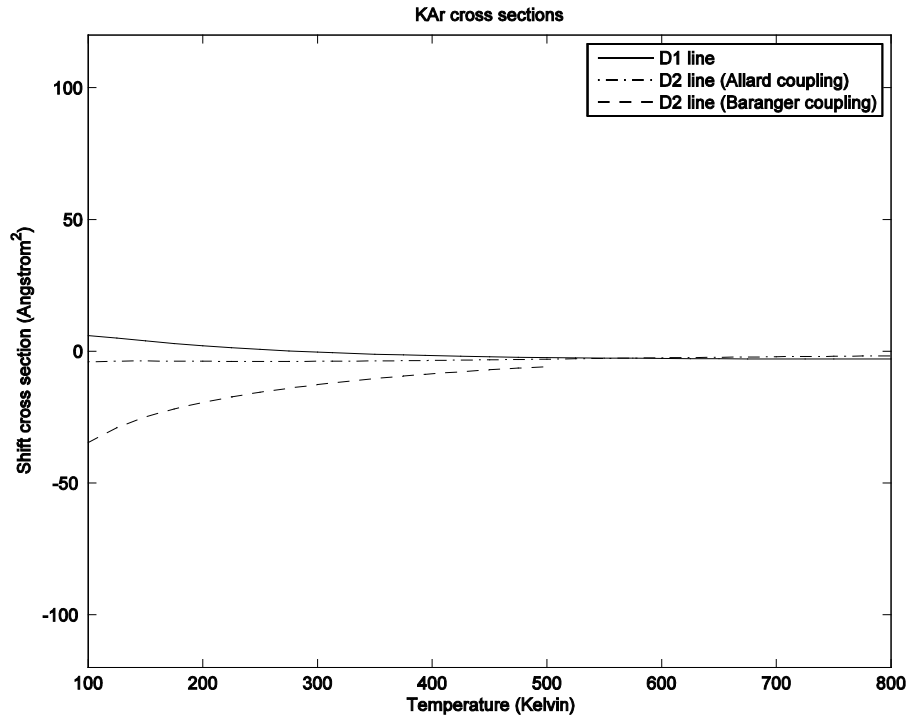Fig. 3.3g: Broadening cross sections vs. temperature for K + Ar.

Fig. 3.3h: Shift cross sections vs. temperature for K + Ar.

3.4.   Rubidium + Helium (Rb + He)

Fig. 3.4a: Broadening coefficients for the D1 line of Rb + He.   The dashed line represents Baranger model calculations at the thermal average energy for each temperature. The solid line represents Baranger model calculations using the Boltzmann distribution and represents our best results. Here the Baranger model provides a good prediction of measured broadening rates (Kazantsev, Kaliteevskii, and Rish, 1978; Izotova, Kantserov, and Frish, 1981; Rotondaro, 1995; Rotondaro and Perram, 1997).

RbHe D1 line
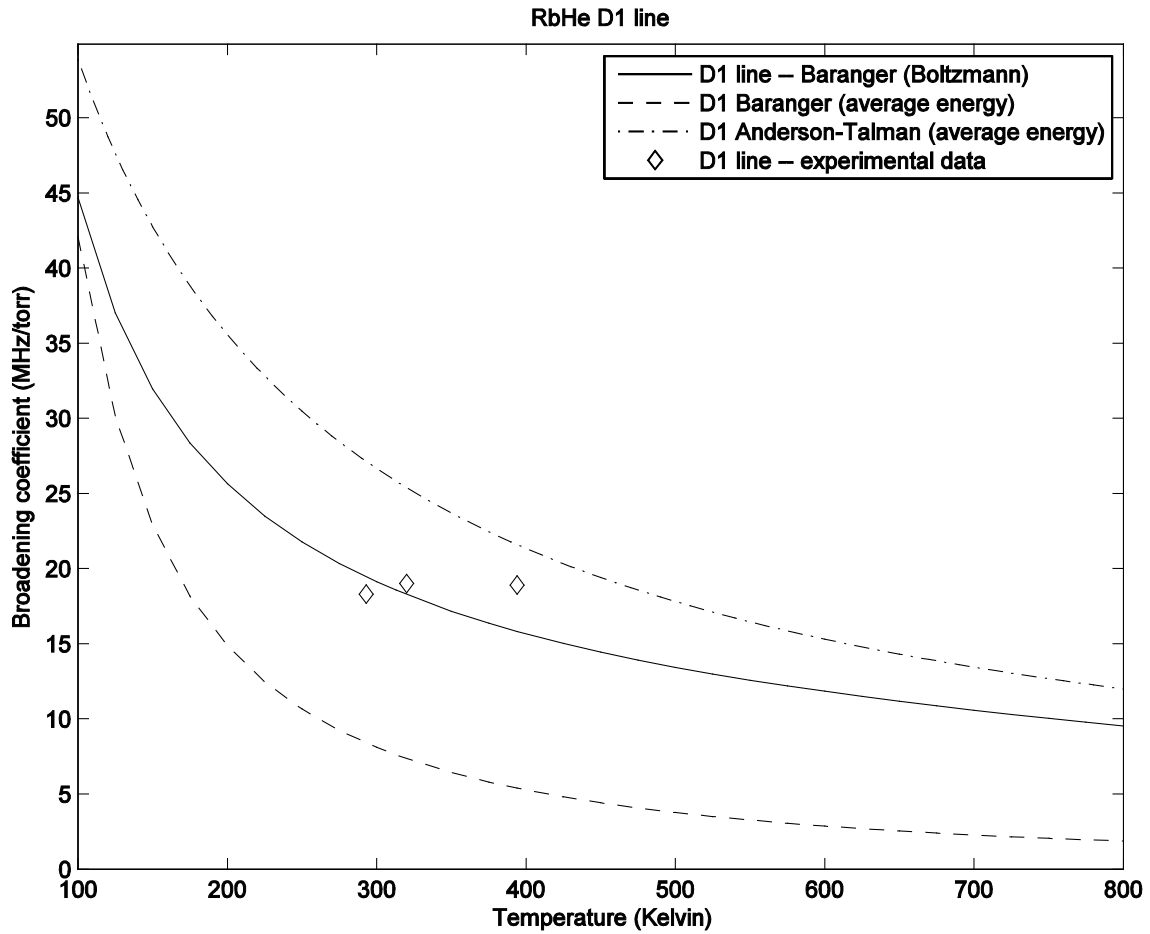
Fig. 3.4b: Shift coefficients for the D1 line of Rb + He. The dashed line represents Baranger model calculations at the thermal average energy for each temperature. The solid line represents Baranger model calculations using the Boltzmann distribution and represents our best results. Here the Baranger model provides a poor prediction of measured shift rates (Kazantsev, Kaliteevskii, and Rish, 1978; Izotova, Kantserov, a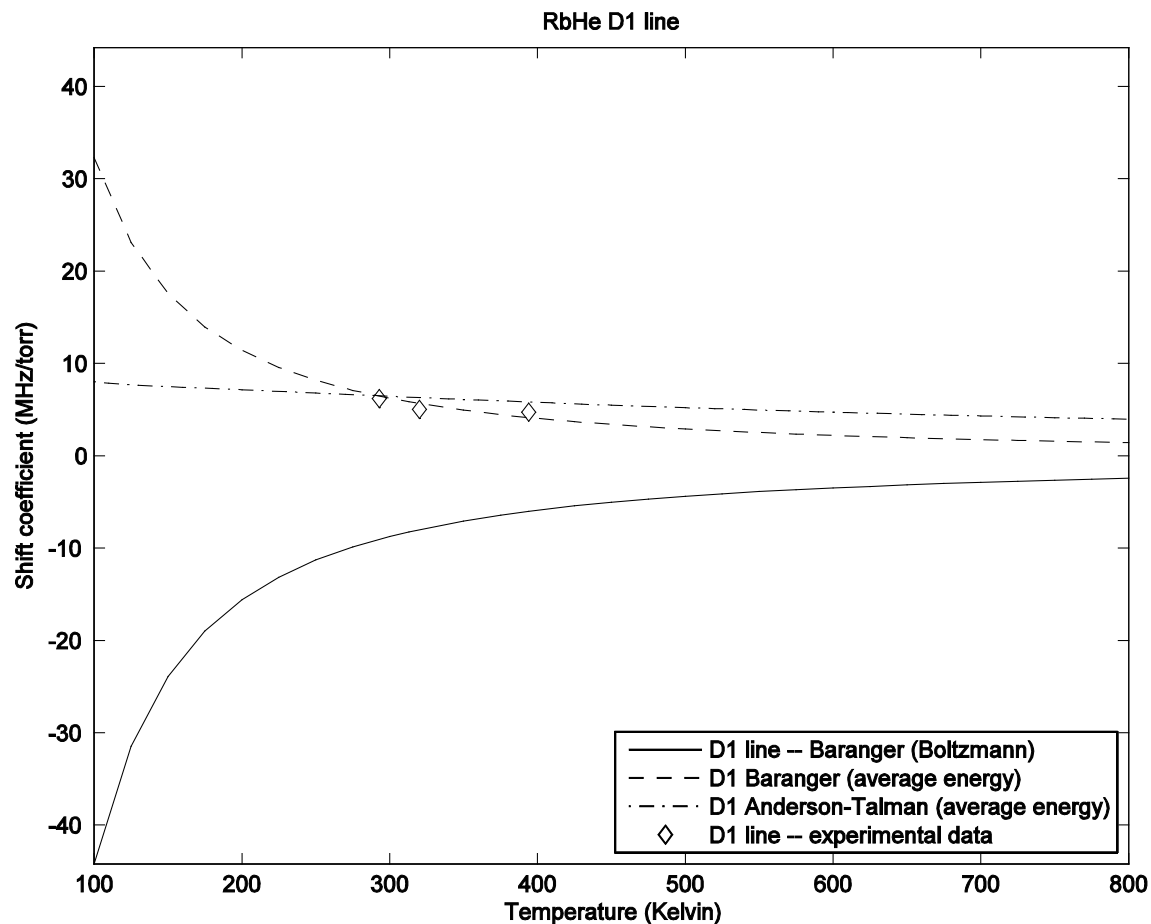nd Frish, 1981; Rotondaro, 1995; Rotondaro and Perram, 1997), perhaps getting the number right but predicting redshifting where experimental results show blueshifting. The Anderson-Talman model seems to provide better predictions.
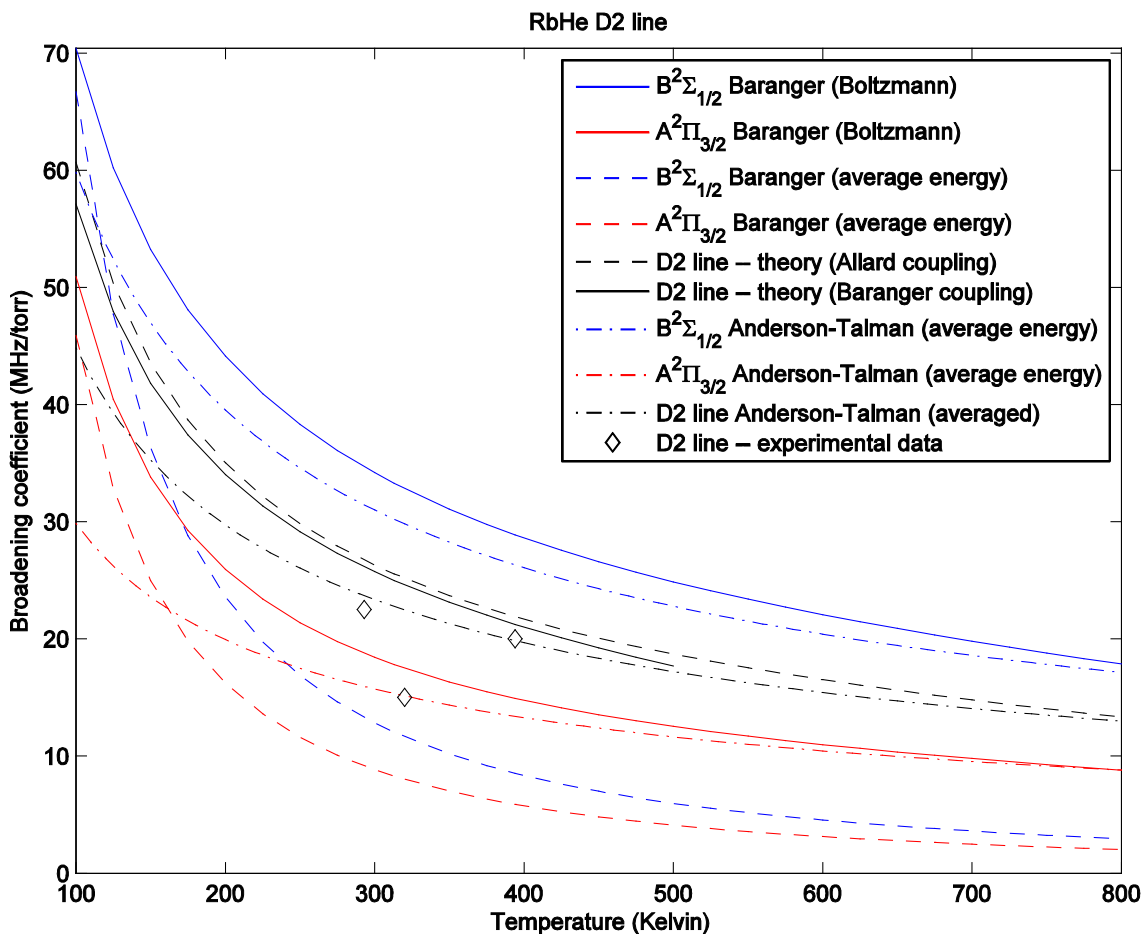
Fig. 3.4c: Broadening coefficients for the D2 line of Rb + He. Red and blue indicate results for calculations on the individual surfaces, while black indicates results on the D2 line (Anderson-Talman by taking an average of the red and blue results, Baranger by calculating a coupled case). The black dashed line represents Baranger model calculations using the Allard coupling (50/50 weighting with uncoupled phase shifts). The black solid line represents Baranger model calculations using the Baranger coupling (weightings and phase shifts determined by the fully coupled scattering matrix elements) and represents our best results. Both the Baranger model and the Anderson-Talman model appear to provide excellent predictions of measured broadening rates (Belov, 1981a, 1981b; Izotova, Kantserov, and Frish, 1981; Rotondaro, 1995; Rotondaro and Perram, 1997).
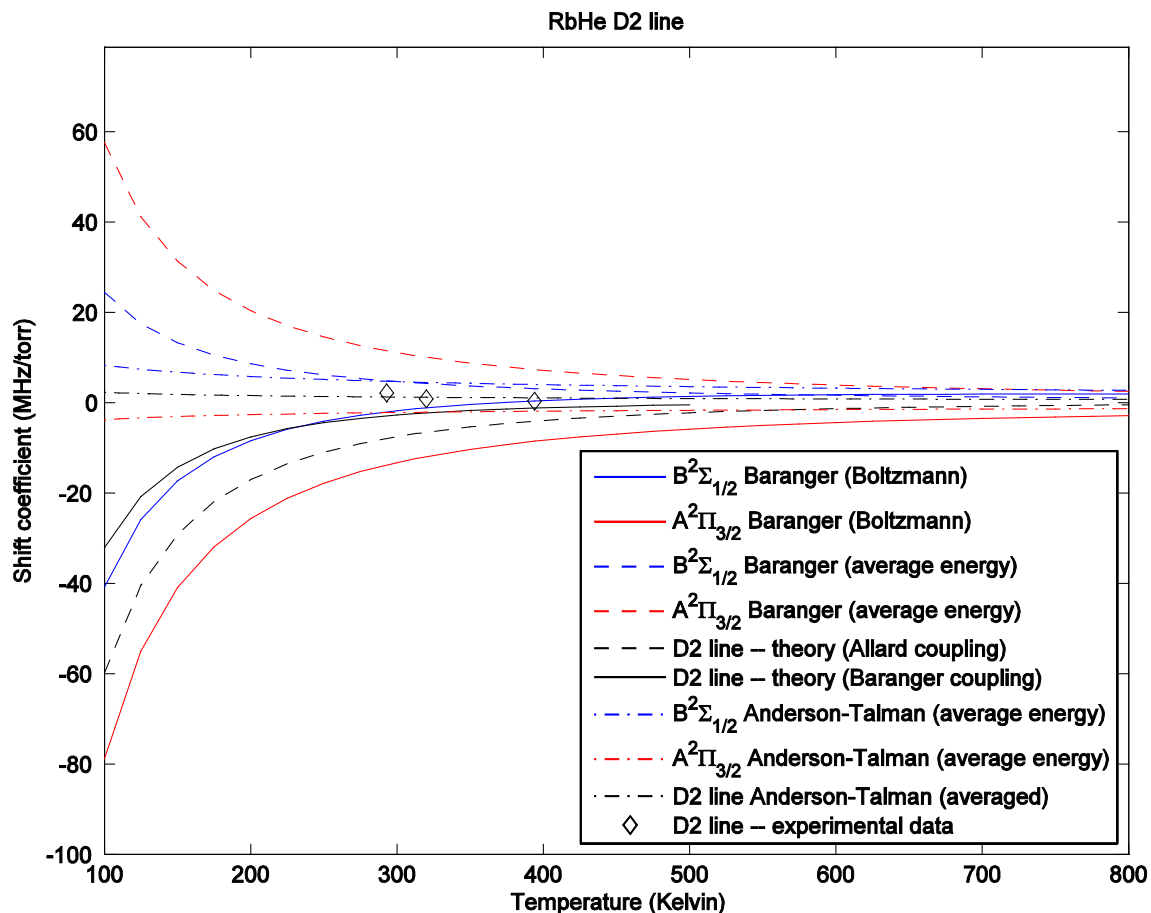
Fig. 3.4d: Shift coefficients for the D2 line of Rb + He. Red and blue indicate results for calculations on the individual surfaces, while black indicates results on the D2 line (Anderson-Talman by taking an average of the red and blue results, Baranger by calculating a coupled case). The black dashed line represents Baranger model calculations using the Allard coupling (50/50 weighting with uncoupled phase shifts). The black solid line represents Baranger model calculations using the Baranger coupling (weightings and phase shifts determined by the fully coupled scattering matrix elements) and represents our best results. Both the Allard coupling scheme and the Anderson-Talman model appear to provide excellent predictions of measured shift rates (Belov, 1981a, 1981b; Izotova, Kantserov, and Frish, 1981; Rotondaro, 1995; Rotondaro and Perram, 1997), but the Baranger coupling model predicts the opposite shift.
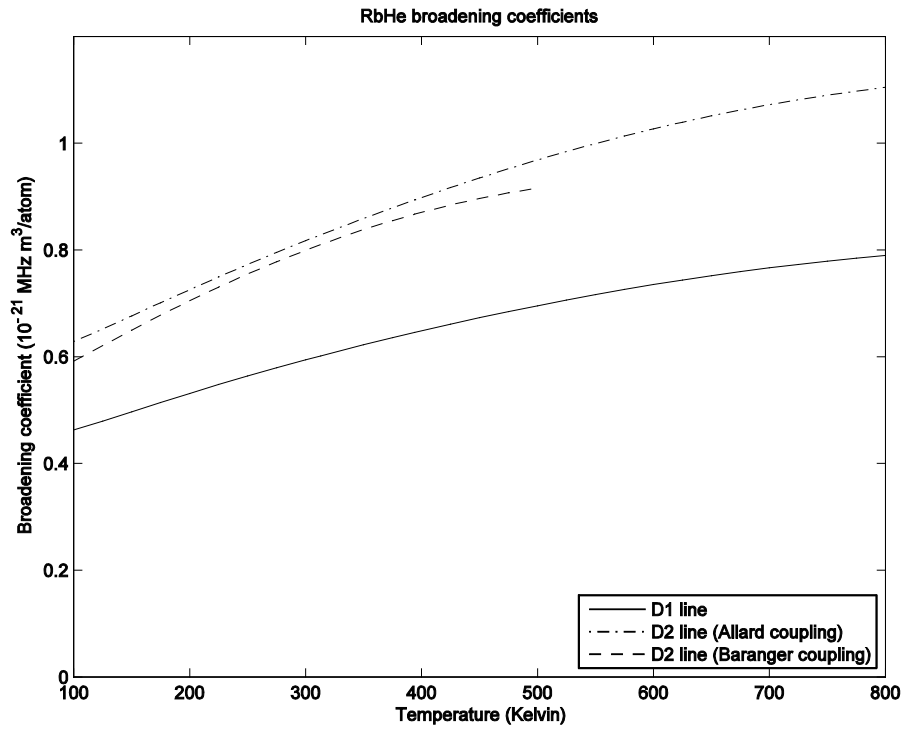
Fig. 3.4e: Broadening rates vs. temperature for Rb + He.
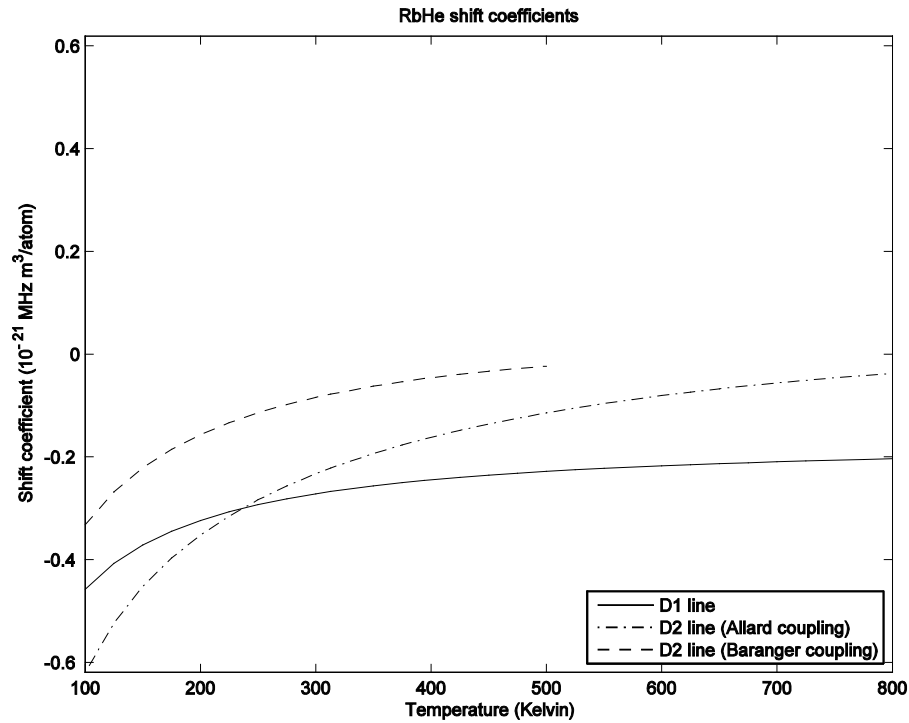
Fig. 3.4f: Shift rates vs. temperature for Rb + He.

105
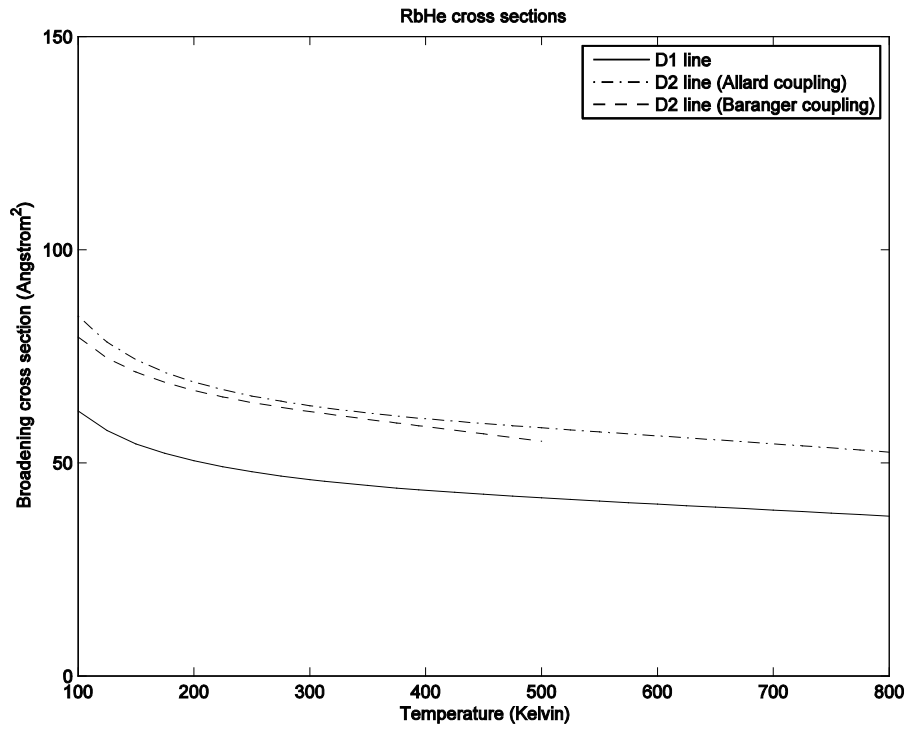
Fig. 3.4g: Broadening cross sections vs. temperature for Rb + He.
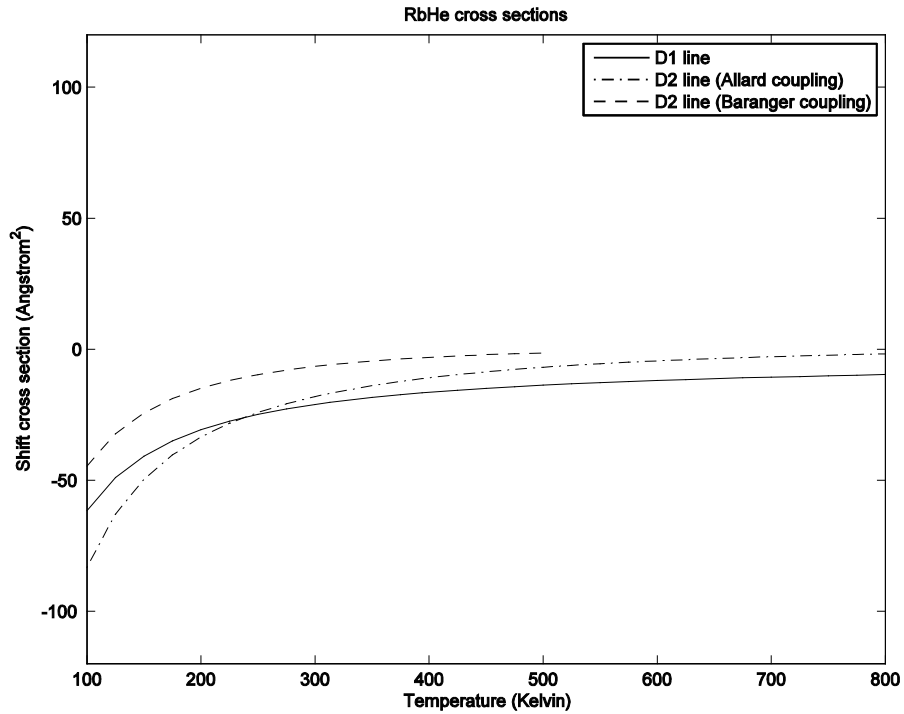
Fig. 3.4h: Shift cross sections vs. temperature for Rb + He.

106

3.5.   Rubidium + Neon (Rb + Ne)
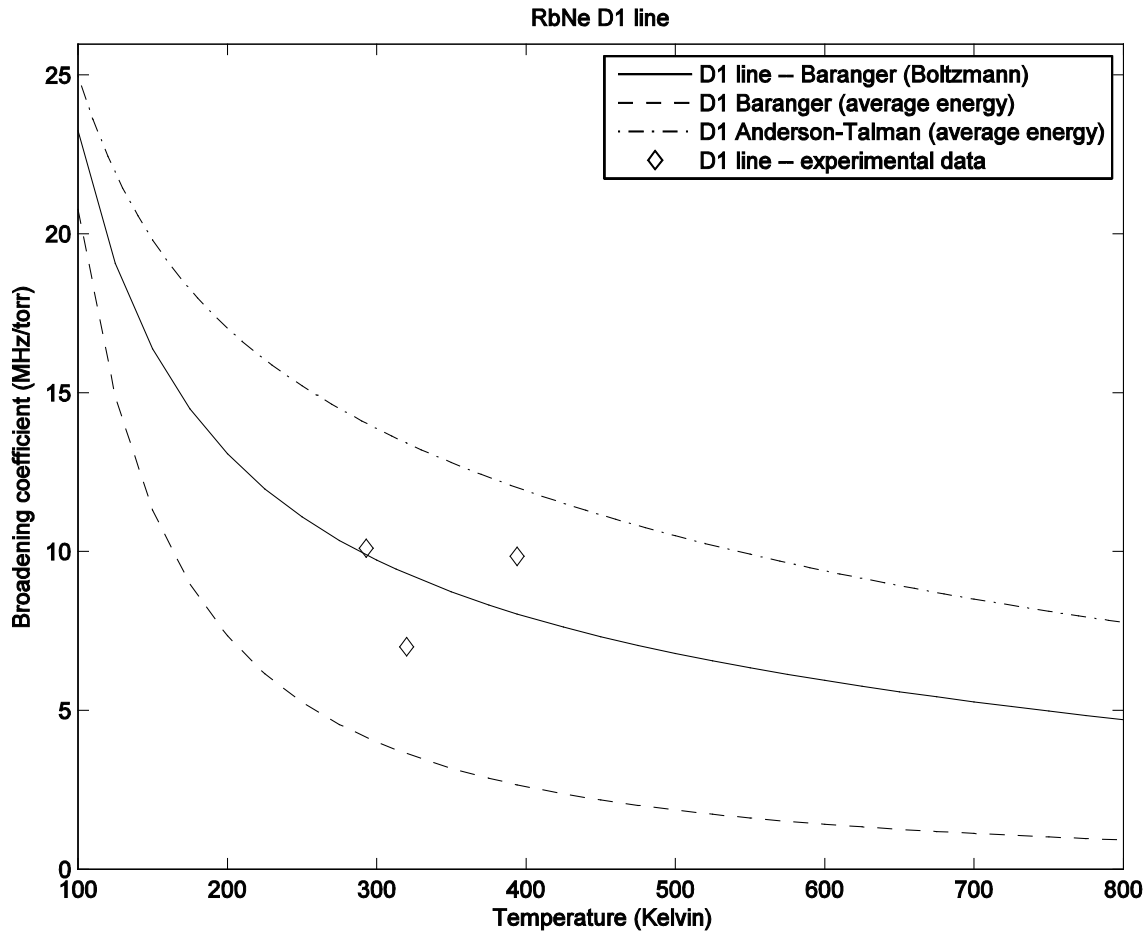
Fig. 3.5a: Broadening coefficients for the D1 line of Rb + Ne. The dashed line represents Baranger model calculations at the thermal average energy for each temperature. The solid line represents Baranger model calculations using the Boltzmann distribution and represents our best results. Here the Baranger model provides a good prediction of measured broadening rates (Kazantsev, Kaliteevskii, and Rish, 1978; Izotova, Kantserov, and Frish, 1981; Rotondaro, 1995; Rotondaro and Perram, 1997) and performs somewhat better than the Anderson-Talman model.

Fig. 3.5b: Shift coefficients for the D1 line of Rb + Ne. The dashed line represents Baranger model calculations at the thermal average energy for each temperature. The solid line represents Baranger model calculations using the Boltzmann distribution and represents our best results. Here the Baranger model provides excellent predictions of measured shift rates (Kazantsev, Kaliteevskii, and Rish, 1978; Izotova, Kantserov, and Frish, 1981; Rotondaro, 1995; Rotondaro and Perram, 1997).

Fig. 3.5c: Broadening coefficients for the D2 line of Rb + Ne. Red and blue indicate results for calculations on the individual surfaces, while black indicates results on the D2 line (Anderson-Talman by taking an average of the red and blue results, Baranger by calculating a coupled case). The black dashed line represents Baranger model calculations using the Allard coupling (50/50 weighting with uncoupled phase shifts). The black solid line represents Baranger model calculations using the Baranger coupling (weightings and phase shifts determined by the fully coupled scattering matrix elements) and represents our best results. Both the Baranger model and the Anderson-Talman model appear to provide excellent predictions of measured broadening rates (Belov, 1981a, 1981b; Izotova, Kantserov, and Frish, 1981; Rotondaro, 1995; Rotondaro and Perram, 1997).

RbNe D2 line

Fig. 3.5d: Shift coefficients for the D2 line of Rb + Ne. Red and blue indicate results for calculations on the individual surfaces, while black indicates results on the D2 line (Anderson-Talman by taking an average of the red and blue results, Baranger by calculating a coupled case). The black dashed line represents Baranger model calculations using the Allard coupling (50/50 weighting with uncoupled phase shifts). The black solid line represents Baranger model calculations using the Baranger coupling (weightings and phase shifts determined by the fully coupled scattering matrix elements) and represents our best results. The Baranger model appears to provide good predictions of measured shift rates (Belov, 1981a, 1981b; Izotova, Kantserov, and Frish, 1981; Rotondaro, 1995; Rotondaro and Perram, 1997), although the Baranger coupling scheme comes closer to experimental results than does the Allard coupling scheme.
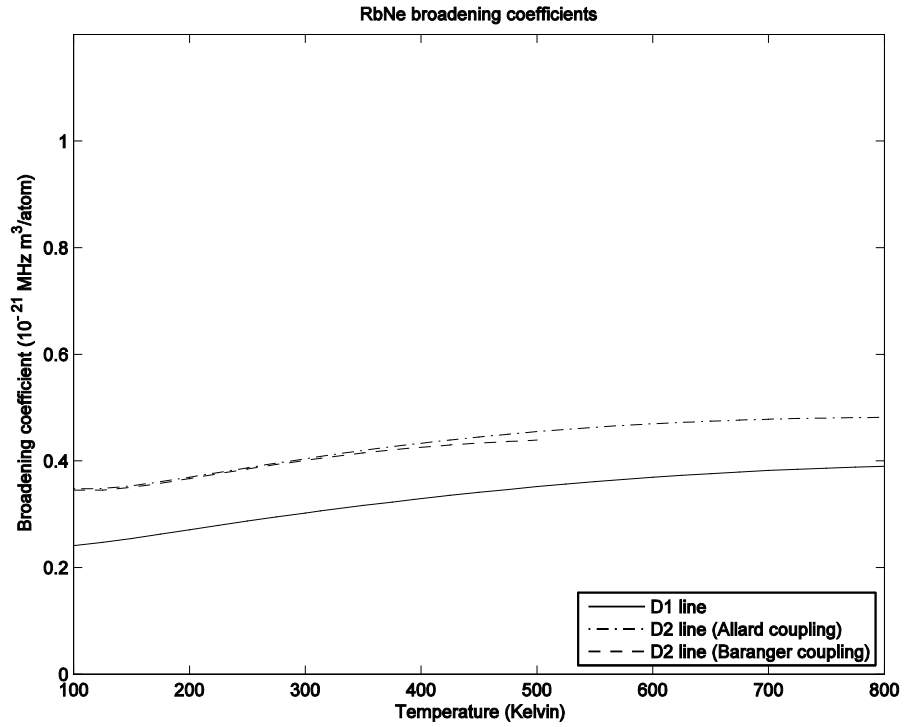
Fig. 3.5e: Broadening rates vs. temperature for Rb + Ne.
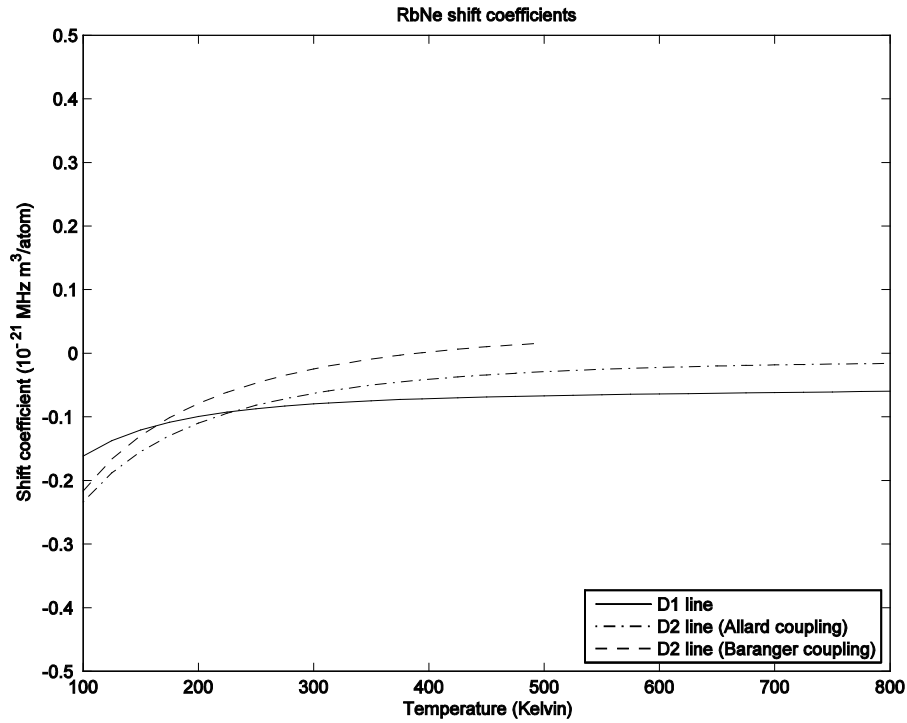
Fig. 3.5f: Shift rates vs. temperature for Rb + Ne.

111
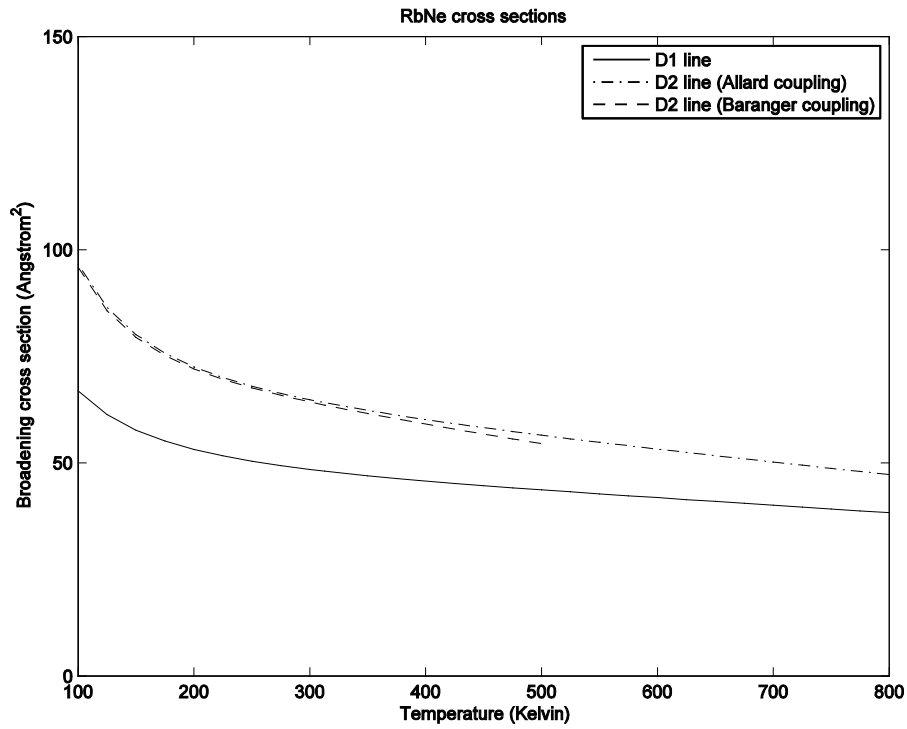
Fig. 3.5g: Broadening cross sections vs. temperature for Rb + Ne.
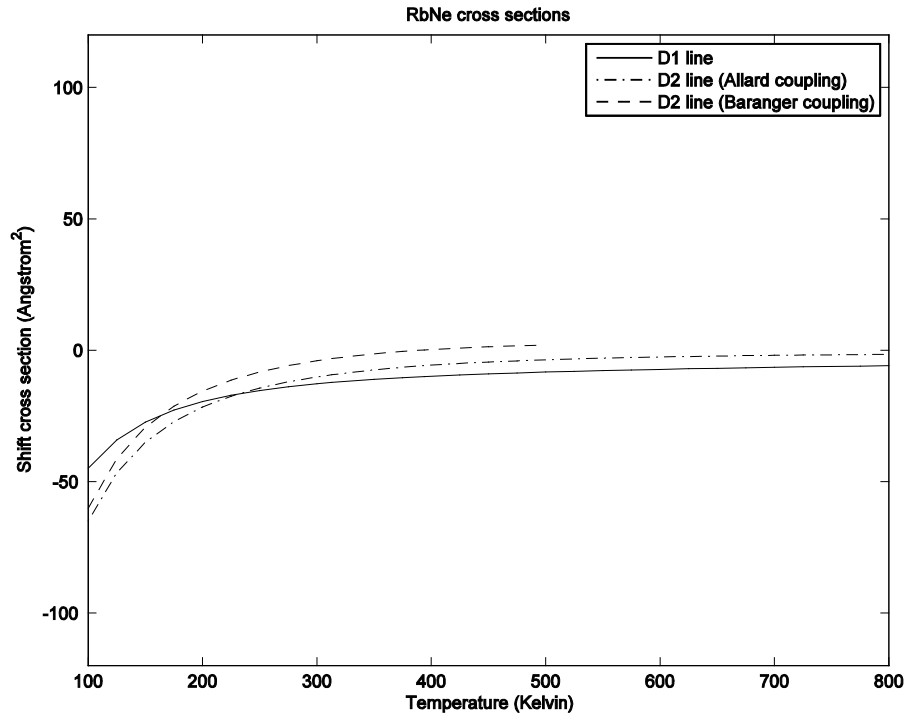
Fig. 3.5h: Shift cross sections vs. temperature for Rb + Ne.
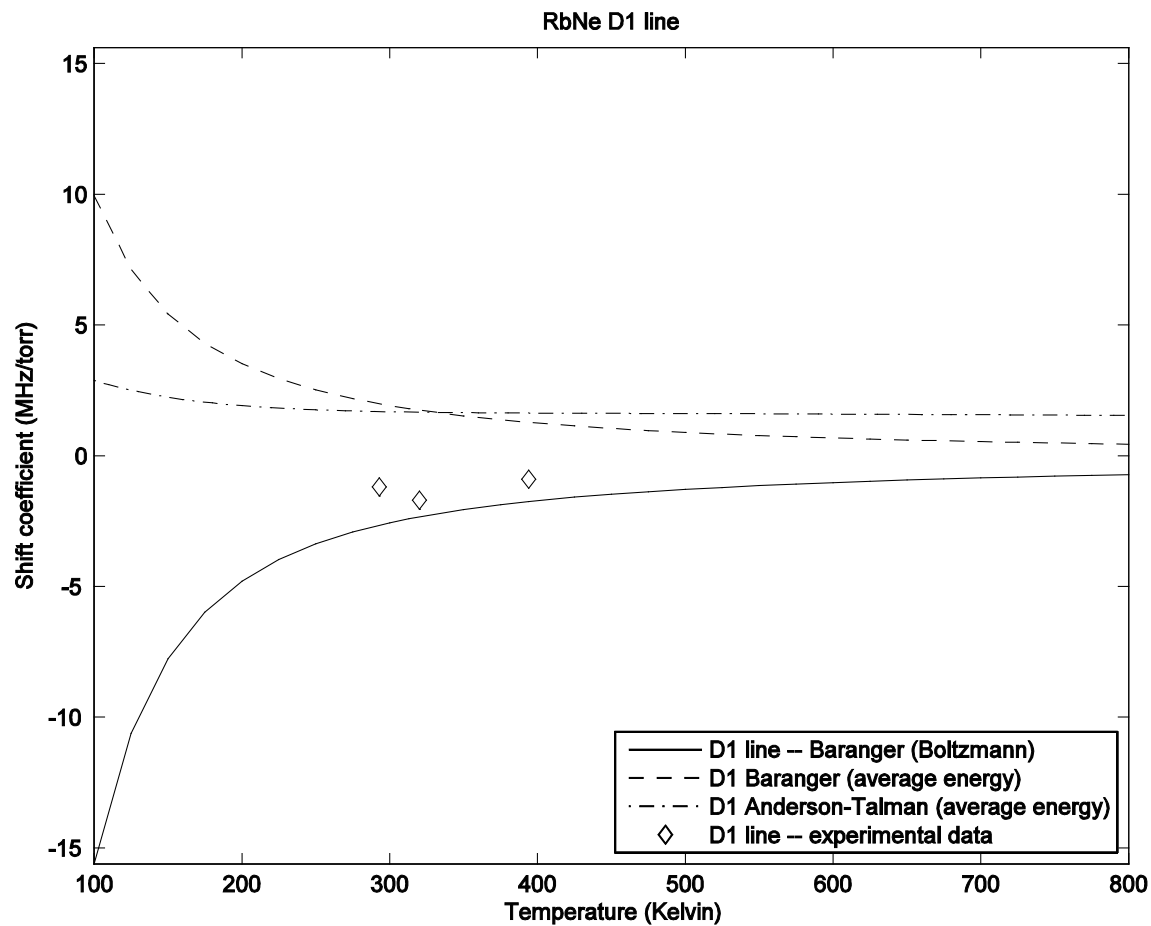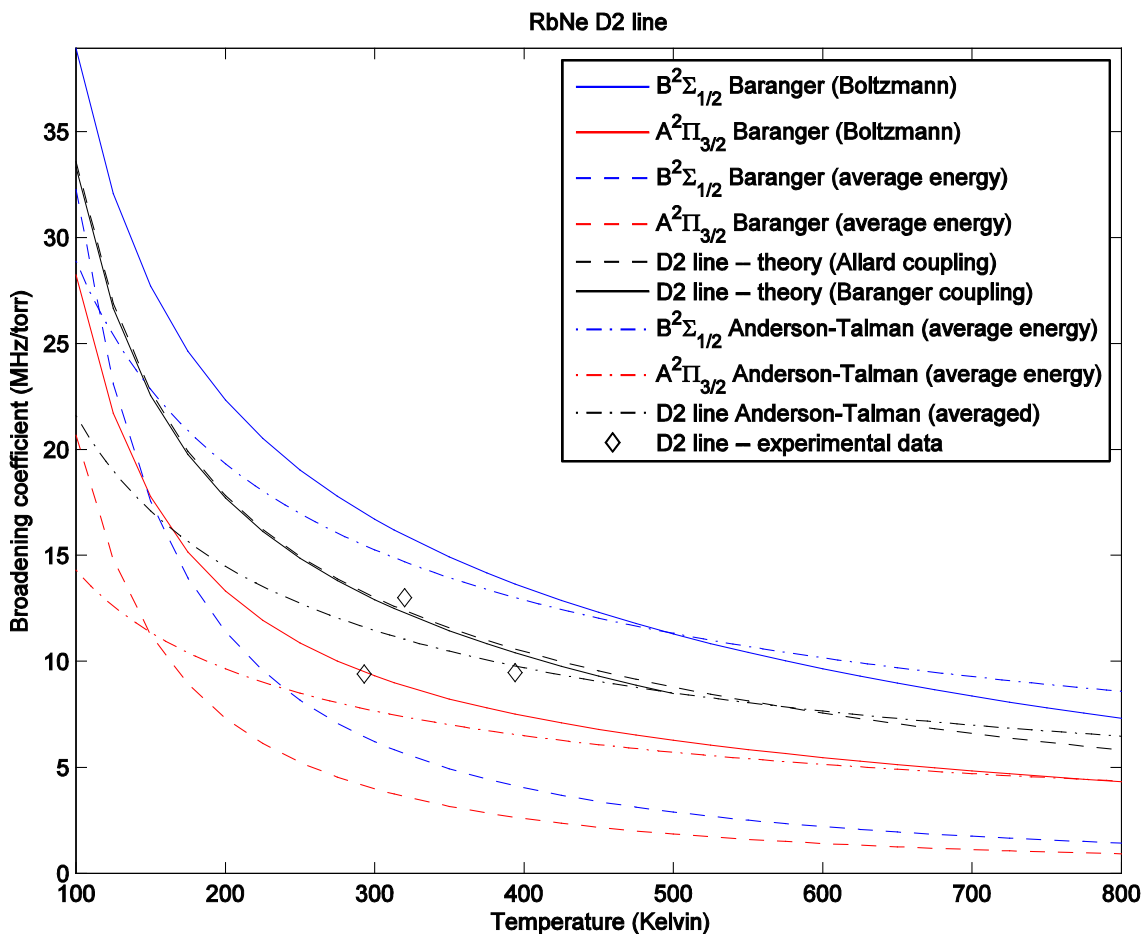
112

3.6.   Rubidium + Argon (Rb + Ar)

Fig. 3.6a: Broadening coefficients for the D1 line of Rb + Ar. The dashed line represents Baranger model calculations at the thermal average energy for each temperature. The solid line represents Baranger model calculations using the Boltzmann distribution and represents our best results. Here both the Baranger model and the Anderson-Talman model provide terrible predictions of measured broadening rates (Kazantsev, Kaliteevskii, and Rish, 1978; Izotova, Kantserov, and Frish, 1981; Rotondaro, 1995; Rotondaro and Perram, 1997).

Fig. 3.6b: Shift coefficients for the D1 line of Rb + Ar. The dashed line represents Baranger model calculations at the thermal average energy for each temperature. The solid line represents Baranger model calculations using the Boltzmann distribution and represents our best results. Here the Baranger model provides fair predictions of measured shift rates (Kazantsev, Kaliteevskii, and Rish, 1978; Izotova, Kantserov, and Frish, 1981; Rotondaro, 1995; Rotondaro and Perram, 1997).

Fig. 3.6c: Broadening coefficients for the D2 line of Rb + Ar. Red and blue indicate results for calculations on the individual surfaces, while black indicates results on the D2 line (Anderson-Talman by taking an average of the red and blue results, Baranger by calculating a coupled case). The black dashed line represents Baranger model calculations using the Allard coupling (50/50 weighting with uncoupled phase shifts). The black solid line represents Baranger model calculations using the Baranger coupling (weightings and phase shifts determined by the fully coupled scattering matrix elements) and represents our best results. Both the Baranger model and the Anderson-Talman model appear to provide poor predictions of measured broadening rates (Belov, 1981a, 1981b; Izotova, Kantserov, and Frish, 1981; Rotondaro, 1995; Rotondaro and Perram, 1997).

Fig. 3.6d: Shift coefficients for the D2 line of Rb + Ar. Red and blue indicate results for calculations on the individual surfaces, while black indicates results on the D2 line (Anderson-Talman by taking an average of the red and blue results, Baranger by calculating a coupled case). The black dashed line represents Baranger model calculations using the Allard coupling (50/50 weighting with uncoupled phase shifts). The black solid line represents Baranger model calculations using the Baranger coupling (weightings and phase shifts determined by the fully coupled scattering matrix elements) and represents our best results. The Baranger model provides good predictions of measured shift rates in this case (Belov, 1981a, 1981b; Izotova, Kantserov, and Frish, 1981; Rotondaro, 1995; Rotondaro and Perram, 1997).
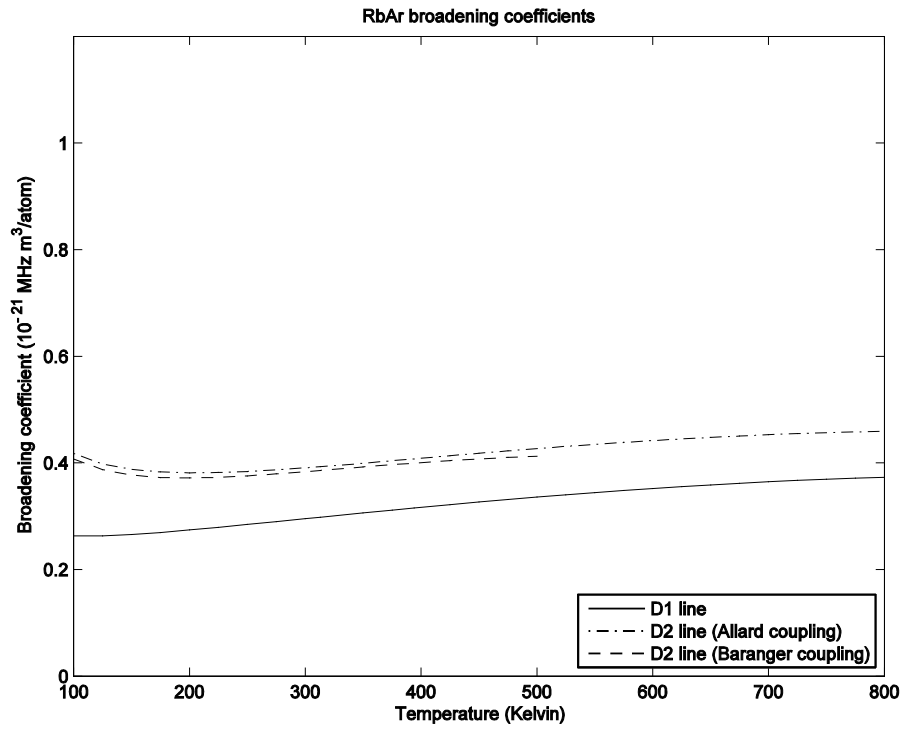
Fig. 3.6e: Broadening rates vs. temperature for Rb + Ar.

Fig. 3.6f: Shift rates vs. temperature for Rb + Ar.

Fig. 3.6g: Broadening cross sections vs. temperature for Rb + Ar.

Fig. 3.6h: Shift cross sections vs. temperature for Rb + Ar.

118

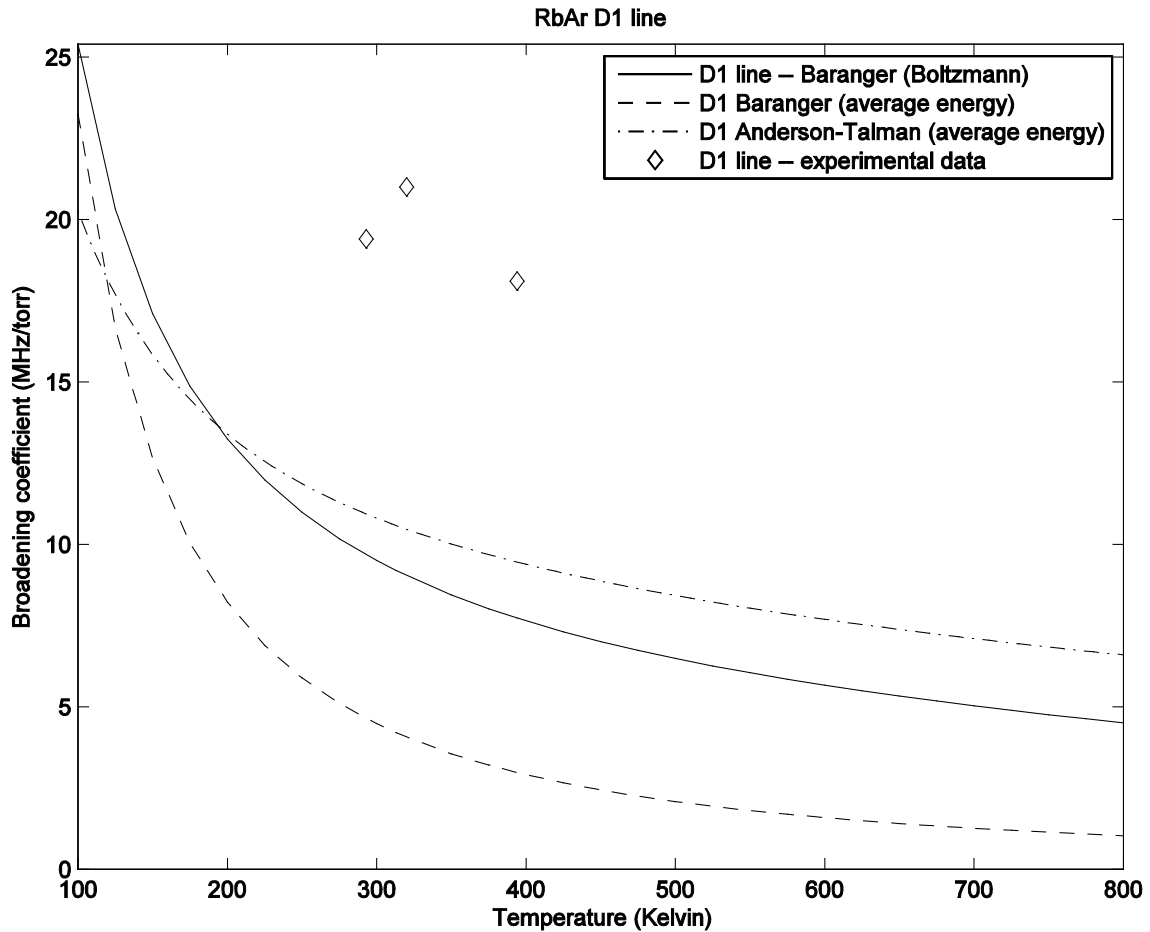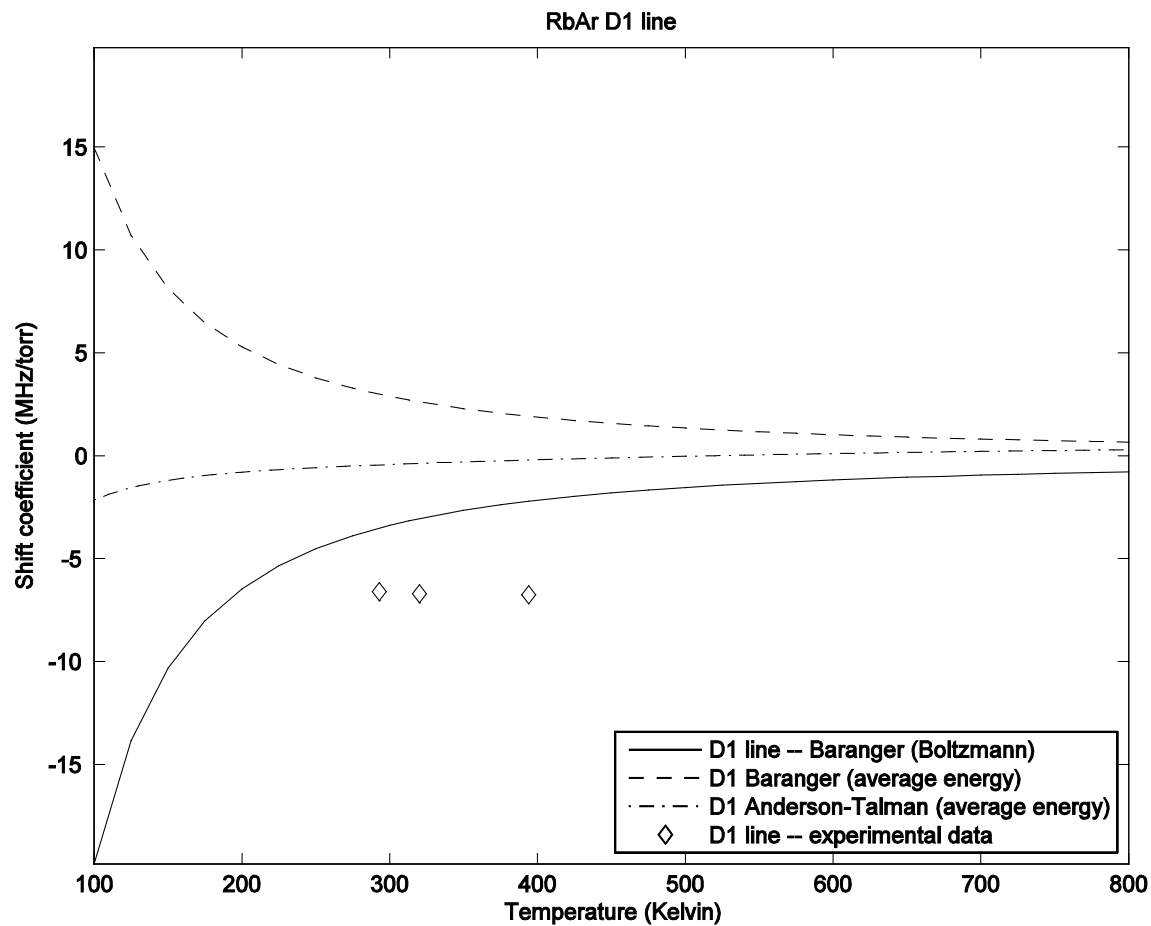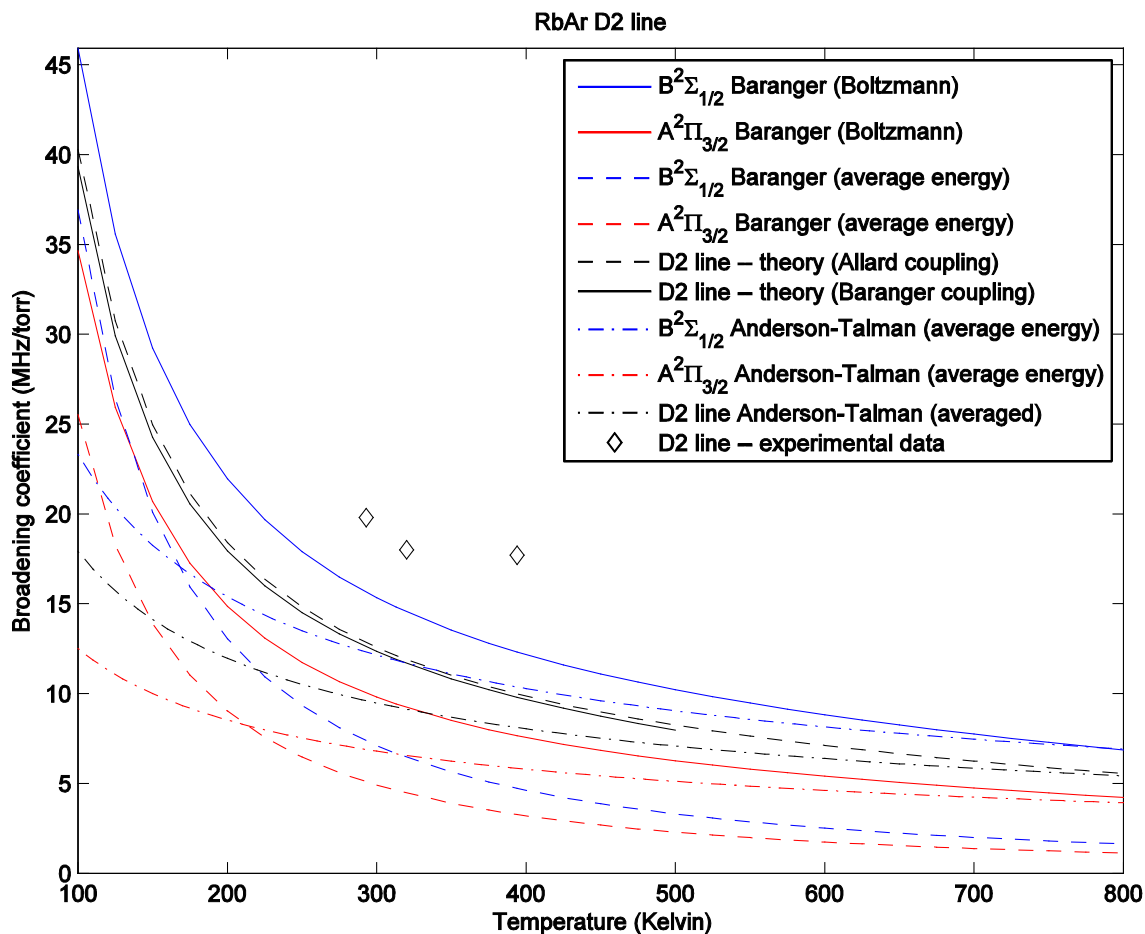## 3.7.   Cesium + Helium (Cs + He)

CsHe D1 line

Fig. 3.7a: Broadening coefficients for the D1 line of Cs + He. The dashed line represents Baranger model calculations at the thermal average energy for each temperature. The solid line represents Baranger model calculations using the Boltzmann distribution and represents our best results. Here the Baranger model provides some good predictions of measured broadening rates at T = 295 K (Bernabeu, 1980), at T = 323 K (Pitz, Wertepny, and Perram, 2009; Pitz, 2010), and at T = 393K (Couture, Clegg, and Drieguys, 2008).

Fig. 3.7b: Shift coefficients for the D1 line of Cs + He. The dashed line represents Baranger model calculations at the thermal average energy for each temperature. The solid line represents Baranger model calculations using the Boltzmann distribution and represents our best results. Here the Baranger model provides fair predictions of measured shift rates at T = 295 K (Bernabeu, 1980), at T = 323 K (Pitz, Wertepny, and Perram, 2009; Pitz, 2010), and at T = 393K (Couture, Clegg, and Drieguys, 2008).

Fig. 3.7c: Broadening coefficients for the D2 line of Cs + He. Red and blue indicate results for calculations on the individual surfaces, while black indicates results on the D2 line (Anderson-Talman by taking an average of the red and blue results, Baranger by calculating a coupled case). The black dashed line represents Baranger model calculations using the Allard coupling (50/50 weighting with uncoupled phase shifts). The black solid line represents Baranger model calculations using the Baranger coupling (weightings and phase shifts determined by the fully coupled scattering matrix elements) and represents our best results. Both the Baranger model and the Anderson-Talman model appear to provide good predictions of measured broadening rates at T = 295 K (Bernabeu, 1980), at T = 313 K (Pitz, 2010; Pitz, Fox, and Perram, 2010), and at T = 393K (Couture, Clegg, and Drieguys, 2008).
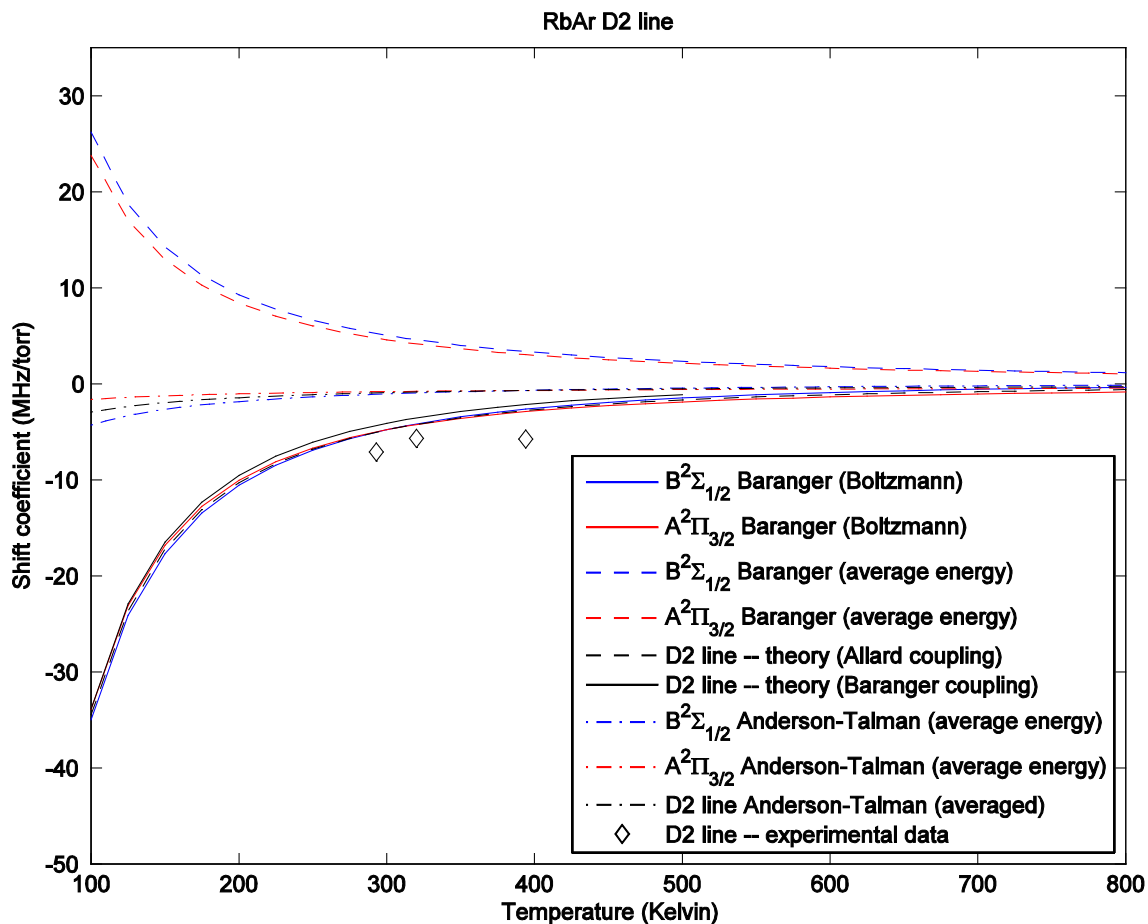
Fig. 3.7d: Shift coefficients for the D2 line of Cs + He. Red and blue indicate results for calculations on the individual surfaces, while black indicates results on the D2 line (Anderson-Talman by taking an average of the red and blue results, Baranger by calculating a coupled case). The black dashed line represents Baranger model calculations using the Allard coupling (50/50 weighting with uncoupled phase shifts). The black solid line represents Baranger model calculations using the Baranger coupling (weightings and phase shifts determined by the fully coupled scattering matrix elements) and represents our best results. Both the Baranger model and the Anderson-Talman model appear to provide fair predictions of measured shift rates at T = 295 K (Bernabeu, 1980), at T = 313 K (Pitz, 2010; Pitz, Fox, and Perram, 2010), and at T = 393K (Couture, Clegg, and Drieguys, 2008), though the Allard coupling scheme appears to perform better than the Baranger coupling scheme in this case.

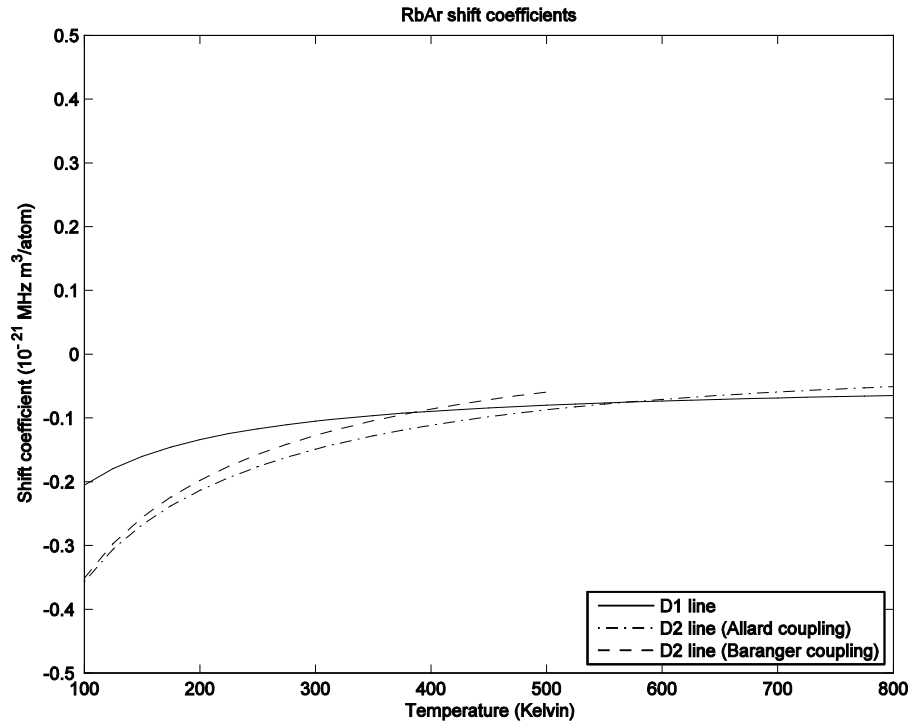Fig. 3.7e: Broadening rates vs. temperature for Cs + He.

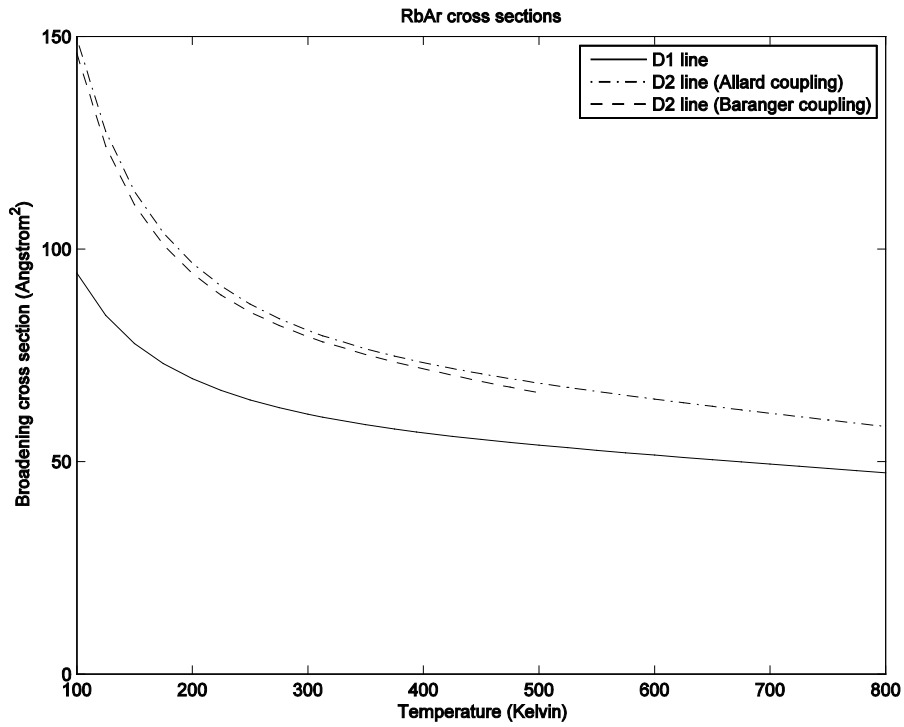Fig. 3.7f: Shift rates vs. temperature for Cs + He.

123

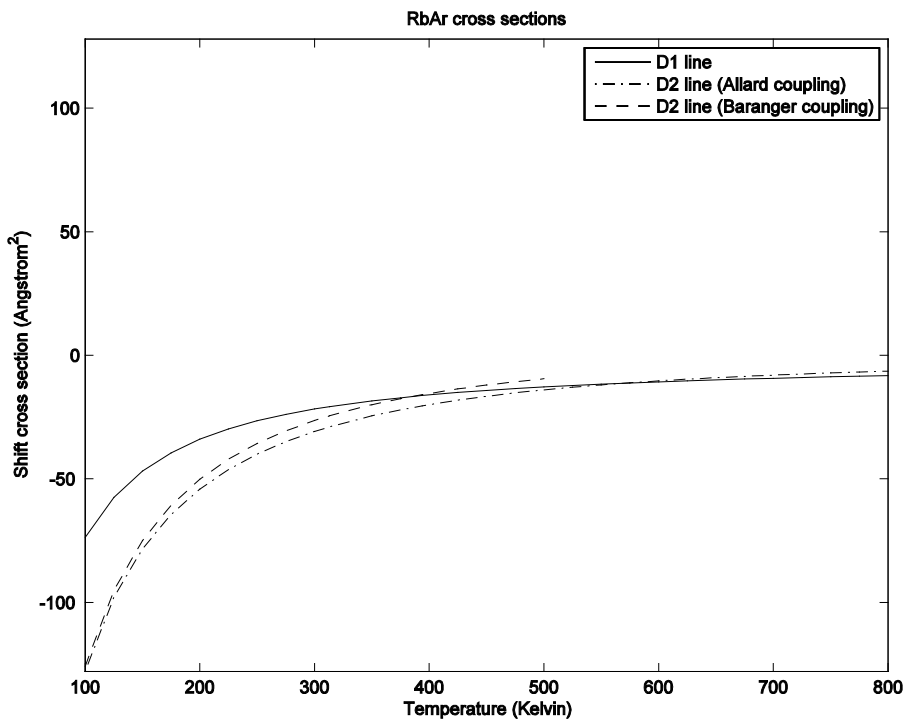Fig. 3.7g: Broadening cross sections vs. temperature for Cs + He.

Fig. 3.7h: Shift cross sections vs. temperature for Cs + He.
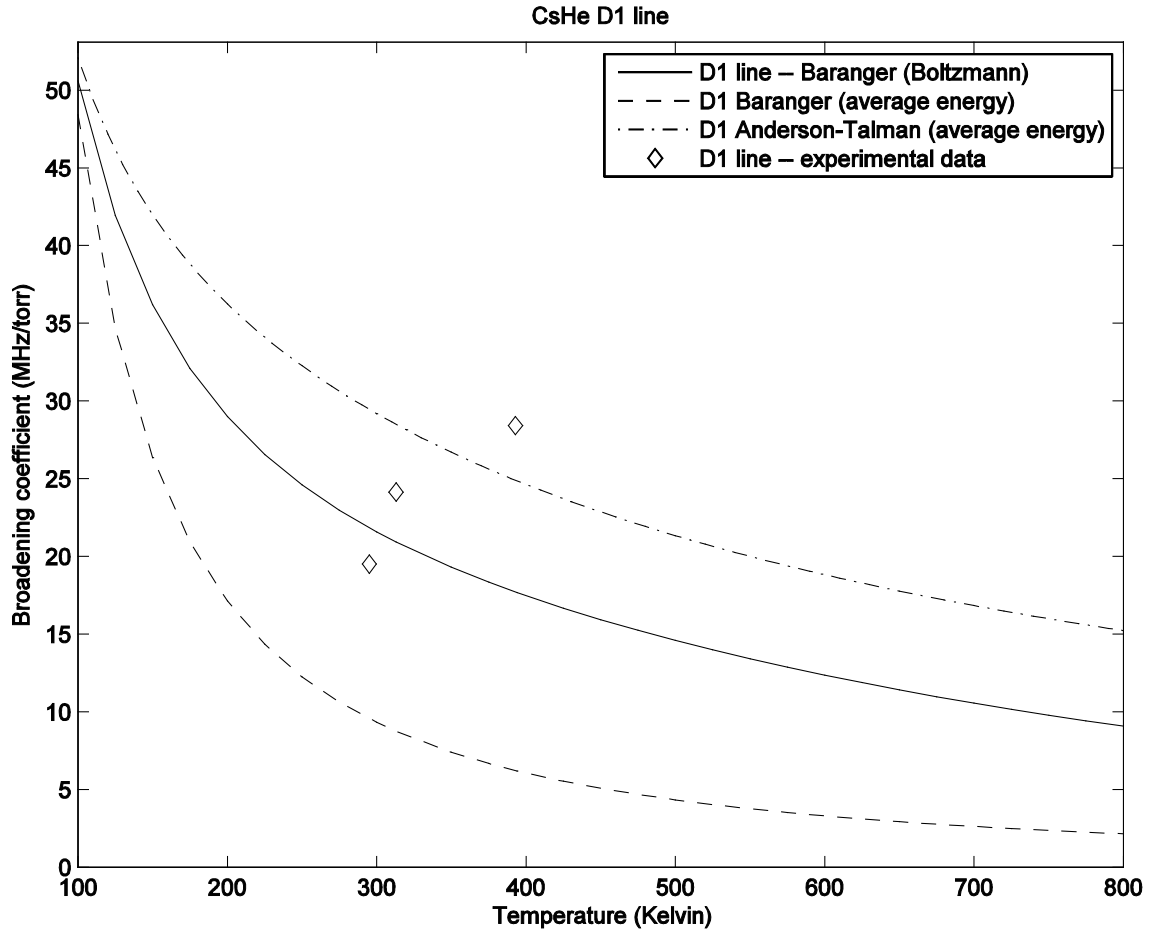
3.8. Cesium + Neon (Cs + Ne)

Fig. 3.8a: Broadening coefficients for the D1 line of Cs + Ne. The dashed line represents Baranger model calculations at the thermal average energy for each temperature. The solid line represents Baranger model calculations using the Boltzmann distribution and represents our best results. Here the Baranger model provides excellent predictions of measured broadening rates (Bernabeu, 1980; Couture, Clegg, and Drieguys, 2008; Pitz, Wertepny, and Perram, 2009; Pitz, 2010; Pitz, Fox, and Perram, 2010).
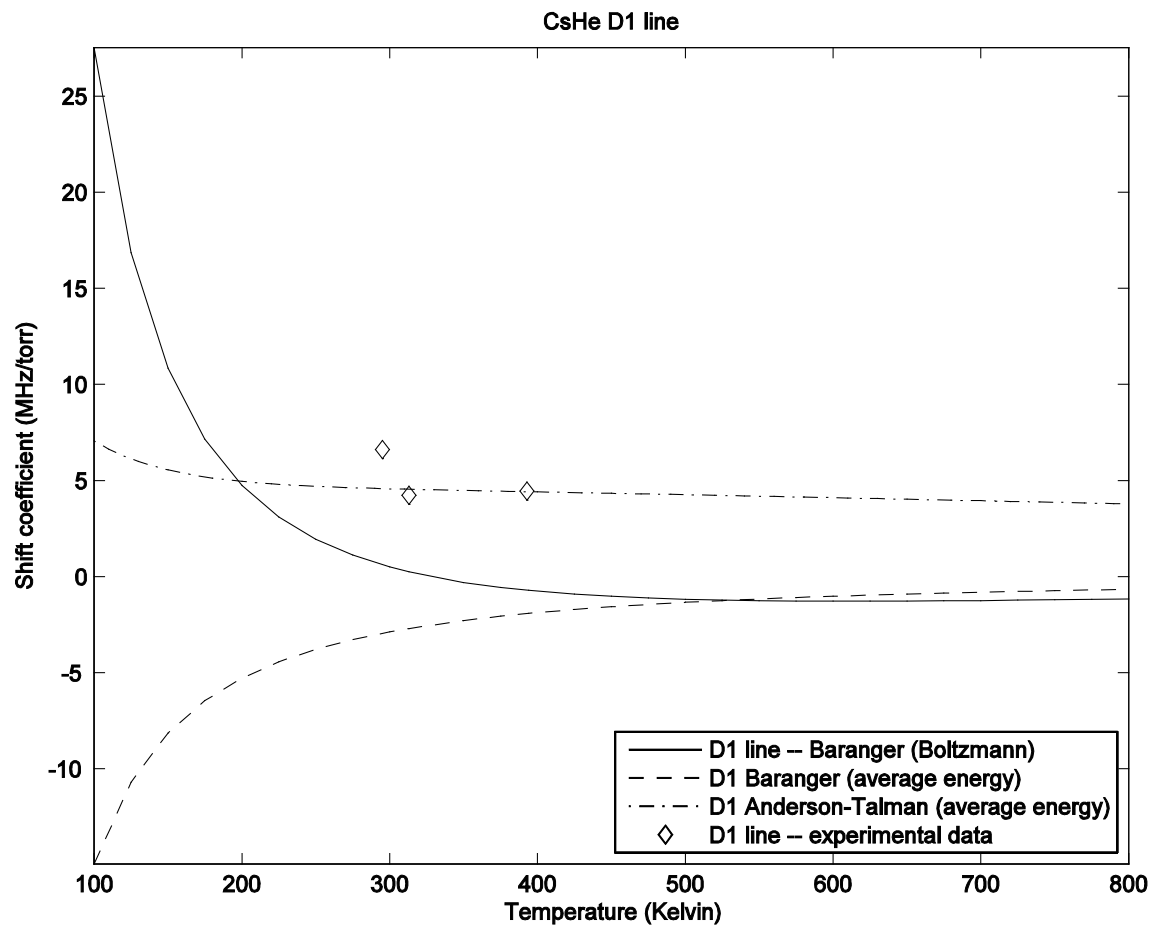
Fig. 3.8b: Shift coefficients for the D1 line of Cs + Ne. The dashed line represents Baranger model calculations at the thermal average energy for each temperature. The solid line represents Baranger model calculations using the Boltzmann distribution and represents our best results. Here Baranger model provides fair predictions of measured shift rates (Bernabeu, 1980; Couture, Clegg, and Drieguys, 2008; Pitz, Wertepny, and Perram, 2009; Pitz, 2010; Pitz, Fox, and Perram, 2010).
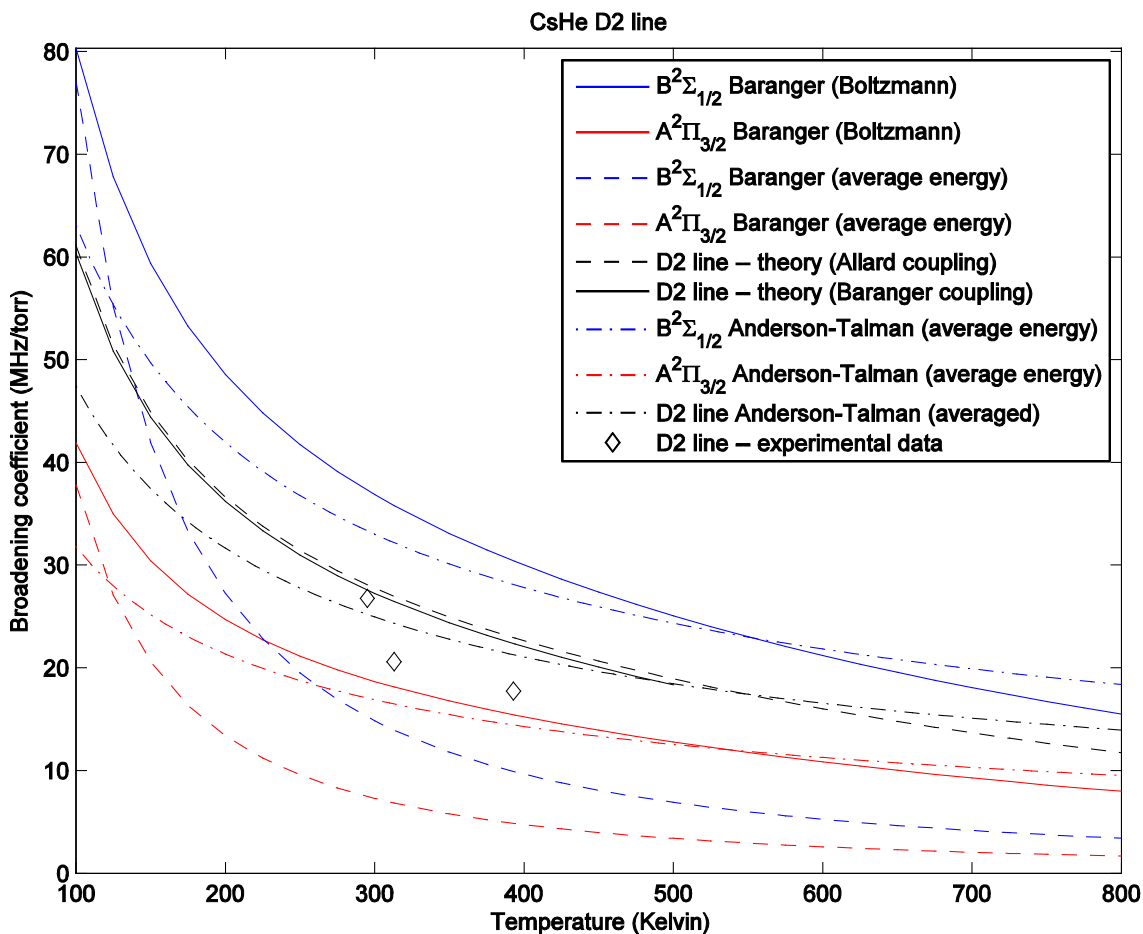
Fig. 3.8c: Broadening coefficients for the D2 line of Cs + Ne. Red and blue indicate results for calculations on the individual surfaces, while black indicates results on the D2 line (Anderson-Talman by taking an average of the red and blue results, Baranger by calculating a coupled case). The black dashed line represents Baranger model calculations using the Allard coupling (50/50 weighting with uncoupled phase shifts). The black solid line represents Baranger model calculations using the Baranger coupling (weightings and phase shifts determined by the fully coupled scattering matrix elements) and represents our best results. Both the Baranger model and the Anderson-Talman model appear to provide fair predictions of measured broadening rates (Bernabeu, 1980; Couture, Clegg, and Drieguys, 2008; Pitz, Wertepny, and Perram, 2009; Pitz, 2010; Pitz, Fox, and Perram, 2010).
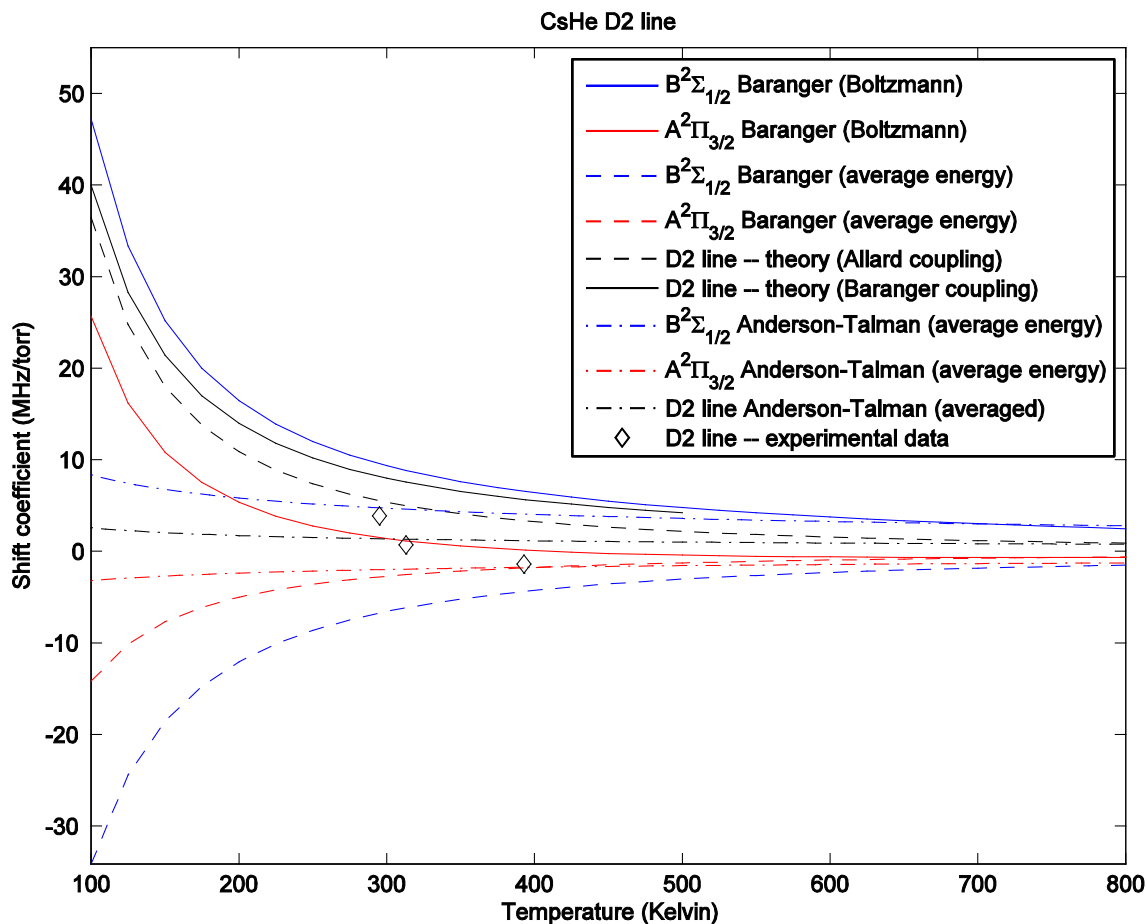
Fig. 3.8d: Shift coefficients for the D2 line of Cs + Ne. Red and blue indicate results for calculations on the individual surfaces, while black indicates results on the D2 line (Anderson-Talman by taking an average of the red and blue results, Baranger by calculating a coupled case). The black dashed line represents Baranger model calculations using the Allard coupling (50/50 weighting with uncoupled phase shifts). The black solid line represents Baranger model calculations using the Baranger coupling (weightings and phase shifts determined by the fully coupled scattering matrix elements) and represents our best results. Both the Baranger model and the Anderson-Talman model appear to provide poor predictions of measured shift rates (Bernabeu, 1980; Couture, Clegg, and Drieguys, 2008; Pitz, Wertepny, and Perram, 2009; Pitz, 2010; Pitz, Fox, and Perram, 2010). The Baranger coupling scheme appears to predict the opposite shift from experiment.
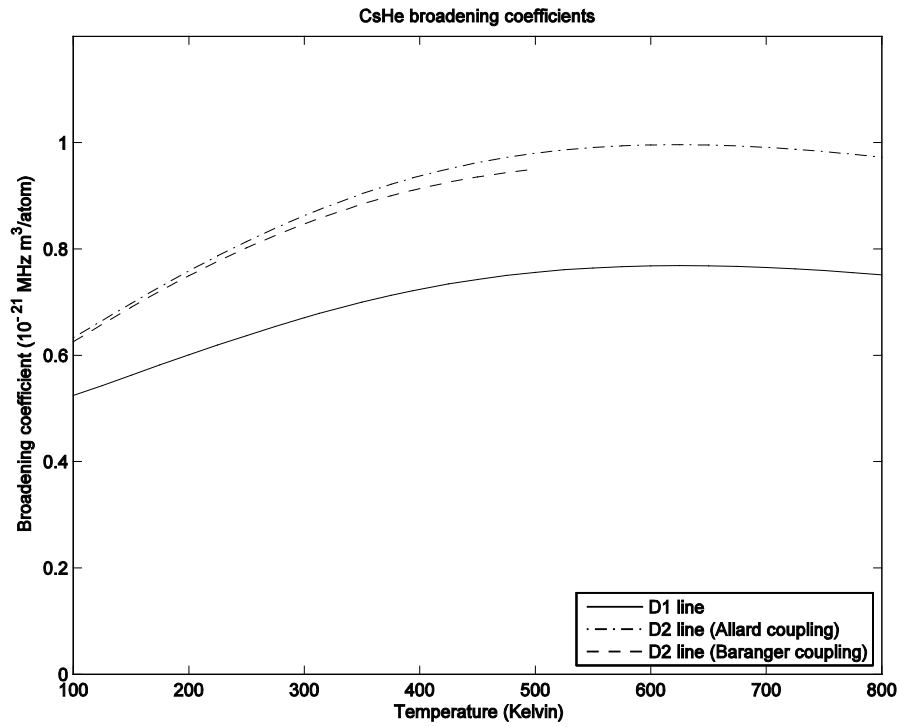
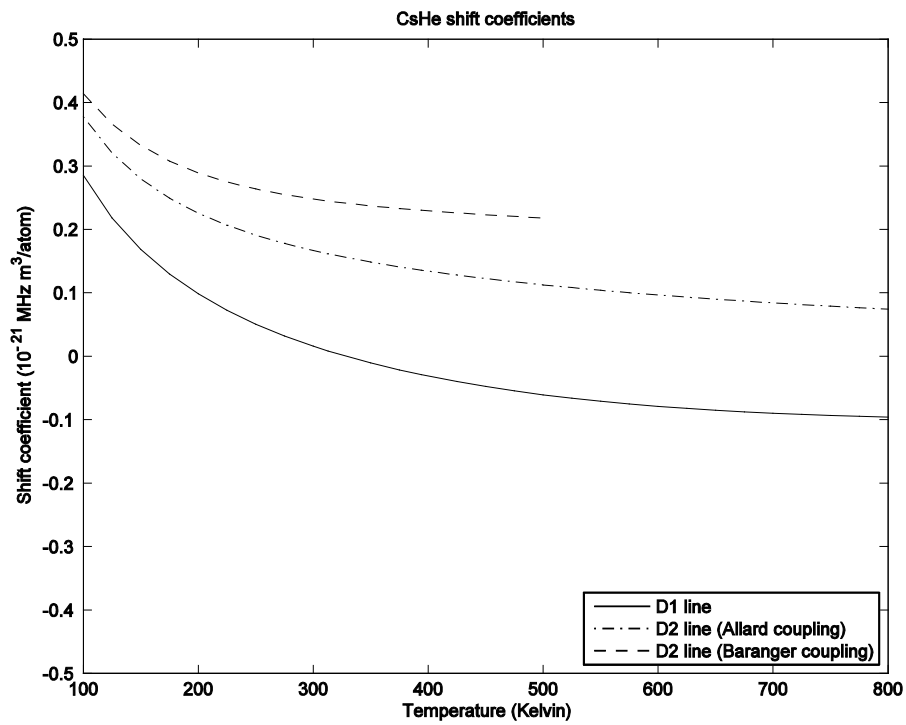Fig. 3.8e: Broadening rates vs. temperature for Cs + Ne.

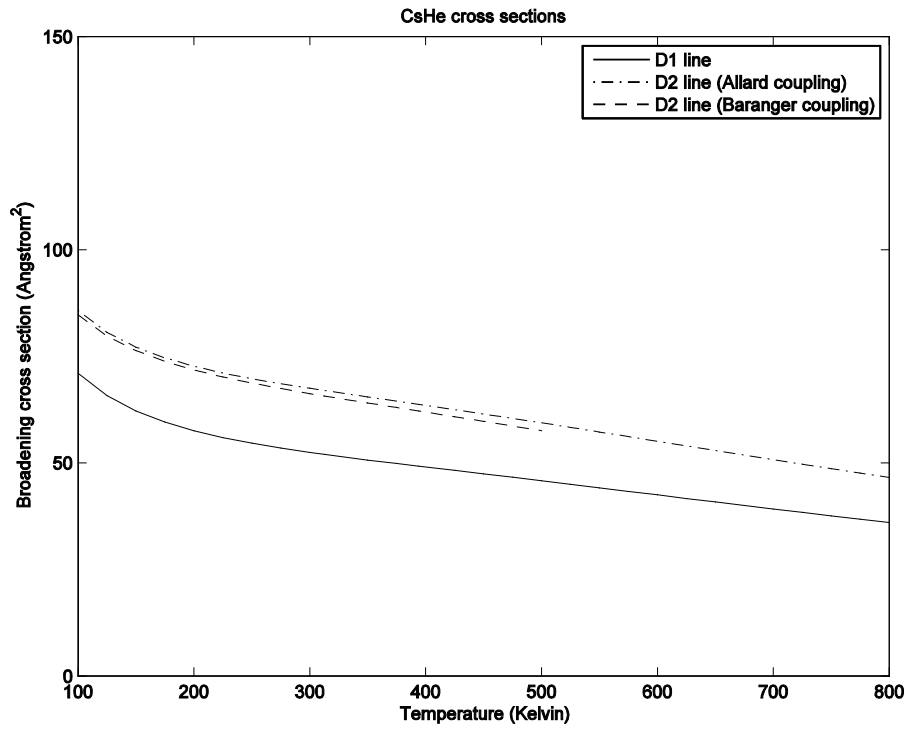Fig. 3.8f: Shift rates vs. temperature for Cs + Ne.

129

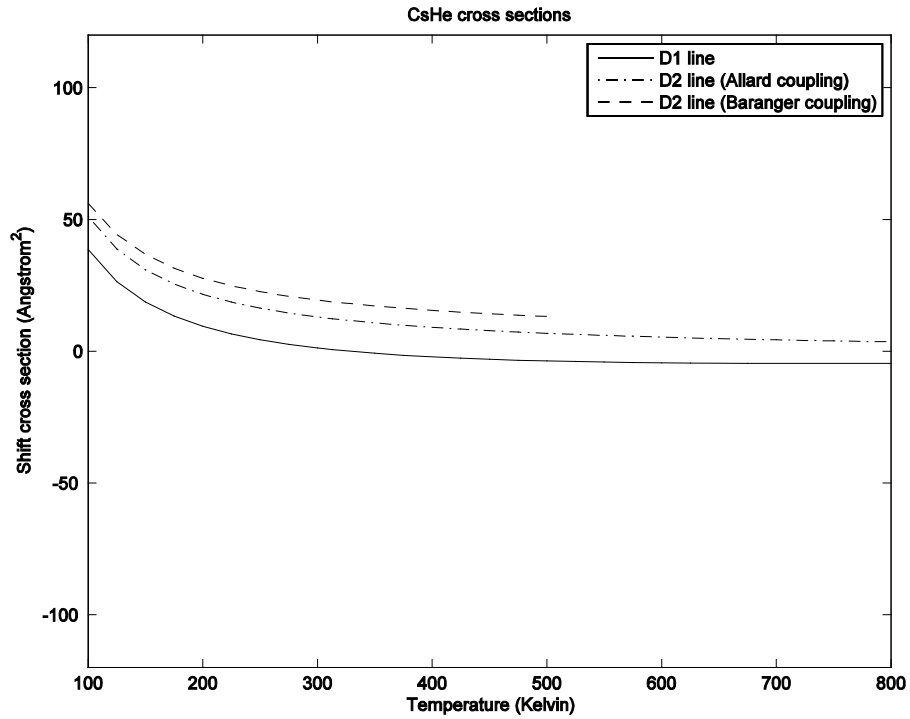Fig. 3.8g: Broadening cross sections vs. temperature for Cs + Ne.

Fig. 3.8h: Shift cross sections vs. temperature for Cs + Ne.
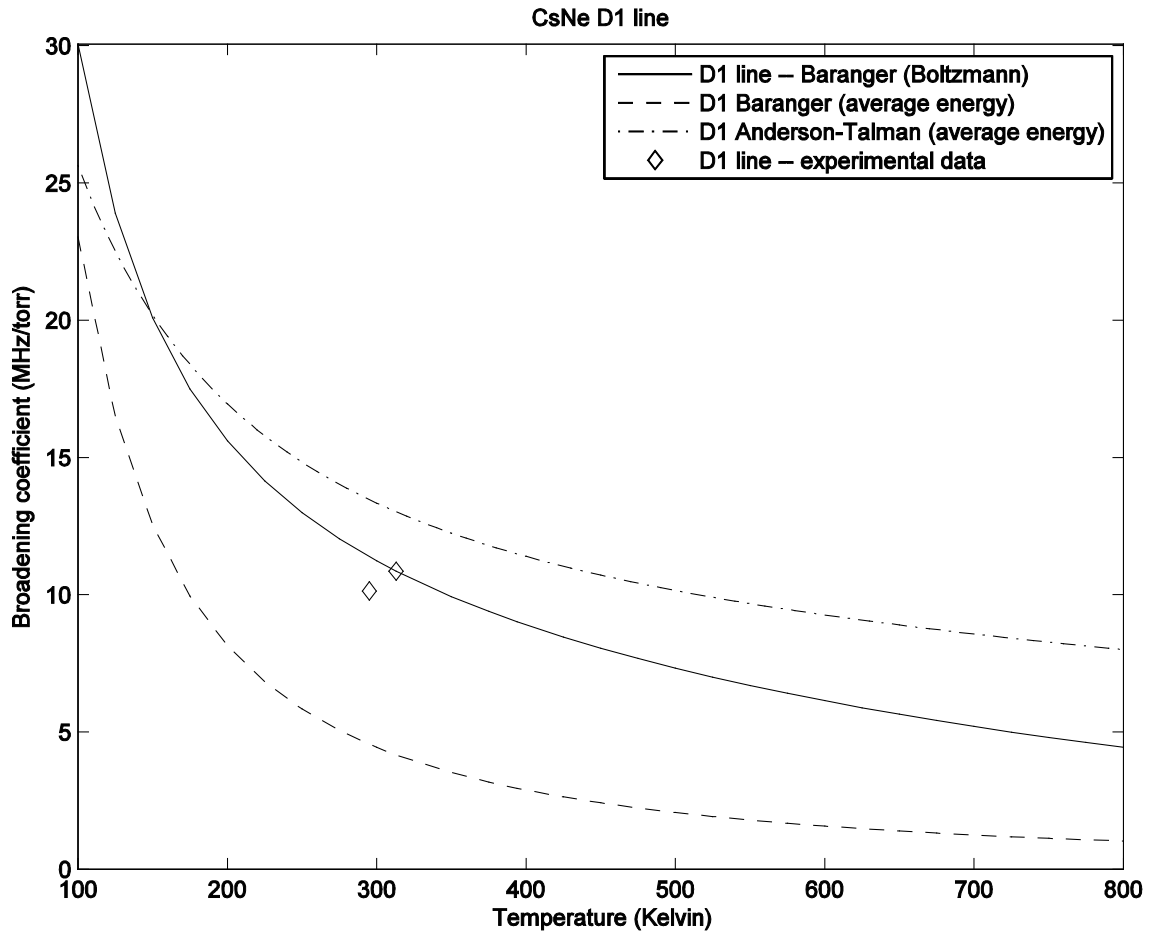
3.9.   Cesium + Argon (Cs + Ar)
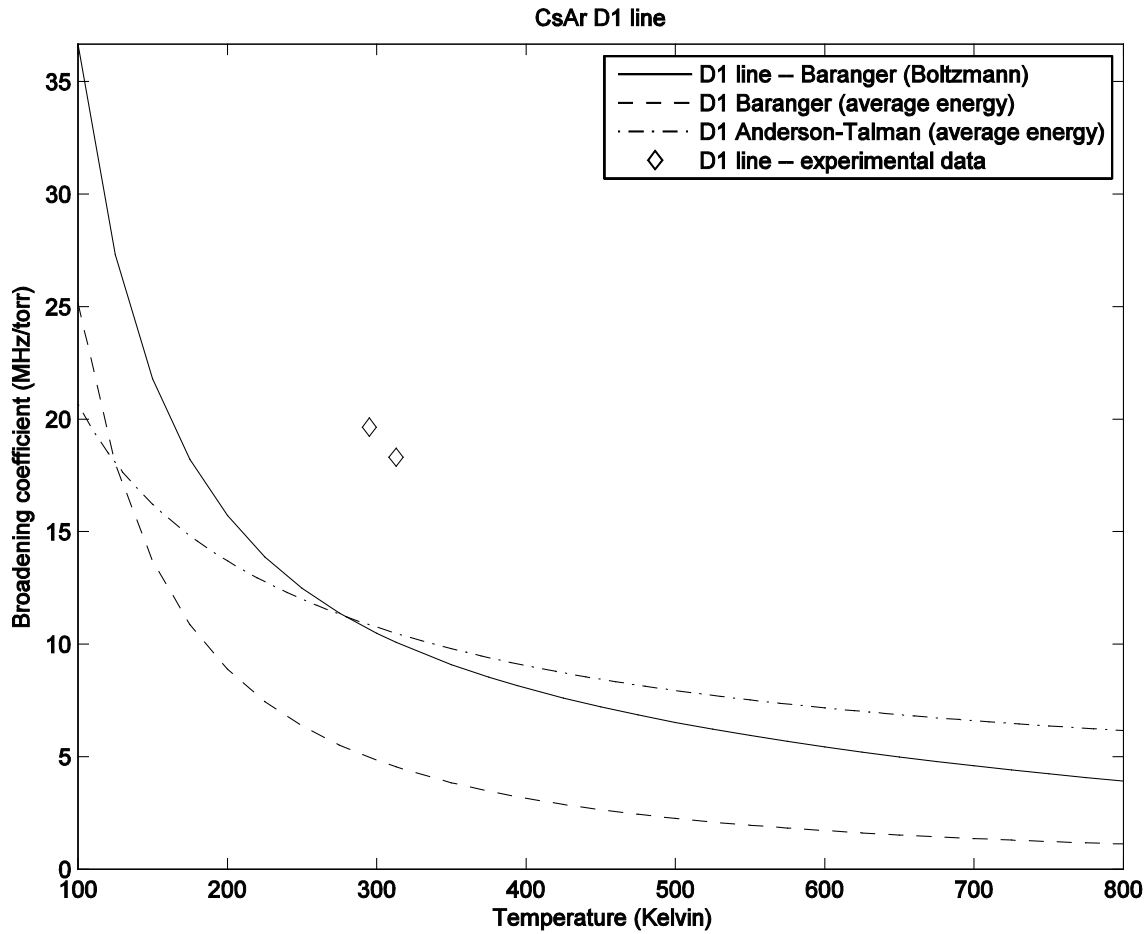
Fig. 3.9a: Broadening coefficients for the D1 line of Cs + Ar. The dashed line represents Baranger model calculations at the thermal average energy for each temperature. The solid line represents Baranger model calculations using the Boltzmann distribution and represents our best results. Here both the Baranger model and the Anderson-Talman model provides terrible predictions of measured broadening rates (Bernabeu, 1980; Couture, Clegg, and Drieguys, 2008; Pitz, Wertepny, and Perram, 2009; Pitz, 2010; Pitz, Fox, and Perram, 2010).
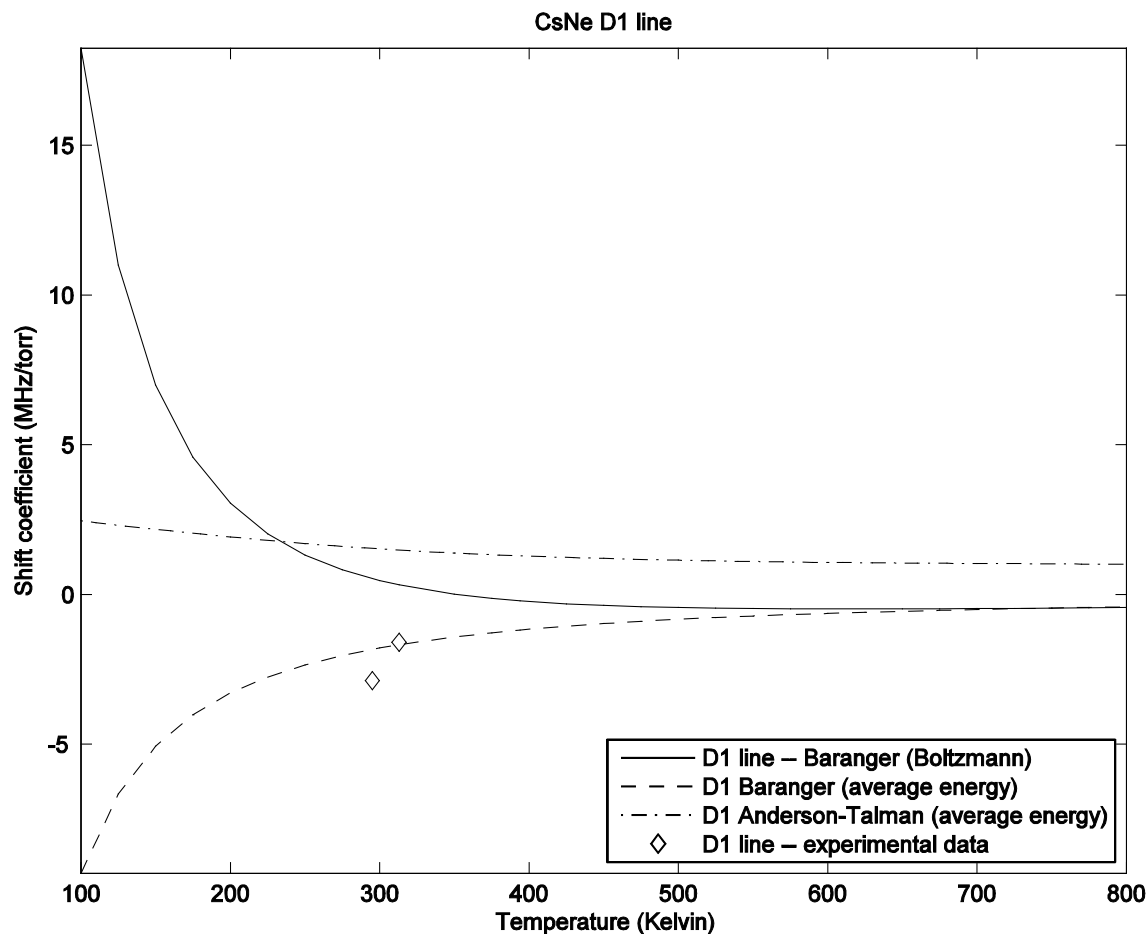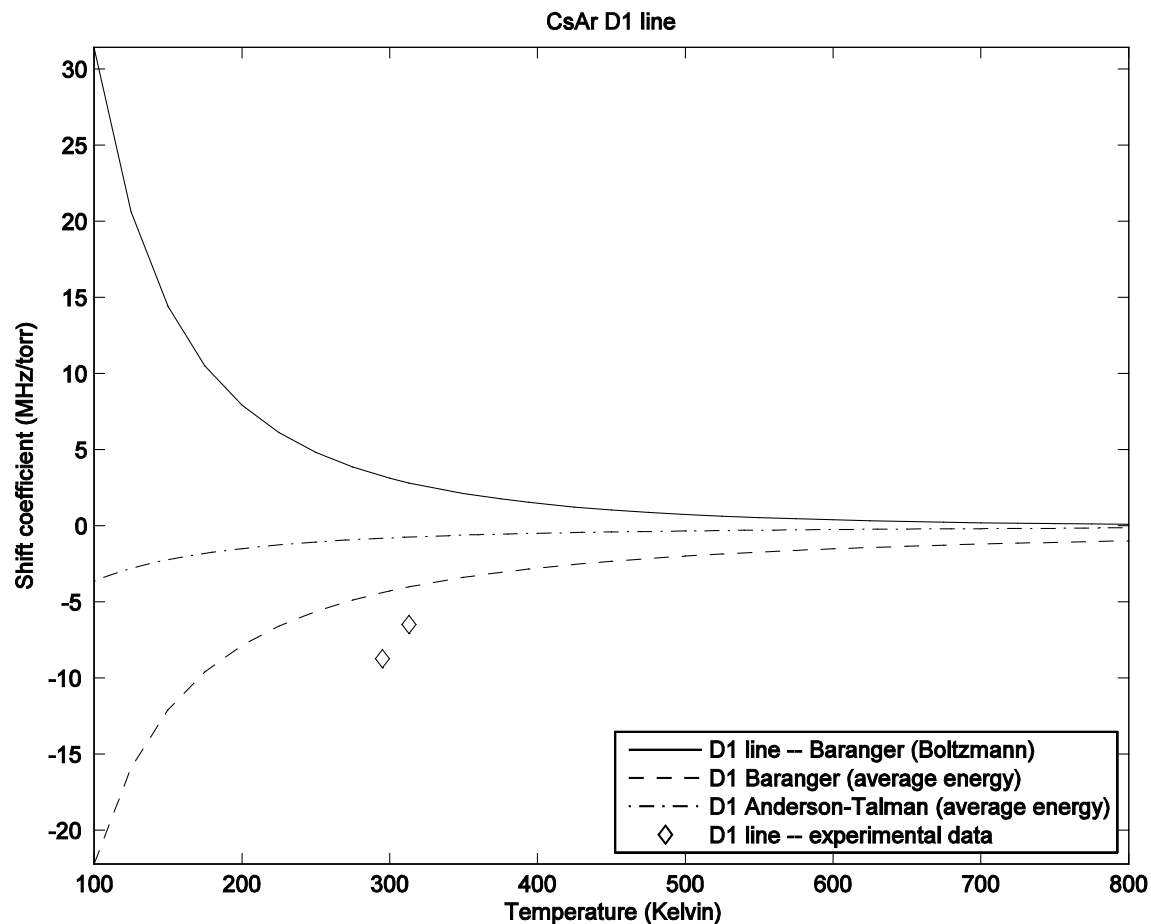
Fig. 3.9b: Shift coefficients for the D1 line of Cs + Ar. The dashed line represents Baranger model calculations at the thermal average energy for each temperature. The solid line represents Baranger model calculations using the Boltzmann distribution and represents our best results. Here both the Baranger model and the Anderson-Talman model provides terrible predictions of measured shift rates (Bernabeu, 1980; Couture, Clegg, and Drieguys, 2008; Pitz, Wertepny, and Perram, 2009; Pitz, 2010; Pitz, Fox, and Perram, 2010).
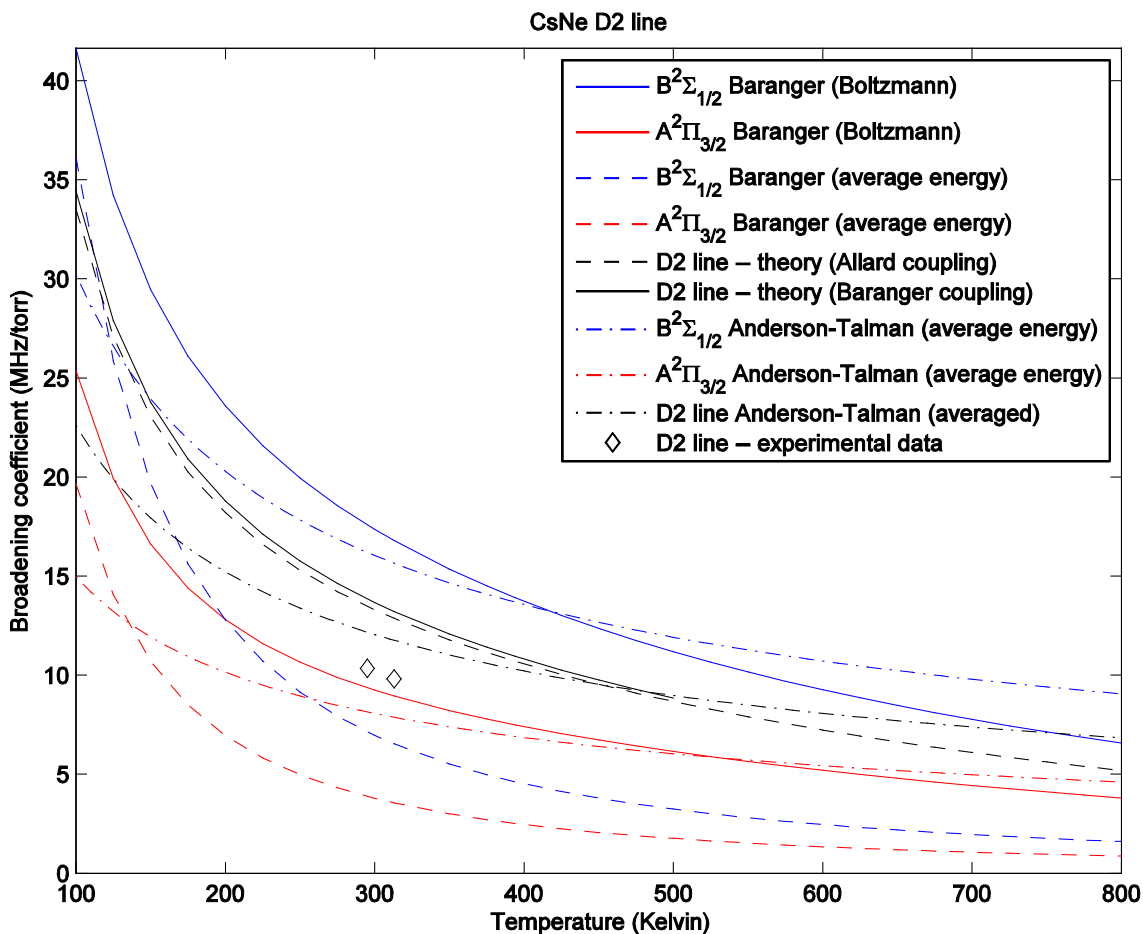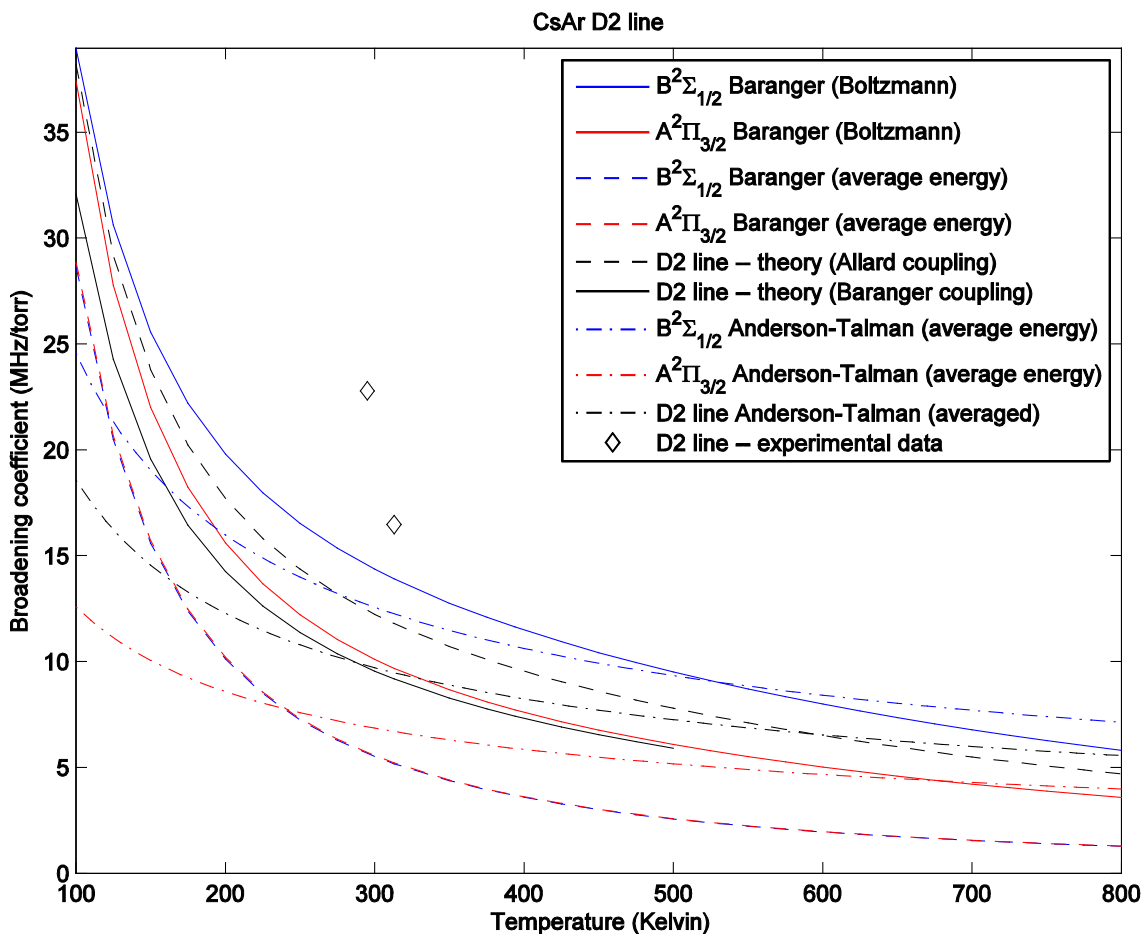
Fig. 3.9c: Broadening coefficients for the D2 line of Cs + Ar. Red and blue indicate results for calculations on the individual surfaces, while black indicates results on the D2 line (Anderson-Talman by taking an average of the red and blue results, Baranger by calculating a coupled case). The black dashed line represents Baranger model calculations using the Allard coupling (50/50 weighting with uncoupled phase shifts). The black solid line represents Baranger model calculations using the Baranger coupling (weightings and phase shifts determined by the fully coupled scattering matrix elements) and represents our best results. The two coupling cases may converge only at very high temperatures (at least 700 K), though we cannot predict the Baranger coupling results at temperatures above 500 K with certainty. Both the Baranger model and the Anderson-Talman model appear to provide poor predictions of measured broadening rates (Bernabeu, 1980; Couture, Clegg, and Drieguys, 2008; Pitz, Wertepny, and Perram, 2009; Pitz, 2010; Pitz, Fox, and Perram, 2010).
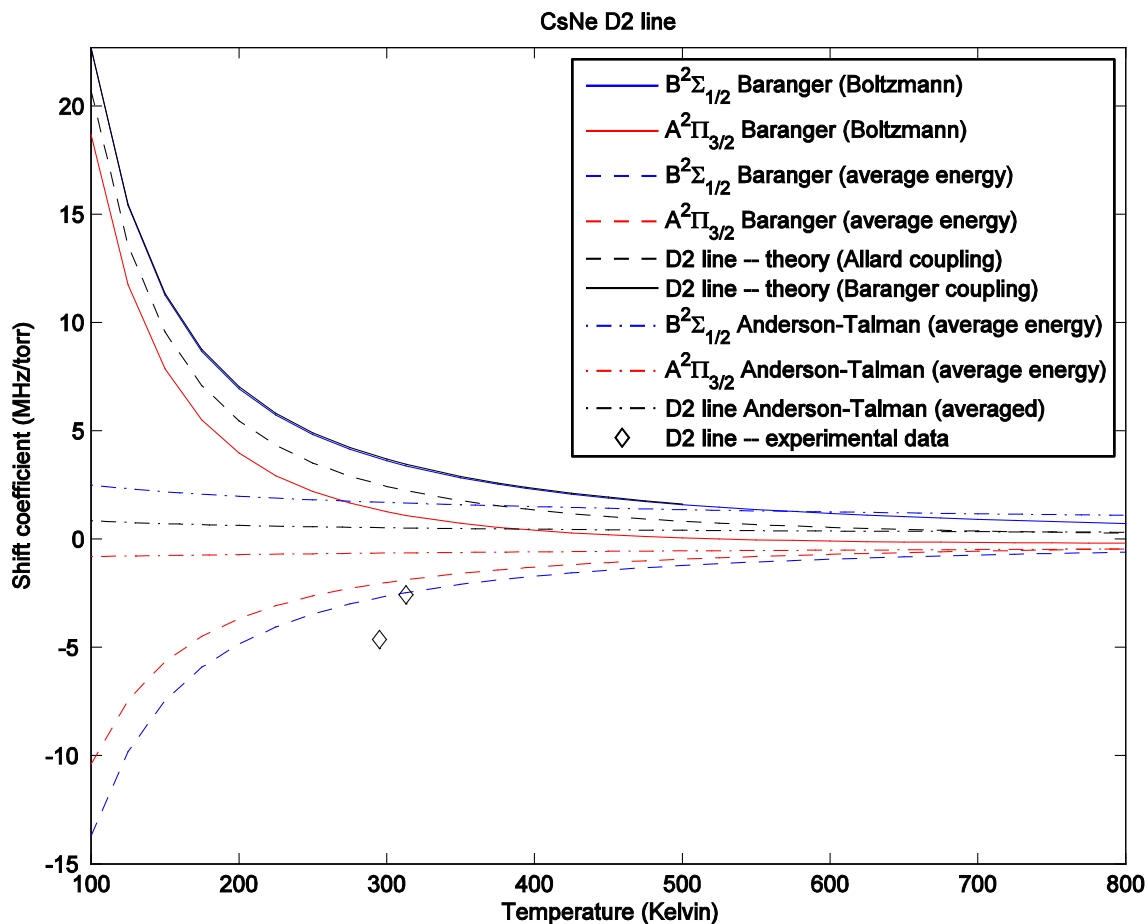
Fig. 3.9d: Shift coefficients for the D2 line of Cs + Ar. Red and blue indicate results for calculations on the individual surfaces, while black indicates results on the D2 line (Anderson-Talman by taking an average of the red and blue results, Baranger by calculating a coupled case). The black dashed line represents Baranger model calculations using the Allard coupling (50/50 weighting with uncoupled phase shifts). The black solid line represents Baranger model calculations using the Baranger coupling (weightings and phase shifts determined by the fully coupled scattering matrix elements) and represents our best results. Both the Baranger model and the Anderson-Talman model appear to provide poor predictions of measured shift rates (Bernabeu, 1980; Couture, Clegg, and Drieguys, 2008; Pitz, Wertepny, and Perram, 2009; Pitz, 2010; Pitz, Fox, and Perram, 2010).
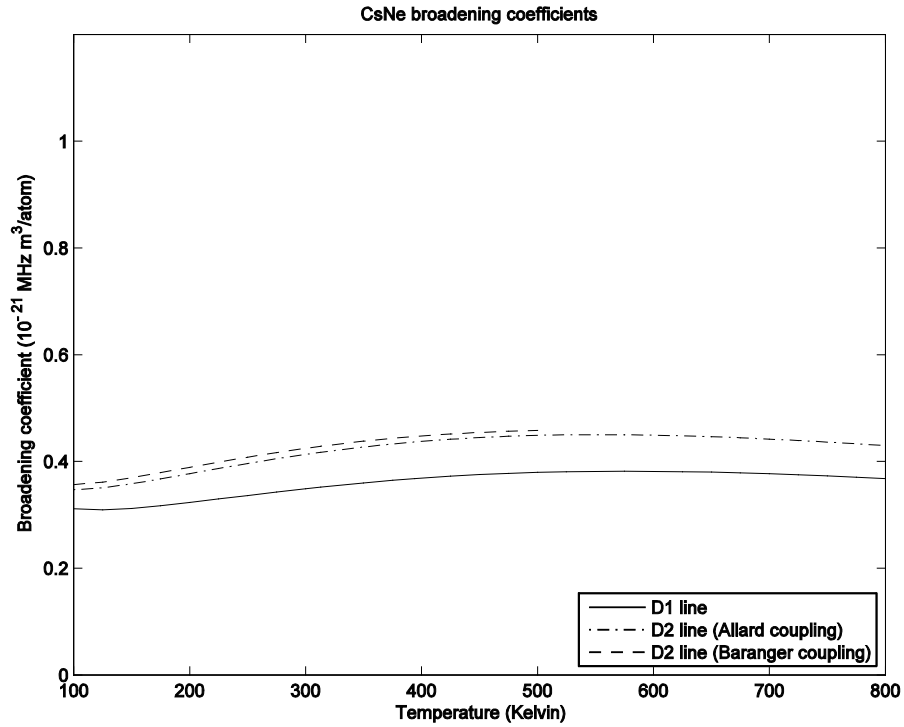
Fig. 3.9e: Broadening rates vs. temperature for Cs + Ar.
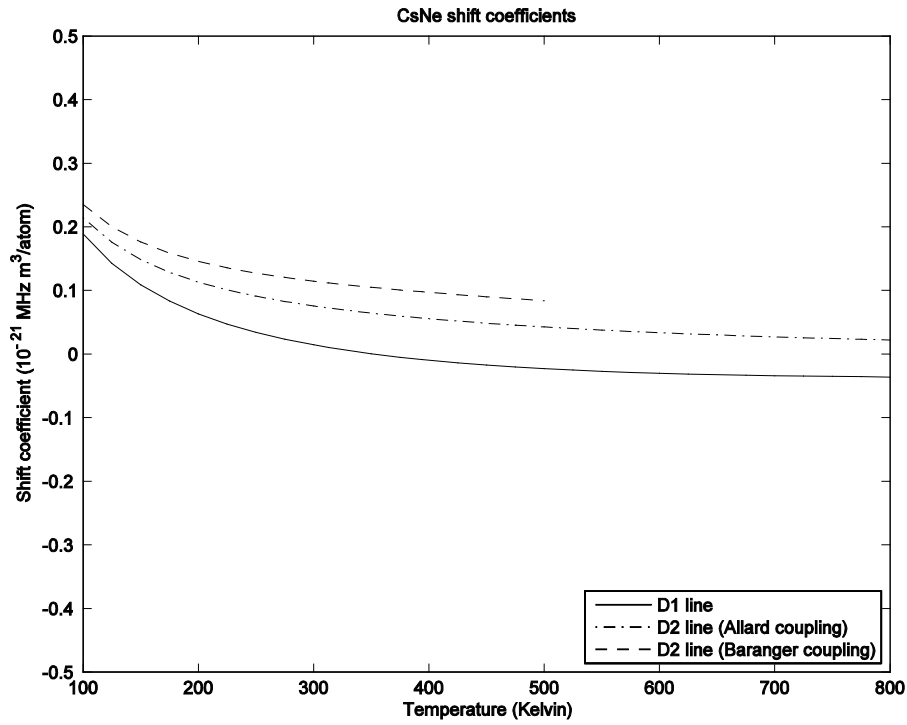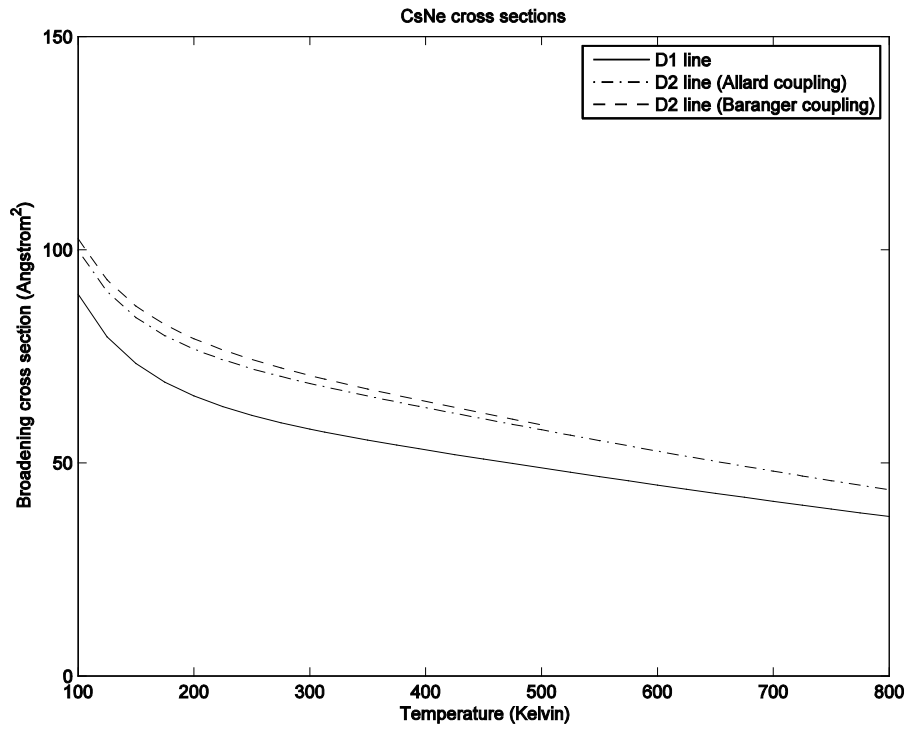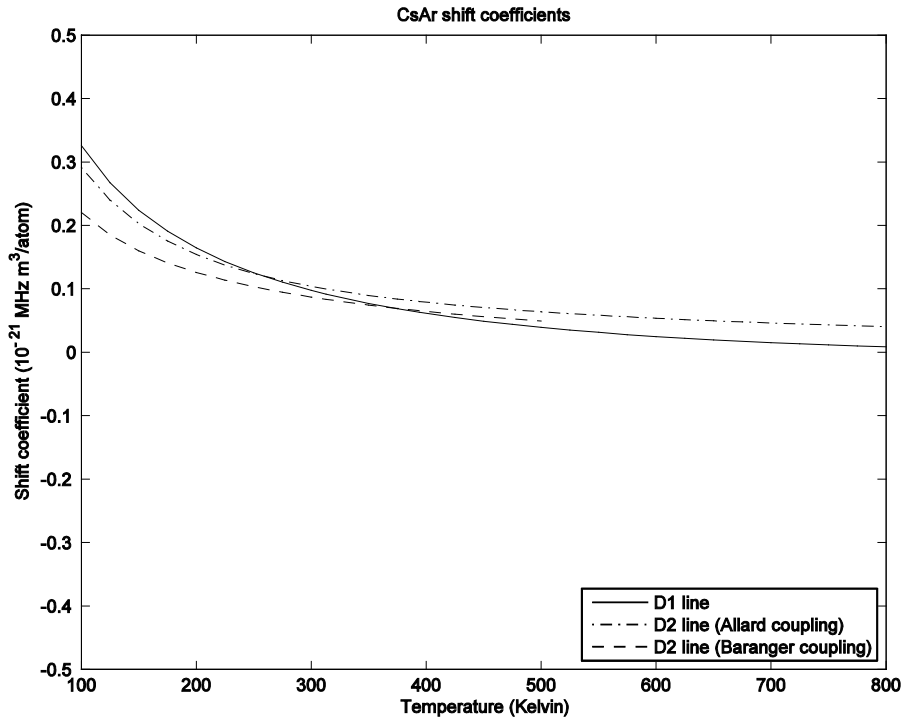

Fig. 3.9f: Shift rates vs. temperature for Cs + Ar.
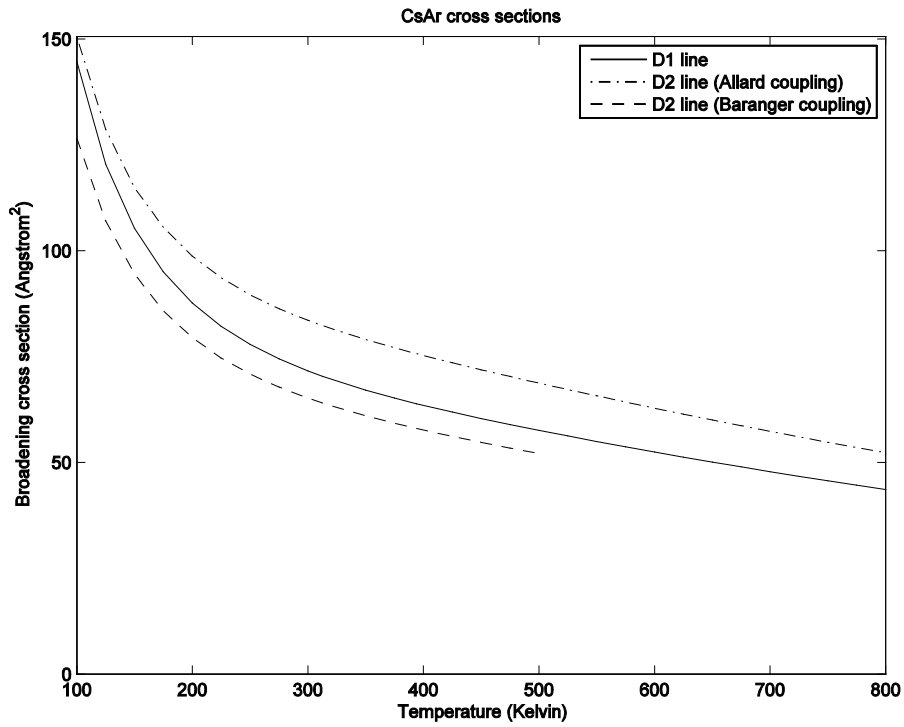
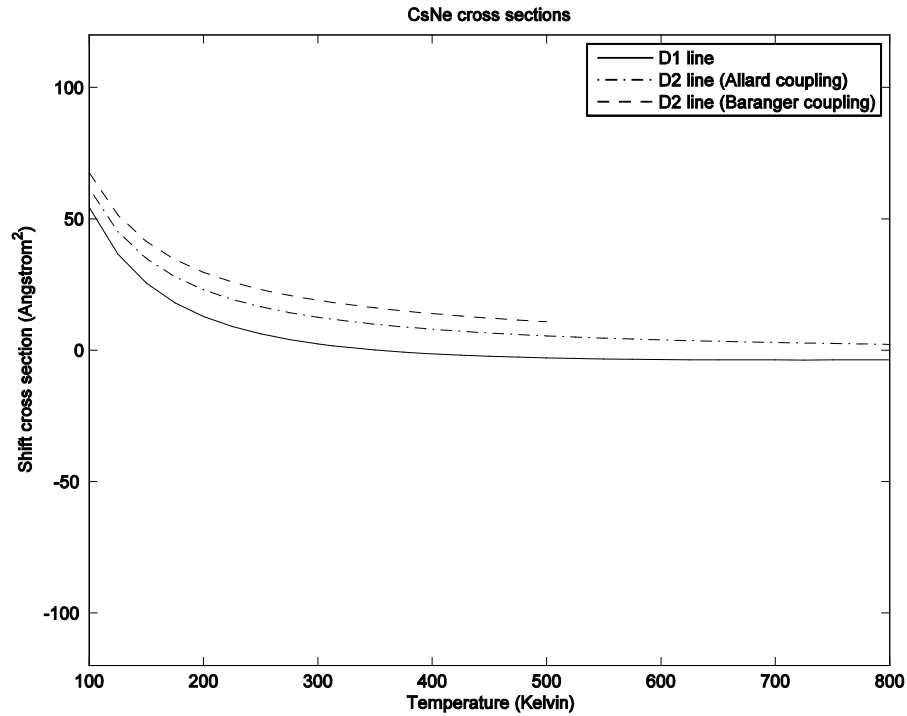Fig. 3.9g: Broadening cross sections vs. temperature for Cs + Ar.
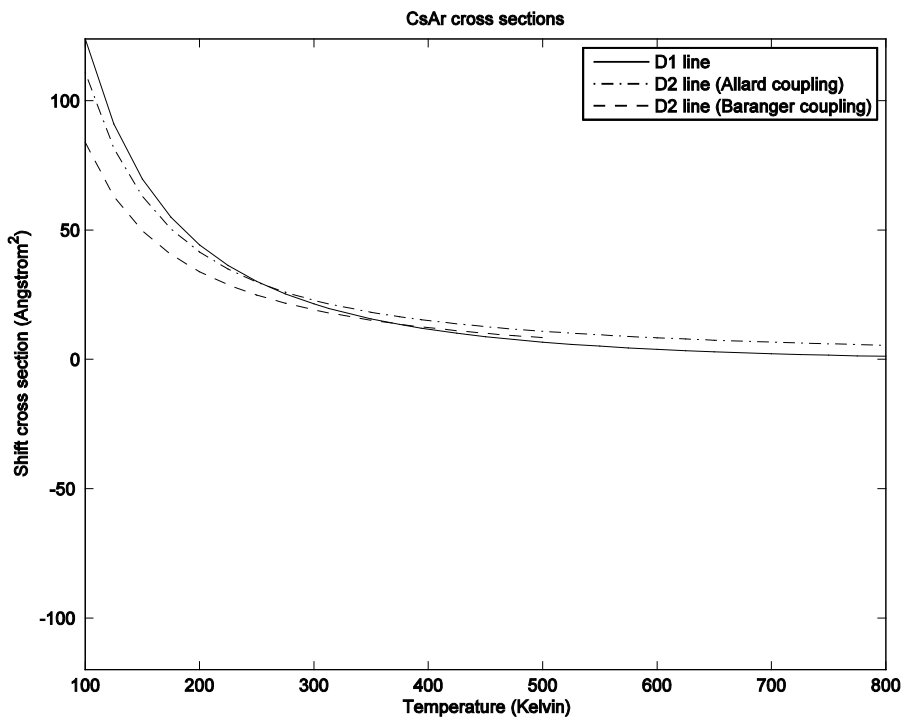
Fig. 3.9h: Shift cross sections vs. temperature for Cs + Ar.

136

3.10   Discussion

3.10.1 Boltzmann distribution of energies versus thermal average energy

In section 2.5, we discussed one of the limitations of the Anderson-Talman model, the assumption that all collisions would have the same relative speed, corresponding to the thermal average kinetic energy for the temperature being considered. In order to provide a point of comparison with the Anderson-Talman model, we have calculated the broadening and shift coefficients by equations (2.136a-b), which replace the Boltzmann distribution with the thermal average energy. The results for the Baranger model using the thermal average energy do not closely match the Anderson-Talman model for any of the lines for the M + Ng pairs considered. This would seem to represent a fundamental dependence of the Anderson-Talman model on using the thermal average speed in a way that is not exhibited by the Baranger model. In particular, using the thermal average energy tends to result in an underestimate of the broadening rate because such a calculation requires one to take a constant-energy slice (or cross-section) of the phase shift differences.

3.10.2 Sources of error

There are several potential sources of error in this research. Since this is a piece of a larger whole of research, it is dependent on the work that has come before. The Baranger model represents the foundation for this research and its construction from first principles. The inputs into the model are the scattering matrix elements, which are generated from the potential energy surfaces; any error in the *ab initio* potentials is reflected in the final results. It is possible that the implementation of the model is flawed in some way, but the work of Lewis on calculating scattering cross-sections (Lewis, 2011) indicates a solid footing on the generation of scattering matrix elements and the expression of the Hamiltonian for the system.

Because there is numerical noise in the scattering matrix elements at low energies (see Fig. 2.4d) associated with the division of the Fourier transform of the correlation function by the initial Moller states (see equation (2.122)), where both quantities are small at low energies, we might expect there to be some noise in the phase shifts and in the scattering phase shift differences as well. In some cases, especially in the uncoupled (diagonal Hamiltonian) cases, the noise is relatively minor.
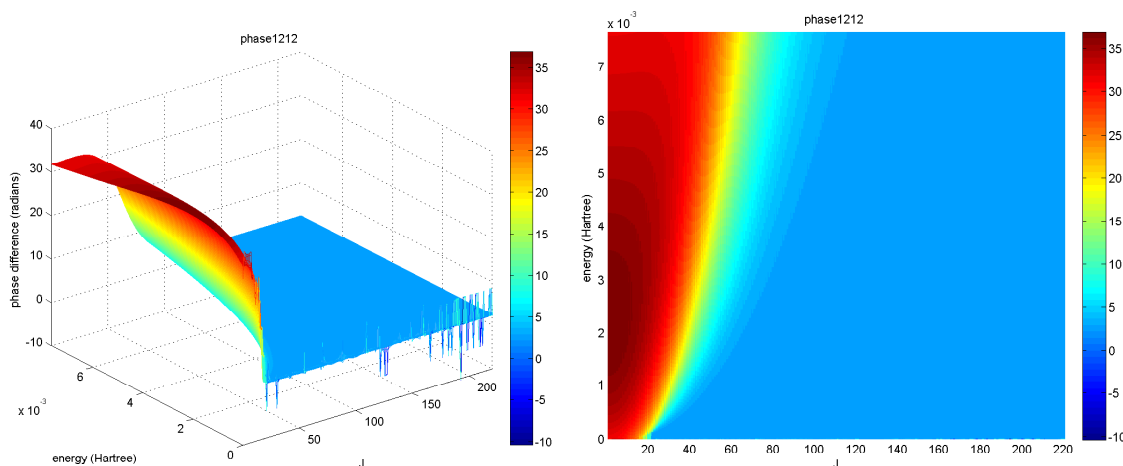
Fig. 3.10.2a: Scattering phase shift difference for the $A^2\Pi_{1/2}$ state of the uncoupled case of Rb + He, side view (left) and top-down view (right). The random spikes along the low energy edge are caused by noise in the scattering matrix elements at low energies. The spikes become more common at higher values of J, which reflects greater influence of the centrifugal effective potential on the reactant Moller states at high J.

In other cases, however, the noise is significant and must be filtered in order to get a reasonable result from the signal. For example, since the intermediate Moller states are generated by propagating a Gaussian wavepacket to the same time before the collision, we expect that the more massive M + Ng pairs do not propagate as far apart during this process, and thus it is more likely that the intermediate Moller states for those more massive pairs will overlap with the centrifugal effective potential in a significant way (see Fig. 2.4a).
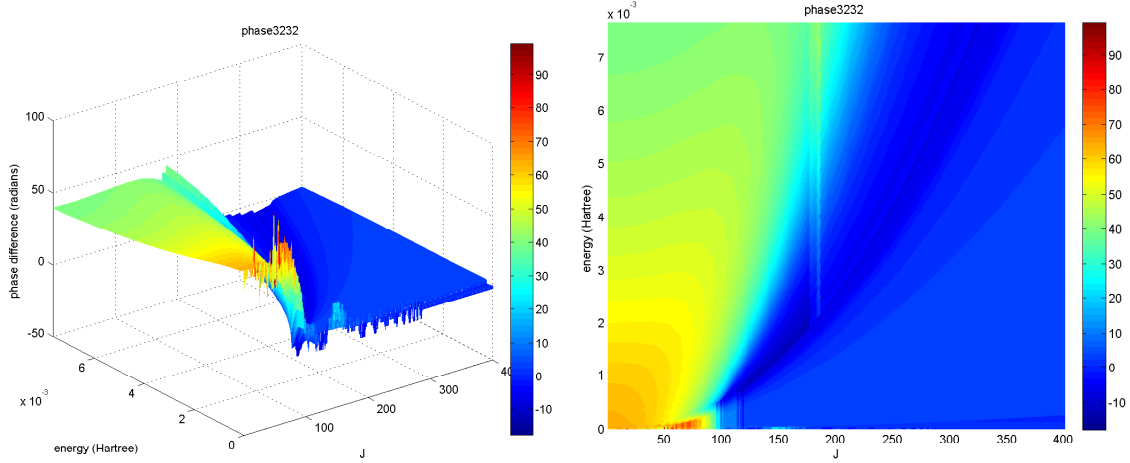
Fig. 3.10.2b: Scattering phase shift difference for the $A^2\Pi_{3/_2}$ state of the uncoupled case of Rb + Ar, side view (left) and top-down view (right). A significant "shelf" appears at the low-energy edge of the plot because of overlap between the intermediate Moller states and the centrifugal effective potential.

We have three significant sources of error in our scattering phase shift differences, which will be shown in Fig. 3.10.2c. First, we are limited at low energies by the calculation of the scattering matrix elements in (2.122):

$$S = \frac{(2\pi)^{-1}[|k'||k|]^{1/2}}{\eta_-^*\eta_+} \int_{-\infty}^{\infty} dt \, \exp(\frac{iHt}{\hbar})C(t)$$
(2.122)

As the energy approaches zero, so do both the numerator and denominator in (2.122), resulting in significant noise as the value of the fraction bounces back and forth. This gives rise to the "shelf" in Fig. 3.10.2b and the low-energy part of Fig. 3.10.2c.

Rb + Ar |3/2, 3/2> phase difference (J = 400.5) (unfiltered)
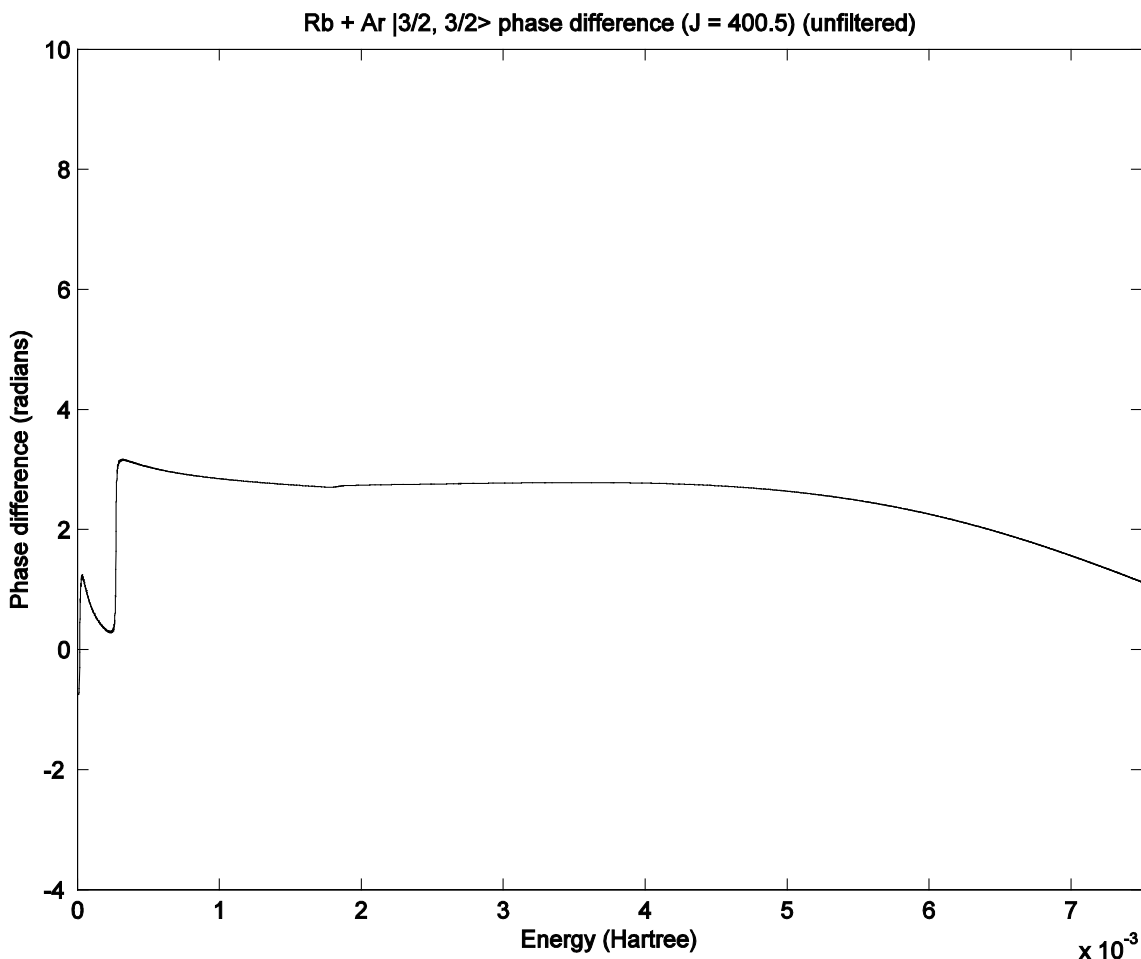
Fig. 3.10.2c: Scattering phase shift difference for the $A^2\Pi_{3/2}$ state, at $J = 400.5$, in the coupled case of Rb + Ar, before filtering. The "shelf" that appears at the low-energy edge of Fig. 3.10.2b can be seen at the left end of this plot and is caused by "divide by zero error". An overall phase difference offset is a computational artifact created by the choice of a nonzero phase at $J = 0.5$, $E = 0$ and represents the separation of the medium-energy portion of this plot from zero phase difference. A third source of error (at higher energies) is caused by Moller state limitations.

A second source of error occurs from a computational choice of overall phase offset. Recall, from (2.115), that we have defined the scattering operator in terms of reactant and product states:

$$|\Psi_{out}\rangle = \hat{S}\,|\Psi_{in}\rangle \tag{2.115}$$

140

Our only rigorous requirements are that $\hat{S}$ be unitary (that is, $\hat{S}^{-1} = \hat{S}^{\dagger}$) and time-independent and contain all of the information about the interaction potential (Tannor and Weeks, 1992; Weeks and Tannor, 1993). We can therefore phase $\hat{S}$ by an arbitrary overall phase without loss of generality:

$$\hat{S}' = \hat{S}e^{i\phi} \tag{3.1}$$

which also satisfies (2.115). Physically, there is no reason to expect a nonzero phase offset. However, our phase-counting algorithm does not restrict the initial phase, so we must account for this phase offset at the end of the calculation of the phase differences. Essentially, the ability to offset the overall phase in (3.1) requires a boundary condition that the overall phase offset be returned to zero.

Our third source of error is significant only in the heavier M + Ng pairs, and stems from limitations in the Moller states. In order to propagate a system with a heavier reduced mass, our wavepacket requires a larger momentum. For the heavier masses, the wavepacket takes up the full grid in momentum space; any excess overlaps to the opposite side of the grid. This effect is relatively minor at all but the highest energies and the heaviest M + Ng pairs, as we see in Fig. 3.10.2d for Rb + Ng, and it is the best balance we can reach with the propagation grid we have selected.

Another potential source of error is that the generation of the reactant Moller states does not include the off-diagonal Coriolis terms for the Hamiltonian in (2.132), but include only the diagonal terms (that is, the centrifugal effective potential). In a manner similar to Fig. 2.4a, we show the reactant Moller states (at $t = 0$) and both the diagonal and off-diagonal Coriolis terms plotted in Figs. 3.10.2e-g. As we can see from these plots, however, the off-diagonal Coriolis terms do not contribute significantly to the Hamiltonian at separations as far as where we start the propagation (100 Bohr), and thus ignoring the off-diagonal Coriolis terms should not introduce a significant source of error.
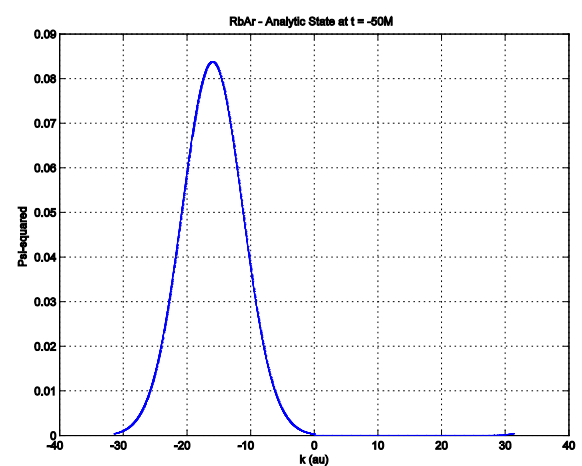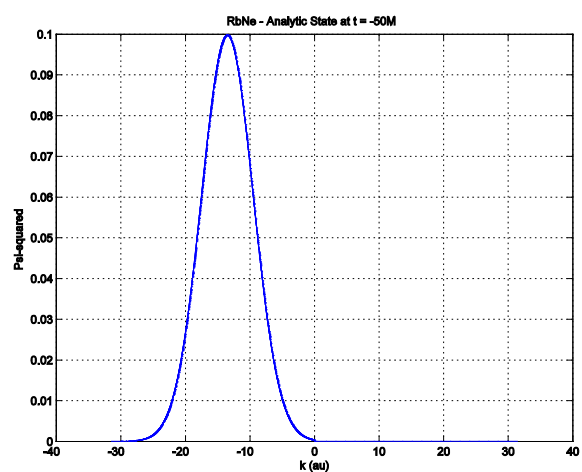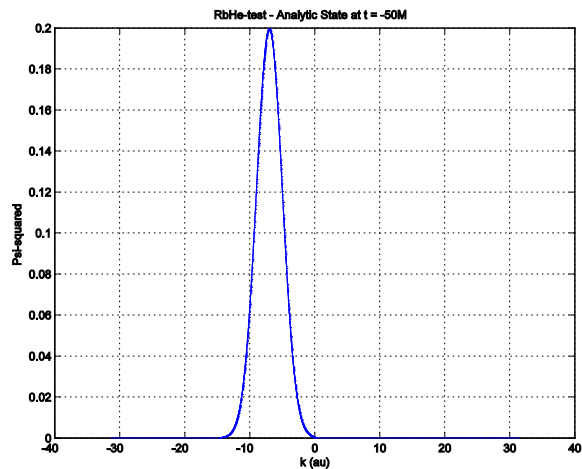
Fig. 3.10.2d: Intermediate Moller state in the momentum representation, for Rb + He (top), Rb + Ne (middle), and Rb + Ar (bottom). There is some leakage of the wavepacket into right-hand side of the grid for Rb + Ar that is a small source of error at high energy.
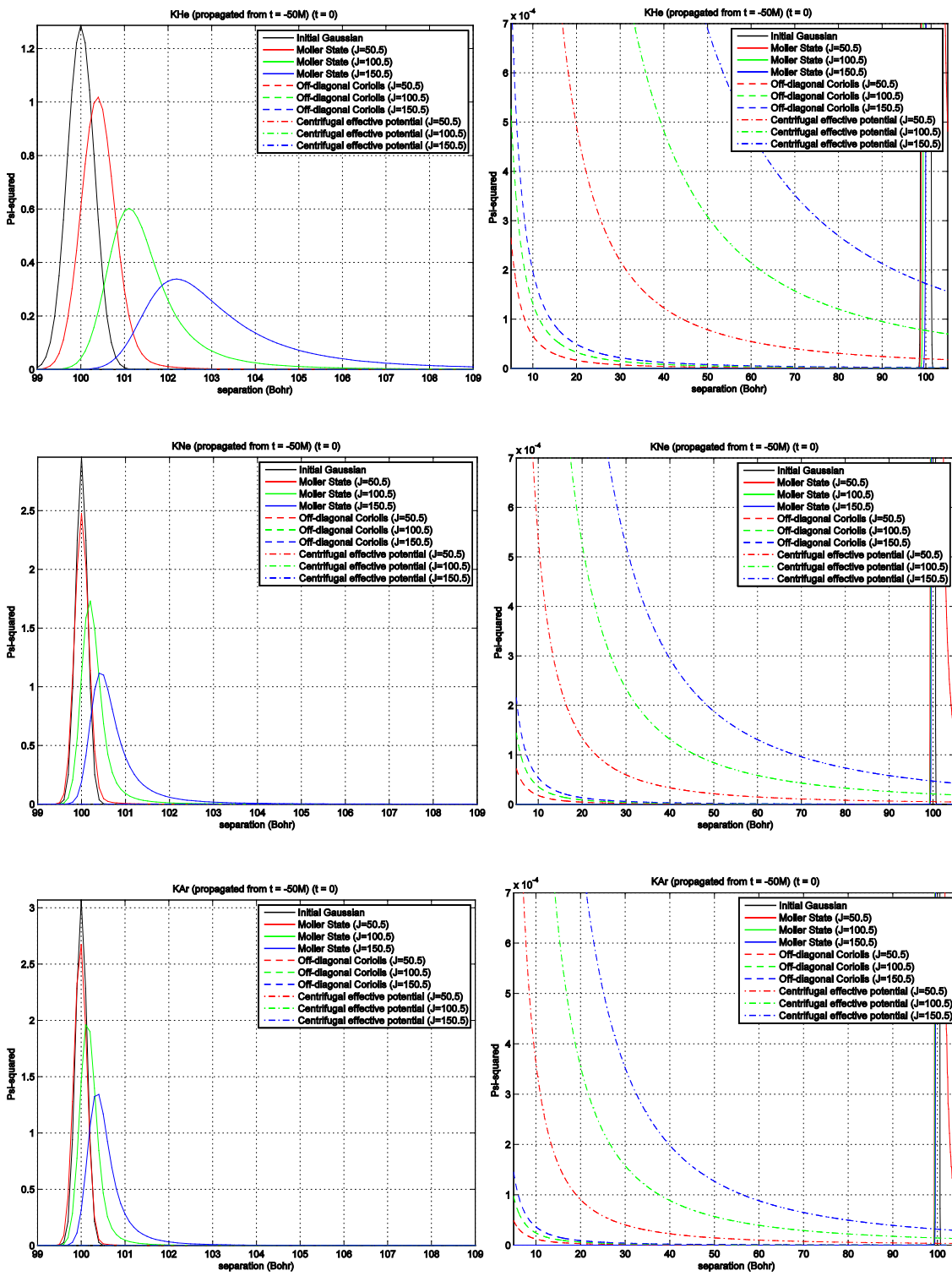
Fig. 3.10.2e: Reactant Moller states (left) and an expanded view of the reactant Moller states and Coriolis terms plotted (right) for K + He (top), K + Ne (middle), and K + Ar (bottom).

143
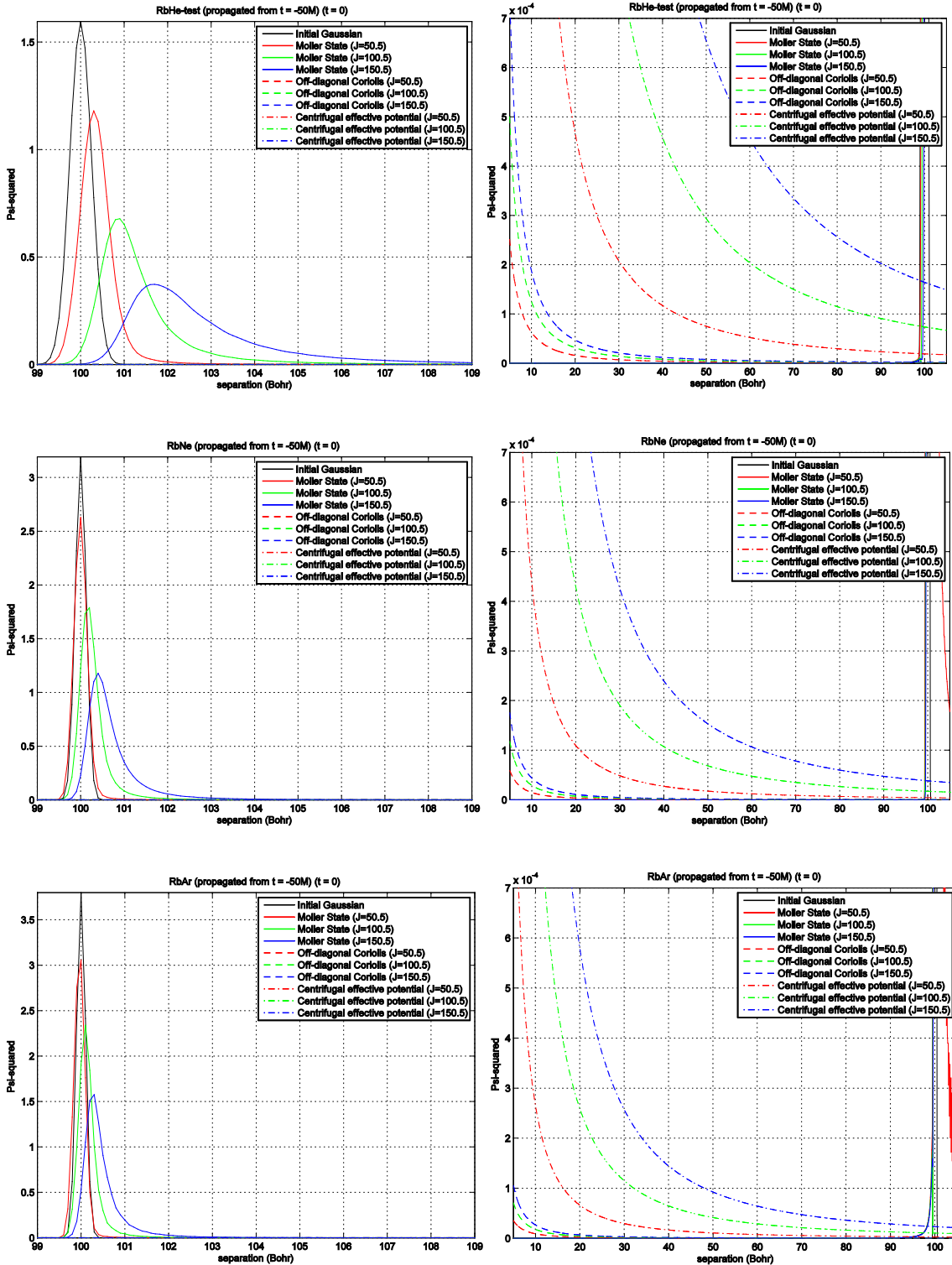
Fig. 3.10.2f: Reactant Moller states (left) and an expanded view of the reactant Moller states and Coriolis terms plotted (right) for Rb + He (top), Rb + Ne (middle), and Rb + Ar (bottom).
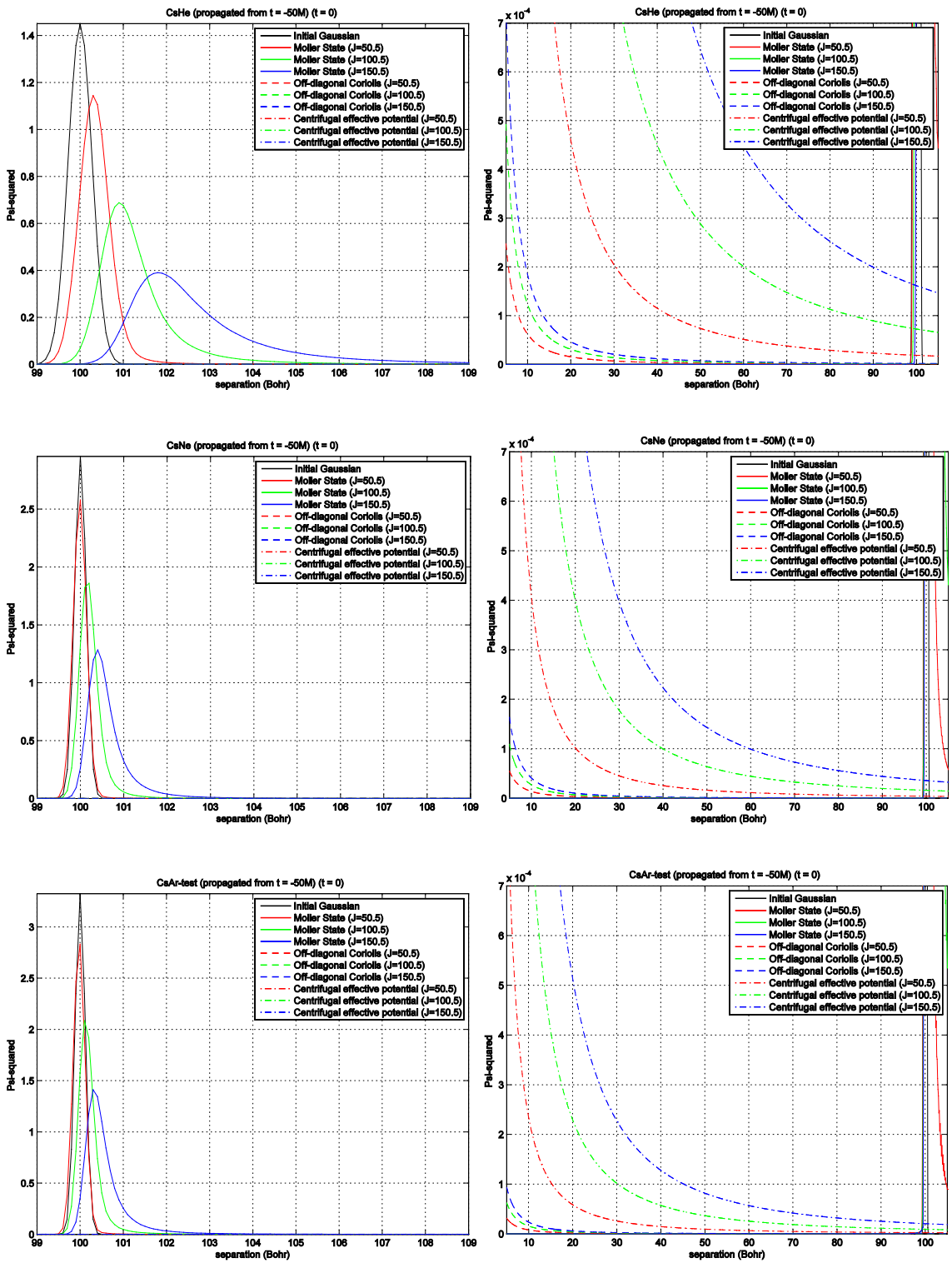
Fig. 3.10.2g: Reactant Moller states (left) and an expanded view of the reactant Moller states and Coriolis terms plotted (right) for Cs + He (top), Cs + Ne (middle), and Cs + Ar (bottom).

We filter out the errors in the phase differences by zeroing out the scattering phase shift difference (plotted in Figs. 3.10.2a-b) in the region in question. We define a shallow J^2 function by defining the J^2 function at $J = J_{max}$, just high enough to get as much of the "shelf" (see Fig. 3.10.2b) as possible with as little impact as possible on the collision process. Below the J^2 function we define the scattering phase shift difference to be zero; since we expect no difference in phase shift to occur in this region, such a process has no effect on the physics of the collision process. Next, we subtract the remainder of the phase difference *versus* energy data at J_{max} from the data for all other J. This has the dual effect of resetting the overall phase offset to zero and removing the Moller state limitation errors, thus removing our second and third sources of error in the phase differences. All of the results in this dissertation apply these two filtering features as well as a J-to-J smoothing that adds or subtracts multiples of 2π from the scattering phase shift difference as necessary to bring each J within 2π of the previous J. Multiples of 2π have no effect on the subsequent calculations, since they are based on the *sine* or *cosine* of the scattering phase shift difference.

The shift coefficients are extremely sensitive to the initial Moller reactant states. This sensitivity is caused by the sine term in (2.110b); for small phase shift differences, $\sin \theta_J(E) \approx \theta_J(E)$ but $\cos \theta_J(E) \approx 1$, so small but nonzero phase shift differences cause the integrand in (2.110a) to vanish but the integrand (2.110b) to remain nonzero. This nonvanishing term then multiplies the Boltzmann distribution and causes a J-independent ridge. Such a ridge appears for any nonzero offset phase as well, but a small but nonzero phase shift difference appears if the Moller reactant state generation has not propagated far enough into the distant past to escape the centrifugal effective potential (see Fig. 2.4a for details). Fig. 3.10.2a shows the sensitivity of the sine term to small phase shifts resulting from inadequate Moller reactant states.
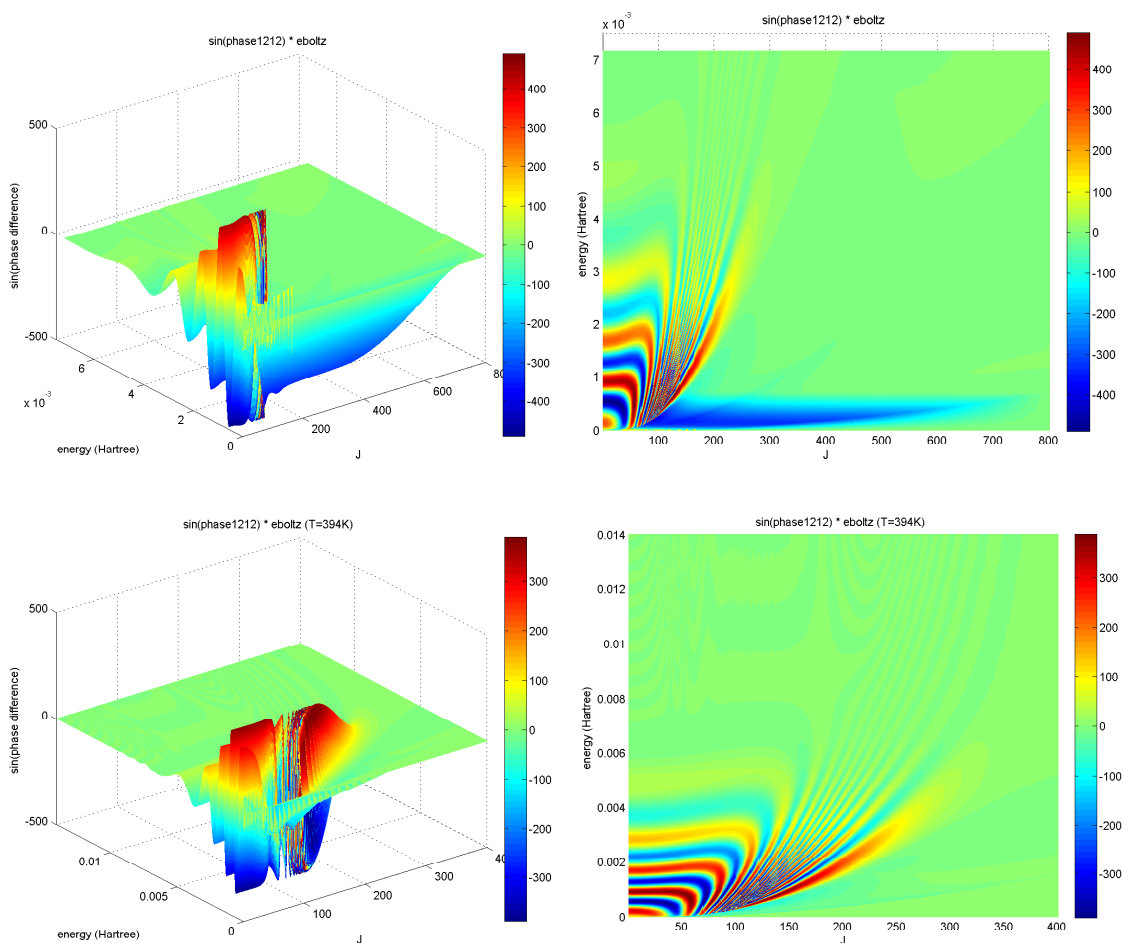
Fig. 3.10.2h: $\sin\theta_J(E) \times$ Boltzmann distribution for the $A^2\Pi_{1/2}$ state of the uncoupled case of Cs + Ar, at T = 394 K, side view (left) and top-down view (right). An early attempt (top) at generating the Moller states proved not to propagate far enough into the distant past. The latest run (bottom) propagates twice as far. Note that there are differences in scale between the runs. The feature appearing across the low-energy edge of the early run (top) is caused by the Moller state issue. Moller states in both data sets satisfied all the needs of the work of Lewis (Lewis, 2011), but give wholly inadequate scattering phase shift differences.

To calculate the phase shift differences in Fig. 2.5d, phase shifts for the excited and ground states were extended linearly from the energy limits of our calculations (E = 0.0075 Hartree) to a larger energy (E = 0.012 Hartree) in order to accommodate calculations at higher temperatures. As we see from Figs. 2.5f and 2.5h, incorporating higher energy collisions to go to higher temperatures also requires us to include higher

values of J. For example, the entire collision phase space in Fig. 2.5h at T = 100 K (top of Fig. 2.5h) can be handled with maximum energy of 0.002 Hartree and maximum J = 65.5. Increasing the temperature to T = 394 K (middle of Fig. 2.5h) requires us to consider energies up to 0.007 Hartree and a maximum J = 110.5 to catch the entire collision phase space. Increasing the temperature to T = 800 K (bottom of Fig. 2.5h) requires a maximum E = 0.012 Hartree and J = 130.5 to capture the entire collision phase space. In other words, calculating at higher temperatures requires larger energies and larger values of J. We can extend phase shifts linearly in energy, but we cannot extend in J without losing critical information about that part of the collision phase space. Calculations at significantly higher temperatures will require calculations at higher values of J to capture the full collision process. Such work will be necessary to perform broadening and shift calculations at higher temperatures than about 800 K.

3.10.3 Allard coupling versus Baranger coupling

As discussed in the introduction to Chapter III, we have calculated the D_2 line broadening and shift coefficients using the Allard and Baranger couplings under different conditions. The Allard-coupled equations (2.143a-b) are assumed in most cases to use the phase shifts $\theta_{fi}^J(E)$ computed from the uncoupled scattering matrix elements. This allows us to perform the calculations much more quickly because the entire set of uncoupled scattering matrix elements can be calculated in a single run, whereas the coupled scattering matrix elements require three runs (one run per input state). The Allard-coupled equations also assume a 50/50 weighting of the two states on the $^2P_{3/2}$ manifold (that is, the $A^2\Pi_{3/2}$ and $B^2\Sigma_{1/2}$ states), as shown by the factor of ½ in front of each *cos* term in (2.143a) and each *sin* term in (2.143b). The Baranger coupling requires the coupled scattering matrix elements to be calculated because of the Q_{fi}^J in (2.144a-b), and the phase shifts $\theta_{fi}^J(E)$ that appear in (2.144a-b) are those from the fully coupled scattering matrix elements. The Baranger-coupled equations do not assume a 50/50 weighting but are weighted according to the reflection probability amplitudes (that is, the

probability of the system exiting the collision on the same potential energy surface on which it entered the collision). The Allard coupling seems to give a good approximation in many cases to the full coupling of Baranger, at a significant increase in computational efficiency. The Allard coupling does not track the Baranger coupling perfectly, especially in some cases at lower temperatures, because the two coupling schemes use different phase difference data. The Allard coupling scheme uses the uncoupled phase differences while the Baranger coupling scheme uses the fully coupled (3x3 Hamiltonian) phase differences, so even if the weighting were the same we could not necessarily expect the same broadening and shift coefficients because we are integrating over different phase differences, as we can see in Figs. 3.10.3a-b.

One further reason to consider the Allard coupling is its ability to make predictions at higher temperatures than the Baranger coupling. As we see in Fig. 3.10.3c, the Boltzmann distribution requires us to integrate over higher energies if we wish to calculate broadening and shift coefficients at higher temperatures without error because the maximum energy used in our integration process is the energy at which we truncate the Boltzmann distribution. The Allard coupling requires only phase differences at higher temperatures, and we can extrapolate the phase shifts to higher energies than we have rigorously calculated as outlined in section 2.5. The Baranger coupling requires that we have rigorously calculated all of the scattering matrix elements for all energies concerned because we need the scattering matrix elements (and not just the phases) to calculate the weighting coefficients in equations (2.144a-b), so we are limited in the Baranger coupling to a maximum energy of $E_{max} = 0.0075$ Hartree. When we calculate broadening and shift coefficients, we truncate the Boltzmann distribution at the maximum energy considered, so we introduce an error, as shown in Fig. 3.10.3d. For example, we introduce a 2% truncation error at $T = 500$ K, but this error grows to 12% if we attempt to calculate at $T = 800$ K. These truncation errors represent potential bounds of error but tend to overestimate the error because the phase shift differences oscillate. We have limited our calculations to $T = 500$ K for the Baranger-coupled D_2 line and $T = 800$ K for the Allard-coupled D_2 line because these limits show approximately the same level of truncation error (Fig. 3.10.3d).
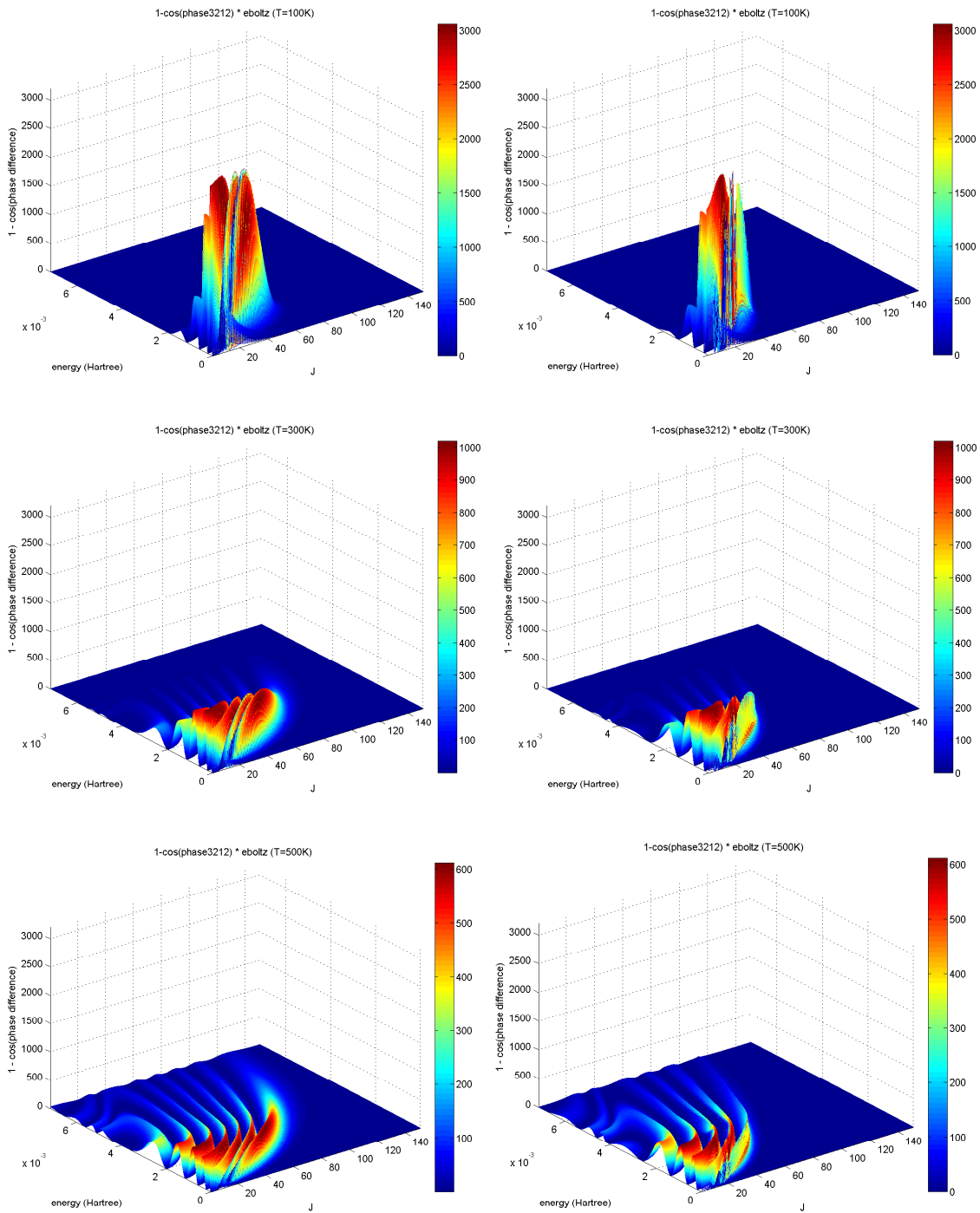
Fig. 3.10.3a: $[1 - \cos\theta_J(E)] \times$ Boltzmann distribution for the $\left|{}^{3}\!/_{2}, {}^{1}\!/_{2}\right\rangle$ state of the uncoupled case (left) and the fully-coupled 3x3 case (right) of Cs + He at T = 100 K (top), 300 K (middle), and 500 K (bottom).
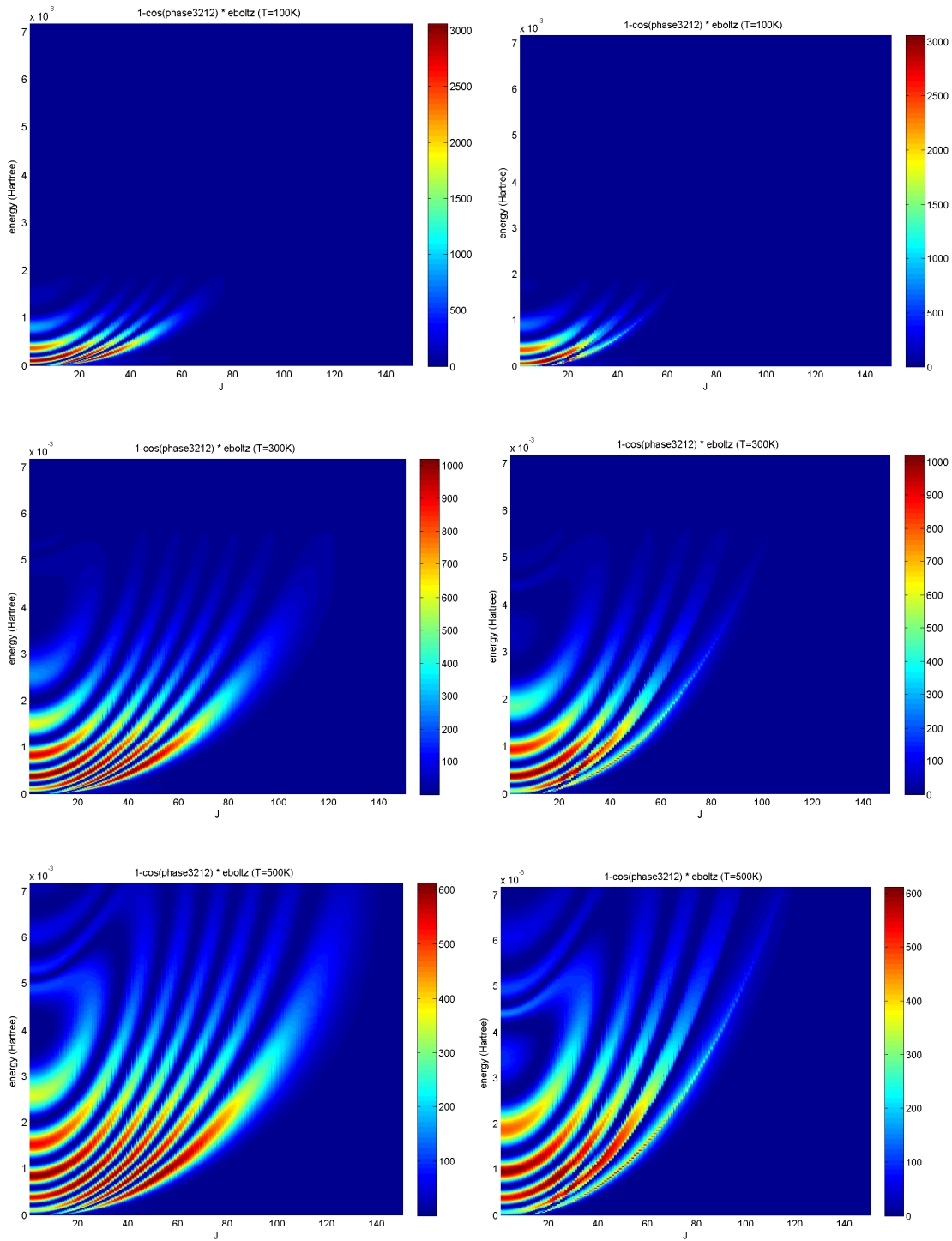
Fig. 3.10.3b: $\left[1 - \cos\theta_J(E)\right] \times$ Boltzmann distribution for the $\left|\frac{3}{2}, \frac{1}{2}\right\rangle$ state of the uncoupled case (left) and the fully-coupled 3x3 case (right) of Cs + He at T = 100 K (top), 300 K (middle), and 500 K (bottom), top-down view.

151
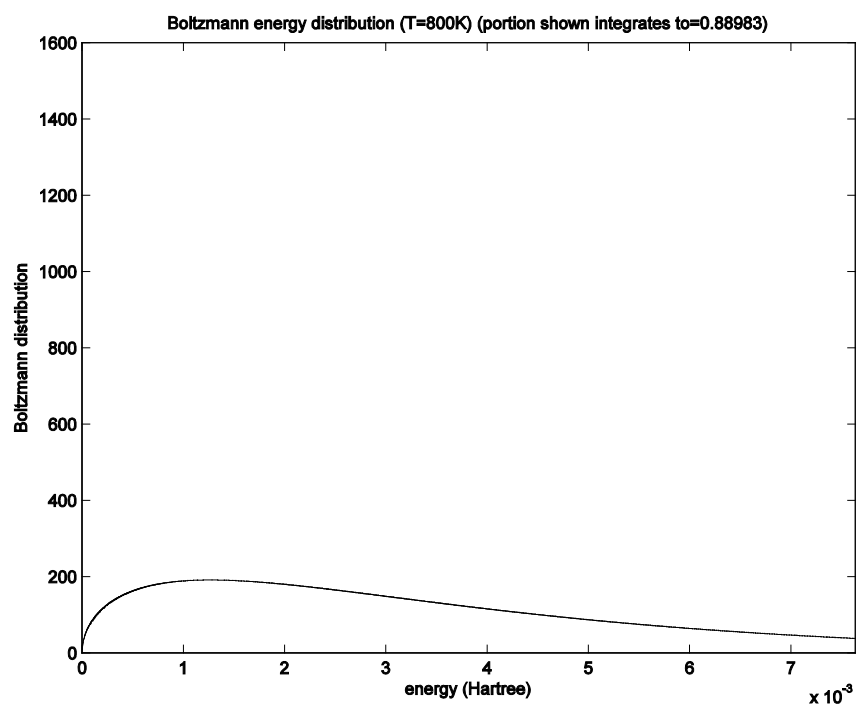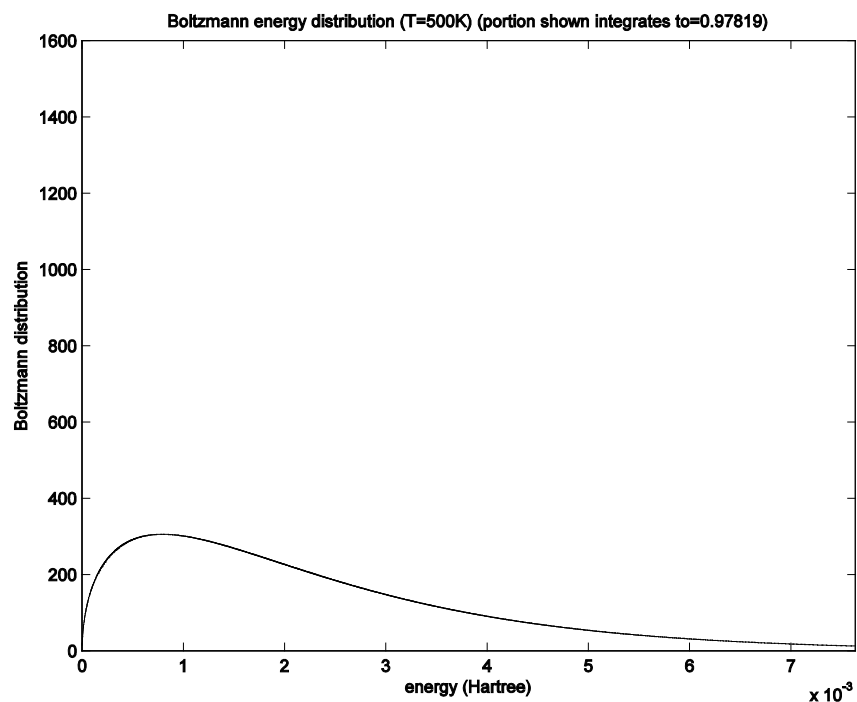
Fig. 3.10.3c: Boltzmann distribution at T = 500 K (top) and T = 800 K (bottom), for energies from E = 0 to E = 0.0075 Hartree. Note that at higher temperatures we truncate more of the total distribution if we stop integrating at E = 0.0075 Hartree.
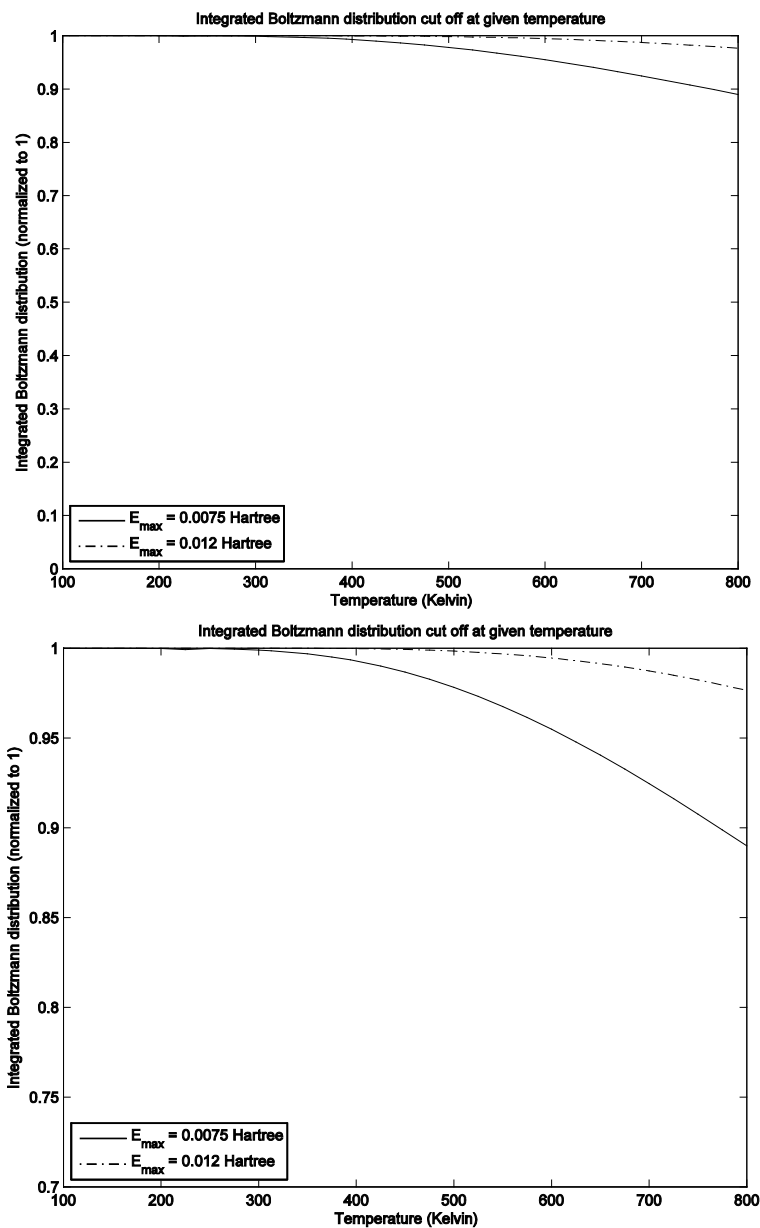
Fig. 3.10.3d: Integrated Boltzmann distribution cut off versus temperature. The top and bottom graphs are the same data, except for the vertical scale, from 0 to 1 (top) and from 0.7 to 1.0 to provide a clearer view of both lines (bottom). At each temperature, the Boltzmann distribution (normalized to 1) has been integrated from $E = 0$ only to $E_{max} = 0.0075$ Hartree (solid line) or $E_{max} = 0.012$ Hartree (dashed-dotted line). The value on the vertical axis is the portion of the Boltzmann distribution retained out to those maximum energies. We have rigorously calculated data out to $E = 0.0075$ Hartree, so the solid line represents our confidence that we have not truncated crucial parts of the collision. For $E_{max} = 0.012$ Hartree, we introduce only about a 2% truncation error at $T = 800K$, but we reach this level of truncation error at only $T = 500$ K for $E_{max} = 0.0075$ Hartree.

IV. Conclusions

This dissertation began with an overview of collisional line broadening, from quantum physics and spectroscopy to the Anderson-Talman model and the Baranger model which are the standards for this field. We then outlined the dissertation research methodology to include a detailed description of the simulation process. The primary programming language used in writing computer simulations for this research is Fortran 90, with some Fortran 77 legacy code used where appropriate, compiled and executed on AFIT's Linux Cluster and on supercomputers run by the DoD High Performance Computing Modernization Program, for the sake of computational efficiency. Preparation of initial wavepackets and analysis of the output data were achieved using Matlab code.

This research exhibits several new features which set it apart from the current state of the field. First, the full *ab initio* potential energy surfaces are used; these potential energy surfaces have been calculated through many-body calculations by Blank (Blank, Weeks, and Kedziora, 2012). Second, collisions are treated quantum-mechanically and adiabatically and include spin-orbit and Coriolis coupling. Third, calculations are made with no approximations beyond those of the impact limit aside from the limits imposed by the Boltzmann (thermal) distribution of energies.

4.1   Summary of Results

The primary goal of this research has been to compare the results of different models for calculating the broadening and shift coefficients. We use the experimental results as a guide for interpreting results, but comparison with experiment is not the primary goal. Here, most of our comparisons are between the Baranger model (in some cases, analyzing both the Allard and Baranger coupling schemes) and the Anderson-

Talman model as calculated by Blank, who uses the same *ab initio* potential energy surfaces. Allard and Kielkopf have identified such a comparison as a necessary step in the theoretical process; they claim to await "new experimental results, improved potentials, and a comparison of quantal and semiclassical line shapes from the same potentials" (Allard, et al, 2007).

We can take a closer look at the shift coefficients calculated in this model. At a glance, we would expect a difference potential well to give rise to a redshift (that is, a negative shift coefficient) and a difference potential barrier to give rise to a blueshift (that is, a positive shift coefficient). In all cases, our $A^2\Pi_{1/2} - X^2\Sigma_{1/2}$ difference potentials are wells (with small barriers around 10-12 Bohr that are slightly larger for heavier alkali), our $A^2\Pi_{3/2} - X^2\Sigma_{1/2}$ difference potentials are wells, and our $B^2\Sigma_{1/2} - X^2\Sigma_{1/2}$ difference potentials are barriers. Tables 4.1a-b show the results for experiment and each method of calculation, in terms of whether each spectral line is redshifted or blueshifted.

In most cases, the Baranger model predicts a D1 line shift direction that corresponds to the well in the $A^2\Pi_{1/2} - X^2\Sigma_{1/2}$ difference potential. Exceptions occur in Cs + Ng, where the small barrier is more pronounced in the difference potential. The D1 line shift direction corresponds with measured data in only five of the nine cases: K + Ne, Ar, Rb + Ne, Ar, and Cs + He. For the others, the Baranger model predicts the opposite shift direction. Similar trends appear in the D2 line shift predictions.

Table 4.1a: Shift direction for experiment and each model for the D1 line at temperatures at which data are measured. Red text indicates redshift (negative coefficient) and blue text indicates blueshift (positive coefficient). The color of the "Well" or "Barrier" text indicates the direction of shift we expect given the difference potential.

D1 line	He	Ne	Ar
K	Well (slight barrier at 12.5 Bohr) (experiment D1) (Mullamphy D1) Anderson-Talman Baranger model	Well (slight barrier at 12.0 Bohr) (experiment D1) Anderson-Talman Baranger model	Well (slight barrier at 12.5 Bohr) (experiment D1) Anderson-Talman Baranger model
Rb	Well (small barrier at 11.5 Bohr) (experiment D1) Anderson-Talman Baranger model	Well (small barrier at 11.0 Bohr) (experiment D1) Anderson-Talman Baranger model	Well (small barrier at 11.8 Bohr) (experiment D1) Anderson-Talman Baranger model
Cs	Well (moderate barrier at 11.2 Bohr) (experiment D1) Anderson-Talman Baranger model	Well (moderate barrier at 10.7 Bohr) (experiment D1) Anderson-Talman Baranger model	Well (moderate barrier at 11.4 Bohr) (experiment D1) Anderson-Talman Baranger model

Table 4.1b: Shift direction for experiment and each model for the D2 line at temperatures at which data are measured. Red text indicates redshift (negative coefficient) and blue text indicates blueshift (positive coefficient). The color of the "Well" or "Barrier" text indicates the direction of shift we expect given the difference potential. In all cases, the $A^2\Pi_{3/2} - X^2\Sigma_{1/2}$ difference potential is a well and the $B^2\Sigma_{1/2} - X^2\Sigma_{1/2}$ a barrier.

D2 line	He	Ne	Ar
K	(experiment D2) (Mullamphy D2) Anderson-Talman Allard coupling Baranger coupling	(experiment D2) Anderson-Talman Allard coupling Baranger coupling	(experiment D2) Anderson-Talman Allard coupling Baranger coupling
Rb	(experiment D2) Anderson-Talman Allard coupling Baranger coupling	(experiment D2) Anderson-Talman Allard coupling Baranger coupling	(experiment D2) Anderson-Talman Allard coupling Baranger coupling
Cs	(experiment D2) Anderson-Talman Allard coupling Baranger coupling	(experiment D2) Anderson-Talman Allard coupling Baranger coupling	(experiment D2) Anderson-Talman Allard coupling Baranger coupling

Mullamphy, et al (Mullamphy, et al, 2007; Peach, et al, 2009), seem to be working with *ab initio* difference potentials that are based on Lennard-Jones (6-12) potentials and appear to be longer-ranged (with significant features out to around 20 Bohr) than our *ab initio* potentials for K + He. The Mullamphy group appears to have difference potential wells for all three excited state surfaces but blueshifts for both the D1 and D2 lines. It may be, however, that the collisions are probing far enough inward on Mullamphy's difference potentials to reach the much-larger barriers on all three surfaces (around 18 Bohr for the $B^2\Sigma_{1/2} - X^2\Sigma_{1/2}$ difference potential, around 7 Bohr for the $A^2\Pi_{3/2} - X^2\Sigma_{1/2}$ difference potential, and around 12 Bohr for the $A^2\Pi_{1/2} - X^2\Sigma_{1/2}$ difference potential). This indicates that, for most collision processes under Mullamphy's difference potentials, the D2 line will be dominated by the $B^2\Sigma_{1/2} - X^2\Sigma_{1/2}$ difference potential barrier, and that both the D1 and D2 lines will be blueshifted because of the large barriers and not the smaller wells. In particular, Mullamphy claims, "The shifts are quite sensitive to the precise details of the potentials as they are produced by a balance between the effects of the long-range attractive potential and the short-range repulsive potential. In particular, for a given energy they are sensitive to where the repulsive wall is located" (Mullamphy, et al, 2007). With the exception of the D1 line shift, Mullamphy's predictions, Blank's Anderson-Talman model calculations, and our Baranger model calculations are quite close to each other for K + He. In the case of the D1 line shift, Mullamphy's predictions are closer to the measured data.

In general, our Baranger model calculations provide good predictions of measured broadening rates and fair predictions of measured shift rates. However, we find poor predictions of the broadening and shift rates for M + Ar. Since our Baranger results are close to Blank's Anderson-Talman results for the same *ab initio* potential energy surfaces, we conclude that the error is not model-specific and therefore there are flaws in the corresponding *ab initio* potential energy surfaces.

The Anderson-Talman model uses thermal average velocity of collisions at a given temperature in a way that the Baranger model does not allow. In every case, the use of the thermal average energy gives predictions in the Baranger model that vary

widely from both the Anderson-Talman model and from experiment. Specifically, using the thermal average energy takes a constant-energy slice of the phase *versus* energy *versus* J plots (for example, a constant-energy slice of Figs. 2.5e-f), which then causes the Baranger model to consistently underestimate the broadening rate (section 3.10.1) at any given temperature.

The calculations of scattering phase shifts, scattering phase shift differences, and line broadening and shift are far more sensitive to flaws in the initial reactant Moller states than are calculations of scattering cross-sections (section 3.10.2). Shift calculations are extremely sensitive because of the sensitivity to minute phase shift differences that appears in the sine term in equation (2.110b).

Ultimately, agreement among broadening coefficients is not sufficiently good to identify conclusively which model is "correct" for a given set of *ab initio* potential energy surfaces, at least at the temperatures at which experimental data have been measured. In most cases, the predictions of the Baranger and Anderson-Talman models diverge at low temperatures, so low-temperature experiments may provide a needed discriminator between the models.

4.2   Recommendations for Future Work

There is still a great deal of theoretical work to be done in this area, from the calculation of potential energy surfaces to refinement of our scattering model and the Baranger model. Any error in the *ab initio* potential energy surfaces is reflected in the final results. In particular, we suspect errors in the surfaces for M + Ar because both the Baranger model and the Anderson-Talman model give results that vary significantly from experiment for these pairs. It is not clear to what degree this implementation of the wavepacket propagation technique and the Baranger model are sensitive to differences in the potential energy surfaces. It is a theoretically straightforward, but computationally intensive, process to replace the potential energy surfaces with new inputs. One could use different classes of potential, such as the Lennard-Jones (6-12) potential that was

used in Chapter II as an estimating tool for the Anderson-Talman model. Hager has achieved some success with the Anderson-Talman model using a 6-8 potential (Hager and Perram, in preparation), and such a potential could be tested in the context of the Baranger model. Testing different sorts of potentials with more localized and controllable characteristics might give more information about what parts of the potential energy surfaces give rise to which characteristics in the broadening and shift rates and intermediate calculations such as the scattering phase shift differences or those calculations illustrated in Figs. 2.5e-h.

The results of this work are sensitive to any flaws in the reactant Moller states, so there is always work to be done to refine those states, since the entire computational model depends on these reactant Moller states. In particular, we have discovered that the shift coefficients are extremely sensitive to such flaws. This sensitivity is caused by the sine term in (2.110b); for small phase shift differences, $\sin \theta_J(E) \approx \theta_J(E)$ but $\cos \theta_J(E) \approx 1$, so small but nonzero phase shift differences cause the integrand in (2.110a) to vanish but the integrand (2.110b) to remain nonzero. This nonvanishing term then multiplies the Boltzmann distribution and causes a J-independent ridge. A small but nonzero phase shift difference appears, along with the resulting nonphysical ridge, if the Moller reactant state generation has not propagated far enough into the distant past to escape the centrifugal effective potential (see Fig. 2.4a for details). Fig. 3.10.2c shows the sensitivity of the sine term to small phase shifts resulting from inadequate Moller reactant states. Future work might focus on generating new Moller states, which would require propagating the initial Gaussian even farther into the distant past to generate the intermediate Moller state. Such work would be necessary in order to calculate phase shifts for higher values of J, which would be required in order to calculate broadening and shift coefficients at temperatures higher than 800 K (using the Allard coupling) or 500 K (using the Baranger coupling).

Future work might simply start a Gaussian wavepacket at a very large separation distance, which could ameliorate the problem with generating reactant Moller states; in essence, the Gaussian wavepacket becomes our reactant state for which we can generate

an analytic form. However, the improvement of a single problem is counteracted by the introduction of two additional problems. First, the reactant state has to be propagated through the collision process and back out to where it started; this counteracts any computational savings one might have gleaned from the lack of Moller state propagation. Second, propagating from a larger separation requires a larger computational grid in order to accommodate the space containing the wavepacket and the origin, which in turn requires FFT code capable of accommodating such a large space. This second problem might be lessened by adopting a moving reference frame that is just large enough to accommodate the wavepacket as it spreads, but we have not attempted this and we are unsure to what degree new error might be introduced through the new propagation algorithm.

To calculate the phase shift differences in Fig. 2.5d, phase shifts for the excited and ground states were extended linearly from the energy limits of our calculations (E = 0.0075 Hartree) to a larger energy (E = 0.012 Hartree) in order to accommodate calculations at higher temperatures. Future work might entail rigorous calculations for higher energies, which will also require calculations at higher values of J to capture the full collision process. Such work will be necessary to perform broadening and shift calculations at higher temperatures than about 800 K.

Finally, we see only the distant past (or what we call the "infinite" past) and distant future before and after the collision (Lewis, 2011). Because we can only look at the distant past and future, we are stuck with the impact limit of Baranger, which assumes that the duration of a collision is short compared with the time between collisions. Any work to take us out of the impact limit will necessarily involve being able to view events that occur during a collision, rather than just the distant past and future, and will require a complete reworking of the computational algorithm.

Bibliography

Alioua, K., and Bouledroua, M.. "Classical and quantal studies of the satellite features in the absorption spectra of lithium (2s-2p) perturbed by helium." *Physical Review A*, 74 (2006): 032711.

Alioua, K., Bouledroua, M., Allouche, A. R., and Aubert-Frécon, M.. "Far-wing profile of photoabsorption spectra of Na(3s-3p) atoms perturbed by helium." *Journal of Physics B*, 41 (2008): 175102.

Allard, N. F., Biraud, Y. G., and Chevillot, A.. "Collision-broadened spectral line profiles in the limit of high perturber density." *Physical Review A*, 37, no. 5 (1 March 1988): 1479-87.

Allard, N., and Kielkopf, J.. "The effect of neutral nonresonant collisions on atomic spectral lines." *Reviews of Modern Physics*, 54, no. 4 (October 1982): 1103-82.

Allard, N. F., Kielkopf, J. F., and Allard, F.. "Impact broadening of alkali lines in brown dwarfs." *European Physics Journal D*, 44 (2007): 507-514.

Allard, N. F., Royer, A., Kielkopf, J. F., and Feautrier, N.. "Effect of the variation of electric-dipole moments on the shape of pressure-broadened atomic spectral lines." *Physical Review A*, 60, no. 2 (August 1999): 1021-33.

Allard, N. F., Sahal-Brechot, S., and Biraud, Y. G.. "Unified theory of collisional line profiles: study of the D lines of caesium perturbed by xenon: width, shift, asymmetry and satellites." *Journal of Physics B*, 7, no. 16 (1974): 2158-72.

Allouche, A. R., Alioua, K., Bouledroua, M., and Aubert-Frécon, M.. "Ab initio potential energy curves and transition dipole moments for the interaction of a ground state He with Na(3s-3p)." *Chemical Physics*, 355 (2009): 85-89.

Anderson, P. W.. "Pressure Broadening in the Microwave and Infra-Red Regions." *Physical Review*, 76, no. 5 (1 September 1949): 647-61.

Anderson, P. W.. "A Method of Synthesis of the Statistical and Impact Theories of Pressure Broadening." *Physical Review*, 86 (1952): 809.

Anderson, P. W., and Talman, J. D.. "Pressure broadening of spectral lines at general pressures." *Bell Telephone system technical publications*, 3117 (1956).

Baranger, M. [1958a]. "Simplified Quantum-Mechanical Theory of Pressure Broadening." *Physical Review*, 111, no. 2 (15 July 1958): 481-93.

Baranger, M. [1958b]. "Problem of Overlapping Lines in the Theory of Pressure Broadening." *Physical Review*, 111, no. 2 (15 July 1958): 494-504.

Baranger, M. [1958c]. "General Impact Theory of Pressure Broadening." *Physical Review*, 112, no. 3 (1 November 1958): 855-65.

Baranger, M.. "Spectral Line Broadening in Plasmas," in *Atomic and Molecular Processes*. Ed. D. R. Bates. New York NY: Academic Press, 1962.

Beach, Raymond J., Krupke, William F., Kanz, V. Keith, Payne, Stephen A., Dubinskii, Mark A., and Merkle, Larry D.. "End-pumped continuous-wave alkali vapor lasers: experiment, model, and power scaling." *Journal of the Optical Society of America B,* 21, no. 12 (2004): 2151-2163.

Belcher, Lachlan T.. "Gradients and non-adiabatic derivative coupling terms for spin-orbit wavefunctions." PhD dissertation, Air Force Institute of Technology, 2011.

Belov, V. N. [1981a]. "Application of the magnetic-scanning method to the measurement of the broadening and shift constants of the rubidium D_2 line (780.0 nm) by foreign gases." *Optika I Spektroskopiya,* 51 (July 1981): 43-47.

Belov, V. N. [1981b]. "Measurement of the constants for the broadening and shift of the D_2 line of rubidium (780.0 nm) by inert gases." *Optika I Spektroskopiya,* 51 (August 1981): 379-381.

Bergland, G. D.. "A guided tour of the fast Fourier transform." *IEEE Spectrum*, 6 (July 1969): 41-52.

Bernabeu, E.. "Shift and Broadening of Hyperfine Components of the First Doublet of Cesium Perturbed by Foreign Gases." *Physical Review A,* 22 (December 1980): 2690.

Blank, L., Weeks, David E., and Kedziora, Gary S.. "M + Ng potential energy curves including spin-orbit coupling for M = K, Rb, Cs and Ng = He, Ne, Ar." *Journal of Chemical Physics*, 136 (2012): 124315.

Blank, L.. PhD dissertation, Air Force Institute of Technology, in preparation.

Bransden, B. H., and Joachain, C. J.. *Physics of Atoms and Molecules*, 2 ed.. Harlow, UK: Pearson, 2003.

Brink, D. M., and Satchler, G. R.. *Angular Momentum*, 3 ed.. Oxford, UK: Oxford University Press, 1993.

Carter, Ashley H.. *Classical and Statistical Thermodynamics*. Upper Saddle River, NJ: Prentice-Hall, 2001.

Chapman, Stephen J.. *Fortran 90/95 for Scientists and Engineers*. Boston, MA: McGraw-Hill, 1998.

Child, M. S.. *Molecular Collision Theory*. Mineola, NY: Dover Publications, 1996.

Ciurylo, R.. "Shapes of pressure- and Doppler-broadened spectral lines in the core and near wings." *Physical Review A*, 58, no. 2 (August 1998): 1029-39.

Ciurylo, R., and Szudy, J.. "Speed-dependent pressure broadening and shift in the soft collision approximation." *Journal of Quantitative Spectroscopy and Radiative Transfer*, 57, no. 3 (1997): 411-23.

Ciurylo, R., and Szudy, J.. "Line-mixing and collision-time asymmetry of spectral line shapes." *Physical Review A*, 63 (2001): 042714-1-6.

Cohen-Tannoudji, Claude, Diu, Bernard, and Laloë, Franck. *Quantum Mechanics*. Singapore: John Wiley & Sons, 2005.

Cooley, J. W., and Tukey, J. W.. "An Algorithm for the Machine Calculation of Complex Fourier Series." *Mathematics of Computation*, 19, no. 90 (1965): 297-301.

Cooper, J.. "Broadening of Isolated Lines in the Impact Approximation Using a Density Matrix Formulation." *Reviews of Modern Physics*, 39, no. 1 (January 1967): 167-177.

Couture, A. H., Clegg, T. B., and Drieguys, B.. "Pressure Shifts and Broadening of the Cs D_1 and D_2 Lines by He, N_1, and Xe at Densities Used for Optical Pumping and Spin Exchange Polarization." *Journal of Applied Physics,* 104 (2008): 094912.

Dirac, Paul A. M.. *The Principles of Quantum Mechanics*, 4 ed.. Oxford UK: Oxford University Press, 1958.

Drake, Gordon W. F., ed.. *Springer Handbook of Atomic, Molecular, and Optical Physics*. New York, NY: Springer, 2006.

Edmonds, A. R.. *Angular Momentum in Quantum Mechanics*, 2 ed., rev., Princeton Landmarks in Physics series. Princeton, NJ: Princeton University Press, 1996.

Goldstein, Herbert, Poole, Charles, and Safko, John. *Classical Mechanics*, 3 ed.. New York, NY: Addison-Wesley, 2002.

Goswami, Amit. *Quantum Mechanics*. Dubuque IA: Wm. C. Brown Publishers, 1992.

Hager, Gordon D., and Perram, Glen P.. "Determination of low pressure broadening and shift rates for Cs collisions with He, Ne, and Ar from Anderson Tallman theory." In preparation.

Hartmann, J.-M., Boulet, C., and Robert, D.. *Collisional Effects on Molecular Spectra.* Amsterdam: Elsevier, 2008.

Haynes, W. M., Editor-in-Chief. *CRC Handbook of Chemistry and Physics, 92nd Edition 2011-2012.* New York NY: CRC Press, 2012.

Hindmarsh, W. R., and Farr, J. M.. "Collision broadening of spectral lines by neutral atoms." *Progress in Quantum Electronics, Vol. 2*, eds. J. H. Sanders and S. Stenholm. (Pergamon Press, 1972): 141-214.

Izotova, S. L., Kantserov, A. I., and Frish, M. S.. "Constants for broadening and shift of D_1 and D_2 rubidium 87 lines by inert gases." *Optika I Spektroskopiya,* 51 (July 1981): 196-199.

Jabłoński, Alexander. "General Theory of Pressure Broadening of Spectral Lines." *Physical Review*, 68, nos. 3-4 (August 1-15, 1945): 78-93.

Jackson, John David. *Classical Electrodynamics*, 3 ed.. Hoboken NJ: John Wiley & Sons, 1999.

Jones, John Edward [1924a]. "On the Determination of Molecular Fields.—1. From the Variation of the Viscosity of a Gas with Temperature." *Proceedings of the Royal Society of London A*, 106, no. 738 (1924): 441-462.

Jones, John Edward [1924b]. "On the Determination of Molecular Fields.—1. From the Equation of State of a Gas." *Proceedings of the Royal Society of London A*, 106, no. 738 (1924): 463-477.

Kazantsev, S. A., Kaliteevskii, N. I., and Rish, O. M.. "Application of the magnetic scanning technique for measuring the broadening and shift of the D_1 resonance line caused by inert gases." *Optika I Spektroskopiya,* 44 (April 1978): 638-643.

Kearney, W. R., and Sando, K. M.. "Classical-path theory for broadening of atomic lines by diatomic perturbers." *Physical Review A*, 46, no. 11 (December 1992): 6977-6986.

Kielkopf, J. F.. "Forces between Excited Alkali Atoms and Noble Gases." *Physical Review A*, 5, no. 2 (February 1972): 484-6.

Kielkopf, J. F.. "On the precise evaluation of the complete semiclassical spectral line shape for pressure-broadened atomic spectral lines." *Journal of Physics B*, 9, no. 9 (1976): 1601-16.

Kielkopf, J. F., and Allard, N. F.. "Observation of the Simultaneous Additive Effect of Several Xenon Perturbers on the Cs 6s-9p Doublet." *Physical Review Letters*, 43, no. 3 (16 July 1979): 196-99.

Kielkopf, J. F., and Knollenberg, R. B.. "Broadening and shift of the sodium diffuse series by noble gas." *Physical Review A*, 12, no. 2 (August 1975): 559-66.

Kincaid, David, and Cheney, Ward. *Numerical Analysis: Mathematics of Scientific Computing*, 3 ed.. Providence RI: American Mathematical Society, 2002.

Krupke, William F.. "Diode-Pumped Alkali Laser." *United States Patent*, US 6,643,311 B2 (November 4, 2003).

Krupke, William F., Beach, Raymond J., Kanz, V. Keith, and Payne, Stephen A.. "Resonance transition 795-nm rubidium laser." *Optics Letters,* 28, no. 23 (2003): 2336-2338.

Leo, P. J., Peach, G., and Whittingham, I. B.. "Investigation of sodium-helium interaction potentials." *Journal of Physics B*, 33 (2000): 4779-97.

Lewis, Charlton D., II. "Non-adiabatic atomic transitions: Computational cross section calculations of alkali metal-noble gas collisions." PhD dissertation, Air Force Institute of Technology, 2011.

Lwin, Nyunt, and McCartan, D. G.. "Collision broadening of the potassium resonance lines by noble gases." *Journal of Physics B,* 11 (1978): 3841-3849.

Messiah, Albert. *Quantum Mechanics, Volume 1*. New York, NY: John Wiley & Sons, 1966.

Mies, Frederick H., Julienne, Paul S., Band, Yehuda B., and Singer, Sherwin J.. "A convergent analysis of radiative matrix elements in atomic lineshape theory." *Journal of Physics B*, 19 (1986): 3249-3264.

Mullamphy, D. F. T., Peach, G., Venturi, V., Whittingham, I. B., and Gibson, S. J.. Collisional broadening of alkali doublets by helium perturbers." *Journal of Physics B*, 40 (2007): 1141-52.

Pathria, R. K.. *Statistical Mechanics*, 2 ed.. Oxford UK: Elsevier, 1996.

Peach, G., and Whittingham, I. B.. "The theory of line shapes relevant to the spectra of cool stars." *New Astronomy Reviews*, 53 (2009): 227-30.

Peach, G.. "Baranger Theory Revisited." *20th International Conference on Spectral Line Shapes.* Ed. J. K. C. Lewis and A. Predoi-Cross. Melville NY: American Institute of Physics, 2010.

Pitz, Greg Anthony. "Collisional dynamics of the Cesium D_1 and D_2 transitions." PhD dissertation, Air Force Institute of Technology, 2010.

Pitz, Greg A., Wertepny, Douglas E., and Perram, Glen P.. "Pressure broadening and shift of the cesium D_1 transition by the noble gases and N_2, H_2, HD, D_2, CH_4, C_2H_6, CF_4, and ^{3}He." *Physical Review A*, 80 (2009): 062718.

Pitz, Greg A., Fox, Charles D., and Perram, Glen P.. "Pressure broadening and shift of the cesium D_2 transition by the noble gases and N_2, H_2, HD, D_2, CH_4, C_2H_6, CF_4, and ^{3}He with comparison to the D_1 transition." *Physical Review A*, 82 (2010): 042502.

Press, William H., Flannery, Brian P., Teukolsky, Saul A., and Vetterling, William T.. *Numerical Recipes in C: The Art of Scientific Computing*. Cambridge UK: Cambridge University Press, 1988.

Rebane, V. N.. "Calculation of the broadening and shift of hyperfine components of rubidium and cesium D_1 lines in collisions with atoms of heavy inert gases." *Optics and Spectroscopy*, 41, no. 5 (November 1976): 526-8.

Rebane, V. N.. "Calculation of the collisional broadening and shift of the hyperfine components D_2 lines of rubidium and cesium during collisions with atoms of heavy inert gases." *Optics and Spectroscopy*, 44, no. 4 (April 1978): 376-9.

Rose, M. E.. *Elementary Theory of Angular Momentum*. New York, NY: John Wiley and Sons, 1957 (Dover edition, 1995).

Rotondaro, Matthew Don. "Collisional dynamics of the Rubidium 5^2P levels." PhD dissertation, Air Force Institute of Technology, 1995.

Rotondaro, Matthew D., and Perram, Glen P.. "Collisional Broadening and Shift of the Rubidium D_1 and D_2 lines ($5^2S_{1/2}$- $5^2P_{1/2}$, $5^2P_{3/2}$) by Rare Gases, H_2, D_2, N_2, CH_4 and CF_4." *Journal of Quantitative Spectroscopy and Radiative Transfer*, 57 (1997): 497-507.

Sakurai, Jun John. *Modern Quantum Mechanics*, rev. ed.. New York: Addison-Wesley, 1994.

Smith, Earl W., Cooper, J., and Roszman, Larry J.. "An analysis of the unified and scalar additivity theories of spectral line broadening." *Journal of Quantitative Spectroscopy and Radiative Transfer*, 13 (1973): 1523.

Szudy, J., and Baylis, W. E.. "Unified Franck-Condon treatment of pressure broadening of spectral lines." *Journal of Quantitative Spectroscopy and Radiative Transfer*, 15, no. 7-8 (1975): 641-68. Errata published in *Journal of Quantitative Spectroscopy and Radiative Transfer*, 17 (1977): 269.

Szudy, J., and Baylis, W. E.. "Profiles of line wings and rainbow satellites associated with optical and radiative collisions." *Physics Reports*, 266 (1996): 127-227.

Tannor, David J., and Weeks, David E.. "Wave packet correlation function formulation of scattering theory: The quantum analog of classical S-matrix theory." *Journal of Chemical Physics,* 98, no. 5 (1993): 3884-3893.

Tsao, C. J., and Curnette, B.. "Line-widths of pressure-broadened spectral lines." *Journal of Quantitative Spectroscopy and Radiative Transfer*, 2 (1962): 41-91.

Van Loan, Charles. *Computational Frameworks for the Fast Fourier Transform* (Frontiers in Applied Mathematics). Philadelphia PA: Society for Industrial and Applied Mathematics, 1992.

Weeks, David E., and Tannor, David J.. "A time-dependent formulation of the scattering matrix using Moller operators." *Chemical Physics Letters,* 207, no. 4 (1993): 301-308.

Weeks, David E., Niday, Thomas A., and Yang, Sang H.. "Inelastic scattering matrix elements for the nonadiabatic collision $B(^2P_{1/2}) + H_2(^1\Sigma^+_g , j) \leftrightarrow B(^2P_{3/2}) + H_2(^1\Sigma^+_g , j')$." *Journal of Chemical Physics*, 125 (2006): 164301.

Weisskopf, Victor F. [1932a]. "Zur Theorie der Kopplungsbreite und der Stoßdämpfung." *Zeitschrift für Physik,* 75 (1932): 287.

Weisskopf, Victor F. [1932b]. "Zur Theorie der Kopplungsbreite." *Zeitschrift für Physik,* 77 (1932): 398.

Zare, Richard N.. *Angular Momentum: Understanding Spatial Aspects in Chemistry and Physics*. New York, NY: John Wiley and Sons, 1988.

Zhdanov, B. V., Ehrenreich, T., and Knize, R. J.. "Highly efficient optically pumped cesium vapor laser." *Optics Communications,* 260, no. 2 (2006): 696-698.

Zhu, Cheng, Babb, James F., and Dalgarno, Alex. "Theoretical study of pressure broadening of lithium resonance lines by helium atoms." *Physical Review A*, 71 (2005): 052710.

Zhu, Cheng, Babb, James F., and Dalgarno, Alex. "Theoretical study of sodium and potassium resonance lines pressure broadened by helium atoms." *Physical Review A*, 73 (2006): 012506.

1. REPORT DATE (DD–MM–YYYY) 21-03-2013	2. REPORT TYPE Doctoral Dissertation	3. DATES COVERED (From — To) Sep 2009 – Mar 2013

4. TITLE AND SUBTITLE
Collisional Broadening and Shift of D1 and D2 Spectral Lines in Atomic Alkali Vapor – Noble Gas Systems

5a. CONTRACT NUMBER

5b. GRANT NUMBER

5c. PROGRAM ELEMENT NUMBER

6. AUTHOR(S)
Loper Jr., Robert D., Captain, USAF

5d. PROJECT NUMBER

5e. TASK NUMBER

5f. WORK UNIT NUMBER

7. PERFORMING ORGANIZATION NAME(S) AND ADDRESS(ES)
Air Force Institute of Technology
Graduate School of Engineering and Management (AFIT/ENY)
2950 Hobson Way
WPAFB OH 45433-7765

8. PERFORMING ORGANIZATION REPORT NUMBER
AFIT-ENP-DS-13-M-03

9. SPONSORING / MONITORING AGENCY NAME(S) AND ADDRESS(ES)
High-Energy Laser Joint Technology Office
801 University Blvd SE
Ste 209
Albuquerque, NM 87106
505-248-8208
Harro.Ackerman@jto.hpc.mil

10. SPONSOR/MONITOR'S ACRONYM(S)
HEL JTO

11. SPONSOR/MONITOR'S REPORT NUMBER(S)

12. DISTRIBUTION / AVAILABILITY STATEMENT
DISTRIBUTION STATEMENT A
APPROVED FOR PUBLIC RELEASE; DISTRIBUTION UNLIMITED

13. SUPPLEMENTARY NOTES This material is declared a work of the U.S. Government and is not subject to copyright protection in the United States.

14. ABSTRACT
The Baranger model is used to compute collisional broadening and shift of the D1 and D2 spectral lines of M + Ng, where M = K, Rb, Cs and Ng = He, Ne, Ar, using scattering phase shift differences which are calculated from scattering matrix elements. Scattering matrix elements are calculated using the Channel Packet Method where the collisions are treated non-adiabatically and include spin-orbit and Coriolis couplings. Non-adiabatic wavepacket dynamics are determined using the split-operator method together with a unitary transformation between adiabatic and diabatic representations. Scattering phase shift differences are thermally weighted and integrated over energies ranging from $E = 0$ Hartree up to $E = 0.0075$ Hartree and averaged over values of total angular momentum that range from $J = 0.5$ up to $J = 400.5$. Phase shifts are extrapolated linearly to provide an approximate extension of the energy regime up to $E = 0.012$ Hartree. Broadening and shift coefficients are obtained for temperatures ranging from $T = 100$ K up to $T = 800$ K and compared with experiment. Predictions from this research find application in laser physics and specifically with improvement of total power output of Optically Pumped Alkali Laser systems.

15. SUBJECT TERMS
Collisional Line Broadening, Non-Adiabatic Collisions, Alkali Metal-Noble Gas System, Optically Pumped Alkali Laser

16. SECURITY CLASSIFICATION OF:			17. LIMITATION OF ABSTRACT	18. NUMBER OF PAGES	19a. NAME OF RESPONSIBLE PERSON Dr. David E. Weeks, AFIT/ENP
a. REPORT U	b. ABSTRACT U	c. THIS PAGE U	UU	184	19b. TELEPHONE NUMBER (Include Area Code) (937)255-3636, ext 4561 David.Weeks@afit.edu

Standard Form 298 (Rev. 8–98)
Prescribed by ANSI Std. Z39.18